

**INFLUENCE OF ZINC OXIDE PARTICLE SIZE
AND SURFACE PROPERTIES ON THE
ELECTRICAL, OPTICAL AND CYTOTOXICITY
CHARACTERISTICS OF ZINC OXIDE DISCS**

SENDI RABAB KHALID M

UNIVERSITI SAINS MALAYSIA

2015

**INFLUENCE OF ZINC OXIDE PARTICLE SIZE
AND SURFACE PROPERTIES ON THE
ELECTRICAL, OPTICAL AND CYTOTOXICITY
CHARACTERISTICS OF ZINC OXIDE DISCS**

By

SENDI RABAB KHALID M

**Thesis submitted in fulfillment of the requirements
for the degree of Doctor of Philosophy**

November 2015

ACKNOWLEDGEMENTS

On this memorable night in my life when I am going to finish the writing of this thesis, first of all I bestow the thanks before Allah Almighty who invigorate me with capability to complete this research work. In the way to the completion of this thesis, my family, teachers, colleagues, and friends all contributed in different ways. At this moment I am very thankful to all of them.

I would like to express my deep sense of gratitude to my supervisor Associate Professor Dr. Shahrom Mahmud for his useful and valuable suggestions, inspiring guidance and consistent encouragement without which this thesis could have never been materialized. Thanks again Doctor for having your door open every time I needed help, even though you never had the time, you always made it.

I would like to thank all my dear colleague's friends; Amna and Prof. Dr. Fauziah for their help and encouragement. Much of this work would have been virtually impossible without the technical support offered by our helpful laboratory assistants at the School of Physics, Universiti Sains Malaysia.

My gratitude will remain incomplete if I do not mention that great supports of the Umm Al-Qura University and Cultural Mission of Royal Embassy of Saudi Arabia during whole my studies. I wish to express thanks for their help and assistance for me in every aspect of life.

Far in distance and connected in hearts, I wish to express my deepest thanks to my parents for their long time support and unconditional love. Last, and most important, I extend special thanks to my sisters and my children to accompany me during this important time in our lives. Without their endless love, patience and support, I could not have a chance to complete this study.

I offer my regards to all of those who supported me in any respect during the completion of the project, my colleges in solid-state lab and NOR lab within these 5 years of this research time.

Finally I would like to thank you for reading this thesis and I hope you will enjoy the reading.

Rabab Khalid Sendi
Pulau Pinang-Malaysia

TABLE OF CONTENTS

	Pages
ACKNOWLEDGMENTS	ii
TABLE OF CONTENTS	iii
LIST OF TABLES	ix
LIST OF FIGURES	xi
LIST OF SYMBOLS	xviii
LIST OF ABBREVIATIONS	xx
ABSTRAK	xxii
ABSTRACT	xxiv
 CHAPTER 1: INTRODUCTION	
1.1 Background of study	1
1.2 Semiconductor nanoparticle properties	4
1.3 Bioactivity of ZnO nanoparticle	7
1.4 Objectives of study	8
1.5 Scope of study	9
1.6 Design of experiment	10
1.7 Outline of study	13
 CHAPTER 2: LITERATURE REVIEW	
2.1 Introduction	15
2.2 Mechanism of surface modification through the main annealing process: recovery, recrystallization and grain growth	15

2.3	Fundamental characteristics of zinc oxide	18
2.4	Physical properties of ZnO	21
2.5	Crystal Structure of ZnO	21
2.6	Electrical properties of ZnO	22
2.7	Optical properties of ZnO	23
	2.7.1 Defects and luminescence in ZnO	23
2.8	Zinc oxide nanoparticles	27
	2.8.1 Nanoscale effects	28
2.9	Definition of zinc oxide varistor	29
2.10	Fundamental properties of zinc oxide (ZnO) varistor	33
	2.10.1 Chemistry and microstructure of varistor	33
	2.10.1.1 Interfacial Microstructure	37
	2.10.2 Electrical characteristics of ZnO varistor	39
	2.10.2.1 Nonlinear current – voltage characteristics of ZnO-based varistor	40
	2.10.3 Optical properties of ZnO varistor	41
	2.10.3.1 Recombination process	43
2.11	ZnO nanoparticles-Bi ₂ O ₃ -Mn ₂ O ₃ varistor system	45
	2.11.1 Bismuth and manganese oxides in varistor ceramic Microstructure	48
2.12	The In vitro toxicity test on ZnO-based varistor	49
	2.12.1 Cytotoxicity	50
	2.12.2 Toxicity mechanisms of ZnO nanoparticles	53
	2.12.2.1 Oxidative stress	55
	2.12.2.2 Coordination effects	56
	2.12.2.3 Non-homeostasis effects	58
	2.12.3 Cell viability	58
	2.12.4 L929 cell line	59

CHAPTER 3: METHODOLOGY

3.1	Introduction	60
3.2	Experimental Details	60
3.3	Sample preparation	65
	3.3.1 Raw materials	65
	3.3.2 Batching and ball milling	67
	3.3.3 Drying and granulating	68
	3.3.4 Pressing	68
	3.3.5 Sintering	70
	3.3.6 Electroding and encapsulating	71
3.4	Microstructural analyses	71
	3.4.1 Transmission electron microscopy	71
	3.4.2 Scanning electron microscope	74
	3.4.3 Energy-dispersive X-ray spectrometry	75
	3.4.4 Polishing process and grain size analyses	77
	3.4.5 X-Ray diffraction	78
	3.4.6 Atomic force microscope	80
3.5	Optical testing	81
	3.5.1 Photoluminescence spectroscopy	81
	3.5.2 Raman spectroscopy	83
3.6	Electrical testing	84
	3.6.1 Current – voltage (I – V) measurement	84
3.7	Cytotoxicity test	84
	3.7.1 Materials required	84
	3.7.2 Experimental procedure	87
	3.7.2.1 Cell culture	87

3.7.2.2	Growth media preparation	87
3.7.2.3	Freezing of L929 cells	87
3.7.2.4	Thawing of L929 cells	88
3.7.2.5	Cell passage (subculture)	88
3.7.2.6	Extraction process	89
3.7.2.7	Cell counting	90
3.8	Summary	92

CHAPTER 4: RESULTS AND DISCUSSION 1

PURE ZnO: EFFECT OF PARTICLE/GRAIN SIZE AND SURFACE MODIFICATION ON THE STRUCTURAL, ELECTRICAL AND OPTICAL PROPERTIES OF PURE ZnO MICRO/NANOPARTICLE BASED DISCS

4.1	Introduction	94
4.2	Physical transformation.	94
4.3	Structural properties of pure ZnO discs prepared from ZnO micro and nanoparticles size	96
4.3.1	Transmission electron microscopy (TEM)	96
4.3.2	Scanning electron microscopy (SEM)	98
4.3.3	X-ray diffraction (XRD)	106
4.3.4	Atomic force microscopy (AFM)	116
4.4	Optical properties of pure ZnO discs prepared from ZnO micro and nanoparticles size	124
4.4.1	Photoluminescence spectra (PL)	124
4.4.2	Raman spectroscopy	135
4.5	Electrical properties of pure ZnO discs prepared from ZnO micro and nanoparticles size	142
4.6	Summary	156

CHAPTER 5: RESULTS AND DISCUSSION 2

ZnO VARISTORS: COMPARISON OF STRUCTURAL, ELECTRICAL AND OPTICAL PROPERTIES OF VARISTORS MANUFACTURED FROM ZnO MICRO AND NANOPARTICLE POWDERS

5.1	Introduction	158
5.2	Growth mechanism and structural properties of composite varistor under different particle size and annealing conditions	160
	5.2.1 Scanning electron microscopy (SEM)	160
	5.2.2 X-ray diffraction (XRD)	171
5.3	Surface modification and ZnO size effects on optical properties of composite ZnO varistor	177
	5.3.1 Photoluminescence spectra (PL)	177
	5.3.2 Raman spectroscopy	185
5.4	Main annealing and ZnO size impacts on the electrical properties of composite ZnO varistors and proposed mechanism of nonlinear behaviours	188
5.5	Summary	203

CHAPTER 6: RESULTS AND DISCUSSION 3
POTENTIAL APPLICATIONS OF PURE AND COMPOSITE (VARISTOR)
ZnO DISCS FABRICATED FROM ZnO MICRO AND NANOPARTICLE
POWDERS IN BIOMEDICAL FIELD

6.1	Introduction	205
6.2	Key factors of toxicity effects	206
6.3	Biocompatibility of ZnO micro and nanoparticles-based discs	209
6.4	In vitro cytotoxicity trypan blue exclusion assay	210
6.5	Effect of different ZnO particle size and various concentrations on cell viability.	212
6.6	Cell Morphology	215
6.7	Summary	222

CHAPTER 7: CONCLUSIONS AND FUTURE WORK

7.1	Conclusions	226
7.2	Future studies	230

REFERENCES	232
APPENDIX A: AVERAGE GRAIN SIZE CALCULATION	263
APPENDIX B: X-RAY DIFFRACTION REFERENCE DATA	266
APPENDIX C: CALCULATION THE STRESS IN TABLE 4.2 FOR X-RAY PHASE ANALYSIS	273
APPENDIX D: ISO DEFINITIONS OF SOLAR IRRADIANCE SPECTRAL CATEGORIES	275
APPENDIX E: CYTOTOXICITY RAW DATA	276
APPENDIX F: RESEARCH PAPER PUBLICATIONS AND CONFERENCES	284

LIST OF TABLES

		Pages
Table 2.1.	ZnO Basic physical parameters at room temperature.	21
Table 2.2.	Electrical properties of ZnO varistor.	40
Table 3.1.	Raw material technical data.	66
Table 3.2.	Varistor batch preparation details.	67
Table 3.3.	Pressing specifications.	68
Table 3.4.	Techniques, instrumentation types and the information that are revealed in this study.	93
Table 4.1.	Summary for SEM images of ZnO discs with different annealing atmospheres.	105
Table 4.2.	Summary for XRD phase analysis of ZnO discs fabricated from micro and nanoparticles size of ZnO powders at different annealing ambients.	113
Table 4.3.	Surface roughness of the ZnO discs at different annealing ambients measured by AFM for scan areas of $5\mu\text{m} \times 5\mu\text{m}$.	122
Table 4.4.	PL and energy band gap of different discs prepared from different ZnO particles sizes at different annealing ambients.	135
Table 4.5.	A comparison of the Raman active modes of the discs fabricated from various ZnO particles sizes with the theoretical results at the different annealing ambients.	142
Table 4.6.	Summarizes the electrical properties of ZnO discs fabricated from different particles sizes of ZnO powder at as-grown and different annealing ambients.	146
Table 5.1.	Summary for SEM images of ZnO varistors with different annealing atmospheres.	170
Table 5.2.	Summary for XRD phase analysis of ZnO varistors at different annealing ambients.	174
Table 5.3.	Summarizes the PL and energy band gap of ZnO varistors at different annealing ambients.	184

Table 5.4.	A comparison of the Raman active modes of the ZnO-Bi ₂ O ₃ -Mn ₂ O ₃ varistor fabricated from micro and nano ZnO powder with the theoretical results at the different annealing ambients.	188
Table 5.5.	Summarizes the electrical properties of W4-VDR, P8-VDR, 40nm-VDR and 20nm-VDR at as-grown and different annealing ambients.	191
Table 6.1.	Summary for main different between ionic, nanoparticle and bulk of ZnO.	225

LIST OF FIGURES

		Pages
Figure 1.1.	Flowchart of experimental techniques applied in this work.	12
Figure 2.1.	Overview of processes occurring during thermal annealing and the driving forces for these processes	16
Figure 2.2.	Schematic presentation of a recovery process and dislocation motion during thermal annealing process	16
Figure 2.3.	Schematic presentation of a grain growth and boundary motion during thermal annealing process	18
Figure 2.4.	The conduction and valence bands energy relative to the vacuum relative to the vacuum level for several of semiconductor materials. The space between the top and the bottom bars explains the bandgap.	19
Figure 2.5.	SEM images of ZnO nanostructures: (a) nanoplates, (b) nanowalls, (c) nanorods and (d) nanowires.	20
Figure 2.6.	Crystal structures of ZnO.	22
Figure 2.7.	Schematic illustration of band diagram for some deep level emissions (DLE) within ZnO dependent on the full potential linear muffin-tin orbital method.	25
Figure 2.8.	Typical Varistor V-I Characteristics.	30
Figure 2.9.	(Top) Circuit scheme with voltage supply, varistor and load connected in parallel. Passive components are usually connected close to the protected device for optimum protective performance. (Bottom) When applied to a voltage surge, the varistor will cut the surge at the desired protective voltage level and the load will continue to work at non-destructive voltage levels.	32
Figure 2.10.	Summary of elements and phases present in the varistor during the sintering process and in the final compact.	34
Figure 2.11.	Scanning electron microscope (SEM) images of the microstructure of a ZnO varistor material obtained in secondary electron mode (left) and in backscattered electron mode (right). The sample surface is polished and lightly etched. ZnO grains, spinel grains and Bi-rich phases are indicated.	35

Figure 2.12.	Schematic illustration of a ternary junction among the grains at thermodynamically equilibrium [100]. Crystalline Bi_2O_3 is present in the triple grain junction, with a thin amorphous Bi-rich film lies continuously among the crystalline phases in the varistor.	38
Figure 2.13.	I – V Characterization of a ZnO varistor.	41
Figure 2.14.	PL spectrum of ZnO varistor, obtained at 5 mW excitation power at room temperature with 350 nm excitation wavelength.	42
Figure 2.15.	(a) Radiative recombination of an hole-electron pair conjugated by the phonon emission with energy $h\nu \approx E_g$. (b) In non-radiative recombination incidents, the energy emanate during the electron-hole recombination is converted to phonons.	43
Figure 2.16.	The energy levels calculated of defects within ZnO.	44
Figure 2.17.	Cell undergoing necrosis.	52
Figure 2.18.	Cell undergoing Apoptosis.	52
Figure 2.19.	Cytotoxicity Test Systems.	53
Figure 2.20.	Schematic diagram of the toxicity mechanisms of ZnO Nanoparticles. (a) Potential mechanisms of ZnO nanoparticles' entry into cells; (b) The ROS impact of intracellular ZnO nanoparticles; (c) The coordination impact of Zn^{2+} released from nanoparticles in cell; (d) The non-homeostasis impact disrupted by Zn^{2+}	55
Figure 3.1.	Experimental flowchart for sample preparation.	61
Figure 3.2.	Photos of equipment (a) Test ball mill with teflon cylinder, (b) Test pressing machine with hydraulic pressure, single punches and die, (c) CARBOLIRE sintering furnace, and (d) Annealing tube furnace.	62
Figure 3.3.	Photos of microstructural measurement equipments (a) Grinder-Polisher machine to do the polishing process for the discs, (b) Transmission electron microscopy, (c) Scanning electron microscopy with EDX function to make microstructural and elemental analyses, (d) Atomic force microscopy to analysis the morphology of the samples, and (e) X-ray diffractometer to make structural analysis.	64
Figure 3.4.	Photos of electrical measurement (a) Keithly Current-Voltage testing quipment, and (b) Typical experimental set-up for electrical measurement.	65

Figure 3.5.	Photos of (a) pure discs and (b) doped discs after sintering process.	70
Figure 3.6.	Schematic ray diagram showing the optical system of the transmission electron microscope in imaging (left) and diffraction modes (right).	73
Figure 3.7.	Schematic diagram of the scanning electron microscopy.	74
Figure 3.8.	SEM-EDX micrograph photos showing locations of EDX scanning at the grain interior (SPOT1) and at the grain boundary (GB) for ZnO varistor.	76
Figure 3.9.	Shows a schematic diagram of Bragg reflection from crystalline lattice planes having interplan distance “d” between two lattice planes.	79
Figure 3.10.	Block diagram of Atomic Force Microscope.	80
Figure 3.11.	Typical experimental set-up for PL measurements.	82
Figure 3.12.	Mouse skin fibroblast cell L929 (No: ATTC CCL-1 (Designation L929).	85
Figure 3.13.	Photos of cytotoxicity equipments (a) Bio-safety cabinet, (b) 37 °C incubator with 5% CO ₂ (c) Laboratory centrifuge device (d) Layout of Hemocytometer counting chamber with trypan blue and inverted microscope.	86
Figure 3.14.	Photos of extraction process for (a) indirect method, and (b) direct method.	90
Figure 3.15.	Layout of Hemocytometer counting chamber.	91
Figure 3.16.	Illustration of Hemocytometer counting chamber.	92
Figure 4.1.	Pure and composite ZnO-based disc transformation from granulated form to finished form.	95
Figure 4.2.	TEM micrographs of (a) White ZnO (W4), (b) Pharma ZnO (P8), (c) 40 nm ZnO, and (d) 20 nm ZnO and (INSET) a higher magnification of each ZnO type.	97
Figure 4.3.	Typical SEM-EDX images of (a) W4-Disc, (b) P8-Disc, (c) 40nm-Disc, and (d) 20nm-Disc annealed at different ambients.	104
Figure 4.4.	Plot of grain size of as-grown and annealed ZnO samples as a function of different particle sizes.	105
Figure 4.5.	XRD pattern of as-grown ZnO discs fabricated from ZnO micro and nanoparticle powders.	106

Figure 4.6.	XRD pattern of ZnO discs fabricated from (a) White ZnO (W4), (b) Pharma ZnO (P8), (c) 40 nm ZnO, and (d) 20 nm ZnO at different annealing ambients.	110
Figure 4.7.	Variation of the stress with ZnO discs prepared from different particle sizes of ZnO powder at various annealing ambients.	116
Figure 4.8.	2D and 3D AFM images, and cross section measurement along the line shown in panel of the discs prepared from different particle sizes of ZnO powder at different annealing ambients on a scan area of $5 \times 5 \mu\text{m}^2$.	122
Figure 4.9.	Plot of AFM roughness (RMS) of the ZnO samples as a function of different particle sizes.	123
Figure 4.10.	PL spectra of ZnO discs fabricated from (a) White ZnO (W4), (b) Pharma ZnO (P8), (c) 40 nm ZnO, and (d) 20 nm ZnO at different annealing ambients.	125
Figure 4.11.	Schematics of the energy band diagram for (a) as-grown, (b) oxygen annealed, and (c) after nitrogen annealed W4-Disc and P8-Disc samples.	127
Figure 4.12.	The UV and visible emissions occurring in the (a) bulk ZnO (b) unannealed and (c) annealed 20nm-Disc.	131
Figure 4.13.	Raman spectra of ZnO discs fabricated from (a) White ZnO (W4), (b) Pharma ZnO (P8), (c) 40-nm ZnO, and (d) 20-nm ZnO at different annealing ambients.	137
Figure 4.14.	Current-voltage characteristics of ZnO discs fabricated from different size of ZnO powders at different annealing ambients.	143
Figure 4.15.	Mechanism of Zener and Avalanche breakdown voltage.	145
Figure 4.16.	Plot of breakdown voltage of as-grown and annealed ZnO samples as a function of different particle size.	146
Figure 4.17.	Plot of nonlinear coefficient α of as-grown and annealed ZnO samples as a function of different particle sizes.	147
Figure 4.18.	Plot of resistivity of as-grown and annealed ZnO samples as a function of different particle sizes.	147
Figure 4.19.	Core shell structure of nanoparticles grains for (a) as-grown and (b) annealed ZnO nanoparticles.	148
Figure 4.20.	Schematic diagram of band bending after chemisorptions of oxygen during annealing process. E_F , E_C , and E_V indicate the energy of the Fermi level, conduction band and the valence band, respectively, while Λ_{air} indicates the thickness of the depletion layer,	152

and eV_{surface} indicates the potential barrier. The conducting electrons are illustrated by e^- and $+$ illustrated the donor sites.

Figure 4.21.	A model characterization the junction between two ZnO nanoparticles having adsorbed oxygen in the pores. Upward band bending due to oxygen promotes the contact potential between the nanoparticles.	154
Figure 4.22.	Structural and band modes showing the role of intergranular contact regions in determining the conductive mechanism during the annealing process. In (a) oxygen and (b) nitrogen atmospheres.	155
Figure 5.1.	Energy band diagram of a double Schottky barrier in equilibrium.	159
Figure 5.2.	Typical SEM-EDX images of (a) W4-VDR, (b) P8-VDR, (c) 40nm-VDR, and (d) 20nm-VDR annealed at different ambients.	169
Figure 5.3.	Plot of grain size of as-grown and annealed ZnO samples as a function of different particle sizes.	170
Figure 5.4.	XRD pattern of ZnO-Bi ₂ O ₃ -Mn ₂ O ₃ varistor system fabricated from (a) White ZnO (W4), (b) Pharma ZnO (P8), (c) 40 nm ZnO, and (d) 20 nm ZnO at different annealing ambients.	172
Figure 5.5.	Plot of (101) peak intensity of as-grown and annealed composite ZnO varistors as a function of different particle sizes.	174
Figure 5.6.	Plot of diffraction angle of as-grown and annealed composite ZnO varistors as a function of different particle sizes.	175
Figure 5.7.	Plot of FWHM of as-grown and annealed composite ZnO varistors as a function of different particle sizes.	175
Figure 5.8.	PL spectra of ZnO-Bi ₂ O ₃ -Mn ₂ O ₃ varistor system fabricated from (a) White ZnO (W4), (b) Pharma ZnO (P8), (c) 40 nm ZnO, and (d) 20 nm ZnO at different annealing ambients.	177
Figure 5.9.	The impact of bandbending on the excitation. With weak luminescence intensity (a), the created charge carriers are divided in space, leading to low quantum efficiency. With higher luminescence intensity (b), the photoexcited charge carriers diminish the bandbending, leading to a higher PL energy as well as strengthens quantum efficiency.	180

Figure 5.10.	Schematic illustration of the energy band diagram proposed for ZnO nanoparticles.	183
Figure 5.11.	Raman spectra of ZnO-Bi ₂ O ₃ -Mn ₂ O ₃ varistor system fabricated from from (a) White ZnO (W4), (b) Pharma ZnO (P8), (c) 40 nm ZnO, and (d) 20 nm ZnO at different annealing ambients.	185
Figure 5.12.	Current-Voltage characteristic of ZnO-Bi ₂ O ₃ -Mn ₂ O ₃ varistor system fabricated from different sizes of ZnO powders at different annealing ambients.	189
Figure 5.13.	Plot of breakdown voltage of as-grown and annealed ZnO samples as a function of different particle sizes.	191
Figure 5.14.	Plot of nonlinear coefficient α of as-grown and annealed ZnO samples as a function of different particle sizes.	192
Figure 5.15.	Plot of resistivity of as-grown and annealed ZnO samples as a function of different particle sizes.	192
Figure 5.16.	Band diagram of the double (back-to-back) Schottky barrier across ZnO grain boundaries (a) before contact, (b) at equilibrium state, and (c) at non-equilibrium conditions.	195
Figure 5.17.	The grain boundary defect model for the (Bi ₂ O ₃ , Mn ₂ O ₃)-composite ZnO varistors.	198
Figure 5.18.	Electronic and atomic defect model suggested for the potential barrier formation in ZnO-Bi ₂ O ₃ -Mn ₂ O ₃ varistors.	201
Figure 6.1.	Schematic overview summarizing the factors responsible for toxic effect of ZnO NPs.	207
Figure 6.2.	Percentage of cell viability and dead cell of L929 at (a) W4-Disc, P8-Disc, 40nm-Disc and 20nm-Disc, and (b) W4-VDR, P8-VDR, 40nm-VDR and 20nm-VDR after 72 hours in cultured with L929. Mean \pm SD (n = 3). (ANOVA) followed by Bonferroni correction suggested statistically obvious variation when compared with control (*P \leq 0.05).	211
Figure 6.3.	Percentage of cell viability of L929 at different concentration (%) of (a) W4-Disc, P8-Disc, 40nm-Disc and 20nm-Disc, and (b) W4-VDR, P8-VDR, 40nm-VDR and 20nm-VDR. Mean \pm SD (n = 3). (ANOVA) followed by Bonferroni correction suggested statistically obvious variation when compared with control (*P \leq 0.05).	213
Figure 6.4.	Cell morphology of L929 after 72 hours in culture medium, untreated with ZnO (Control).	217

Figure 6.5. Cell morphology of L929 after 72 hours in culture medium at (a) 25; (b) 50; (c) 75; and (d) 100 concentrations ($\mu\text{g/ml}$) of pure and composite discs made from different particle sizes of ZnO powder.

221

LIST OF SYMBOLS

ρ	Resistivity of material
V	Potential difference across a material
V_b	Breakdown voltage
I	Current flowing through the material
R	Resistance of the material
α	Non-linearity degree of the conduction of varistor
Σ	Mean stress in ZnO
λ	Optical wavelength
Φ_B	Schottky barrier height
Φ_m	Metal work function
E_{CB}	Conduction band energy level
E_{VB}	Valence band energy level
E_F	Fermi level of semiconductor
E_g	Energy band gap
h	Plank's constant
c	Uniaxial lattice constant
d_{hkl}	Interplanar spacing of the crystal planes
e^*	Effective charge
$2\theta-w$	2 theta-omega scan mode for XRD measurements
n	Number of Wigner-Seitz cells per unit volume
O_2^-	Superoxide anion
H_2O_2	Hydrogen peroxide
$\bullet OH$	Hydroxyl radical
E	Energy

d	Lattice place distance
p	Statistical p -value
ε_z	Strain
σ	Stress
e	electron
D	Grain size
V_O	Oxygen vacancy
V_{Zn}	Zinc vacancy
Zn_i	Zinc interstitial
O_i	Oxygen interstitials
Zn_O	zinc anti-sites
O_{Zn}	oxygen anti-sites

LIST OF MAJOR ABBREVIATIONS

VDR	Voltage-dependent resistor
Bi_2O_3	Bismuth (III) oxide
Mn_2O_3	Manganese (III) oxide
XRD	X-ray diffraction
SEM	Scanning electron microscope
EDX	Energy dispersive X-ray
TEM	Transmission electron microscopy
AFM	Atomic force microscope
PL	Photoluminescence
I-V	Current-voltage
UV-VIS	Ultraviolet-visible
CBM	Conduction band minimum
VBM	Valence band maximum
DSB	Double Schottky Barrier
GB	Grain boundary
e-beam	Electron beam
FWHM	Full width at half maximum
LED	Light emitting diode
MBE	Molecular beam epitaxial
NBE	Near band edge
DLE	Deep level emission
RMS	Root mean square
SC	Semiconductor
MOS	Metal Oxide Semiconductor

MOV	Metal Oxide Varistor
R_g	Grain Resistance
R_{gb}	Grain Boundary Resistance
bcc	Body-centred cubic structure
hcp	Hexagonal close-packed structure
dc	Direct current
ac	Alternating current
DMEM	Dulbecco's Modified Eagle Medium
PBS	Phosphate Buffer Saline
FBS	Fetal Bovine Serum
ROS	Reactive oxygen species
TO	Transverse optical
LO	Longitudinal optical
V_o	Oxygen vacancy
Zn_i	Zinc interstitial
OD	Optical density

PENGARUH SAIZ PARTIKEL DAN SIFAT PERMUKAAN ZINK OKSIDA TERHADAP CIRI KEELEKTRIKAN, KEOPTIKAN DAN KESITOTOKSIKAN CAKERA ZINK OKSIDA

ABSTRAK

Kesan saiz butiran / partikel yang berbeza dan pengubahsuaian permukaan melalui penyepuhlindungan haba, struktur elektrik, dan sifat optik daripada cakera ZnO tulen dan koposit (varistor) yang difabrikasi daripada mikro atau nanopartikel ZnO dikaji dalam kajian ini berhubung dengan ketoksikan mereka. Empat sampel ZnO dengan saiz berbeza iaitu ZnO-White, ZnO-Pharma, 40nm ZnO dan 20nm-ZnO dicirikan. Sifat keelektrikan dan struktur bagi cakera-cakera W4, P8, 40nm dan 20nm amat dipengaruhi oleh ambient penyepuhlindungan, khususnya cakera yang disepuh lindap dalam ambien oksigen. Selepas resinteran pada 1200 °C dalam udara, saiz butiran ialah 1.701, 1.523, 2.610, dan 3.423 μm bagi cakera W4, P8, 40nm dan 20nm, masing-masing. Penyepuhlindungan oksigen juga meningkatkan kehabluran butiran sebagaimana yang digambarkan oleh transformasi tegasan mampat daripada -0.784 , -0.601 , -0.349 , dan -0.261 terhadap tegasan tegangan (tensile stress) pada 0.174, 0.087, 0.697, dan 1.046 bagi cakera-cakera W4, P8, 40nm dan 20nm, masing-masing. Puncak (101) sampel meningkat secara signifikan daripada $2\theta = 36.195^\circ$, 36.212° , 36.334° , dan 36.381° kepada $2\theta = 36.230^\circ$, 36.271° , 36.350° dan 36.385° , masing-masing. Keamatan puncak menggambarkan darjah kehabluran yang tinggi pada cakera 20nm. Jurang jalur optik berkurangan dengan pertambahan saiz butiran dan berkurangan dengan pertambahan tegasan tegangan. Cakera-cakera ZnO yang dibuat dari partikel lebih halus mempamerkan prestasi elektrik yang lebih baik dengan pengurangan voltan pecah daripada 340 V (W4-Disc) kepada 110 V (20nm-Disc) dan kerintangan daripada 362.4 k Ω .cm (W4-Disc) kepada 98.86 k Ω .cm (20nm-Disc). Struktur fizikal, dan sifat elektrik cakera ZnO yang difabrikasi dalam kajian ini membuktikan bahawa serbuk nano ZnO boleh menjadi pilihan yang terbaik bagi fabrikasi varistor ZnO. Sistem varistor ZnO–Bi₂O₃–Mn₂O₃ yang difabrikasi daripada serbuk ZnO dengan saiz partikel yang berbeza berjaya dihasilkan.

Kesan daripada beberapa penyepuhlindapan dalam atmosfera yang mengoksida dan lengai dikaji dengan teliti. Pertumbuhan butiran varistor berasaskan ZnO didapati meningkat dengan penambahan Bi_2O_3 dan Mn_2O_3 . Pancaran UV optimum diperhatikan dalam varistor yang disepuh lindap dalam atmosfera O_2 , yang konsisten dengan keputusan XRD. Ciri-ciri voltan (I-V) arus bukan linear yang terbaik (I-V) daripada 20 nm-VDR, dengan voltan pecah (218 V) yang rendah dan kerintangannya ($3887.4 \text{ k}\Omega\cdot\text{cm}$) adalah disebabkan oleh sawar keupayaan yang terbentuk di antara butiran ZnO jika dibandingkan dengan W4-VDR. Ketoksikan pelbagai saiz partikel dalam cakera ZnO tulen dan komposit (varistor) disaring oleh asai *vitro trypan blue* pada sel tikus (L929). Keputusan menunjukkan bahawa W4-ZnO, P8-ZnO, 40nm-ZnO dan 20nm-ZnO menyebabkan ketidakfungsian sel mitokondria, apoptosis, perubahan morfologi pada kepekatan 25–100 $\mu\text{g}/\text{ml}$, dan darjah ketoksikan mempamerkan kebergantungan pada dos. Ketoksikan yang tinggi diperhatikan dalam 20nm-VDR, dan diikuti oleh 40nm-VDR, P8-VDR, dan W4-VDR.

INFLUENCE OF ZINC OXIDE PARTICLE SIZE AND SURFACE PROPERTIES ON THE ELECTRICAL, OPTICAL AND CYTOTOXICITY CHARACTERISTICS OF ZINC OXIDE DISCS

ABSTRACT

The effects of different particle/grain sizes and surface modification by thermal annealing process on the structural, electrical, and optical characteristics of pure and composite (varistors) ZnO discs fabricated from ZnO micro or nanoparticles were investigated in this study with respect to their toxicity. Four ZnO powder samples with different particle sizes namely ZnO-White (130 nm), ZnO-Pharma (80 nm), 40nm-ZnO and 20nm-ZnO were characterized. ZnO-White is abbreviated as W4 while ZnO-Pharma as P8. The structural and electrical properties of the W4-Disc, P8-Disc, 40nm-Disc and, 20nm-Disc were strongly affected by the annealing ambient, which was more obvious for the discs annealed in oxygen atmosphere. After sintering at 1200 °C in air, the grain sizes were 1.701, 1.523, 2.610, and 3.423 μm for W4-Disc, P8-Disc, 40nm-Disc and 20nm-Disc, respectively. Oxygen annealing also enhanced the grain crystallinity as clarified by transformation of compressive stress from -0.784 , -0.601 , -0.349 , and -0.261 to tensile stress at 0.174 , 0.087 , 0.697 , and 1.046 for the W4-Disc, P8-Disc, 40nm-Disc and 20nm-Disc, respectively. The (101) peaks of the samples increased significantly from $2\theta = 36.195^\circ$, 36.212° , 36.334° , and 36.381° to $2\theta = 36.230^\circ$, 36.271° , 36.350° , and 36.385° , respectively. The intensity of the peaks reflected the high degree of crystallinity of the 20nm-Disc. The optical band gap decreased with increasing grain size and decreased with increasing tensile stress. The ZnO discs made from finer particles exhibited better electrical performance with a pronounced drop in the breakdown voltage from 340 V (W4-Disc) to 110 V (20nm-Disc) and resistivity from 362.4 k Ω .cm (W4-Disc) to 98.86 k Ω .cm (20nm-Disc). The physical, structural, and electrical properties of the ZnO discs fabricated in this study proved that ZnO nano-powder

can be the best candidate for ZnO varistor fabrication. The ZnO–Bi₂O₃–Mn₂O₃ varistor system fabricated from ZnO powder with different particles sizes was successfully produced. The effects of thermal annealing in oxidizing and inert ambients were briefly investigated. The grain growth of ZnO-based varistors can be markedly enhanced by adding both Bi₂O₃ and Mn₂O₃. Optimal UV emission was observed in the varistor annealed in O₂ atmosphere, which is consistent with XRD results. The superior nonlinear current–voltage (I–V) behavior of 20 nm-VDR, with lower breakdown voltage (218 V) and resistivity (3887.4 kΩ·cm) was due to the potential barriers created between successive grains of ZnO if compared with W4-VDR. The toxicity of various particles sizes of pure and composite (varistor) ZnO discs were screened by in vitro trypan blue assay on mouse (L929) cells. Results showed that the W4-ZnO, P8-ZnO, 40nm-ZnO and 20nm-ZnO caused cellular mitochondrial dysfunction, apoptosis, and morphological modifications at a concentration of 25–100 µg/ml, and the degree of toxicity exhibited a dose-dependent manner. The highest toxicity was observed in 20nm-VDR followed by 40nm-VDR, P8-VDR, and W4-VDR.

CHAPTER 1

INTRODUCTION

1.1 Background of study

ZnO has attracted considerable interest of investigators due to its promising use in varistors, electronics, sensors, and optoelectronics. ZnO has 3.3 eV direct band gap energy at room temperature and a 60 meV exciton binding energy that provides an extremely high degree of stability for excitonic transitions. These characteristics make ZnO a promising substance for UV optoelectronic employments such as UV light emitting diodes and photo detectors [1-3]. ZnO has a crystalline wurtzite structure that exhibits strong piezoelectric characteristics because its c-axis is directed perpendicular to the substrate [4, 5]. These properties of ZnO, as well as its transparency to visible light and gas-sensing capability, make ZnO one of the most important materials in varistor devices, gas sensors [6, 7], surface acoustic wave devices [8, 9] and solar cells [10]. These notable essential properties of ZnO could be enhanced by nanotechnology. ZnO nanoparticles with improved electrical and optical properties and increased surface areas have the ability to improve varistor, gas sensor, optoelectronic, and biosensor applications [11].

The development of ZnO varistors has been one of the great successes for ceramics. In 1970, varistors were initially developed by Matsuoka [12] through solid-state admixture of ZnO and several of metal oxide additives, and this method is still preferred in the industry [13, 14]. This method involves mixing of ZnO micro-particles with dopant oxides, such as Mn_2O_3 , Bi_2O_3 , Sb_2O_3 , CoO , Cr_2O_3 , and NiO . The mixed powder is compressed with a pressure of 4 ton/cm^2 and then sintered at elevated temperatures (1200–1300 °C). This simple preparation method has led to its action in the industrial field. The very low cost related with the usage of relatively inexpensive oxide powders is likewise commercially attractive. However, the major disadvantage in use this process is its high manufacturing

temperature (exceeding 1100 °C), which causes zinc to vaporize consequently causing problems in quality. Moreover, compositional homogeneity is difficult to attain, which is significant for the construction of the miniature devices desired for modernistic electronic supplies [13, 14].

Methods of preparation, additive homogeneity, and size of crystallite are evaluative parameters in the production of better varistor devices [15-26]. Heterogenous microstructures can cause varistors deterioration during electrical performance [13]. Electronic and electrical behaviors depend on different the microstructure at the ZnO grain boundaries [14, 24, 27]. Therefore, the microstructure precise control is desired to manufacture high-performance varistors.

In compared with coarse-grained ceramics, nanoparticles can be sintered at a minimal temperature due to narrow grain size distribution in nanoparticles [14, 24, 27, 28]. Sintering temperature also depends on the dopants distribution between the singular grains and the particle size. Nanomaterials have significant volume of boundaries among the grains and must consequently allow additional effective grain boundaries per unit volume, permitting the development of a superior device with minimal dimensions. However, precise control in the growth of grain during sintering process is an essential challenge in ZnO nanoparticle investigation. Ya et al. [26] used zinc nitrate, ethylene glycol and citric acid to prepare 20 nm ZnO. But, sintering temperature and dopant additive generated 2 μm grains. At the molecular level, the dopant ions homogeneity between the ZnO grains is achievable by use wet chemical methods, which is complicated to produce by using any conventional ceramic method.

Different efforts have been reported for manufacture of the varistor devices by chemical methods [12, 21, 24, 27]. ZnO nanoparticles with improved electrical properties and increased surface areas have the potential to produce advanced varistors with better properties. Moreover, varistors of core-shell type, which made by using coating metal salts on sintered ZnO nanoparticles yielded excellent electrical behaviors, which were caused by

the superior homogenous dispersion of dopants ions between the grains [12]. Furthermore, the varistor densification gained by sintering process at 1050 °C was inadequate for optimum industrial fabrication [12, 19-21]. Therefore, a modern industrial method that can produce a fully dense varistor with superior electrical properties at lower sintering temperature is needed. In this work, ZnO nanoparticles were used for fabrication of a high-performance varistor with lower breakdown voltage compared with commercial samples. ZnO nanoparticles have high densification at lower sintering temperature.

Thermal annealing process is also vastly applied to develop crystal quality and reduce structural defects in substances. During thermal treatment, other structural defects, dislocations, and decomposition/ adsorption may happen on the material surface; so, the ratio of stoichiometric and structure change (Yang et al. 2008) [29]. The electrical and optical properties of varistors are controlled by sintering, annealing, or atmospheric temperatures, which significantly affect the crystallization and densification of thin varistors. A reduction of varistor resistivity is achieved during the thermal annealing step if microstructure optimization and formation of free electrons or oxygen vacancies are obtained [28].

Through thermal annealing treatment, diverse diminution ambients with single gas or two gases have been introduced to improve the electrical conductivity of varistors. In 1992, Butkhuzi et al. [30] used oxygen annealing treatment of ZnO to produce intrinsic p-type conduction for the first time. Subsequent, Xiong et al. [31] achieved essential p-type ZnO through modifying the oxygen partial pressure during sputtering. Several studies were also reported comparable results [31-33]. A considerable number of studies attributed the formation of defects in materials to the sensitivity of the concentration and type of intrinsic defects within ZnO to the thermal treatment conditions [34-38].

Studies on thermal annealing of different particle sizes of ZnO powder, such as W4-ZnO, P8-ZnO, 40nm-ZnO, and 20nm-ZnO, remain inconclusive. Further studies are desired to investigate the surface defect and optoelectronic properties of annealed ZnO under various atmospheres. The non-stoichiometric chemical component within the materials is related to

the defects formation, predominantly oxygen vacancies. Numerous studies are wanted to observe and relate the modifications on the surface of ZnO ions and oxygen concentration after annealing of samples in ambient oxygen-rich or oxygen-deficient environments. Differences in the properties are attributed to the effects of the band bending of sample surface and the oxygen to zinc ratio (O:Zn), which will be studied in this work.

In a majority of experiments, the temperatures of thermal annealing were usually below 700 °C, which was presumed adequate for the effective control of intrinsic defects in ZnO. Annealing significantly affects the various characteristics of the samples such as structural properties. At minimal temperatures of annealing process, the crystal quality can be improved as the defects reduce within the sample. At maximal temperatures of annealing, recrystallization of the samples changes the amount and type of defect. Different characteristics could be achieved above the annealing temperature of 700 °C. In fact, previous studies demonstrated that annealing at high temperatures improves the crystal quality of ZnO varistors and changes the O:Zn and defects of the sample [39].

1.2 Semiconductor nanoparticle properties

The last few years have shown a significant rise in semiconductor nanoparticles researches following the great studies related to the study of the quantum size impacts in these particles by Efros and Efros [40], and Brus [41]. Experimental researches proved that most of the physical properties were affected by semiconductor nanoparticles size less than 100 nm. For example, the band gap in the prototypical material, CdS, can be changed from 2.5 eV to 4 eV [42], the temperature of melting also varies between 400 °C and 1600 °C [43-45], and the pressure required to produce conversion from a four to a six-coordinate phase raised from 2 GPa to 9 GPa [46]. These observed changes in the fundamental properties of CdS were caused by decreasing the crystal size, not changing the chemical composing. These changes in the fundamental properties of semiconductor nanoparticles can be attributed to two factors, namely, the quantum size effects, which are the effects of the

quantum confinement of the charge carriers within the materials, and the large S/V ratio of the nanoparticle compared with the corresponding bulk semiconductor.

The most important effect of quantum confinement on semiconductor nanoparticles is the widening of the energy band gap. This electronic structure change leads to major changes in the optical properties of the nanoparticle compared with its bulk counterpart. Variations in the electrical and optical properties resulting from variation of a systematic transformation in the density of electronic energy levels with the particles size are also observed. Qualitatively, it is likened to a small particle within a box problem, in which the levels of energy become discrete accordingly the box dimensions are decreased because of quantum confinement [44]. This illustration gives a depiction of the increment in energy band gap in accordance with reducing particle size. Several methods have been used for quantitative investigations of these effects. The most commonly used methods are the empirical pseudo potential approach [41], effective mass approximation (EMA) approach [41, 44, 47, 48], and tight binding method [49, 50]. Calculation results of the energy band gaps by EMA conforms to the experimental results for larger nanoparticles, but are usually overestimated for smaller particles.

Although several theoretical explanations of the quantum-size effect of semiconductor nanoparticles exist, UV-visible absorption spectroscopy is most widely applied in determining the variation of band gap as a function particle size, according to the absorption threshold compatible to the direct band gap in the sample. The evident blue shift of the absorption edge in the absorption spectra possible to be caused by the decrease in size of particles [51]. An important observation in semiconductor spectroscopy is the presence of the weakly bound Mott-Wannier excitons. These excitons have a considerable impact on the material optical absorption characteristics. The photon-induced transitions among the hydrogen atoms, similar to the system of energy levels of the excitons, produce a series of absorptions peaks in the spectra. Quantum confinement in semiconductor nanoparticles results in a blue shift of these excitonic absorption features toward higher energies with a

decrease in particle size [51]. This blue shift is observed when the size of the nanoparticle becomes comparable with the exciton Bohr radius. Furthermore, this shift is caused by the improved spatial overlap of the hole and electron wave functions with restricted translational motion of the exciton in the decreasing size of particle. Consequently, the motion of the hole and electron is enhanced and the exciton binding energy is increased. The increase in exciton binding energy of nanoparticles allows visibility of excitonic absorption peaks at room temperature. However, the electron–hole interaction becomes independent and the exciton is absent when nanoparticles are significantly smaller than the exciton Bohr radius [44].

Most of the atoms located on the surface of nanoparticles greatly contribute to optical properties compared with their bulk counterpart. A strong perturbation to the surface of any lattice results in numerous dangling bonds. In nanoparticles, these dangling bonds create a high concentration of deep or shallow levels of energy in the band gap. These surface states act as electron hole recombination centers, causing non-radiative transitions of holes and electrons prior to the radiative recombination, thereby causing emissions at lower energies than the nanoparticles band gap energy. Deterioration of the optical properties is more apparent in nanoparticles than in bulk semiconductors because of the larger contribution of atoms on the surface of nanoparticles. Passivation techniques have been employed by bonding the surface atoms with different material that a much larger band gap to improve the properties [52, 53].

The thermodynamic properties of nanoparticles differ from their bulk counterparts; the differences are caused by the atoms on their surface. The decrease in particle size results in the decrease in solid to liquid transition temperature [54-56]. In nanoparticles, a great atoms proportion are stabilized at the surface accompanied by significant energy, which accounts for the change in thermodynamic properties. Melting presumably begins on the surface as a result of the reduction of total surface energy from the solid phase. Smaller nanoparticle leads to more dramatic reduction of melting temperature. Likewise, the

necessary pressure in solid to solid transformations of nanoparticles differs from that required by their bulk counterparts [57].

The above mentioned findings are just some of the important characteristics of semiconductor nanoparticles, which account for the rapid development of this science. The steady improvement in the range of materials for nanoparticles is expected to continue in the future. Current developments in semiconductor nanoparticles provide sufficient quality basis for future generations of experiments on the functional integration of these nanoparticles into devices. A critical application lies on the dependence of varistor properties on nanoparticle size; that is, one type of semiconductor can be used to produce different kinds of varistors with different properties simply by changing the particle diameter. The large surface-area-to-volume ratio of nanoparticles is currently undergoing research for its applications in varistors.

1.3 Bioactivity of ZnO nanoparticle

The scientific and technological developments of nanoparticles are accompanied by a rising exposure of humans to nanomaterials; thus, bioaccumulation and complex physical and chemical interactions may also arise. These possibilities mandate the development and validation of protocols used in the characterization of delicate nanodevices and nanoparticles, which could predict hazardous and toxic reactions. These protocols must accurately predict and assess positive and negative results, including possible hazards and health risks related to exposure to nanoparticles, as their use is becoming more extensive in medicine and manufacturing. With the commercialization of nanotechnology products, exposure of human to nanoparticles will significantly increase, and an assessment of their potential toxicity is fundamental. Lately, several manufactured nanoparticles have exhibited adverse effects in vitro and in vivo [58-60]. These nanoparticles have a number of unique physiochemical properties attributed to their small size, surface structure, chemical composition, solubility, aggregation, and shape [58]. Harmful reactions of organisms to

engineered nanostructures cannot be screened because of the lack of information on the effects of the abovementioned properties on biological systems [61]. Hence, a new sub discipline of nanotechnology named nanotoxicology has emerged.

Various studies have proposed that in vitro nanotoxicity data can minimize animal testing by identifying a suitable starting dose for in vivo studies and limiting the quantity of toxic waste generated [62]. In vitro methods can be applied to evaluate toxic kinetic parameters affecting organs; thereby increasing the accuracy of predictions and decreasing animal testing under controlled conditions [63]. Toxic kinetics is essentially the study of "how a substance gets into the body and what happens to it in the body". Four processes are involved in toxic kinetics: absorption, distribution, biotransformation, and excretion. A considerable number of methods have not been evaluated for relevance and reliability, and their limitations in diagnosing serious toxicity have not been identified. Furthermore, published data in the biological activity of ZnO micro- and nanoparticle-size-based discs is poorly understood. There are only a few published reports on this subject, even though that ZnO-based discs can induce of inducing apoptosis and cell death or inflammatory responses. Further research studies are needed to assess the risks and applications of these materials [64].

The purpose of this experiment was to determine the cytotoxicity level of ZnO micro- and nanoparticle-size-based discs. The cytotoxicity of these materials was investigated by mouse skin fibroblast cells (L929) in vitro assay.

1.4 Objectives of study

The aim of this research was to develop the microstructure of high-voltage varistor materials, with focus on the various particle sizes of ZnO powder and different annealing conditions. This work dealt with the microscopic characteristics of ZnO and their impacts on the electrical, optical, and structural characteristics of ZnO varistors. The specific objectives of the research include the following:

1. To study the effects of different particle sizes of ZnO powder on the electrical, optical, and structural properties of pure ZnO discs.
2. To study the effect of annealing in ambient oxygen-rich or oxygen-deficient conditions on the surface properties of pure ZnO discs.
3. To fabricate ZnO–Bi₂O₃–Mn₂O₃ varistor discs and to investigate the effect of surface modification and different particle sizes of ZnO powder on the different properties of these varistor composites.
4. To investigate the in vitro cytotoxicity of pure and composite ZnO discs using connective mouse skin fibroblast cells (L929).

The electrical, optical, and structural characteristics of pure and doped (varistors) ZnO discs have been studied by several non-destructive and non-contact equipment, which include structural characterizations, such as transmission electron microscopy (TEM), scanning electron microscopy (SEM), energy dispersive X-ray (EDX), X-ray diffraction (XRD), and atomic force microscopy (AFM), whereas the electrical and optical characterizations include I-V testing and photoluminescence (PL) spectroscopy.

In general, this work gives a superior understanding of the fundamental properties of pure ZnO discs and ZnO varistors fabricated from ZnO micro- and nanoparticle.

1.5 Scope of study

A possible scope of research was defined to determine the direction for this work; considering that research on the particle size of ZnO covers a wide area. Only discoveries and results related to the scope were cited in the thesis.

Nanomaterials can be defined as a length scale of less than 100 nm, either in one dimension (thin films), two dimensions (nanowires), or in all three dimensions (nanoparticles). This thesis focused on the three dimensional nanostructured materials. The main scope of this thesis is to demonstrate how varistor properties can be modified by ZnO properties either directly by size or indirectly by modification of the oxide additives or surface modification through thermal annealing under different conditions. This thesis consists of three main parts:

In the first part, the preparation of pure ZnO discs fabricated from different sizes of ZnO particles through the conventional ceramic method is investigated. Characterization of discs that underwent different annealing treatments was also carried out. In this part, the aim was to obtain the standard conditions for manufacturing ZnO varistors with optimal properties and lower fraction voltage values.

The second part of this thesis focused on the use of ZnO micro- and nanoparticles for varistor preparation. This part includes studies on the effect of oxide additives (Bi_2O_3 and Mn_2O_3) on the particle growth of ZnO, and a comparison of the electrical optical behaviors between composite varistors and pure ZnO discs. Furthermore, modifications on the surface of varistor samples annealed under different conditions were studied.

The last part of the thesis is focused on the cytotoxicity studies of pure and composite (varistors) ZnO discs in animal cells (L929). These studies provide rule for the effective use of these varistors devices in both medical and non-medical fields.

1.6 Design of experiment

The experimental techniques applied in this work can be divided into six major sections, namely sample preparation, annealing process, microstructural testing, electrical testing, optical testing and cytotoxicity testing.

Four types of ZnO powder was used to make the ZnO discs and varistors, which include ZnO-White (W4), ZnO-Pharma (P8), 20nm-ZnO (MK Nano) and 40nm-ZnO (MK Nano).

Different types of samples were annealed in ambient oxygen or nitrogen at 700 °C. Moreover, structural, optical and electrical behaviors may be altered through various annealing conditions such as period, pressure and type of gas, and annealing temperature.

Microstructural tests that were investigated involve particle size test. Transmission electron microscopy (TEM) and scanning electron microscopy & energy dispersive X-ray analysis (SEM/EDX). Atomic force microscopy (AFM) was investigated to study the morphology and surface structure of samples. The crystalline phases were carried out by using a high resolution X-ray diffractometer (XRD).

The I–V behaviors of the materials were obtained employment a high voltage source measure unit. The values of α , ρ and V_b was evaluated from Current (I) - Voltage (V) characteristics.

Photoluminescence (PL) spectra were conducted at room temperature. Raman spectroscopy was obtained as a supplementary tool to determine structural information.

The cytotoxicity test was conducted to show the toxicity level of different samples towards specific live cells.

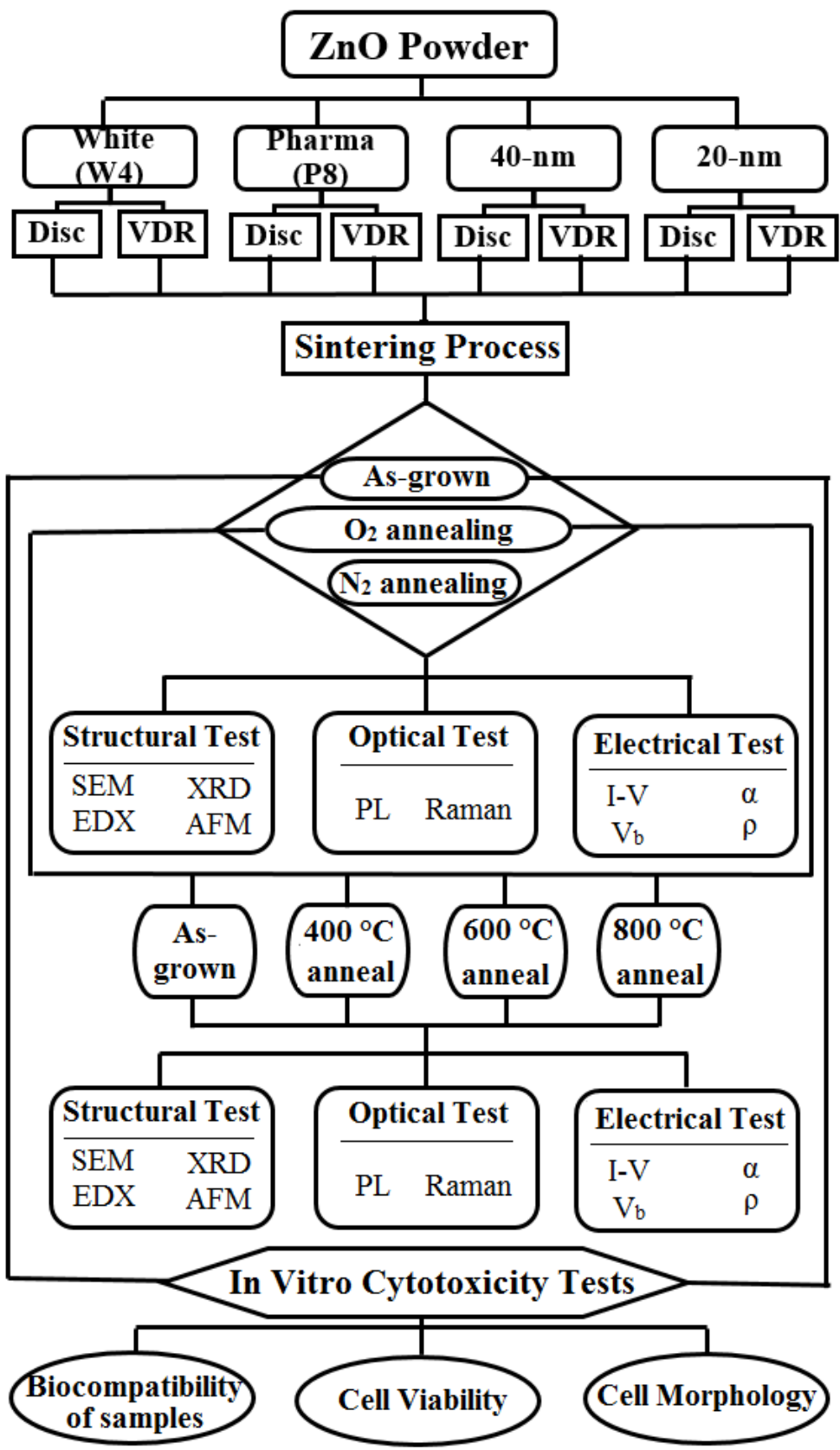


Figure 1.1. Flowchart of experimental techniques applied in this work

1.7 Outline of study

The thesis contains an introductory chapter on the general properties and usage of ZnO powder. The development of varistor properties through annealing and nanotechnology is also introduced. This chapter is intended to be understandable even for the non-physicist. The objectives, scope, and design of this work is also presented in this chapter.

Chapter 2 gives a brief literature review on other work that has been carried out on the mechanism of surface modification through the main annealing processes of as grown and annealed (in oxygen or nitrogen) W4-Disc, P8-Disc, 40nm-Disc and 20nm-Disc. Then, the fundamental properties (physical, structural, electrical, and optical) of ZnO micro- and nanoparticles are discussed. Subsequently, the definition of the ZnO varistor and its characteristics are presented. The mechanism of toxicities of various ZnO particles towards the L929 cell line is also briefly described in this chapter.

In Chapter 3, the basic principles underlying the characterization tools, processing equipment, and materials are discussed. These principles include the experimental details for each instrumental set-up, sample preparation, the operating conditions including the resolution, and the samples. All the samples in this work were prepared by the conventional ceramic processing method that involved ball-milling, drying, pressing, and sintering. The ZnO samples characterization was conducted in Nano-Optoelectronic Research (NOR) and Technology Laboratory in the School of Physics. Structural, electrical, optical, and morphological characteristics were carried out by spectroscopy and microscopy in the NOR laboratory, whereas the morphology were studied by TEM in the Electron Microscopy Laboratory in the School of Biology. The cytotoxicity test for ZnO was investigated in the Advanced Medical and Dental Institute. This research is multi-disciplinary, which collaborated with other schools to evaluate the prepared materials for biomedical functions.

In Chapter 4, Characterization of the different discs was also carried out. The effects of different particle sizes and various annealing atmospheres on the morphology, physical, structural, optical, and electrical behaviors of the samples are also discussed in this chapter.

Chapter 5 focused on the characterization results for as grown and annealed W4-VDR, P8-VDR, 40nm-VDR and 20nm-VDR. The effects of different particle sizes and various annealing ambients on the morphological, physical, structural, optical, and electrical characteristics of the samples are also discussed in this chapter.

In Chapter 6, the toxicity reactions induced by pure and composite (varistor) ZnO disc samples and their effects on animal cells (L929) are explained, and the effects are related to the particles size of the ZnO grains and additives in the samples.

In the final chapter, a summary of the research and a conclusion are reported. Several recommendations for future research are also presented.

CHAPTER 2

LITERATURE REVIEW

2.1 Introduction

The theories and principles of this work are displayed in this chapter. In the beginning of the chapter, the mechanism of surface modification through the main annealing process is explained briefly. Then, the fundamental characteristics (physical, structural, optical, and electrical) of ZnO micro- and nanoparticles are discussed. Thereafter, the definition of ZnO varistor and its properties are presented. The toxicities mechanism of various sizes of ZnO particles towards the L929 cell line is likewise briefly described in this chapter.

2.2 Mechanism of surface modification through the main annealing process: recovery, recrystallization and grain growth

In the thermal annealing process, a ZnO material is heated to the temperature of recrystallization and then cooled down. The key factor of this process is to develop the properties of cold work by increasing ductility and retaining most of the hardness. The cold-worked state is a status of higher internal energy than the unreformed material. Although the cold-worked dislocated cell structure is mechanically stable, it is not thermodynamically stable [65].

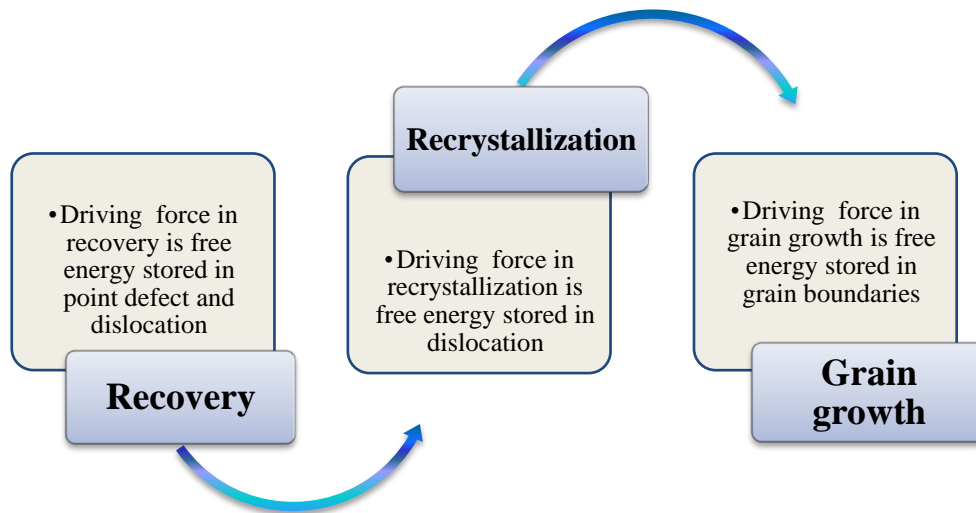


Figure 2.1. Overview of processes occurring during thermal annealing and the driving forces for these processes.

In annealing at an elevated temperature, the microstructure and characteristics may be partly restored to their initial values by recovery in which rearrangement of the dislocations take place. In most cases, the modifications in the microstructure during the recovery process are relatively homogeneous and do not have any effect on the boundaries among the deformed ZnO grains.

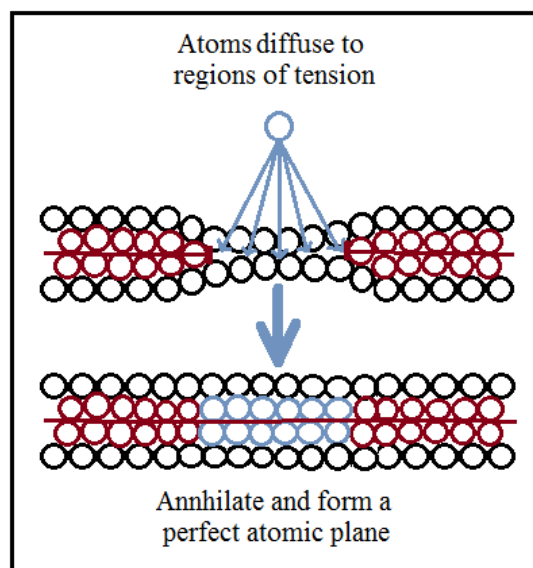


Figure 2.2. Schematic presentation of a recovery process and dislocation motion during thermal annealing process.

During the recovery process, a portion of the stored internal strain energy is relieved through dislocation via atomic diffusion at the high temperatures. However, the dislocations are not completely removed during the recovery, which results in a partial restoration of properties. The process of further restoration is known as recrystallization.

After the recovery process, the grains are still in a partial high-strain energy state. Recrystallization is the production of new uniaxial and strain-free grain structure that has low numbers of dislocation motions. The difference in the internal energy among strained and unstrained samples is the driving force in the formation of new grain structure. The reduction in free energy because of a diminution in grain-boundary as a result of increasing grain size is the driving force of the growth of new ZnO particles during the rise in temperature. Grain size dramatically increases when the new strain-free grains are heated to a temperature higher than necessary for recrystallization.

Therefore, the recovery process covers all alterations that do not involve the deformed structure of ZnO grain by migrating high-angle grain boundaries. However, during the recrystallization process, the crystal orientation of any area within the distorted sample is changed at least once, which can be observed in high-angled grain boundaries crystals [66].

Upon initiation of recrystallization in strain-free grains, crystals continuously grow with increasing the annealing temperature; thus, the total grain boundary area reduces. Large grains still grow at the expense of smaller grains. In particular cases, a number of ZnO with normal grain growth continues to grow, which is known as abnormal grain growth or secondary recrystallization.

New ZnO grains nucleate in the grain boundaries between the grains and grow at the expense of the distorted structure till it is entirely annihilated [67]. Grain boundaries continue to migrate at a decreasing rate between the new grains, which is also known as “grain growth” (Fig. 2.3). Generally, all grain boundaries move to a regular size area; but this motion is confined to only a minority of grain boundaries. Therefore, only specific grains grow large at the expense of other grains [66].

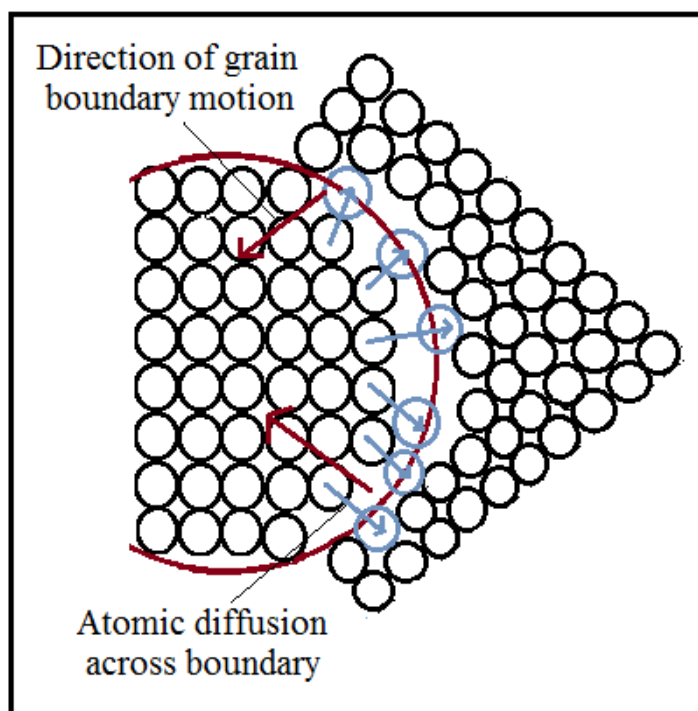


Figure 2.3. Schematic presentation of a grain growth and boundary motion during thermal annealing process.

2.3 Fundamental characteristics of zinc oxide

ZnO was discovered a long time ago and has been used in commercial products in a variety of ways such as a white pigment in paint, food and cosmetics additive, UV-absorbing material in sunscreen, anti-inflammatory component in ointments and creams, and an additive in car rubber tires and concrete. The widespread use of ZnO is attributed to its natural abundance and easy preparation by a variety of chemical methods. Furthermore, ZnO is non-toxic to the human body and is environment-friendly. It is also an air-stable semiconductor, and a considerable number of studies have focused on its semiconducting properties for applications in several electronic and optoelectronic devices. However, a higher level of purity is required for some applications. ZnO is a bilateral chemical substance from the II-VI group and in its pure compose is appear transparent because of its broad direct band gap, as explained in Fig. 2.4 [68]. ZnO has a very significant electron affinity (approximately 4.7 eV) and ionization potential (approximately 8 eV) compared with other

semiconductor materials, which partly explains the ease of n-doping. At room temperature, an elevated exciton energy of binding (approximately 60 meV) is a unique property of ZnO, which allows efficient near-band-edge excitonic emission. The large exciton binding energy decreases the distance between the hole and electron pairs. As a consequence, ZnO nanoparticles are fluorescent. Several features of ZnO are worth mentioning, such as its tolerance for high-energy radiation, availability of significant size ZnO substrates, and its ability for wet chemical etching. [69, 70]. All these characteristics make ZnO a favorable semiconductor for novel (opto) electronic applications [71].

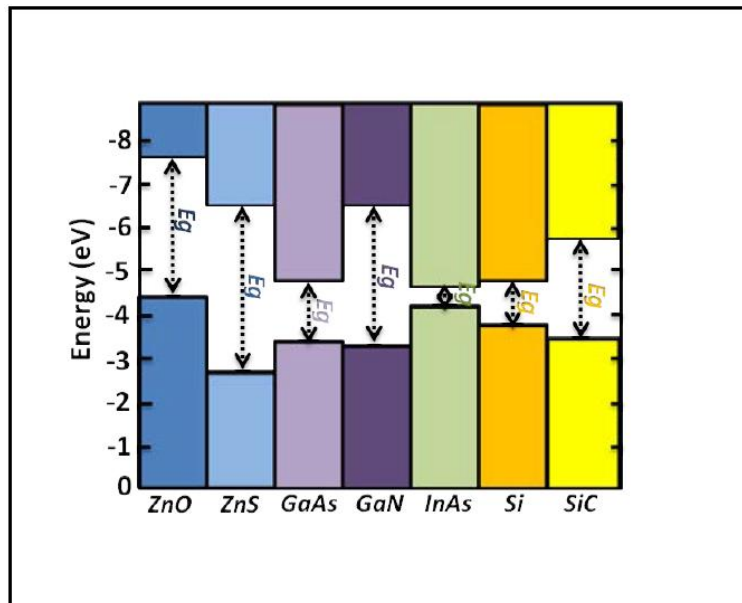


Figure 2.4. The conduction and valence bands energy relative to the vacuum level for several of semiconductor materials. The space between the top and the bottom bars explains the bandgap, (taken from ref. [68]).

Early studies on ZnO concentrated on its possible applications and fundamental properties, such as band structure, doping [72], and lattice parameters [73]. However, interest on ZnO decreased progressively during the 1980s because of unmanageable impurities and intrinsic defects naturally generated on the material apart from those generated by methods

of growth. Moreover, its electrical conductivity cannot be controlled. ZnO is inadvertently n-type doped, and it is rather unstable when p-doped on purpose. Moreover, the investigation of stable and reproducible p-type polarity is among the most challenging and has not been accomplished yet [74]. The p-type ZnO is a fundamental prerequisite for obtaining the p-n junction that is essential in optoelectronic applications. A considerable number of researches have been achieved to overcome the p-type doped ZnO through growing thin ZnO films on different p-type substrates. However, minimal success has been achieved because of lattice mismatch at the p-n junction interface, which results in poor device performance [75].

ZnO has a unique capability to generate a variety of one-dimensional structures as nanofibers, nanorods, nanowalls, nanorings and nanocombos [76-116], see Fig. 2.5. Some nanostructure attracted attention quickly due to their unique characteristics and simplicity of the synthesis. Here some of the properties of ZnO are highlighted:

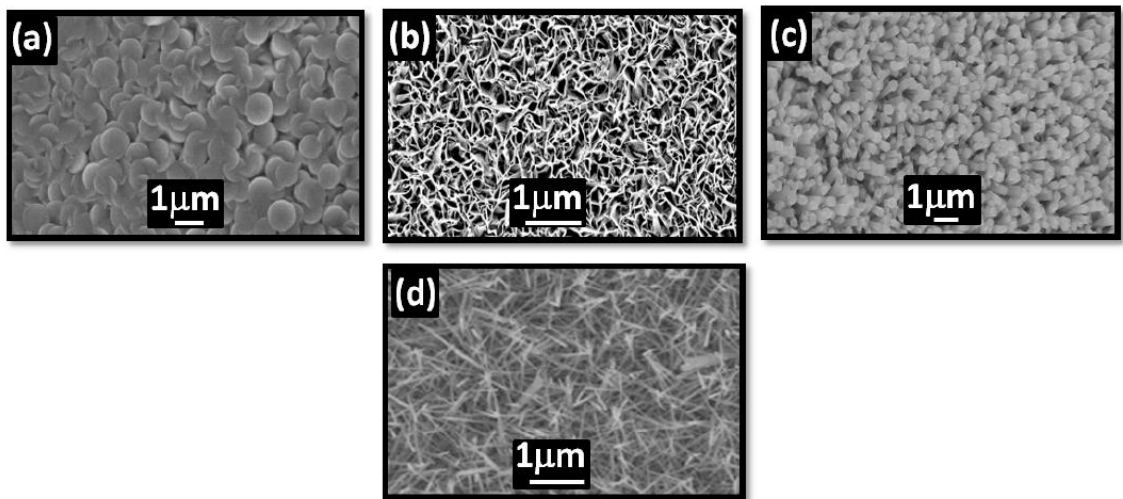


Figure 2.5. SEM images of ZnO nanostructures: (a) nanoplates, (b) nanowalls, (c) nanorods and (d) nanowires, (*taken from ref. [116]*).

2.4 Physical properties of ZnO

Table 2.1 shows several physical characteristics of ZnO at room temperature [69, 82, 95, 118]. The values for the thermal conductivity are still in question because of the presence of some crystal defects in the material [119]. Moreover, a reproducible and stable p-type doping in ZnO remains a problem and cannot be obtained. The results regarding the values related to the mobility of hole and its efficient mass are still debatable. The values of carrier mobility can be certainly enhanced by effective control of the material defects [119].

Table 2.1. ZnO Basic physical parameters at room temperature, (taken from ref. [15, 16, 24, 26]).

S.No	Parameters	Values
1	Lattice constant at 300 K	a = 0.32495 nm, c = 0.52069 nm
2	Density	5.67526 g/ cm ²
3	Molecular mass	81.389 g/ mol
4	Melting point	2250 K
5	Electron effective mass	0.28 m _o
6	Hole effective mass	0.59 m _o
7	Static dielectric constant	8.656
8	Refractive index	2.008, 2.029
9	Bandgap energy at 300 K	3.37 eV
10	Exciton binding energy	60 meV
11	Thermal conductivity	0.6 – 1.16 W/ Km
12	Specific heat	0.125 cal/ g °C
13	Thermal constant at 573 K	1200 mV/ K
14	Electron mobility	~ 210 cm ² / Vs

2.5 Crystal Structure of ZnO

ZnO crystals assume three different forms depending on the conditions during crystallization. These three forms are wurtzite, zinc blende, and rock-salt (Fig. 2.6). The wurtzite structure is thermodynamically stable under ambient conditions [74, 120]. If ZnO is grown on a cubic crystal surface, zinc blende is the expected structure, whereas the rock-salt structure can be obtained only under high pressure (approximately 10 GPa) [82].

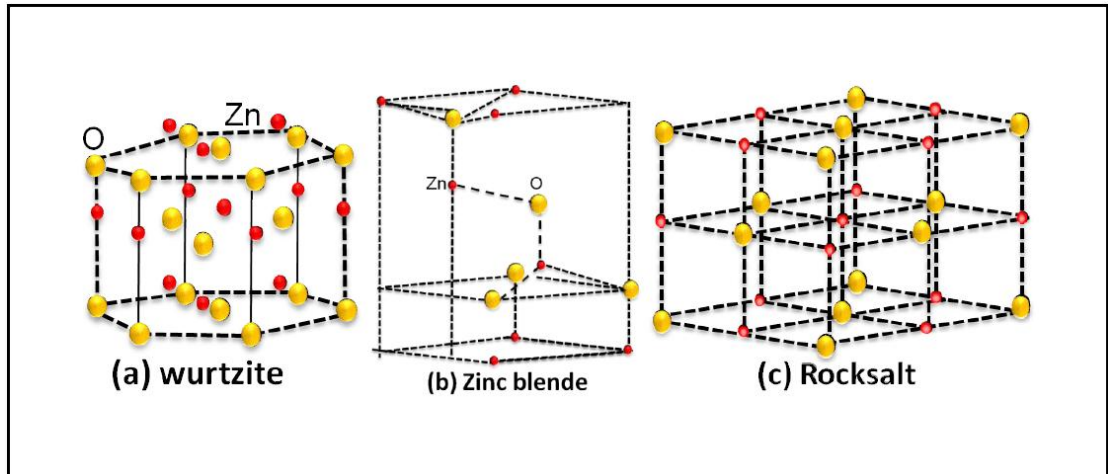


Figure 2.6. Crystal structures of ZnO, (taken from ref. [117])

The crystal structure of ZnO wurtzite has a unit cell in hexagonal form with $a = 0.324$ nm and $c = 0.521$ nm lattice parameters [121]. The ZnO crystal structure contains a number of zinc (Zn) and oxygen (O) surfaces paved alternatively along the c -axis. Every Zn cation is surrounded by four O anions arranged at the tetrahedron edges. The tetrahedral structure mechanical deformation causes a polarization, i.e. the electric dipole formation at the microscopic scale, which in turn leads to the piezoelectric property of ZnO [122].

2.6 Electrical properties of ZnO

Fundamental research on the electrical properties of ZnO nanoparticles is critical in the development of its application in nano electronics. ZnO has a 3.3 eV broad band gap at room temperature. A significant band gap indicates interesting properties such as higher values of breakdown voltages, continuous large electric fields, high-energy running, and high temperature. ZnO has an n-type nature when doping is lacking. Non-stoichiometry is generally the origin of its n-type character. ZnO nanowires reportedly act as n-type semiconductor because of various defects such as oxygen vacancies and zinc interstitials. The main constraint in broad-range applications of ZnO in photonics and electronics rests within the p-type doping difficulty. Successful ZnO nanoparticles doping of p-type will

significantly enhance their potential use in nano scale optoelectronics and electronics. N-type and p-type ZnO nanowires can act as light-emitting diodes (LED) and p-n junction diodes [123].

2.7 Optical properties of ZnO

The optical characteristics of semiconductor are based on both the extrinsic and intrinsic defects within the structure of crystalline. Achievements in research on ZnO optical properties have a long history that began in the 1960s. Recently, its direct broad band gap about 3.3 eV with high energy of exciton about 60 meV for ZnO at room temperature has made it very important among materials with wide band gap. [124]. The high efficiency of ZnO in radiative recombinations has made it a promising material for optoelectronics devices. The ZnO bulk and nanoparticles optical characteristics have been obtained widely by using photoluminescence spectra techniques at different room temperatures. The UV and a broad emission bands were obtained. The UV emission band is caused by the transition recombination of free excitons in the near-band-edge of ZnO. An exciton is the state wherein an electron and a hole are bound by the electrostatic Coulomb force. It is a quasi-particle present in semiconductors, insulators, and a number of liquids. An exciton can move over the crystal and transmit energy but cannot influence the charge where it is electrically neutral. An exciton is generated when a semiconductor absorbs a photon, which leads to the electron excitation from the valence band.

2.7.1 Defects and luminescence in ZnO

The electrical and optical characteristics of a semiconductor material can be modified by controlling the nature and amount of intrinsic defects. These defects are generated in the process of growth or by post-growth treatments such as ion implantation or annealing. An understanding of the behaviors of these defects in ZnO is very important. Since the 1960s, the dependence of both intrinsic and extrinsic properties of ZnO

luminescence on intrinsic and extrinsic defects has been investigated. Particularly, the origin of intrinsic luminescence in ZnO is still debatable because of native point defects. The ZnO has acceptor and donor energy levels above and below the valence and conduction bands, respectively, and these are responsible for the near-band-edge emissions. Furthermore, the band gap within ZnO has deep levels of energy, which are related to the emissions in the entire range of the visible region from 400 nm to 750 nm. The source of these deep level emissions is of interest and remains under review, and a considerable number of researchers have proposed different origins of these deep level emissions [82, 84, 85, 93, 95, 101, 107, 111, 116, 125-134].

There are also extrinsic and intrinsic point defects that determine the properties of ZnO luminescence. [82, 95]. Extrinsic point defects are defined as the inclusion of foreign atoms as impurities. If the defects are composed of only host atoms, the defects are thus intrinsic. Intrinsic optical recombinations occupy the electrons within the conduction band and the holes within the valence band [95]. The ZnO deep level emission (DLE) band used to be attributed to the ZnO crystal structure intrinsic defects such as zinc vacancies (V_{Zn}) [93, 111, 125, 134], oxygen vacancies (V_O) [135-139], zinc interstitials (Zn_i) [84, 128], oxygen interstitials (O_i) [116, 129, 131, 132], oxygen anti-sites (O_{Zn}), and zinc anti-sites (Zn_O) (Fig. 2.7) [140]. The substitutions with Li and Cu are extrinsic defects, which are also proposed to be involved in DLEs [79, 141].

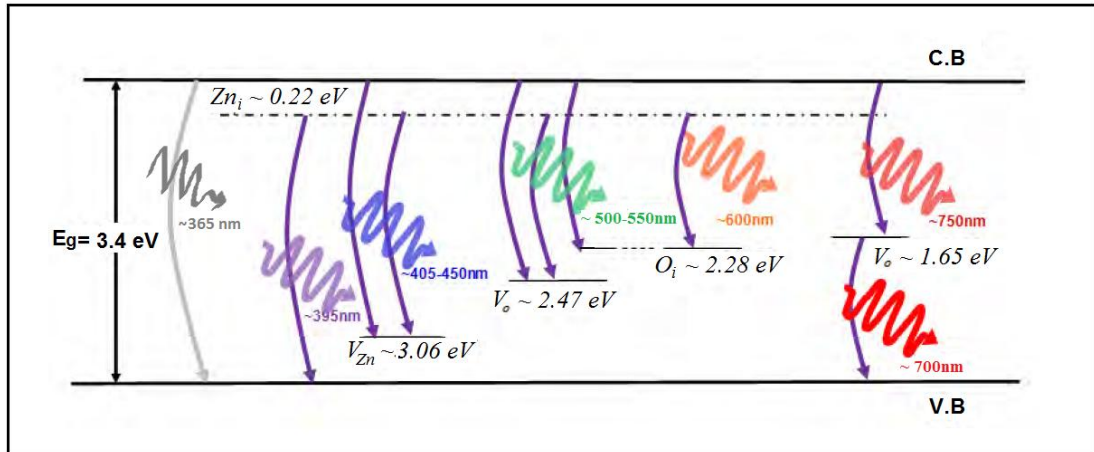


Figure 2.7. Schematic illustration of band diagram for some deep level emissions (DLE) within ZnO dependent on the full potential linear muffin-tin orbital method, (taken from ref. [140]).

A vacancy defect is created when a host atom C is missing within the crystal, designate as V_C . V_{Zn} and V_O are the most famous intrinsic defects in the ZnO. The green emission of ZnO is caused by single ionized oxygen vacancies. The energy required to formation an oxygen vacancy is minimal than that of a zinc interstitial and controls growth conditions of zinc. Doubly ionized oxygen vacancies cause the red luminescence of ZnO [141]. The green emission formation in ZnO is the most debatable, and a considerable number of experiments have been carried out for this emission [115, 127, 144-150]. Zinc vacancies were accurately investigated by numerous researchers and were proposed as the origin of the green emission observed at 2.4–2.6 eV below the ZnO conduction band [93, 125, 151]. Numerous investigators also proposed that oxygen vacancies are the origin of the ZnO green emission [84, 85, 107, 152]. Extrinsic deep levels such as Cu and oxygen interstitials lead to the ZnO green emission [120, 153, 154]. Currently, several deep levels are presumably involved in the ZnO green emission. Combined V_O and V_{Zn} reportedly lead to the green emission [34, 152, 154]. The blue luminance of ZnO is caused by zinc vacancies. The blue emission is formation from the recombination among Zn_i and V_{Zn} energy levels, and it is approximately 2.84 eV (436 nm). The method of full potential linear

muffin-tin orbital shows that the V_{Zn} level location is approximately at 3.06 eV under the conduction band, and the Zn_i level situation is theoretically existed below the conduction band at 0.22 eV [142].

When an excess D (D refers to any atom within the crystal) atom occupies an interstitial position among the normal positions within the crystal structure, an interstitial defect called D_i is generated. Zn_i and O_i are the two popular intrinsic defects in ZnO. Zn_i is usually located below the conduction band at 0.22 eV and has a major role in ZnO visible emissions. Recombination among various defects and Zn_i within the ZnO deep levels, as O_i , V_{Zn} , and V_O , generate blue and green emissions [142]. O_i is usually located below the conduction band at 2.28 eV and generate red-orange emissions in ZnO [34, 86, 93, 101, 145, 149, 151, 152, 154-158].

Anti-site defects are generated when atoms occupy wrong sites in the crystal lattice such as when oxygen occupies the zinc site or vice versa. These defects can be generated by irradiation or ion implantation treatments. The shifts above the valence band at 1.52 eV and 1.77 eV are attributed to O_{Zn} -related deep levels [140].

Extrinsic defects also have a major role in ZnO luminescence. The ZnO UV emissions at 3.35 eV are normally related to the excitons bound to the extrinsic defects such as Li and Na acceptors in ZnO [74]. The emission at 2.85 eV is caused by Cu impurities in ZnO [79]. The yellow emission was obtained in ZnO thin film doped with Li at 2.2 eV and is situated below the conduction band at 2.4 eV [159, 160]. Fe, Mn, Li, Cu, and OH are popular extrinsic defects in ZnO and these defects affect ZnO luminescence. Defects that have different energies emit the same color, such as ZnO:Co and ZnO:Cu that both emit the green color [120]. Hydrogen also has a significant role in ZnO luminescence. It is not a deep level defect and is located below the conduction band at 0.03–0.05 eV [161]. Hydrogen is usually positive in ZnO and significantly acts like a donor with low ionization energy, more explanation on this topic can be found in [95, 120]. Investigations on defects and luminescence in ZnO, along with their abilities to transition, demonstrate that ZnO could

emit luminescence that covers the entire visible region; thus, ZnO has great potential for use in the fabrication and improvement of white LEDs [120].

2.8 Zinc oxide nanoparticles

ZnO is usually in the powder form of a white color and is rather insoluble in water. The ZnO powder is vastly utilized as an additive in ceramics, plastics, glass, cement, lubricants, paints, rubber, sealants, ferrites, foods (as a Zn nutrient source), fire retardants, and so on. ZnO is extracted from the crust of the earth as zincite, but most ZnO used for commercial purposes are synthetic. ZnO is non-poisonous and does not irritate skin of human; making it a compatible addition for surfaces and textiles that relates to the human body. The increased surface to volume ratio (S/V) of ZnO nanoparticles may improve the quality of functions of this material compared with its bulk counterpart. The surface structure of ZnO has been mathematically obtained using novel atomistic potentials.

The concern in nanomaterials arises from the reality that novel characteristics are obtained at nanoscale length scale and, equally significant, that these characteristics vary with their sizes. Several factors in various substances cause the characteristic changes. In semiconductors, changes are more from the electronic motion imprisonment to a length scale that is similar to or minimal than the length scale differentiating the electronic motion in bulk semiconducting substances (named the electron Bohr radius). As the size of a number of metals is decreased to tens of nanometers, a relatively robust absorption emerges attributed to collective electron oscillation within the conduction band from one particle surface to another. This oscillation process among the electrons possesses a frequency, which absorbs the visible light. This is known as the surface Plasmon absorption. In transition metals, the reduction in size to the nanometer scale results in an incremented S/V ratio, which changes the properties of the material. The feature and surface formation of the nanoparticles primarily determine their function in potential applications. The small size of nanoparticle results in an unstable surface because of the significant energy of the surface and the

considerable surface bowing. Therefore, the characteristics of materials alter as nanoparticles are employed. The structure of the surface can be altered, as well as its chemical nature. In addition, these nanoparticles require connection to macroscopic objects for example in varistor applications. Changes in the properties of nanoparticles caused by the disorder at interconnections could be greater than those caused by quantum confinement or any physical force contained in the area of the nanoparticles. Hence, the application of these nanoparticles should be based on their comprehensive properties, particularly, the stability and characteristics of the surface.

2.8.1 Nanoscale effects

The two most significant properties of nanoscale dimensions are quantum confinement and the very large surface area [162]. First, this confinement leads to a shift in the energy levels (band structure more precisely) and therefore the difference between the highest occupied level and the lowest unoccupied level (or band of levels) may shift, thus changing the band gap. This phenomenon is known as quantum confinement. The quantum confinement affects state density (trap/donor carrier concentration), total power, and thermodynamic stability of semiconductor materials; hence, influencing optical, electronic, and magnetic characteristics. ZnO nanoparticles tend to exhibit the quantum size effect for dimensions less than 7 nm, wherein band gap expansion and blue-shifting is apparent in the test of light absorbance [163, 164]. Second, nanometric dimensions significantly increase the surface area to volume ratio. For a 1 nm nanosphere that has a density similar to ZnO (5.6 g/cm^3), the theoretical surface area is approximately $536 \text{ m}^2/\text{g}$ [165]. If the nanosphere includes internal interfaces (grain boundaries), the surface area would be highly increased just like in metastable structures. The extremely high surface-area-to-volume ratio, together with a size comparable to the Debye length, results in the high sensitivity of nanomaterials to surface modification during the annealing process and interactions at the surface (e.g. with

gas molecules). Moreover, their confinement size facilitates band gap tunability, greater optical gain, and ultrafast speed of operation [166].

2.9 Definition of zinc oxide varistor

ZnO varistors are electro-ceramic components made of ZnO as the base material sintered with other metal oxide additives. ZnO varistors provide economical and reliable protection against surges and high voltage transients, which may originate from inductive discharges, electrical switching or electrical noise on AC or DC power lines, and lightning strikes [167]. They were found far superior to transient suppressor diodes in terms of absorption of significantly higher transient energies and suppression of positive or negative transients. The structure of the varistor body contains series and parallel P-N junctions caused by separation of conductive ZnO grains by grain boundaries. P-N junctions make ZnO-based varistors voltage-dependent devices. Non-linear conduction is performed at higher voltages, and conduction is blocked at low voltages. Furthermore, ZnO varistors are bidirectional devices that exhibit a current-voltage (I-V) characteristic similar to back-to-back zener diodes. This characteristic is attributed to the presence of both forward-biased and reverse-biased P-N junctions. The sharp breakdown characteristics, which enable varistors to provide excellent surge protection for devices, are shown in Fig. 2.8.

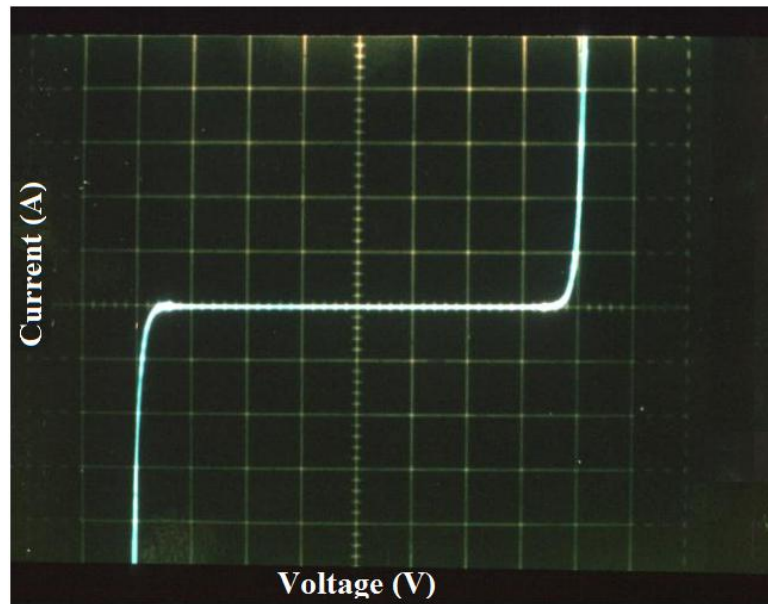


Figure 2.8. Typical Varistor V-I Characteristics, (taken from ref. [168]).

In overvoltage transients, the resistance of the ZnO varistor varies from a huge value of stand-by to extremely low conductive value (1Ω to 10Ω) [169], thus, the transient is absorbed and clamped to a safe level to protect sensitive circuit components [170]. The destructive energy is transferred as current to a neutral or ground wire, which may cause a dramatic increase in the varistor temperature. High transit voltage may yield high heat quantities that will be experienced by the varistor device. Ideally, all this energy is absorbed equally by the entire body of the varistor and heat is evenly distributed to all parts. The rate of voltage is proportional to the device thickness, heat is proportional to volume, and current capability is proportional to area [171].

Varistors are fabricated from a non-homogeneous material, allowing a modification action at the contact points of two particles. Many parallel and series connections identifies the current capability and the voltage rating of the varistor [172]. The basic features of the ZnO varistors are listed below.

- ZnO varistors have response time of less than 20 ns to over-voltage transient, so that the clamping the transient the instant it occurs.
- ZnO varistor's capability to absorb energy is very high ranging from a few joules to thousand of kilojoules with respect to size of component.
- Their capacitance is low, which make it appropriate for the protection of digital switching circuitry.
- ZnO varistors can sense and clamp transients frequently, in thousands of times, without being affected [171, 173].
- Their stand-by power is very low, which has led to the difficulty of using the current in stab-by condition, which means the lowest power used while performing at least one function.
- ZnO varistors have I-V behavior is nonlinear similar to the current-voltage characteristic of a Zener diode.
- ZnO varistors are bidirectional, which mean they can perform suppression of surges in both forward and reveres biases as two diodes arranged back-to-back.
- The insulation of ZnO varistor body is very high and epoxy resin coating gives protection up to 2500 V, in order to prevent short circuits to adjacent tracks or components.
- They can be used in electronic circuits which employ both direct current (dc) and alternating current (ac) in a wide ranges of current (1 microampere to kiloamperes) and voltage (one volt to megavolts) [174].

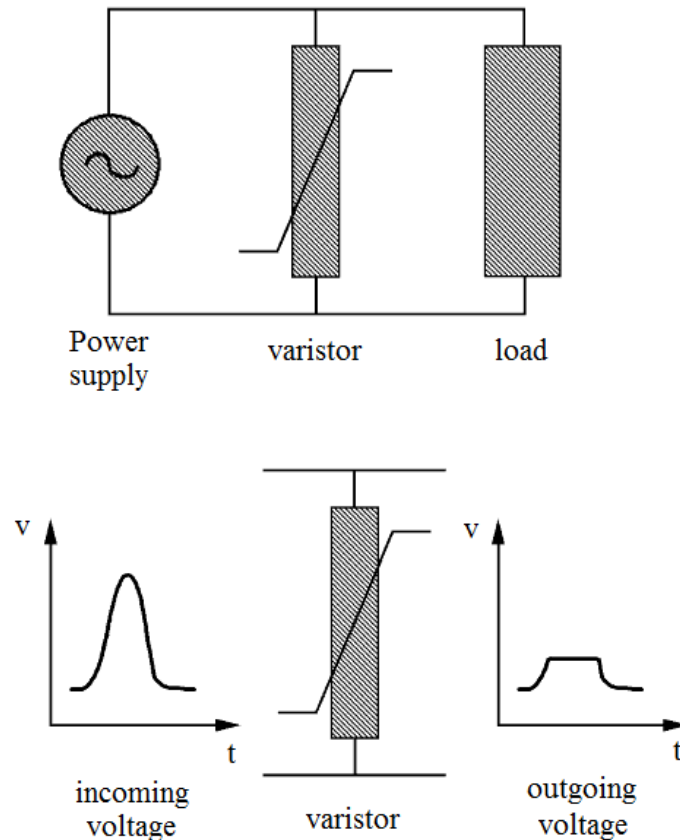


Figure 2.9. (Top) Circuit scheme with voltage supply, varistor and load connected in parallel. Passive components are usually connected close to the protected device for optimum protective performance. (Bottom) When applied to a voltage surge, the varistor will cut the surge at the desired protective voltage level and the load will continue to work at non-destructive voltage levels, (taken from ref. [175]).

Dugan [176] and Clarke [172] examine the advantages of ZnO-based varistors and noted to the importance of ZnO varistors as compared to other surge protection devices. Below is an advantages list for ZnO varistor [173, 177].

- a) ZnO varistors have high non-linear coefficient values ranging from 10 to 100 which are substantial for better protective function and fast response.
- b) Sharp switching voltage with no slowing that is the reversible of current-voltage characteristic.
- c) High energy-absorption capability with energy density up to 300 J/cm^3 .

- d) Power loss for varistor is very low ranging from 10 to 100 mW/cm³.
- e) ZnO varistor very responsive to over-voltage transients.
- f) Gapless design which making ZnO varistors compact.
- g) ZnO varistors have small sizes with different geometric shapes.
- h) Long lifetime under different environments for more than 10 years.
- i) Diverse with different applications from low to up of mega-volt range applications.
- j) The price of varistor is very cheap if bought in bulk
- k) Wide range of voltage selection from 14 V_{RMS} to 680 V_{RMS}, making the varistor easier to choose the correct item for any specific application.
- l) Available in the form of tape with accurately defined dimensional tolerances which making the varistor ideal for automatic insertion.
- m) Non-flammable even under loading conditions.
- n) Non-porous lacquer, making the varistor safe for use in toxic or humid environments.

2.10 Fundamental properties of zinc oxide (ZnO) varistor

2.10.1 Chemistry and microstructure of varistor

Pure ZnO is a semiconductor with a linear I–V characteristic; thus, other oxides must be added to get a non-linear characteristic. Common additive oxides are Bi₂O₃, Mn₂O₃, NiO, Cr₂O₃, Co₃O₄, SiO₂, Sb₂O₃ and, Al₂O₃ which have different effects and functions during the sintering process and in varistor devices [178-181]. As shown in Fig. 2.10.

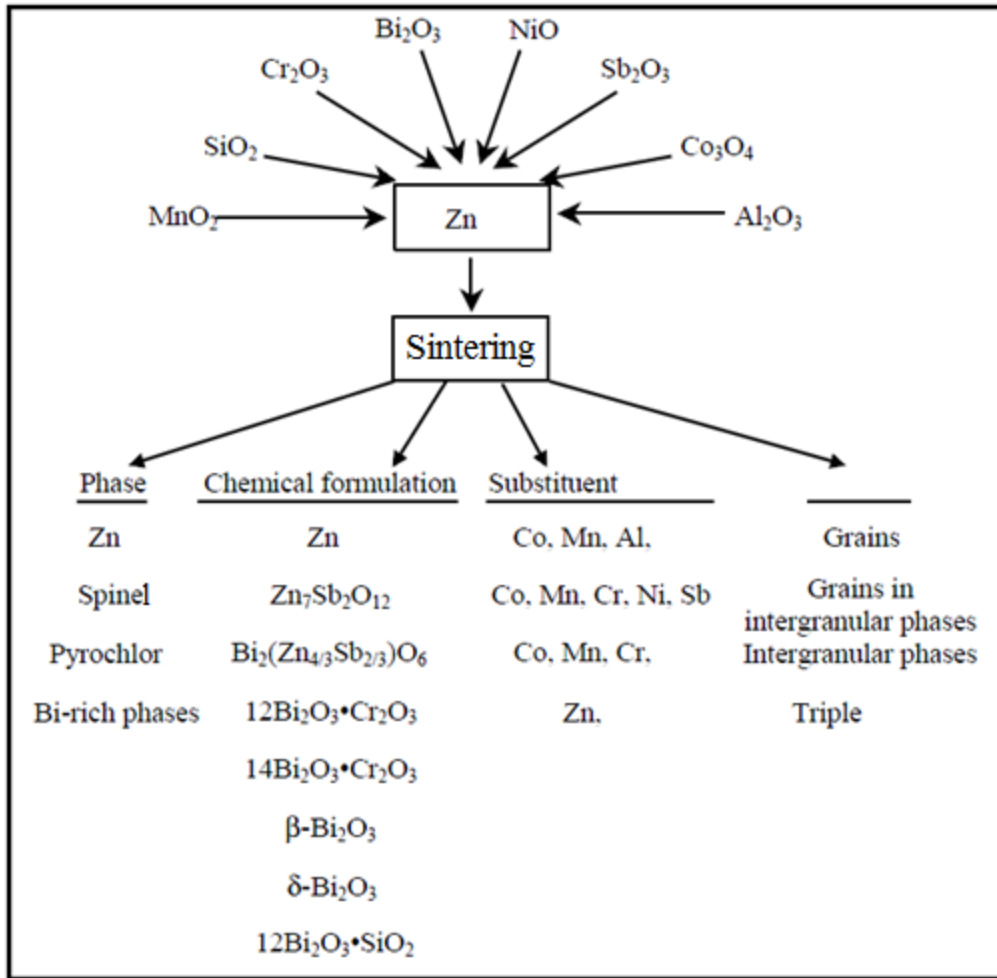


Figure 2.10. Summary of elements and phases present in the varistor during the sintering process and in the final compact, (taken from ref. [170]).

ZnO varistor materials are made of multi-phase polycrystalline ceramics. The basic components of these varistor samples are grains of ZnO, spinel grains, and intergranular Bi-rich phases [178, 179, 182]. The main constituents and microstructure of the varistor are shown in Fig. 2.11.

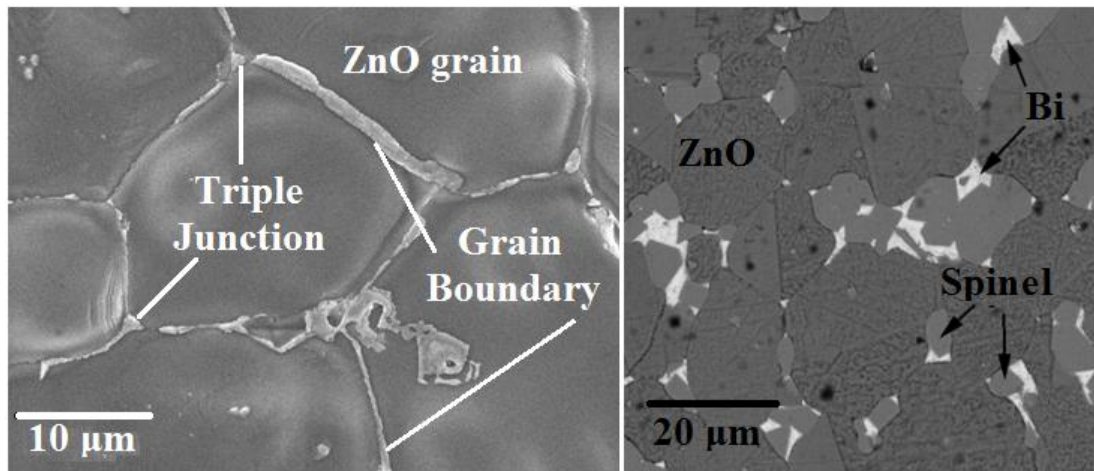
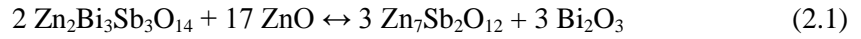


Figure 2.11. Scanning electron microscope (SEM) images of the microstructure of a ZnO varistor material obtained in secondary electron mode (left) and in backscattered electron mode (right) [175]. The sample surface is polished and lightly etched. Grains of ZnO, spinel grains and bismuth-rich phases are observed.

The grains of ZnO range from 10 μm to 20 μm in diameter and are the essential constituents of the ZnO-based varistor. The grains have the similar chemical structure in spite of the large variations in their geometric shape. The size of these grains may be affected by temperature and sintering time and also by different oxide additives in the varistor. Higher temperature and longer extent of sintering cause the increase in grain size [183, 184]. Be and Ti are used to enhance growth of grains, and Si and Sb are used for suppression of grain growth [185]. Small quantities of dopants, primarily Mn and Co, settlement and formation in the ZnO grains.

The spinel grains ($\text{Zn}_7\text{Sb}_2\text{O}_{12}$) are ranging from 2 to 4 μm in diameter and may impede the growth of the ZnO grains during the sintering process by pinning the migrating ZnO grain boundaries. The spinel grains range from 2 μm to 4 μm in diameter and may impede the grains growth through the sintering process by pinning the migrating boundaries among the grains. These spinel phases are usually in massive clusters encompassed by Bi-rich phases, but they may also be individually formed between, sometimes even within, the

ZnO grains. Spinel grains resulted from reaction by ZnO with ($\text{Zn}_2\text{Bi}_3\text{Sb}_3\text{O}_{14}$) during the early stages of sintering according to the following Equation (2.1) [180]:



Addition of dopants, such as Mn, Co, and Cr, to the varistor enhances the formation of spinel grains [178]. These grains do not have any direct impact on the non-ohmic properties of the varistor despite being effective insulators [185]. More precisely, high concentrations of dopants such as Co, Mn, Ni and Cr, can be investigated in the spinel grains [180].

There are three major parts from bismuth-rich phases:

- crystalline Bi_2O_3
- an amorphous bismuth-rich phase
- pyrochlore ($\text{Zn}_2\text{Bi}_3\text{Sb}_3\text{O}_{14}$)

All these three phases create a network in three-dimensional through the varistor volume. Bi_2O_3 crystalline is initially found in triple and double junctions of grains within varistor samples and is formed during reducing temperature to normal temperature. The morphology of the sintered varistor material depends mainly on the sintering temperature and atmosphere, cooling rate, and the composition [182, 183]. The stable high temperature δ - Bi_2O_3 , which has a high degree of turbulence, is formed as a result of melt crystallization [186]. Thereafter, the δ - phase may transform into the metastable β and γ forms or the stable low temperature polymorph α - Bi_2O_3 . The phase composition of Bi_2O_3 has a considerable impact on the varistors non-linearity behavior [187]. All polymorphs, except the α polymorph, can melt large amounts of other elements [188]. The emergence of several metal

additive stabilizers can be attributed to the metastable and high temperature δ forms at room temperature. The continuous network of crystalline bismuth-rich phases is a result of the transport of O into the material during annealing [172].

Pyrochlore formation varies with different ZnO varistor materials. Pyrochlore is first formed during heating and reacts with ZnO to form Bi-rich liquid and spinel phases in the early stages of sintering [180, 181, 183, 186-190]. During cooling process to room temperature, Pyrochlore established again, which decreases the cooling rate [172]. The pyrochlore content also increases with decreasing sintering temperature [180]. Small quantities of Ni, Co and Mn detectable in the pyrochlore and the pyrochlore crystallographic detail is taken from reference [181].

The amorphous Bi-rich phase is stabilized mainly between the grains at boundaries, particularly in the interfaces of ZnO/ZnO grains, which accounts for the appearance of Schottky barriers in the ZnO/ZnO junctions [191].

2.10.1.1 Interfacial Microstructure

Most studies on ZnO varistor materials have focused on the grain boundaries because they have an observed impact on most of the varistor behaviors. The grain boundaries function as barriers against electrical conduction, which leads to the improvement in non-linear current/voltage characteristics of ZnO varistors. Generally, most of the grain boundaries in polycrystalline materials grow indiscriminately and do not have identical high-angle grain boundaries. Occasionally, special grain boundaries, such as inversion twin boundaries, appear in polycrystalline materials, which may lack electrical activity and show morphology completely different from the general types of grain boundaries.

These results are also compatible with the grain boundaries found in ZnO varistors. Preliminary researches on the varistors microstructure achieved that the ZnO grains were entirely surrounded by a crystalline phase [170], However, more recent studies concluded

that the crystalline Bi-rich phase is located primarily in the ZnO triple and multiple grain junctions [182]. The boundaries between two grains of ZnO can be divided into two different types with different structural properties as follows [192]:

- interfaces formed by impurities incorporation of up to two atomic layers, and
- interfaces with a second phase characterized between the two grains, which are usually suitable for the nanometer scale.

The first type is the ZnO/ZnO grain boundaries. Electron microscopy revealed that these boundaries do not contain intergranular film but has segregated Bi atoms [193-196]. Bi segregation in the grain boundaries has also been reported by X-ray photoelectron spectroscopy [197] and Auger electron spectroscopy [198].

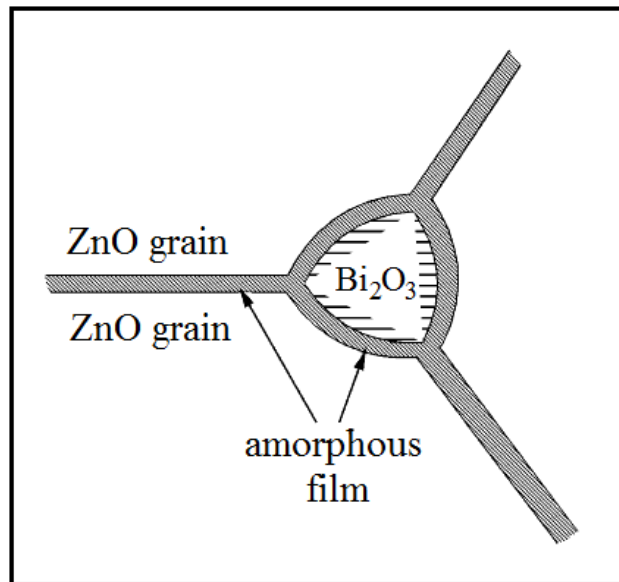


Figure 2.12. Schematic illustration of a ternary junction among the grains at thermodynamically equilibrium [199]. Crystalline Bi_2O_3 is present in the triple grain junction, with a thin amorphous Bi-rich film lies continuously among the crystalline phases in the varistor.

The second type is composed of interfaces between grains of ZnO, and electron microscopy studies showed that these interfaces contain a constant amorphous Bi-rich phase [181, 193, 194, 200].

2.10.2 Electrical characteristics of ZnO varistor

The ZnO-based varistor is a voltage-dependent, mutable resistor, non-linear device whose resistance reduces as the voltage raises across the device. The relationship between voltage and current in the ZnO varistor can be defined by the following equation:

$$I = KV^\alpha \quad (2.2)$$

where:

$$\alpha = \frac{\log (I_1 / I_2)}{\log (V_1 / V_2)} \quad (2.3)$$

K : Is a constant value based on the materials and geometry of the varistor sample.

α : Shows the non-linearity degree of the conduction of varistor.

(V_1, V_2) and (I_1, I_2) are the voltage and current values used to calculate α .

The typical electrical properties of ZnO varistors are mentioned in Table 2.2 [172, 201]. Most varistor characteristics are based on semiconducting properties, which include the placement of impurity donors, the presence of depletion layers, very short response time, and the presence of boundary capacitance. All properties of the ZnO varistor are related to the P-N junction phenomena of silicon MOSFET devices such as the very high resistivity in the varistor [202].

Table 2.2. Electrical properties of ZnO varistor.

ZnO Varistor Characteristics	Electrical Characteristic Values
Depletion Layer Thickness	50 – 100 nm
Grain-boundary Resistivity	$10^8 - 10^{16} \Omega \cdot \text{cm}$
Grain Resistivity	1 – 10 $\Omega \cdot \text{cm}$
Donor Density	about $10^{17} / \text{cm}^3$
Interfacial Trap Density	about $10^{14} / \text{cm}^2$
Voltage Drop at Grain Boundary	1 – 4 V per boundary
Nonlinear Voltage Range	1 V – 10 kV
Nonlinear Coefficient (α)	10 – 100
Grain-boundary Capacitance	about $0.2 \mu\text{F} / \text{cm}^2$
Apparent Relative Dielectric Constant	$10^3 - 10^4$
Energy Absorption Capability	100 – 300 J / cm^3
Response Time	5 – 30 ns
Power Loss	10 – 100 mW / cm^3

2.10.2.1 Nonlinear current – voltage characteristics of ZnO-based varistor

The ZnO varistor has a very strong semiconducting behavior and significant nonlinear current–voltage (I–V) characteristics, making it the focus of a considerable number of prominent varistor scientists such as Matsuoka [12], Clarke [193], and Gupta [173].

The I–V graph for the ZnO varistor shows a considerable variation in terms of its shape and turning points (Fig. 2.13). This phenomenon resulted from the manufacture of varistors using several voltage and current ratings that led to large variations in their diameter and thickness; from a few millimeters to 400 millimeters in diameter and from micrometers to 40 centimeters in thickness [201]. Therefore, if the varistor has large variations in physical properties, it must explain the current and voltage values with respect to a certain denominator; that is, current is represented by the current density J (A/cm^2) and the voltage is represented by electric field E (V/cm).

The I–V curve is divided into three regions, namely, the pre-switch region (sleep mode), the switched region (triggered mode), and the upturn region (high-current zone).

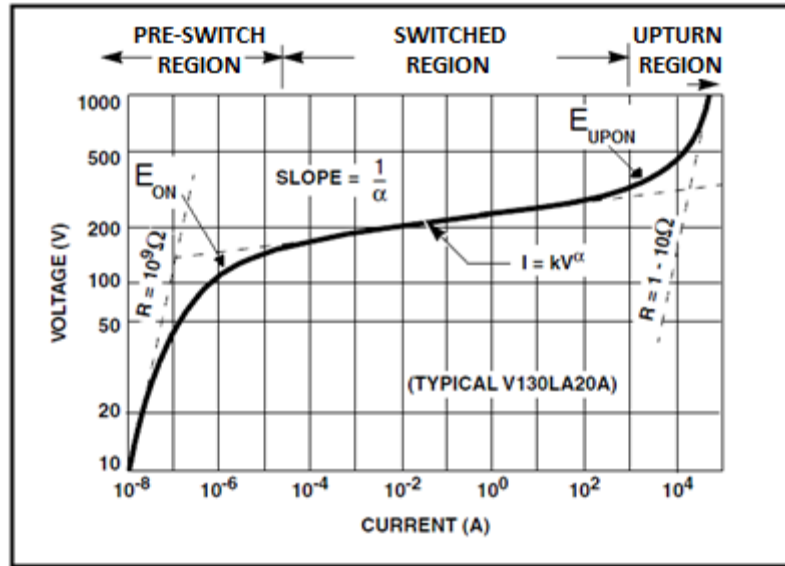


Figure 2.13. I – V Characterization of a ZnO varistor,(taken from ref. [203])

2.10.3 Optical properties of ZnO varistor

Research studies on optical properties of ZnO varistors, as well as their refractive properties, have been discussed a lot during the past years. The first study on the ZnO began in the 1960s [156, 204]. The interest in ZnO has grown tremendously in fields of optoelectronics because of its direct broad band gap at room temperature (3.3 eV), as well as its 60 meV exciton energy and functional radiative recombination. The 25 meV thermal energy at room temperature and the significant exciton binding energy that is significantly greater than that of GaN (25 meV) can confirm an effective exciton emission under low excitation energy at room temperature.

The optical characteristics of ZnO include photoluminescence, optical absorption, reflection, transmission, and so on. In the next section, an introduction on the photoluminescent and optical properties of a semiconductor is explained first. Second, UV emission and the sources of the deep level emission (DLE) band in the varistor photoluminance spectra are briefly discussed. Third, the surface recombination is described

in detail. Finally, the impact of surface band bending on the ZnO nanoparticle-based varistor is discussed as a large ratio of S/V in nanoparticles.

The photoluminance spectrum of the varistor is characteristic of a UV and a broad emission bands (Fig. 2.14). At normal temperature, the peak of UV emission forms from a near-band-edge transition of ZnO, which is the free excitons recombination. The broad peak ranging from 420 nm to 700 nm spotted in almost all varistors irrespective of growing states is known as the DLE band. The presences of the DLE band may be attributed to the various types of defects in the crystal structure, including oxygen vacancy (V_O) [85, 107], oxygen interstitial (O_i) [116], zinc vacancy (V_{Zn}) [93, 111], zinc interstitial (Zn_i) [84], and extrinsic impurities as substitutional Cu [79]. In the present study, the DLE band was investigated, and a few defect generates (V_{Zn} and V_O) with several optical properties were identified as contributors to the DLE [86, 115].

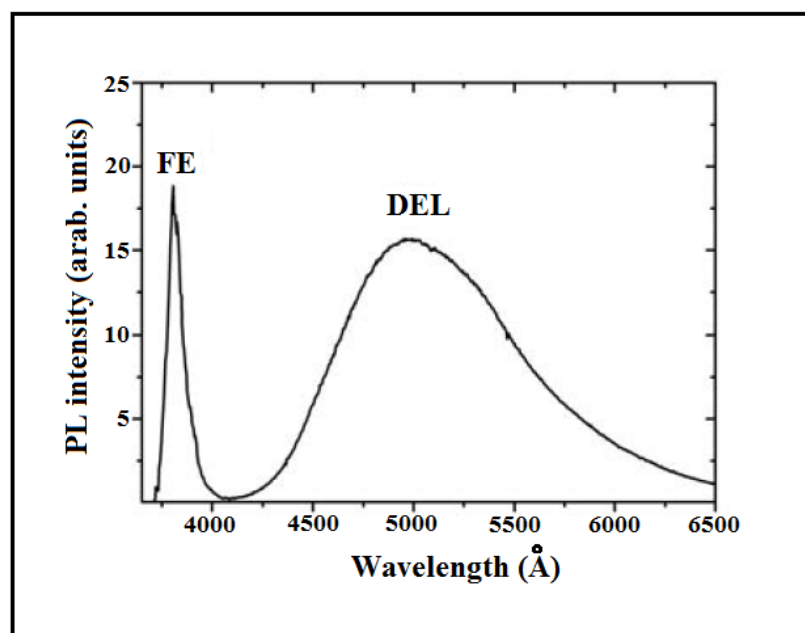


Figure 2.14. PL spectrum of ZnO varistor, obtained at 5 mW excitation power at room temperature with 325 nm excitation wavelength, (taken from ref. [110]).

2.10.3.1 Recombination process

There are two main types of mechanisms of recombination process in semiconductors, namely, radiative and non-radiative recombinations. In radiative recombination, the energy released from one photon is equal or close to the band gap energy of the semiconductor (Fig. 2.15) [96]. In non-radiative recombination, the electron energy is transformed to vibrational lattice atomic energy (phonons); thus, the electron energy is transferred to heat. For these causes, the occurrence of non-radiative recombination is undesirable in LED devices.

Basically, There are three mechanisms via which non-radiative recombination can occur:

- Non-radiative via deep level.
- Auger recombination.
- Surface recombination.

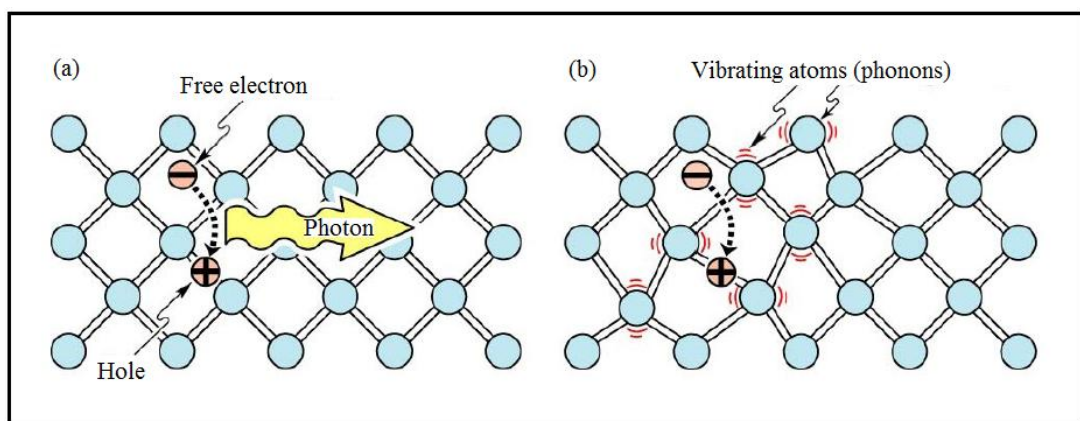


Figure 2.15. (a) Radiative recombination of a hole-electron pair conjugated by the phonon emission with energy $h\nu \approx E_g$. (b) In non-radiative recombination incidents, the energy emanate during the electron-hole recombination is converted to phonons, (taken from ref. [96]).

(i) *Non-radiative via deep level*

Non-radiative recombination is frequently generated from the crystal structure defects, such as native defects, impurities, dislocations, and several defect clusters. In compound semiconductors, native defects, such as vacancies, interstitials, and antisite defects, are present. These defects are known for their ability to form one or more of the levels inside the semiconductor forbidden gap. The investigated energy levels of defects in ZnO from previous research studies are illustrated in Fig. 2.16 [90, 91, 106, 108].

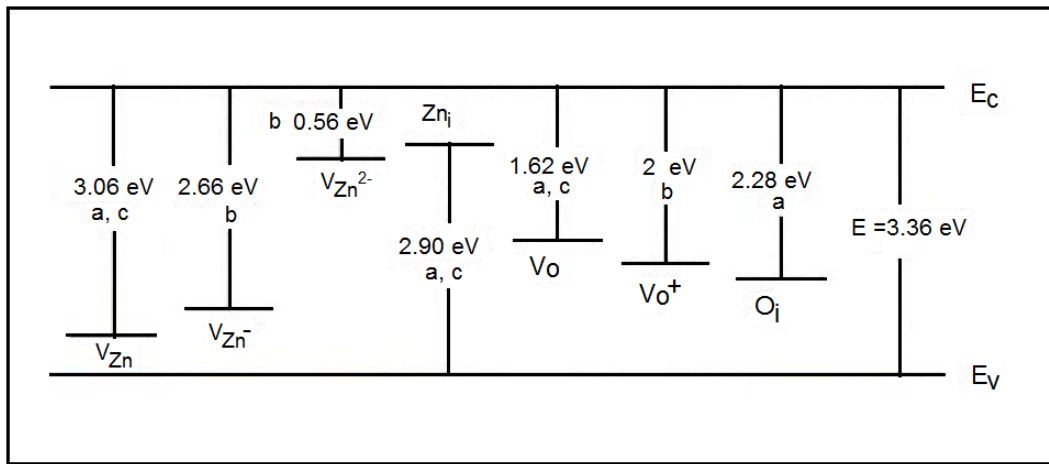


Figure 2.16. The energy levels calculated of defects within ZnO, (taken from ref. [90, 91, 106, 108]).

(ii) *Auger recombination*

The third carrier (an electron in the conduction band) gains energy and undergoes excitation to a upper energy level without jumping to different energy band. After interaction, the third carrier will normally get rid of its excess energy in the form of thermal vibrations. The recombination of carriers by Auger process is described schematically in Figure 2.15 (b). In this process, interactions among the three particles are significant only in non-equilibrium conditions when the density of carriers is very high. Generation by the Auger process is not simple because the third particle causes an unsuitable high-energy state.

(iii) Surface recombination

From the structural viewpoint, compared with the material bulk counterpart, the structure of the surface is entirely different when the crystal growth is dangling bond. The crystal lattice periodicity is strongly disturbed at the surface. The model of the band diagram is apparently based on the strict periodicity of the lattice. Thus, it is certain that the band structure will be adjusted by the surface because of the termination of periodicity. As a consequence, additional electronic states will be generated in the semiconductor within the forbidden gap, which will behave as non-radiative centers that will strongly suppress the efficiency and intensity of the luminescence of the material.

2.11 ZnO micro and nanoparticle-Bi₂O₃-Mn₂O₃-based varistor system

ZnO varistor ceramics have been generated in massive numbers in the 1970s. The electronic components fabrication produced from ceramics is still an manufacturing challenge despite several improvements. Several problems may emerge in a ceramic procedure because of numerous industrial operations that require particular attention such as raw materials quality, slip identity, pressing, spraying processes, and so on. Synthesis after sintering is difficult because a considerable oxides with huge vapor pressure are applied as arresters in power transmission in standard ZnO varistor production. Composition is probably modified through sintering step attributed to vaporization of components. In the domination of varistors electrical behaviors, problems in production, including furnace lifespan and vaporized oxide (Bi and Mn) toxicity, are most probably present.

Given the superior nonlinear behavior and low leakage current of varistor devices, they have been used in electronic and electrical systems such as surge protection systems for several years. During the operation process, a varistor is connected between the ground and the power source. If the electric field overrides the switching field, the surge is absorbed and shunted by the varistor, and in this way, it protects the electrical circuit. Controlling the

characteristics of the varistor is therefore desirable to improve particular protection requirements.

The breakdown voltage and resistance of these varistors rely heavily on microstructural conditions; thus, the grain size and microstructural homogeneity are the most significant parameters. One way to achieve these objectives is to use homogeneous zinc oxide nanoparticle powder for varistor manufacturing. Homogeneous ZnO nanoparticle powder is a requisite for the production of high-performance ZnO varistors because it increases the microstructure homogeneity, which is necessary to improve the electronic and electrical characteristic of these varistor ceramics.

Many researchers have researched the impacts of microstructure and processing on the electrical conduction in varistor system [14, 205]. They reported that varistors with inhomogeneous microstructures frequently suffer from a significant deviation in the I-V behaviors because of elevated local currents and overloads due to single massive grains, which lead to the quick degradation of the varistor in electronic and electrical procedures. Hence, controlling the ZnO microstructure is required to achieve the good nonlinear exponent and breakdown voltage.

ZnO nanoparticles have various chemical and physical properties compared with bulk materials. High homogeneity, good sinter ability, and other unusual characteristics may be anticipated caused by their large surface areas, nano-sized crystallites, and various surface properties. Thus, the fabrication of varistors with ZnO nanoparticle powder could dramatically develop new and better features.

In the current research, the effects of nanoparticle powder on the structural, electrical, and optical characteristics of the 40nm-VDR and 20nm-VDR were investigated and compared with those of the W4-VDR and P8-VDR, (VDR means a Voltage Dependent Resistor). A conventional ceramic method was used to fabricate varistors using ZnO micro and nanoparticle powder with certain additives. Thermal annealing process in oxygen and nitrogen ambients was applied on the varistor. The effect of ambient treatment on the α and

breakdown voltage of the varistor was studied. The degradation of the ZnO-based varistors' voltage barrier when thermal treated in nitrogen atmosphere and the subsequent retrieval of this voltage barrier by annealing in oxygen ambient indicate that the interface states' chemical origin may be the oxygen chemisorption on the grain surfaces.

Bueno et al. [206] distinguished the nature of the potential barrier within ZnO–Bi₂O₃–Mn₂O₃ varistor systems by Mott–Schottky and complex plane analysis techniques and observed that these varistor systems have a Schottky-type nature (electrostatic potential barrier). These results are very important because they prove that the nature of nonlinearity within ZnO–Bi₂O₃–Mn₂O₃ varistor systems may be attributed to a Schottky-type barrier at the boundaries among grains. Given that the nonlinear electrical behaviors of the varistors are dependent on the nature of the grain boundary, they are somehow connected to the capacitance of the barrier layer at the grain boundary. The oxygen that adsorbs at the grain boundaries during the annealing process has a substantial function in the mechanism of the generation of the potential barrier at the grain boundaries. The literature includes numerous studies on the effect of heat treatment of varistor ceramics in oxidizing or reducing (N₂ gas) atmospheres on the electrical behaviors [207-209].

Varistors are ceramic-based semiconductors that are applied in numerous areas of electronics and communication technology. A varistor senses and limits over-voltage surges and works constantly without decreasing the performance. ZnO-based varistors are prepared by the conventional ceramic processing method that involves mixing of ZnO with other metal oxide dopants such as Bi₂O₃ and Mn₂O₃. The additives responsible for the behavior of the varistor are cations, such as Bi [210], with large ionic radii and low solubility in ZnO. These additives are often called varistor formers. Other oxide additives, such as Mn₂O₃, are added to develop the non-ohmic behaviors of the varistor. This simple processing method has led to its exploitation on an manufacturing range. Furthermore, the low cost related with the usage of inexpensive oxide powders is commercially attractive. However, the major fault of this method is the high manufacturing temperature that causes the zinc content to

vaporize, thereby leading to quality problems. Therefore, the usage of ZnO nanoparticles is a promising solution to the problem because its high surface-to-volume ratio can reduce the manufacturing temperature of the varistor.

The other fault of this processing method is the difficulty of achieving structural homogeneity, which is essentially critical for the manufacturing of varistor systems that are desired to protect electrical devices. The crystallite size, additive homogeneity, and preparation methods are significant parameters needed to generate a good varistor system. Particularly, inhomogeneous structures of varistor can lead to varistor degradation during electrical functionality. The electronic and electrical characteristics of a varistor can be changed by diverse the microstructure at the boundaries among grains. Consequently, controlling the microstructure is necessary to form an ideal varistor. Nanoparticles exhibit a narrow grain-size distribution and can be sintered at a minimal sintering temperature comparison with microparticle ZnO varistors. The sintering temperature also depends on the particle size and the distribution of oxide additives between individual ZnO grains. Nanoparticle materials contain significant volumes of boundary among the grains and subsequently produce widely active boundaries per unit volume, thereby developing a good varistor system with small dimensions. But, dominant the development of ZnO grain during the sintering process is a challenge for nanomaterial study. Nano-ZnO with oxide additives like Bi_2O_3 and Mn_2O_3 can be utilized to fabricate varistors with improved breakdown voltage and electrical properties of varistor device.

2.11.1 Bismuth and manganese oxides in varistor ceramic microstructure

The interaction between ZnO and Bi_2O_3 in varistors is supposedly significant for the I–V properties. Notably, the Bi atoms are fairly concentrated in the regions of grain boundary in varistor materials [188, 193, 211-213]. A considerable portion is in the form of Bi_2O_3 existing in the triple junctions. Moreover, the Bi atoms are more or less in amorphous Bi_2O_3 phases, which cover the ZnO grains, or as individual atoms that deck the grain

boundary [191, 212-215]. The concentration of Bi within the ZnO grains is relatively low, and Bi also appears as the Zn condensation in the Bi₂O₃ phase at the triple junctions is apparently low despite the considerably high concentration of Bi and Zn in the spinel phase [198, 216].

The phase diagram for the ZnO and Bi₂O₃ mixture by Rousset and Peigney [217] suggested that mixing of these oxides fundamentally caused separation of phases into pure ZnO and Bi oxides of extremely low Zn concentration. Analysis of XRD of sintered Bi₂O₃ and ZnO mixtures shows the formation of Bi₂O₃ β -phase on ZnO grains [217]. Therefore, establishing a representative process for Bi in ZnO [218] and Zn in Bi₂O₃ [219] to obtain an understanding of the separation of the Bi₂O₃ and ZnO phases is interesting.

Meanwhile, Mn additive had considerable impacts on ZnO conductivity, though the degree of doping is relatively low. The Mn-doped ZnO electrical conductivity was significantly less than that of the pure ZnO, and the resistivity within the boundary of grains was superior than within the grain itself. Mn presumably works as a deep donor within ZnO, and it decreases the intrinsic donors concentration at the temperature of sintering process. If the temperature were rapidly reduced to room temperature, the state during the high temperature possible to be retained, and the intrinsic donors concentration also reduced [220, 221]. Owing to the similar impacts of the 3d transition metal on the oxygen adsorption within the boundary area among the grains, the Mn additive impact was more considerable on the grain boundary rather than the grain, consequently, the boundary area was higher resistive than the ZnO grain. Furthermore, Mn is generally used as a additive in varistor, which forms the potential barrier within the boundary area.

2.12 The In vitro toxicity test on ZnO-based varistor

The cytotoxicity test was conducted to underline the toxicity effect on the industrial environment where the varistors were being fabricated. As mentioned under the preparation and fabrication methods, the as-synthesized varistors were milled and sintered at high

temperatures. During this process gases such as CO₂, CO and NO are usually evolved. These gases can enter into human system via two routes. First, the gases and ZnO powder can diffuse into human respiratory system, flow through the blood and reached to human tissues. Second, the gases penetrate can be through the skin. Similar to our observation that ZnO powder is toxic on normal cell, several studies revealed its toxicity to be concentration and time dependent.

The varistor by-products can increase the risk of developing different type of cancers such as leukemia, lung, and lymph cancer. Different organs possess different response to ZnO. Srikanth showed that the cytotoxicity of nanomaterials possesses specific selection in cells [222]. Usually, factories employed several workers of different ages, and where likely to experience and be affected differently. The result of cytotoxicity test in chapter three on normal cells showed ZnO powder was toxic to normal cell (L929), at low doses and at short exposure periods. In addition, the cell death increased at high concentrations. Thus the safety of ZnO varistors should be highly considered when dealing with the samples either during fabrication or during application.

2.12.1 Cytotoxicity

According to the mentioned in medical dictionary by Farlex it means the degree to that an agent takes possession of a certain destructive action on specific cells. Any material or substance capable of destroying or killing live healthy cells, such as animal lymphocytes or snake venom, is called cytotoxic [222].

ZnO nanoparticles have been consumed as component in several cosmetics and in many dermatological equipments. The nanoparticles size increase the probability of reaction with DNA, and DNA has reportedly damaged a human epidermal cell line (A431). The genotoxic impacts are presumably intermediated by oxidative stress and lipid peroxidation mechanisms. Cytotoxicity developments with increasing the ZnO concentrations for the samples and length of exposure or treatment period [223]. Comparably, ZnO nanoparticles

have been studied to produce cytotoxicity in L2 cells [224]. Another research demonstrated a time- and concentration dependent increment in intracellular $[Ca^{2+}]$ levels, oxidative stress, and damage of cell membrane in a cultured BEAS-2B cell line. The modifications in gene term as a result of apoptosis and oxidative stress were considered to be the major reasons that caused the cytotoxicity [225]. ZnO nanoparticles (8–10 nm) have produced more toxicity than ZnO microparticles (< 44 nm) toward human colon cancer cells (RKO). Both particle sizes were established to agglomerate to particles in micrometer-sized within media of cell culture and produce toxicity effects via apoptotic pathways [226]. At high concentration or superior doses, the nanoparticles have produced small cytotoxic responses in epithelial cell/macrophage co-cultures, and primary alveolar macrophages [227]. Zhao et al. [228] reported depolarization-caused neuronal injury in rats through activation of voltage-gated Na^+ channels by exposure to ZnO nanoparticles. Thus, these nanoparticles can possibly lead to neuronal apoptosis [219].

Treating live cells with the cytotoxic component can lead to a variation of cell deaths as follows:

- **Necrosis:** Through this process, the healthy cells lose membrane solidity and then die immediately as a lysis result. Cells during rapid necrosis usually present instantaneous swelling, shut down metabolism, lose membrane integrity, and liberated (released) their contents out to the environment (Fig. 2.17). These cells in vitro do not possess enough energy or time to activate apoptotic machinery and do not express apoptotic indication [222].

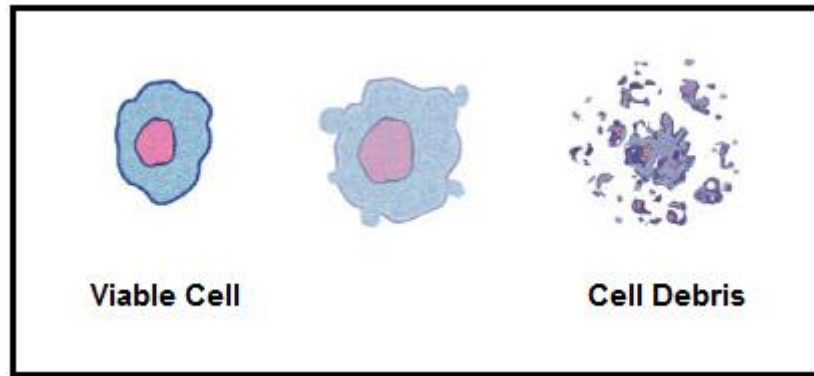


Figure 2.17. Cell undergoing necrosis, (taken from ref. [222])

- Apoptosis:** In this process, a variation in refractive index happens first; followed by cytoplasmic shrinkage and unclear intensification. Spikes or blebs protrude from the cell membrane as part of the dying process, and they form apoptotic bodies depending on the type of cell. These cells also discontinue the maintenance of the integrity of the phospholipid cell membrane. Furthermore, the mitochondrial outer membrane is also subjected to alterations that include loss of its electrochemical gradient. Then, macrophages or adjacent cells phagocytose the dying cell and apoptotic bodies. There is no any inflammatory response such as in the previous the case (Fig. 2.18).

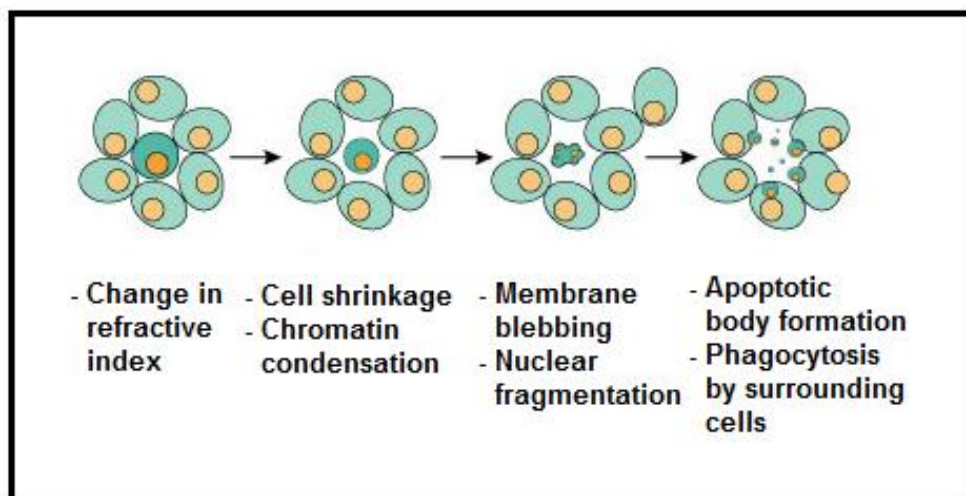


Figure 2.18. Cell undergoing Apoptosis, (taken from ref. [229])

Morphology modifies during apoptosis: the cell membrane starts to show spikes or blebs, depending in cell type. Finally, these separate from the dying cell and from the apoptotic bodies, which are phagocytosed by neighboring cells.

The following diagram (Fig. 2.19) shows the area within a cell, where a particular cytotoxicity test would act up. The test and their effecting region are as follows:

- Membrane integrity (LDHe)
- Metabolic activity (GLU)
- Respiratory chain activity (XTT/MTT)
- Total protein synthesis (SRB)/below mentioned
- DNA content and (CVDE) and
- Lysosomal activity (PAC, NR)

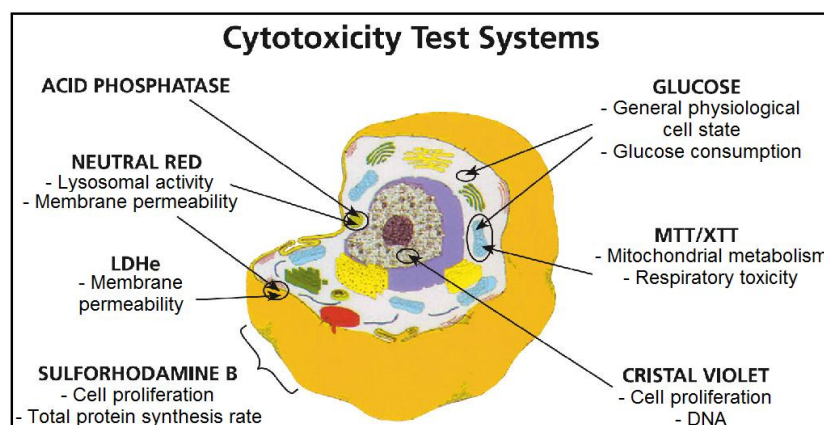


Figure 2.19. Cytotoxicity Test Systems, (taken from ref. [229])

2.12.2 Toxicity mechanisms of ZnO nanoparticles

The toxicity mechanisms of ZnO nanoparticles are most based on the reaction among biomolecules and nanoparticles, and the toxicity effects fundamentally include

protein unfolding [230], enzymatic activity loss, thiol cross-linking, and fibrillation. The potential mechanisms that demonstrate why ZnO nanoparticles exert toxic impacts are discussed below: oxidative stress, coordination effects, and non-homeostasis effects (Fig. 2.20).

Fig. 2.20 (a) explains the mechanism of the ZnO nanoparticles' entry into the cells. Nanoparticles can diffuse through the cell membrane immediately if the particle size is small adequate, when positive ions are present on the surface of nanoparticle, or when another variable exists [231]. At the same time, transporter proteins and ion channels allow nanoparticles to pass over the plasma membrane. Several nanoparticles enter the cells via endocytosis. The membrane of cells wraps around them, and vesicles carry the nanoparticles into the cells. The Zn^{2+} solute from ZnO nanoparticles can enter the cells through transfer and voltage-gated ion channels [232, 233]. The intracellular ROS impact generated by the ZnO nanoparticles is displayed in Fig. 2.20 (b). ZnO nanoparticles can immediately react with oxidative organelles, such as mitochondria. The ions (e.g., Zn^{2+}) generated by the nanoparticles stimulate ROS production in the cells by several chemical reactions, and redox active proteins can induce ROS within the cells. ROS have ability to produce DNA strand breaks and influence gene expression. Furthermore, Zn^{2+} ions can induce chelates with biomolecules or remove the metal ions in certain metalloproteinase, leading to disruption of protein function (Fig. 2.20 (c)). The Zn^{2+} induced by the ZnO nanoparticles develops their local concentration and inactivation cellular metal cation homeostasis to cause toxicity of cells (Fig. 2.20 (d)).

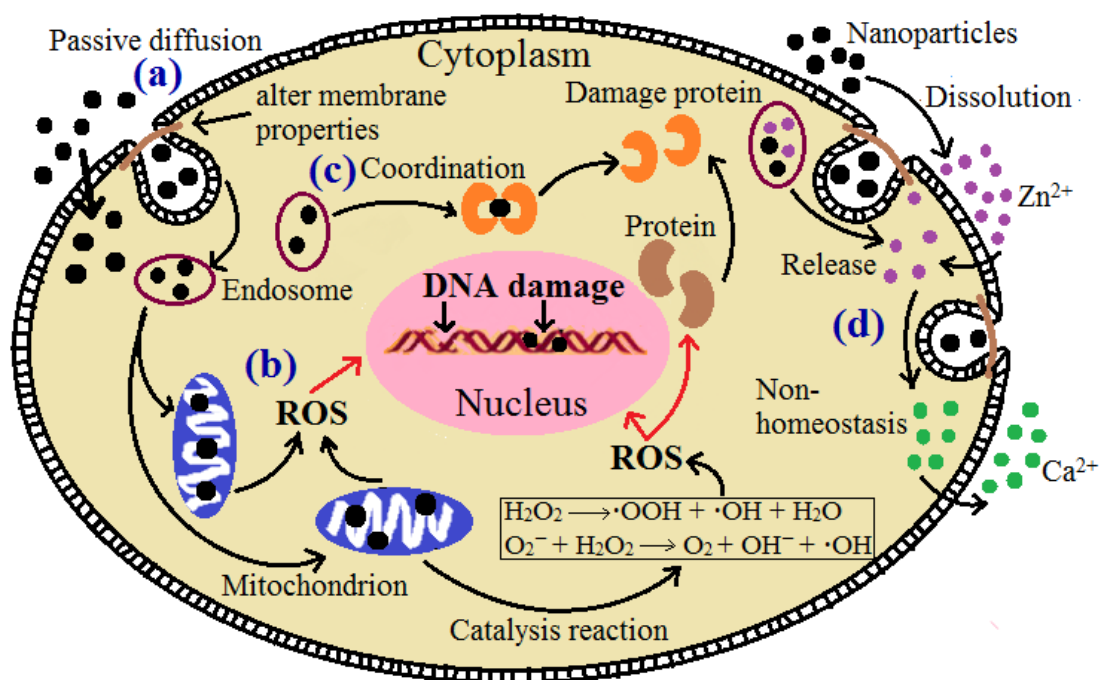


Figure 2.20. Schematic diagram of the toxicity mechanisms of ZnO Nanoparticles. (a) Potential mechanisms of ZnO nanoparticles' entry into cells; (b) The ROS impact of intracellular ZnO nanoparticles; (c) The coordination impact of Zn²⁺ released from nanoparticles in cell; (d) The non-homeostasis impact disrupted by Zn²⁺.

2.12.2.1 Oxidative stress

Oxidative stress production and ROS creation are the main toxicological mechanisms of ZnO nanoparticles. Significant ROS quantities could be produced when little quantities of ZnO nanoparticles are integrated into the cells [234]. Nanoparticles can directly generate ROS the moment that they react with oxidative organelles, such as mitochondria, or subjected to the lysosomes' acidic environment [235]. ZnO nanoparticles can interact with biomolecules because of their huge surface-to-volume ratio with high electronic density and reactive activity. Through this process, chemical interactions occur and enhance superoxide radical (O_2^-) formation, which causes ROS aggregation and oxidative stress induction [236]. ROS are oxygen derivatives that originates in an oxygenated environment and contains of superoxide anions (O_2^-), hydrogen peroxide (H_2O_2), and hydroxyl radicals ($\cdot OH$). ROS have ability to interact with biomolecules, leading to an imbalance among the reactive oxygen

generation and the biological system's efficiency to reform the product damage or detoxify interactive intermediates [237].

Nanoparticle-stimulated ROS generation can cause wide biological responses that based on the ROS generation proportional multitude, the anti-oxidant response element that is utilized in the oxidative stress, and the cellular pathway type [237]. The oxidative stress generated by ZnO nanoparticles was examined by exposing living cells to nanoparticles. The findings indicated that the amount of $\cdot\text{OH}$ within the ZnO nanoparticle suspensions were higher than in bulk ZnO, and oxidative stress and oxidative damage were produced in the absence of light [62]. The $\cdot\text{OH}$ radical is one of the most toxic ROS that can oxidize most cellular compositions. The extracellular $\cdot\text{OH}$ produced by nanoparticles may lead to oxidative harm on cell membranes, inducing toxic impacts in organisms. Studies have confirmed that oxidative stress present a general mechanism for cell destruction caused by nanoparticles, and this mechanism has been validated in several cytotoxicity research [238]. During entering the cell, particles cause intracellular oxidative stress by disturbing the balance among oxidant and anti-oxidant processes. Extravagant oxidative stress process may also change the nucleic acids, proteins, and lipids, thereby catalyzing the anti-oxidant defense system or causing death of cells. Moreover, with rise amount of ROS induction, nanoparticles can damage the DNA or produce single- or double-strand breaks [239]. Several illnesses such as cardiovascular, lung, and autoimmune illnesses have been related to oxidative stress.

2.12.2.2 Coordination effects

The reactions among ZnO nanoparticles and proteins *in vivo* or *in vitro* include coordination and non-covalent reactions. The proteins that bind with ZnO nanoparticles can cause main structural modifications and unfolding property of the periplasmic range of the ToxR protein by the essential reduction in the α -helical content of the free protein [230]. Metal cations support the protein folding or bind to folded proteins to promote, variety, or

decrease their work. Several of all familiar proteins include metal cations, and Zn^{2+} ions can bind to proteins under physiological conditions [240]. When mutations take place in metal-binding sites, the activity and structure of the protein may be decreased or wasted [241]. Solubility is the major factors that lead to toxicity. Zn^{2+} ions can induce chelates with donor molecules. A significant biomolecules number in organisms include coordination atoms, fundamentally O and N atoms, which have the ability to donate lone electrons to produce chelates with Zn^{2+} . The biomolecule coordination atoms are normally existing in active sites. Thus, coordinating with biomolecules may present chances to disrupt them, predominately by deteriorating the functions that preserve normal physiology procedures, thereby leading to toxicity. The metal cation affinity for a specific lig and is controlled via the metal's charge, charge-accepting ability, and ionic radius/ polarizability. Various metal ions have different binding sites and attraction toward a functional protein [242]. Dudev and Lim [240] reported that if Mg^{2+} ion binds with a particular protein, it could be ejected via Zn^{2+} ions because Zn^{2+} have ability to accept more charge from the lig and than Mg^{2+} and the Zn^{2+} compound is more stable. Coordination have the ability to indirectly and directly enhance cellular DNA destruction. ZnO nanoparticles can cause physical harm to the genetic substance by an immediate reaction with the DNA or DNA-correlated proteins due to nanoparticles have the ability to diffuse through the compounds of nuclear pore or gain entrance while the nuclear membrane dissolves through mitosis if the nanoparticles are sufficiently small [243]. Proximal perinuclear nanoparticles can prevent cellular translation and transcription machinery. Freed metal ions cause cytoplasmic mRNA decay through reacting with mRNA-stabilizing proteins that include metal responsive ranges. Nanoparticles can react with cellular signal molecules, which induce the signaling cascade activation and lead to destruction of DNA and death of cell [244].

2.12.2.3 Non-homeostasis effects

Functional metals have serious functions *in vivo*. Certain metals role separately, but another have composite functioning. Zn^{2+} ions perform major functions in preserving an organisms' homeostasis, and high or low Zn levels can disrupt the homeostatic mechanisms. When the homeostasis alteration exceeds the physiological tolerance range, toxicity takes place. Furthermore, ZnO nanoparticles may release Zn^{2+} , which increases the metal ion local concentrations and cause the disruption of metal cation cellular homeostasis. Oxidative stress can catalyze the enhance of the intracellular Ca^{2+} concentration [237]. The variation in intracellular Ca^{2+} flux and Ca^{2+} homeostasis have key functions in the pro-inflammatory effects of ultra-fine particles. Moreover, intracellular Ca^{2+} can control a considerable variety of cellular processes [245].

2.12.3 Cell viability

Cell viability is known as the healthy cells amount within a sample, whether they are quiescent or actively dividing. Viability of cells experiment are predominantly beneficial when non-dividing cells are separated and retained in culture to set superior culture conditions for cell populations. The most direct method for selecting number of viable cell is determining cell count using a hemocytometer. Cell viability can be based on morphology alone; however, trypan blue staining is necessary [246].

In this state, viability is determined by the cells ability with uncompromised membrane integrity to select the dye cells. Otherwise, metabolic activity can be examined as an designation of cell viability. Typically, metabolic activity is investigated in cells populations via incubation with a tetrazolium salt, such as trypan blue, MTS, MTT, XTT, and WST-1, that is cleaved into a colored formazan production via metabolic activity [246].

2.12.4 L929 cell line

The L929 cell line is a known model that has been deeply used by global organizations, such as the U.S Food and Drug Administration (FDA) to estimate safety and potential toxicity of various products e.g. ocular, dermatological etc. In the industry of contact lens, the cell line was also usually used in evaluating the contact lens packaging solution and biocompatibility of lens care solution. The model was founded during 1940 as a subclone of the parental L strain. The L strain was produced from a normal subcutaneous areola and adipose tissue of a 100-day-old male C3H/An mouse (ECACC No.85011425 Mouse C3) [247].

In the work, L929 cell line was used to achieve the interaction of ZnO with the cells. The cell line was determined as it is commonly used in *in vitro* researches to assess cytotoxicity of contact lens solutions. Furthermore, it is also a cost efficient, reliable and reproducible cell line. The L929 cells also grow into a confluent cell layer through 3-5 days, which was suitable for the time constraints associated with this study.

CHAPTER 3

METHODOLOGY

3.1 Introduction

This chapter briefly discusses several techniques that were used in the preparation and characterization of structural, optical, and electrical characteristics of the pure ZnO discs and composite varistors. The cytotoxicity protocols are also briefly described in this chapter includes limitations, operating conditions, and capabilities of the scientific set-up, as well as the resolutions of the instruments. Finally, a summary will be given.

3.2 Experimental Details

The experimental techniques applied in this work can be divided into six major sections, namely sample preparation, annealing process, microstructural testing, electrical testing, optical testing and cytotoxicity testing.

(i) Sample preparation

ZnO discs were prepared via the conventional ceramic processing method involving ball milling, drying, pressing, and sintering, as explained in Fig 3.1. Four types of ZnO powder was used to make the ZnO discs, which include ZnO-White (W4), ZnO-Pharma (P8), 20nm-ZnO (MK Nano) and 40nm-ZnO (MK Nano). Photos of some of the main equipments used for this work are shown in Fig. 3.2: (a) for test ball mill, (b) for cold pressing machine, (c) sintering furnace and (d) annealing furnace. The ZnO discs were sintered at 1200 °C in air.

Details on the sample preparation are explained in section 3.3.

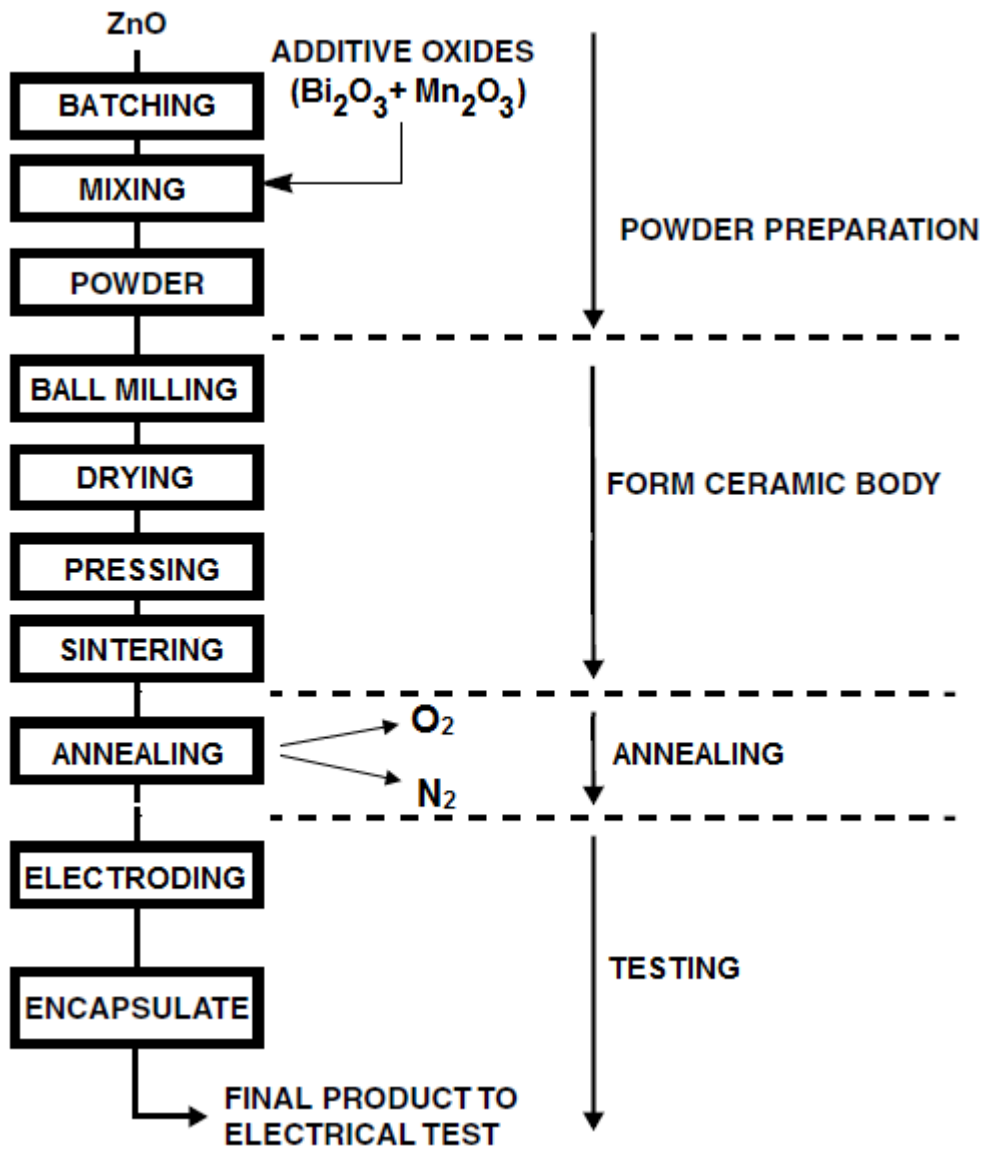


Figure 3.1. Experimental flowchart for sample preparation

(ii) *Thermal annealing*

Different types of ZnO powders were annealed in ambient oxygen or nitrogen at 700 °C. In this work, the annealing process was done by using a tube furnace model LENTON VTR/12/60/700 that was presented in Fig. 3.2 (d). The furnace has a extreme operating temperature at 1200 °C, and heat is prepared by a resistance wire wound onto the center of

the horizontal ceramic tube. In science of materials, thermal annealing process is a very simple technique, whereby the material is heated at certain temperature and time and then gradually cooled. This heat treatment increases ductility, softens, reduces internal stresses, and rearranges the atomic structure of a material. Moreover, optical and electrical behaviors may be altered through various annealing conditions such as period, pressure and type of gas, and annealing temperature [248-250].

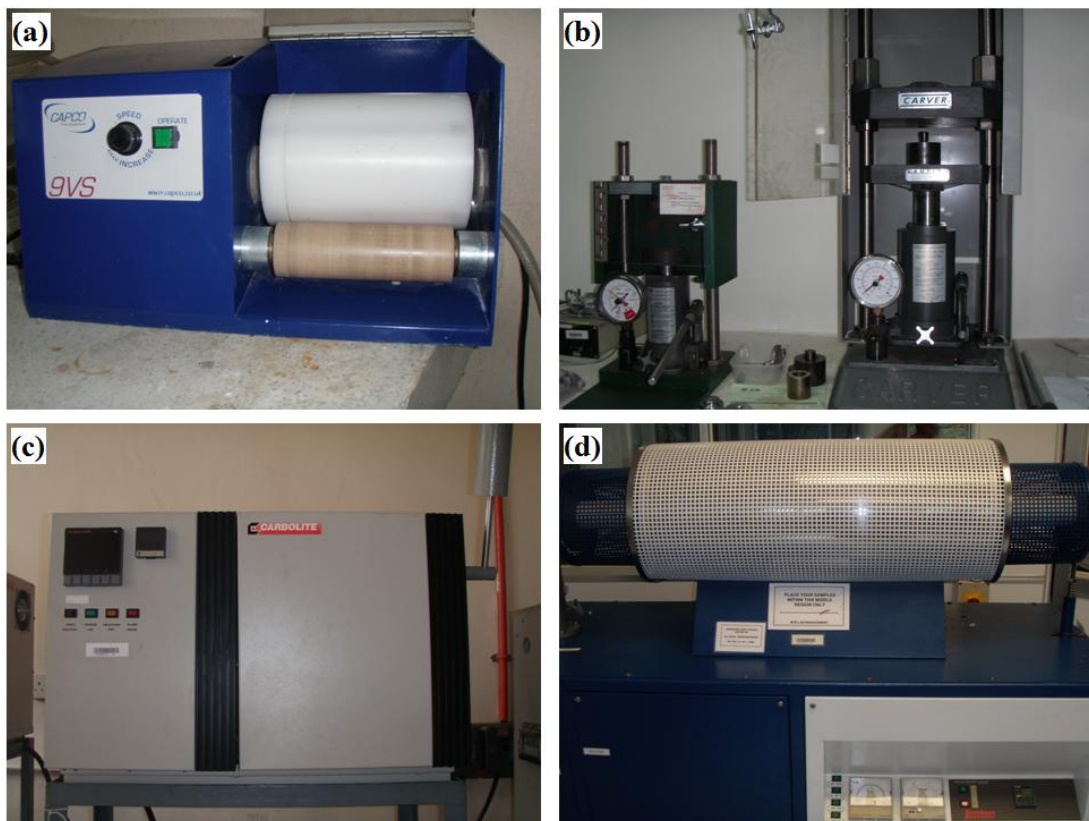


Figure 3.2. Photos of equipment (a) Test ball mill with teflon cylinder, (b) Test pressing machine with hydraulic pressure, single punches and die, (c) CARBOLITE sintering furnace, and (d) Annealing tube furnace.

(iii) *Microstructural testing*

Microstructural tests that were investigated involve particle size test (Malvern Mastersizer 1.2b tester), polished surface test (GRINDER-POLISHER, model: Metaserv

250, BUEHLER), Transmission electron microscopy (TEM, model Phillips CM12) and scanning electron microscopy & energy dispersive X-ray analysis (SEM/EDX, model: JSM – 6460 LV). Atomic force microscopy (AFM, model: Dimension EDGE, BURKER) was used to study the morphology and surface structure of samples. The crystalline phases were carried out by using a high resolution X-ray diffractometer (XRD, model: PANalytical X'Pert PRO MED PW3040) with Cu K α radiation ($\lambda=1.5406\text{\AA}$).

The photos in Fig. 3.3 (a), (b), (c), (d) and (e) clarify the equipments used for the mentioned tests. Details on the microstructural analyses are laid in sections 3.4.



Figure 3.3. Photos of microstructural measurement equipments (a) Grinder-Polisher machine to do the polishing process for the discs, (b) Transmission electron microscopy, (c) Scanning electron microscopy with EDX function to make microstructural and elemental analyses, (d) Atomic force microscopy to analysis the morphology of the samples, and (e) X-ray diffractometer to make structural analysis.

(iv) *Electrical testing*

The I–V behaviors of the materials were investigated by using a high voltage source measure unit (KEITHLEY instruments 246 high voltage supply). The resistance R was

evaluated from Current (I) - Voltage (V) characteristics in accordance with Ohm's Law. The photos in Fig. 3.4 (a) and (b) show the equipments used for the mentioned tests.

Section 3.6 provides more explanations on the electrical experiments.

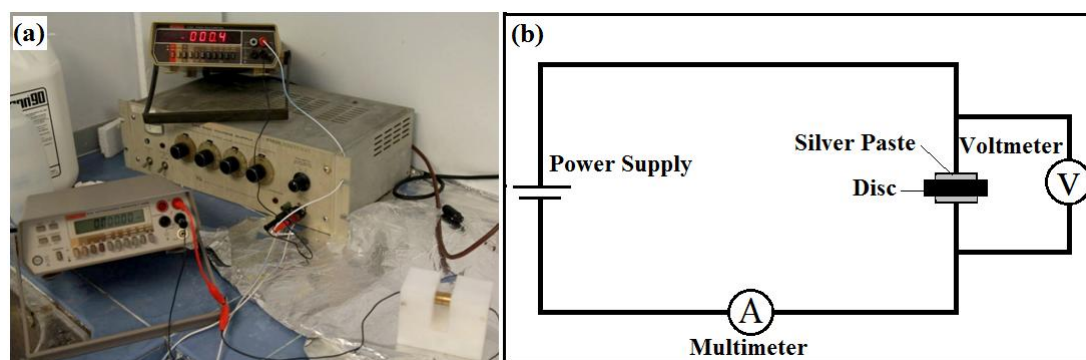


Figure 3.4. Photos of electrical measurement (a) Keithly Current-Voltage testing equipment, and (b) Typical experimental set-up for electrical measurement.

(v) *Optical testing*

Photoluminescence (PL) spectra were conducted using a Jobin Yvon HR 800 UV spectrometer system at room temperature. Raman spectroscopy was investigated as a supplementary tool to determine structural information (514.5 nm, argon ion laser, Labram-HR).

Details on the optical tests are explained in sections 3.5.

3.3 Sample preparation

3.3.1 Raw materials

The raw materials applied in this work were of significant purity and quality. Below are the raw materials list and their corresponding properties. The technical specifications of the raw materials are posted in Table 3.1.

Table 3.1. Raw material technical data.

Material	Chemical formula	Purity (%)	Mean size	Supplier
Zinc Oxide (White)	ZnO	> 99.8	0.23 μm	Approfit, Malaysia
Zinc Oxide (Pharma)	ZnO	> 99.8	0.19 μm	Approfit, Malaysia
Nanoparticles Zinc Oxide	ZnO	>99.9	20 nm	MKNANO Canada
Nanoparticles Zinc Oxide	ZnO	>97	40 nm	MKNANO Canada
Bismuth Trioxide	Bi_2O_3	>99	10 μm	SEGMA-ALDAICH
Manganese Trioxide	Mn_2O_3	>99	0.7 μm	SEGMA-ALDAICH

Addition to each 200-g batch of sample, the materials mentioned below was added to produce varistor slurry with better rheological properties.

- i. 40 grams of binder (polyvinyl alcohol PVA) or 6.0% of the formula.
- ii. 40 grams of deflocculant (sodium silicate) or 1.0% of the formula.
- iii. 170 grams of distilled water or 50% of the formula.
- iv. 4 grams of antifoam.
- v. 8 grams of bismuth trioxide and 4 grams of manganese trioxide also added in order to prepare the doped ZnO discs (varistors).

The binder has the capability to maintain homogeneity, to prevent oxides sedimentation, and to support in the following pressing process [251]. For better fluidity during ball milling process, the deflocculant was applied. The slurry possessed a significant solid content of about 67% that is the similar condition used in the industry of varistor.

3.3.2 Batching and ball milling

The ball mill (model: 9 Variable Speed) employed in this experiment was made of Teflon that is very appropriate for varistor ball milling because of its extinction and its inability to produce impurities. The milling nylon jar has a length of 19.2 cm length and diameter of 9.1 cm. Zirconia cylinders with 0.95 cm length and 0.95 cm diameter were employed as the grinding media. The zirconia cylinders were stabilized with magnesia to prevent introduction of impurities into the slurry [252].

For better cascading ball milling [253], the following optimized conditions were used:

- i. The zirconia cylinders occupied around 60% of the jar volume whereas the slurry occupied half of the volume of jar.
- ii. The weight ratio of zirconia cylinders to the oxides was about 7:2. In other words, 700 grams zirconia to 200 grams oxides.
- iii. The angular speed of the milling nylon jar was 40 revolutions per minute, which was around 75% of the rotation critical speed (rotation critical speed is the speed in which the zirconia cylinders are taken to the revolution summit) [252, 253].
- iv. The milling time was 6 hours.

Table 3.2. Varistor batch preparation details.

Sample	Weight of oxides (g)	Weight of binder + deflocculant (g)	Weight of distilled water (g)	Ball milling time (h)	Special conditions
W4-Disc	200	40	170	6	ZnO (Aprofit Whight)
P8-Disc	200	40	170	6	ZnO (Aprofit Pharma)
20nm-Disc	200	40	170	6	ZnO (Aprofit 20 nm)
40nm-Disc	200	40	170	6	ZnO (Aprofit 40 nm)
Varistors	200	40	170	6	Doped ZnO

One special condition was applied on the varistor is a mixture of ZnO with bismuth trioxide (Bi_2O_3) and manganese trioxide (Mn_2O_3).

3.3.3 Drying and granulating

Hot-plate drying and granulating processes were done manually. The ZnO slurry from the ball milling was poured into a beaker, which was putted on a hot plate at 60 °C, and stirred with a quartz rod. It lasted about one hour to expel the water content and then sample was granulated by sieving through a 20-mesh sieve.

After sieving, the granules had a size of between 50 and 150 micron, and with about 0.6% of moisture content. The granulated powder kept in plastic containers of at least 24 hours for ageing process to allow the humidity to homogenize.

3.3.4 Pressing

For every ZnO disc, the granulated powder was weighed separately by using a 4-decimal weighing scale (Sartorius model 3311318) and pressed at 4 ton/cm² pressure. Table 3.3 lists down the details of pressing process.

Table 3.3. Pressing specifications.

Parameters	Specifications	Remarks
Disc Weight	4.10 g	Tolerance ± 0.0010 g
Disc Diameter	26 mm	Pressing area = 530.66 mm ²
Disc Thickness	3 mm	Tolerance ± 0.010 mm
Pressing Force	4 – 10 tones	Different particle sizes had differences in force

Depending on the specifications in Table 3.3, the green density (the initial density of the pressed disc before sintering process) of the pressed discs can be calculated to be around 3.55 g/cm^3 that are 62% of the theoretical density (5.72 g/cm^3). The varistor green density and pressing pressure were identical to that used by many varistor manufacturers.

More than 250 discs have been pressed through the experiment. Several pressing problems were encountered owing to disc delaminating problem, which is a horizontal cracking [253, 254]. Within that time, 60% of the pressed discs were rejected because of the cracking problem. The problems were solved while the granules moisture content was adjusted to around 1.0% and the granules were sieved by a 100 micron sieve; in other words, the granules were become finer and wetter to support the pressing process in next step.

For every disc, pressing process had to be performed many times because of high rejection rate for the pressed discs. And for every pressing cycle, about 50 discs were generated at a rejection rate of 50%. Disc rejection owned too few of these reasons; non-uniform thickness, incorrect thickness, poor filling or delaminating cracking. Poor filling is case whereby the disc green density is not uniform and a process to check for poor filling is via visually checking for spots (on the surface of disc) that are “poor-shining” or “over-shining”. Most of the pressing activity time was wasted on performing this manual disc inspection. However it is necessary to examine for these pressing defects due to it is a precautionary measure that can prohibit rejection during the electrical testing. Based on the researcher's experience in varistor manufacturing, each non-uniformity at the pressing step can lead to cracking/puncture rejects when the varistor discs are subjected to significant current surge of over than 50 A peak current.

An overall of 20 cycles of pressing activity have been completed in order to perform 5 good batches for the 5 sample types, and over than 200 discs have been pressed in the experiment. A total of about 250 pieces of quality green discs have been investigated with good uniformity in green density and thickness that meet the rigorous pressing specifications listed in Table 3.3.

3.3.5 Sintering

The pressed discs were placed inside a box of furnace. The samples were sintered at the same temperature and time; this stage was significant in order to prevent any difference in sintering conditions among the discs.

The varistor sample discs were stacked horizontally on the base that made of varistor material (to avoid impurities that may generated by contact with the furnace). All the samples were exposed to the similar amount of heat and same atmosphere type.

The firing cycle was about 2.5 °C per minute for ramp-up, one hour soaking at 1200 °C and 6 °C per minute for ramp-down. In other words, heating time was 8 hours from room temperature to 1200 °C, soaking were 1 hour at 1200 °C and cooling time was 4 hours with exit temperature of 70 °C. To summarize, the whole sintering cycle was around 12 hours in normal atmospheric air.

The discs had a diameter shrinkage of about 15% (26 mm to 22 mm) and a thickness shrinkage of about 13% (3 mm to 2.6 mm) with nearly no warping problem. The color changed from green to black in doped discs. Whereas the color still white for undoped discs, as shown in Fig. 3.5.

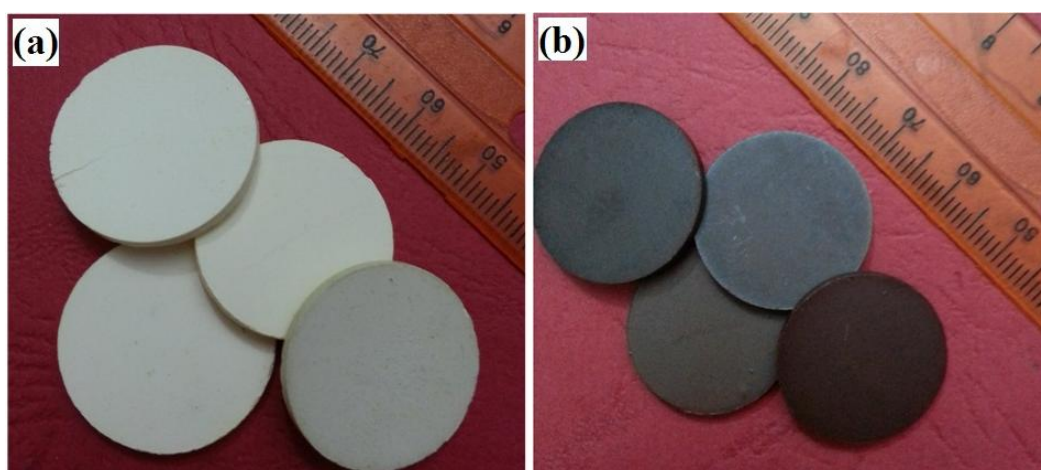


Figure 3.5. Photos of (a) pure discs and (b) doped discs, after sintering process

3.3.6 Electroding and encapsulating

The sintered samples were labeled via the screen-printing method where silver paste was screen-printed on each face of the sintered sample. The silver paste involved a little percentage (10%) from low-melting glass frit. After every silver printing, the disc was dried in 100 °C for 30 minutes. The silvered samples were then sent for heat treatment. The peak temperature was around 650 °C with soaking of 30 minutes. Every silver electrode layer had a diameter of 15 mm with a disc diameter of 26 mm.

Wire leads were stuck to the both surfaces of discs in a gripping manner and they were dipped into a solder bath involving tin-plumbum alloy solder material at a temperature of around 230 °C. Then the soldered discs were ultrasonically cleaned to remove impurities. Lastly encapsulation was done on the discs by submersion them in epoxy resin and cured at 80 °C for 1 hour, and then at 145 °C for 2 hours. After encapsulation, the epoxy-coated samples were prepared for electrical and optical testing.

3.4 Microstructural analyses

Microstructural analyses of ZnO discs at different particles size and various annealing conditions were performed including the following testing:

3.4.1 Transmission electron microscopy

The transmission electron microscope (TEM) is one of the popular multilateral and efficient instruments for materials labeled ionization. The fundamental advantages are the very significant spatial resolution (approximately 1 Å) and the broad range of secondary signals produced by the electron beam. These secondary signals are similar to those found in the SEM system; however, electrons are transmitted through the sample in TEM. Several produced signals could be detected by modern analytical TEMs and thus be used in the investigation of various properties of materials. The spatial resolution of the information obtained from TEM is superior to that from SEM, whereas the interaction volume is

significantly smaller because of the thin specimen ($< 0.5 \mu\text{m}$) required for electron transparency.

The transmitted electrons carry crystallographic information from an extremely small volume, which makes the TEM a strong tool for diffraction experiments on a centralized level. If the sample is crystalline, several of the electrons will elastically scatter in accordance with Bragg's law, which reflects structural information. Lost energy from electrons as a result of inelastic interactions in the sample can be detected by an electron energy-loss spectrometer that will classify the electrons by energy-loss and generate an energy-loss spectrum. These electrons carry considerable information on structural arrangement and local chemical composition.

The transmitted electrons form either a diffraction pattern or image of the specimen. The image formation in TEM can be understood using a methodical ray diagram (Fig. 3.6). The diffraction spots generate by diffraction waves on the back focal plane. In an electron microscope, electron lenses allow the visualization of the regular arrangement of diffraction spots on a screen; thus, a pattern of electron diffraction is obtained. The transmitted and the diffracted beams intervention on the image results in an observable magnified image (image of electron microscope). The area where the diffraction pattern is generated is known as the reciprocal space, whereas the area of a specimen or image plane is called the real space.

In TEM, both the diffraction patterns (information in reciprocal space) and the microscopic image (information in real space) can be investigated through modification of the electron lenses. Thus, both methods of observation can be related successfully in order to analysis of nanoparticle materials. In an electron diffraction pattern investigation, the electron microscope image is first observed and a diffraction pattern of the area is investigated by inserting a selected area aperture in a specific space and modifying the electron lenses. The latter mode of observation is known as selected area electron diffraction. The crystal structure and reciprocal orientation relationship among adjacent grains can readily be identified because the chosen area diffraction pattern can be investigated from

each ZnO grain within a polycrystal. The observational dimension identified from the object is generally selected to approximately 0.1 μm in diameter. However, the diffraction pattern of an area with a diameter close to a nanometer can be investigated using the micro diffraction mode. An image with enhanced contrast can be seen by passing the transmitted or diffracted beams over a slot and varying the method of imaging.

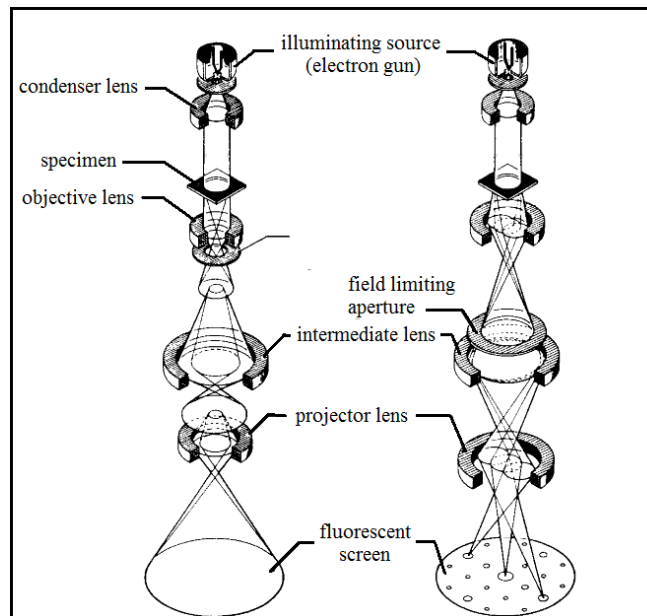


Figure 3.6. Schematic ray diagram showing the optical system of the transmission electron microscope in imaging (left) and diffraction modes (right), (taken from ref. [255]).

In the present work, particle morphology of the powder samples were inspected by TEM, and high-resolution lattice imaging was employed for the detection of inter-planar spacing. The particle morphology was investigated using a Phillips CM12 transmission electron microscope working at 200 kV. Several of the characteristic features of the Phillips CM12 are as follows:

- The electron gun is a LaB6 filament operating at 200 kV.
- The gun brightness is $3 \times 10^6 \text{ A/cm}^2$.

- The coefficient of spherical (C_s) aberration for objective lens is about 1.7 mm.
- The optimum defocus is about 770Å and the limit of interpretable resolution is around 3Å.
- The through-focus images involving the value of optimum defocus are registered at the magnification in the domain of $(2 \text{ to } 5) \times 10^5$.

3.4.2 Scanning electron microscope

The scanning electron microscope (SEM) is an instrument that generates an image of the surface of the specimen by scanning with high-energy electron beams in a scan pattern [256]. The electrons react with the specimen atoms, which produces several signals that consist of specimen information such as composition, surface topography, and so on. The types of signals generated by an SEM contain transmitted electrons, property X-rays, back scattered electrons, current of specimen, light (cathode luminescence), and secondary electrons. Each signal requires specialized detectors, which do not generally exist in a single machine.

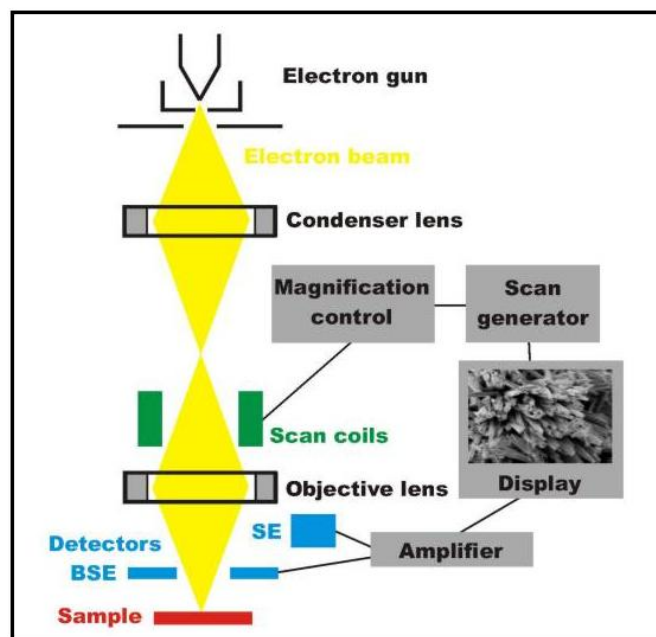


Figure 3.7. Schematic diagram of the scanning electron microscopy, (taken from ref. [257]).

The SEM schematic image is illustrated in Fig. 3.7 where the SEM employs electrons to generate an image instead of light. An electron beam is formed at the upper of the microscope by heating of a metallic filament. The beam passes through the lenses, which focus the beam down towards the sample. Other electrons, such as secondary or backscattered electrons, are ejected from the specimen when hit by the beam. Detectors gather the backscattered and translate them to a signal, which is move to a display screen identical to the one in a normal television; thus, producing an image.

The SEM gives information on the sample surface morphology that can aid in the detection of growth. The SEM generates images in 2D and detects topographic characteristics of the specimen that enables us to inspect the shape, diameter, density, and particles length. However, the images obtained by SEM cannot confirm the composition of the nanoparticles, that is, if the nanoparticles are composed of ZnO. The confirmation of the composition can be carried out by EDX that is generally attached to the SEM system.

A JSM-6460 LV SEM was used in our experiments to characterize the morphologies of ZnO discs. The chamber pressure was approximately 6–10 mbar. The gun voltage was 0.3–30 kV. A maximum resolution of approximately 3.0 nm to 4.0 nm for the secondary-electron image and backscattered-electron image, respectively, can be obtained. general-purpose sample chamber can accommodate a 150 mm diameter sample.

3.4.3 Energy-dispersive X-ray spectrometry

Between other signals, the essential electrons produce X-rays when interacting with the specimen. When a core electron of an atom in the sample is knocked out by an incident electron, the atom enters an excited state. The atom reverts to its ground state by filling the core hole with an electron from an external state, and the excess energy will be released either as an Auger electron or as a photon [257].

The electronic energy state is specific for every element; thus, the X-rays created by the fall of electrons from a higher to a lower state will also be element-specific. An energy-

dispersive X-ray spectrum was investigated by detecting X-rays from the specimen and plotting the intensity against energy. The elements present in the sample can be identified by comparing results with tabulated values. Hence, energy-dispersive X-ray spectrometry (EDX) is suitable for qualitative chemical analysis of an unknown sample. A number of factors, such as sample thickness, absorption, background radiation, escape-peaks, fluorescence, sum peaks, and k-factors, should be considered for better quantitative analysis [258-260].

For this work, all samples were tested for the SEM-EDX testing. The aim of this elemental analysis was to observe the impacts of W4-ZnO, P8-ZnO, 40nm-ZnO, and 20nm-ZnO and annealing process in oxygen and nitrogen ambients on the elements that might be existent at the grain boundary and inside the grain. Moreover, the relative atomic percentages possible to be obtained from the EDX scan. Fig. 3.8 show the micrograph photos of a couple of the SEM-EDX images (at 4000 times magnification) in which the site of the EDX scan for the ZnO grain interior is situated at a spot labeled “SPOT1” whereas the location for the grain boundary scanning is situated at the triple junction and is labeled “GB”.

However, the EDX scan can only reveal elements that are more than 1 atomic percent in the sample depending on the SEM (Ortec) equipment manual; thus, only four elements, namely, Zn, O, Mn and Bi, can be detected in the varistor specimens.

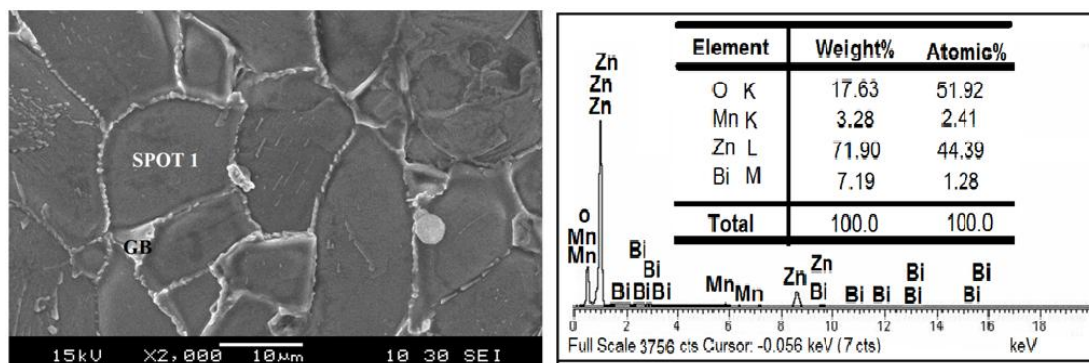


Figure 3.8. SEM-EDX micrograph photos showing locations of EDX scanning at the grain interior (SPOT1) and at the grain boundary (GB) for ZnO varistor.

3.4.4 Polishing process and grain size analyses

Micrographs of the polished sample surface are necessary for the study of the development of varistor grains after sintering and annealing. A specimen holder must be fabricated to clasp the samples in place during polishing.

Polishing forms a smooth and shiny sample surface using an abrasive and a work wheel and resulting a surface with lower diffuse reflection and large specular reflection. Polishing is also employed in several applications such as removal of oxidation, enhancement of the appearance of the samples, and generating a very flat surface, which is appropriate for inspection by microscopy.

Complete polishing involves several stages. First, rough abrasion is applied until the required finish is obtained. The abrasive removes nicks or scratches on the sample surface. After this stage, the buffing is achieved by hand or automated equipment. There are two kinds of buffing motion as follows:

- a cut motion that provides a smooth, uniform, semi-bright surface finish, and
- a color motion that provides a bright, clean, shiny surface finish.

Rough sand paper (number 800 or 500) is initially used in polishing, which possesses a fineness of approximately 3–5 μm . Fine polishing is achieved when polishing or grinding reaches the midpoint of the samples. A silicon carbide sandpaper with approximately 2 μm fineness was employed followed by sandpaper with 1 μm fineness.

In this work, the polishing process was done by using a Grinder-Polisher (Metaserv 250, BUEHLER).

The average size of grain was obtained by the boundary-crossing method as explicitly explained in Appendix A.

3.4.5 X-Ray diffraction

X-ray is an electromagnetic radiation with a 1 \AA wavelength at the region of gamma-rays and ultraviolet, which is similar with the atom size. The first using of X-rays in 1895 allowed researchers to investigate crystalline structure at the atomic level [258-260].

One obtains a diffraction pattern when X-rays interact with a crystalline material (phase) [261]. An introduction on the crystal lattice is necessary in understanding fundamental principles of X-ray diffraction (XRD). The distribution of atoms in a crystal is not random. The distribution is a uniform three-dimensional pattern that forms the crystal lattices. These lattices are composed of parallel planes in spacing distance d . The atoms generally segregate within a number of directions in the crystal resulting in several planes with various orientations, each of them possessing its own particular d spacing. Fig. 3.9 shows the X-ray image generated from two planes of atoms within a crystal. On the basis of the Bragg's law, diffraction exists when X-ray beam with λ wavelength is released at θ angle onto a crystal lattice, and the rays distance reflected from planes varies by a wavelengths number n that provides Bragg's Law:

$$n\lambda = 2 d \sin(\theta) \quad (3.1)$$

whereby n is an integer 1, 2, 3..... (Commonly equal 1), d is inter atomic spacing in angstroms, λ is wavelength in angstroms (1.54 \AA for copper), and θ is the diffraction angle in degrees. Deviations in the angle θ as a result of the various d -spacing within the polycrystalline material satisfy the conditions of Bragg's Law. Plotting the intensities and angular positions of the consequent radiation-diffracted peaks yields a characteristic pattern of the materials.

A multitude of physical and structural information about a substance can be obtained using the XRD principle. XRD has been applied in two major purposes, namely, fingerprint description of crystalline samples and the their structure definition. Approximately 95% of

all solid materials could be classified as crystalline. Each crystalline solid possesses a unique XRD pattern, which employed as a “fingerprint” for its similarity. Currently, around 25,000 organic and 50,000 inorganic single compounds, diffraction patterns, and crystalline phases have been compiled as standards. Once the substance has been specified, XRD applied to obtain its structure; that is, the atoms arrangement, interatomic distance, angles, and so on in the crystalline state. Altogether, XRD has become a powerful and important tool for structural description in materials science.

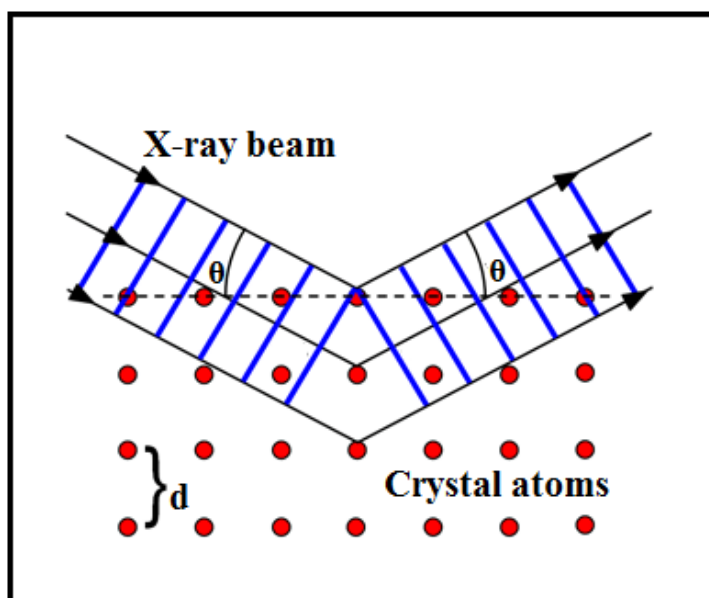


Figure 3.9. Shows a schematic diagram of Bragg reflection from crystalline lattice planes having interplan distance “d” between two lattice planes, (taken from ref. [262]).

In this work, the crystalline phases were studied using a high resolution X-ray diffractometer (XRD), model PANalytical X’ Pert PRO MED PW3040.

The radiation source is Cu- α where their wavelength is 1.5406 Å. Two type of XRD measurement are performed; 2θ - ω symmetric scan and also ω symmetric rocking curve (RC).

3.4.6 Atomic force microscope

Even today, atomic force microscope (AFM) has become one of the strong tools for imaging and measuring nanomaterials [263]. Gerber, Binnig, and Quate fabricated the first AFM equipment in 1986, which is a type of scanning probe microscope with significant resolution in nanometer scales, 1000 times above the optical diffraction limit. In the name of AFM, “microscope” implies imagery as it provides information on the morphology of the surface, which is collected by “feeling” the surface with a mechanical probe.

Fig. 3.10 explains the AFM block diagram [263, 264]. The AFM system is constructed from a microscale cantilever that end with a sharp probe to scan the surface of sample. The cantilever is generally manufactured from silicon or silicon nitride. During the measurement process, a semiconductor tip or fine ceramic scans the surface of the specimen. As the tip approaches the surface, Van der Waals force among the sample and the probe cause a cantilever deflection. The deflection magnitude is hold by a laser. The laser deflection image gives the resolution of the valleys and hills that represent the topography of sample surface.

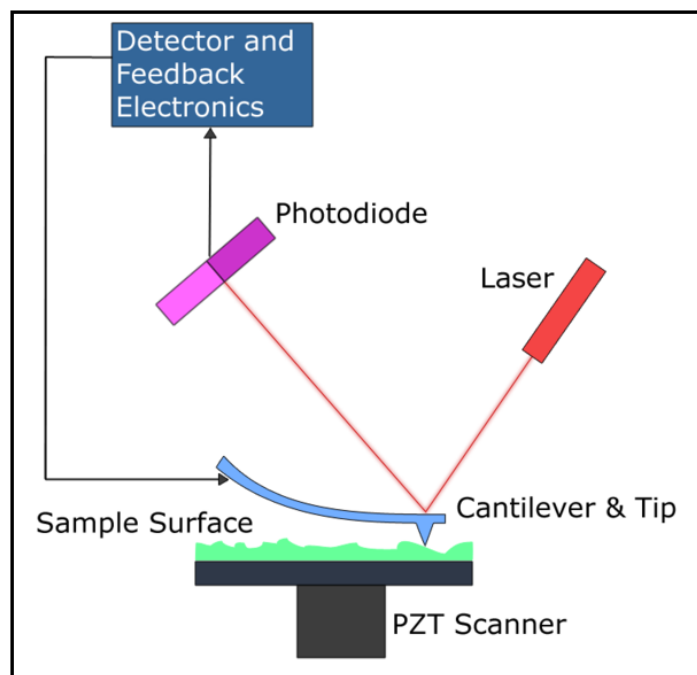


Figure 3.10. Block diagram of Atomic Force Microscope, (taken from ref. [264])

The AFM has many features more than the SEM as follows [263, 264]:

- the SEM provides 2D image of a specimen, whereas it gives 3D surface profile;
- the specimens used for an SEM generally need some coatings, which may irreversibly damage or alter the specimen, to improve the surface conductivity to improve resolution, whereas, the specimens can be directly measured by AFM without any pre-treatment or preparation;
- a high-vacuum environment is always necessary for suitable operation in SEM, whereas, most AFM methods can operate completely in air atmosphere or also in a liquid surrounding, which allows research of biological macromolecules and even living organisms; and
- AFM has been shown to provide true and high atomic resolution within ultra-high vacuum ambient, which means it can obtain superior resolution than SEM.

In this work, we employed AFM (AFM model Dimension EDGE, BURKER) to study the surface morphology of specimens. It makes surface structure measurements with significant resolutions within the nanometer scale potential as they are common in scanning probe microscopy.

3.5 Optical testing

Vital PL spectroscopy and Raman spectroscopy were applied in this work to study the optical properties of the ZnO discs with different grain sizes and annealing conditions. The details on the PL and Raman spectroscopies are discussed below.

3.5.1 Photoluminescence spectroscopy

Photoluminescence (PL) is the automatic light release from a substance under optical excitation [265]. PL measurement is a nondestructive and powerful technique, which has been implemented on most semiconductors. Until today, various kinds lasers have been

widely employed in the PL spectroscopy set-up such as Nd: YAG pulsed laser with 266 nm. A pulsed excitation laser emits by pump laser, and the PL lifetime can be carried out. The set-up is then designated Time-Resolved PL (TRPL). Photons are absorbed and excitations are generated as light of sufficient energy illuminates a substance. These excited carriers relax and release a photon, and the PL spectrum can be obtained and analyzed. However, absorption only occurs in substances with photon energy equal to or greater than the band gap. Subsequently, it has to select various sources of excitation appropriate for each material with diverse electronic band structure. The position of the PL peaks reflects transition energies, and the PL intensity includes the proportional rates of radiative and non-radiative recombination. PL can be altered by external parameters such as excitation power, temperature, and used outer disturbance (electrical or magnetic field), which allow in the comprehension of bands and electronic conditions.

The ideal PL experimental set-up is shown in Fig. 3.11. Excitation of specimens was carried out by a pulse laser or continuous-wave. The luminescence was diffused with a monochromator, and measured by a significantly sensitive detector appropriate for the detection range. A CCD or a Hamamatsu R5509-72 InP/InGaAs nitrogen-cooled photomultiplier tube is used for UV, whereas, a germanium detector is used for near infrared emission, visible, and near infrared emission.

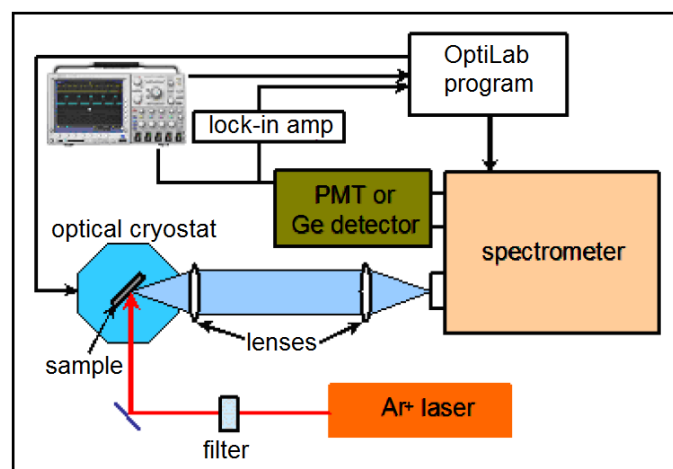


Figure 3.11. Typical experimental set-up for PL measurements, (*taken from ref. [266]*)

The PL measurement has three major steps as follows:

- First, the semiconductor is excited optically to generate electron–hole pairs. Nd:YAG of wavelengths of 266 nm are applied for the excitations in ZnO. The laser beam is thereafter projected on the semiconductor specimen with the support of a set-up as explained in the schematic diagram.
- Next, the excited electron–hole pairs recombine radiatively and release light.
- In the last step, the emitted light is revealed and scattered by a paired grating monochromator and photomultiplier detectors. The definitive spectrum is gathered and analyzed in a computer.

PL characterizations in this work were investigated by applying a Jobin Yvon HR 800 UV spectrometer system at room temperature. This system employs a visible and ultraviolet spectrometers, which is especially beneficial in the characterization of semiconductor substances and able to give knowledge immediately associated to the optical and electronic characteristics of the specimen.

3.5.2 Raman spectroscopy

Light scattering can be divided into two kinds, namely, Rayleigh Scattering and Raman Scattering. In Rayleigh Scattering, the photon is elastically dispersed without shifts in frequency. In Raman Scattering, the photon is dispersed inelastically associated with frequency alteration [267]. The shift in frequency of Raman scattered light is associated to the excitation frequency. Notably, the magnitude of the shift is not based on the excitation frequency but on the structure of the crystal. Hence, this “Raman shift” can be a result of an intrinsic characteristic of the sample. Undoubtedly, Raman Scattering is a strong light-scattering technique for the diagnosis of the interior structure of crystals and molecules [268]. In this work, we performed the Raman spectra by employing a Jobin Yvon HR 800 UV spectrometer system which described previously in section 3.5.1.

3.6 Electrical testing

The I–V characteristics, including the resistance R and the sheet resistance, of the samples were investigated. In this research, we related the difference in electrical behaviors of ZnO disc with the variation in the size of ZnO grains and annealing conditions. The details of the electrical testing are shown below.

3.6.1 Current – voltage (I – V) measurement

For I–V measurement, the current is the independent variable, whereas the voltage is the dependent variable. The current was chosen as the independent variable because of its electrical transient nature, and it can be varied in orders magnitude for a varistor [269].

The I – V properties of the samples were performed by applying a high voltage source measure unit (KEITHLEY instruments 246 high voltage supply). The resistance R was evaluated from Current (I) - Voltage (V) characteristics in accordance with Ohm's Law.

3.7 Cytotoxicity test

The cytotoxicity test was conducted to show the toxicity level of different samples towards specific live cells (L929). This section describes the general methods, reagents, and instruments used in this test. The standard cell culture techniques used to freeze, thaw, and grow the cells prior to treatment with different treatments are described.

3.7.1 Materials required

This testing method required the following basic materials:

- Bio-safety cabinet: This was required to conduct experiments in a sterile contamination free environment.
- 37 °C incubator: It is a conditioned environment for cell culture and cell storage.
- Inverted microscope: It was used for conducting cell counts.

- Reagents: Trypsin, PBS (Phosphate Buffer Saline), DMEM (Dulbecco's Modified Eagle Medium), Sodium Dodecyl Sulfate (SDS) and Blue dye.
- Readily available cell culture: Fibroblasts L929 mouse cell lines were used in this study due to their fast growth and proliferation in media culture.

The image of L929 cells are shown in Fig. 3.12.

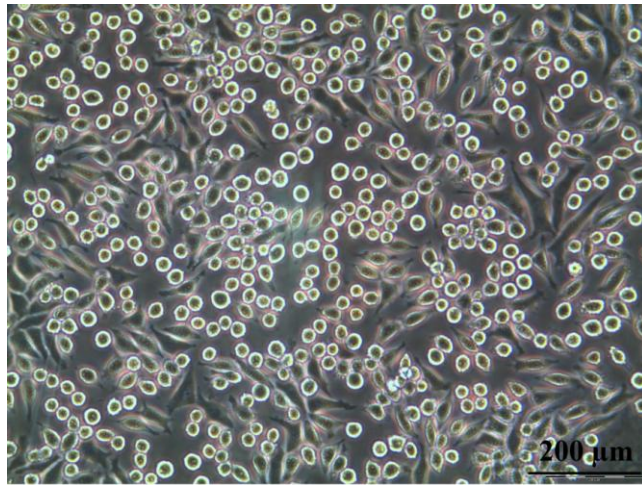


Figure 3.12. Mouse skin fibroblast cell L929 (No: ATTC CCL-1 (Designation L929))

- Test material: 8 types of ZnO materials; W4-ZnO disc, P8-ZnO disc, 20nm ZnO disc, 40nm ZnO disc, W-ZnO varistor, P-ZnO varistor, 20nm ZnO varistor, and 40nm ZnO varistor. The amount of material used per assay, was according to the standard specifications for cytotoxicity testing. According to the standard, the contact surface per ml of DMEM has to be 6 cm²/ml or 3 cm²/ml depending on the thickness of the material and for powder materials it has to be 10 mg/ml of DMEM.
- Centrifuge: Required for separation of material from DMEM.
- Vortex Mixer: Required for mixing the material with DMEM.

- Other handling equipments: Sterile Microtiter Plates (2x6=12 well plate), Multi-channel pipette, Sterile tubes (2ml), Serological pipettes and Sterile pipette tips (200µl, 100µl, 50µl).

The photos in Figure 3.13 (a), (b), (c), and (d) clarify the equipments used for the mentioned tests.

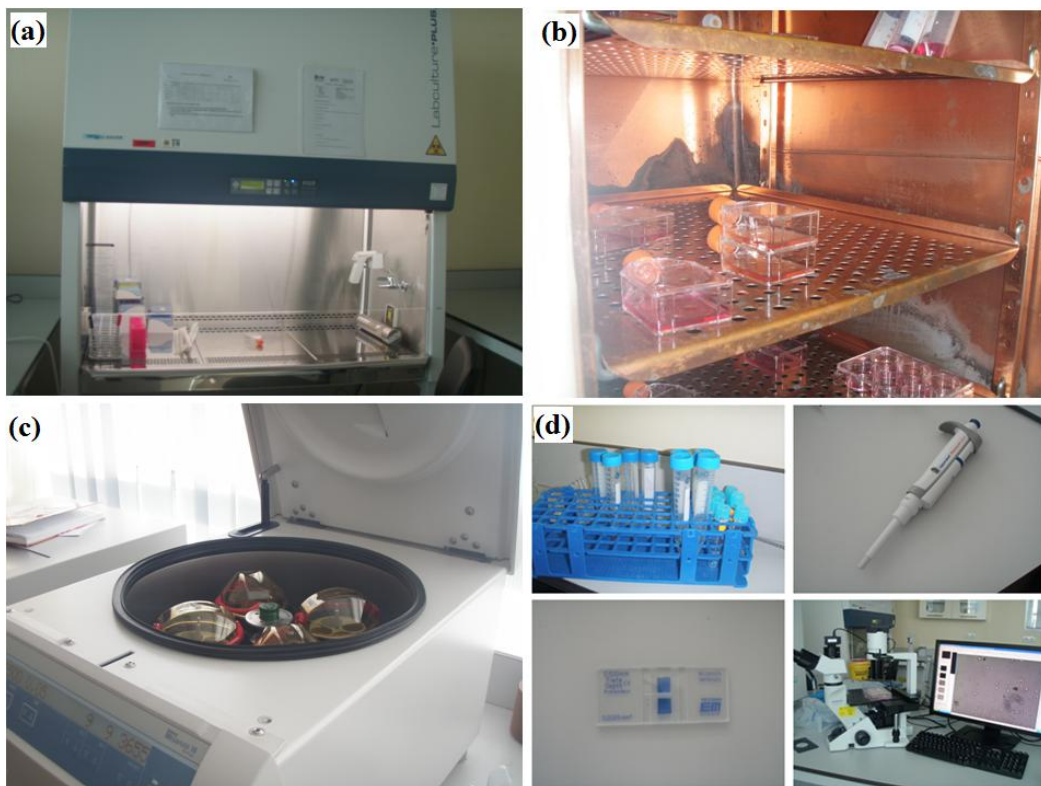


Figure 3.13. Photos of cytotoxicity equipments (a) Bio-safety cabinet, (b) 37 °C incubator with 5% CO₂ (c) Laboratory centrifuge device (d) Layout of Hemocytometer counting chamber with trypan blue and inverted microscope.

3.7.2 Experimental procedure

3.7.2.1 Cell culture

All cell culture processes were carried out inside the bio-safety cabinet under appropriate aseptic conditions. L929 cells with batch No. ATCC CCL-1 was used in all experiments. This cell line is derived from healthy subcutaneous areolar tissue (fibroblast connective tissue) of 100-day old male C3H/An mouse (ECACC No. 85011425 Mouse C3) [247].

The L929 mouse fibroblast cells were maintained in DMEM containing high glucose, and complemented with 10% (v/v) fetal bovine serum (FBS) and 1% penicillin 10000 units.ml⁻¹/streptomycin 10000 µg.ml⁻¹ solutions. The supplemented essential cell culture medium is henceforward referred to as “growth medium”. L929 cells were cultured in growth medium and incubated at 37 °C with 5% CO₂ in a humidified air incubator before use.

All cytotoxicity experiments described in this work were performed using L929 cells between cell passage 8 and 21. In cell biology, cell passage is known as the number of times that cells split to enable L929 cell growth *in vitro*. For example, passage 8 refers to the eighth splitting of the cells.

3.7.2.2 Growth media preparation

Careful execution of techniques is critical to avoid contamination of the medium, which affects the cells. The medium used for growing L929 cell line was DMEM. FBS (10.0%) was poured into 500 mL DMEM. After which, 0.5% of streptomycin/penicillin was added. The media was then shaken and kept inside a freezer at 4 °C for further use.

3.7.2.3 Freezing of L929 cells

L929 cells were produced from a confluent cell layer grown in a cell culture flask and detached from the flask by trypsinization (explained in Section 3.7.2.5) and re-

suspended in the growth medium. Prior to long-term usage, cells were kept in liquid nitrogen at a low temperature ($< 150\text{ }^{\circ}\text{C}$). L929 Cells were counted and cell suspensions were prepared with 1 million cells in 500 μL of 10% (v/v) dimethyl sulfoxide (DMSO) in FBS. DMSO was used in this test as a cryoprotective agent. The suspensions were kept in properly labelled cryovials stored overnight at $-80\text{ }^{\circ}\text{C}$ for slow cooling. The cryovials were then transferred to a cryogenic freezer with liquid nitrogen at a temperature of $-150\text{ }^{\circ}\text{C}$.

3.7.2.4 Thawing of L929 cells

The frozen L929 mouse fibroblast cell line was used. The frozen cells from the liquid nitrogen cell storage were retrieved, rapidly thawed and then submerged in water at $37\text{ }^{\circ}\text{C}$. The contents of the cryovial were then transferred to a 15 mL centrifuge tube, followed by the addition of 5 mL pre-warmed DMEM to the cell suspension. The suspensions were centrifuged at 1200 rpm for 10 min. Meanwhile, 15 mL DMEM was pipetted into a T-75 flask.

After centrifugation, the supernatant was removed and 1 mL DMEM was gradually added to re-suspend the pellet. The suspension was transferred slowly into the flask and slowly shaken to ensure even distribution of cells, and floating cells were observed using the integrated microscopic Zeiss-Axiovert 40-C. The cells were then placed inside a $37\text{ }^{\circ}\text{C}$ humidified incubator supplemented with 5% CO_2 . The cells were closely monitored for 24 h.

3.7.2.5 Cell passage (subculture)

The cells were grown in a T-25 cell culture flask. Cell passage or splitting occurred when cells reached 80%–100% confluency. Cell confluency was assessed by a light optical microscope. The cells were examined carefully for signs of contamination or deterioration. Prior to cell passage, the old growth medium in the flask was discarded and the flask was rinsed with 2.5 mL sterile phosphate buffered saline to flush out all traces of serum that will inhibit the action of trypsin. Trypsinized solution (2 mL) was added to coat the surface of the

flask. The flask was then incubated at 37 °C in CO₂ for 5 min. The trypsinization was continued until 90% of the cells aggregated and floated. Trypsin was deactivated by adding 2 mL of DMEM containing 10% (v/v) FBS, and the ratio between the DMEM and trypsin was 1:1. The cells were dispersed into the single cell suspension by repeated pipetting on the surface of the culture flask. The single cell suspension was then transferred into 15 mL centrifuge tubes and centrifuged at 1500 rpm for 5 min. Simultaneously, 7.5 mL of completed growth medium was transferred to two separate fresh flasks. The supernatant was discarded from the centrifuge tube (falcon tube), and 2 mL DMEM was added to re-suspend the pellet. Finally, 300 µL of cells was mixed with 7.5 mL medium in the culture flask. When the cells were stable and confluent in the flask, 1 mL of the cell suspension was transferred into a conical tube. Then 50 µL of the cell suspension were mixed with 50 µL trypan blue in the falcon tube. A portion of the cell suspension was dropped into the chamber grid. The numbers of live cells z were counted using a light microscope. The initial 10000 cells seeded in each well were used as the control, and the number of suspended cells added to the 6 well-plate y was determined from the ratio as below:

$$\frac{z \text{ cells}}{10000 \text{ cells}} = \frac{1000 \text{ } \mu\text{l}}{y \text{ } \mu\text{l}} \quad (3.2)$$

3.7.2.6 Extraction process

The extraction protocol was in accordance with ISO standard 10990-12 that allows the determination of possible toxicological risk without leading to a considerable alters to the sample parts or change the chemical construction. On one hand, the samples were incubated in a 15 mL extraction apparatus containing DMEM inside a 50 mL centrifuge tube under strict sterile conditions (Fig. 3.14 (a)) for the indirect method. On the other hand, the samples were incubated in a 3 mL extraction apparatus containing DMEM inside 6-well plates (Fig.

3.14 (b)) for the direct method. The materials were placed in an incubator with CO₂ at 37 °C for 72 h for the indirect method and 24 h for the direct method.



Figure 3.14. Photos of extraction process for (a) indirect method, and (b) direct method

After incubation, the cells stabilized and attached to the well-plates. The media were subsequently removed and changed with new media. For the indirect method, the samples were harvested from the media and treated media was then dropped into the cell culture. The cell treatment was achieved in triplicate. The cells morphologies were determined under a light microscope (Olympus CKX41) after 24, 48, and 72 h incubation. For the direct method, the morphologies of the cells were observed directly, without removal of the samples from the media, under the microscope after 24, 48, and 72 h incubation. A negative control (without ZnO sample) was prepared for purposes of comparison.

3.7.2.7 Cell counting

Cell counting was carried out using trypan blue solution 0.4% (Sigma) after 72 h incubation. The trypsinized cells were transferred into falcon tubes (conical) and centrifuged for 5 min at 1500 rpm. The supernatant was then discarded, and 2 mL of DMEM was moved in to tube and re-suspended. When the cells were stable and confluent in the flask, 50 μ L of

mixture were mixed with 50 μL trypan blue stain in a falcon tube and suspended until the solution and cells were homogenous.

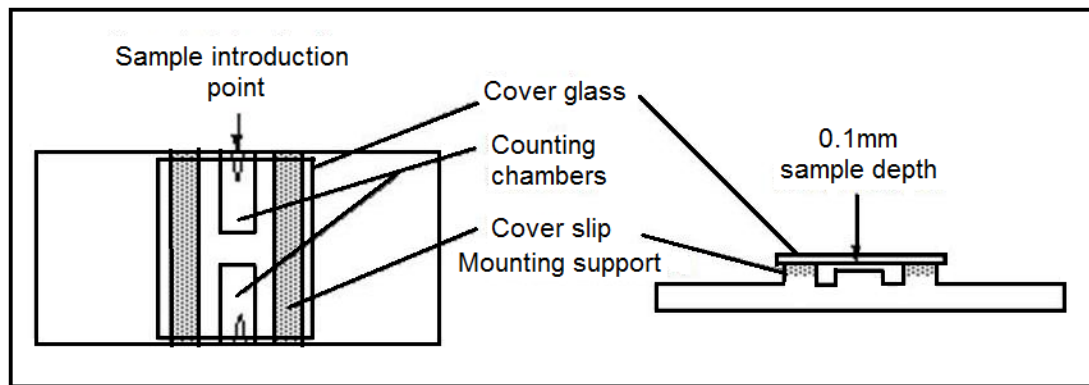


Figure 3.15. Layout of Hemocytometer counting chamber

A portion of the stained cells were pipetted into the counting chamber grids (hemocytometer). The chamber was placed on the microscope stage, and the microscope was focused until a clear cells image was visible via the eyepiece. The four corners of squares each have 16 squares within an area of 1.0 mm^2 . Each laboratories have various counting protocols, however there is a general rule stating that cells touching the upper and left limits should be counted, whereas cells touching the lower and right limits should not be taken into account. An enlargement of a corner square indicates that cells should be included in the count, wherein the stained (dead cells) should be ignored, and unstained cells (live cells) should be counted.

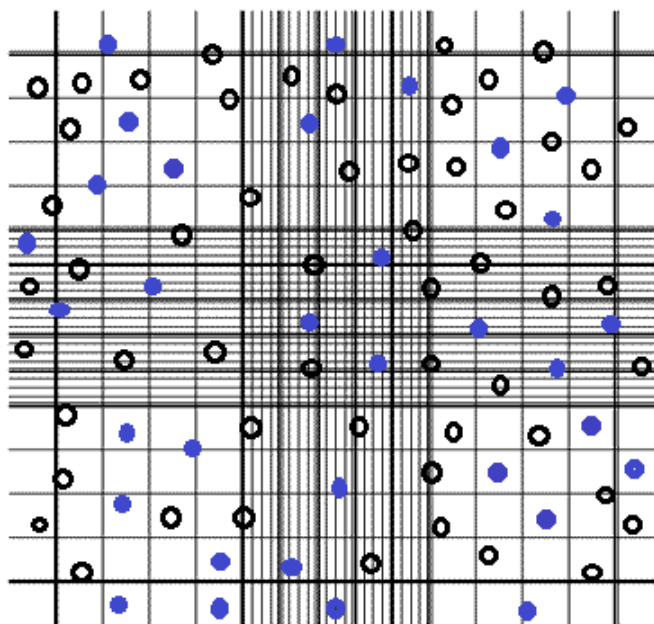


Figure 3.16. Illustration of Hemocytometer counting chamber

Number of live cells (z) was calculated. The number of live cells (A) were calculated by using the equation 3.3.

$$A = z \times 2 \times 2500 \quad (3.3)$$

The number of stained (dead cells) and unstained cells (live cells) were calculated using a hemocytometer and then matched with the control set. The levels of samples toxicity were selected from observation the viability of cells.

3.8 Summary

The instrumentations with their basic characterization methods and materials used in this study have been described briefly in this chapter. The experimental sets up as well as the details of the ZnO materials used have also been discussed. Table 3.4 summarized the instruments and the information revealed from each of them.

Table 3.4. Techniques, instrumentation types and the information that are revealed in this study.

Technique	Instrument	Information revealed
Ball Milling	BALL MILL, 9 Variable Speed	Grind materials into extremely fine powder
Pressing Process	CARVER	Formation discs
Sintering Process	CARBOLIRE sintering furnace	Consolidation of powder particles
Polishing process	GRINDER-POLISHER Metaserv 250, BUEHLER	Flat surface
Annealing Process	Tube Furnace, LENTON VTR/12/60/700	Heat treatment
TEM	Phillips CM 12	Internal structure of materials
SEM	JSM – 6460 LV	Image the sample surface and near surface
XRD	PANalytical X'pert Pro MRD PW 3040	Crystal structure, chemical composition, and physical properties of materials
EDX	JSM – 6460 LV	Elemental analysis or chemical characterization of a sample
AFM	Dimension EDGE, BURKER	Morphology of sample and image the topography of surface
I – V Testing	KEITHLEY 237	Current and Voltage measurement
PL Spectroscopy	Jobin Yvon HR 800 UV	Energy band gap , discs quality
Raman Spectroscopy	Jobin Yvon HR 800 UV	Study vibrational, rotational, and other low-frequency modes in a system
Bio-safety cabinet	ESCO Class II BSC	Conduct experiments in a sterile contamination free environment
37 °C incubator	Thermo Scientific Heraeus Incubator BB 15	Conditioned environment for cell culture and cell storage
Centrifuge	Thermo Scientific Heraeus Megafuge 16	Separation of material from DMEM
Inverted microscope	OLYMPUS CKX41	Conducting cell counts
Integrated microscope	Zeiss-Axiovert 40-C	Cell morphology observation

CHAPTER 4: RESULTS AND DISCUSSION 1

PURE ZnO: EFFECT OF PARTICLE/GRAIN SIZE AND SURFACE MODIFICATION ON THE STRUCTURAL, ELECTRICAL AND OPTICAL PROPERTIES OF PURE ZnO MICRO/NANOPARTICLE BASED DISCS

4.1 Introduction

In this chapter, the successful fabrication of pure ZnO micro/nanoparticle-based discs is discussed. The results of the investigation on the different physical, structural, electrical, and optical properties of these discs at different annealing conditions were related to the various structures of ZnO discs, different particle sizes of ZnO powder, and different annealing conditions. The chapter also focused on the probable mechanisms of surface modification by annealing. Several mechanisms are proposed for the results and observations obtained. The structural properties of samples are investigated by SEM. The optical characteristics of the discs are investigated by using Raman and PL spectroscopes. The electrical behaviors were extracted from a high-voltage source. The conclusions are summarized in the last section of the chapter.

4.2 Physical transformation

Fig. 4.1 explains the physical transformation of the raw material from the green form (granules) into the green compacts (discs). The green discs were sintered at 1200 °C for 1 h to form hard discs; white in color for pure ZnO discs and black in color for composite disc. At this phase, the electrical properties of the samples were completely formed. Electroding by applying a thin silver layer onto both surfaces of each disc was carried out. These silver electrodes provide the conducting interface (ohmic contact) with the insulative ZnO discs (little effects of silver contact on discs properties). To test for suitability, the silver-electrode discs were connected to conducting lead wires by dipping them in a soldered bath.

Eventually, the lead-soldered discs were encapsulated by epoxy resin for insulation and protection of the connections.



Figure 4.1. Pure and composite ZnO-based disc transformation from granulated form to finished form.

4.3 Structural properties of pure ZnO discs prepared from ZnO micro and nanoparticles size

4.3.1 Transmission electron microscopy (TEM)

The precise morphological structure and particles sizes in two dimensional imaging were inspected by TEM micrographs. Fig. 4.2 shows TEM micrographs of ZnO-White (W4), ZnO-Pharma (P8), 40nm ZnO, and 20nm ZnO. All samples exhibited varying morphologies such as micro/nanoplates, tetrapods, tripods, and pebble-like structures. Micro/nanoplates with lengths ranging from 60–250 nm were observed in ZnO-White (Fig. 4.2 (a)). Different morphologies were observed in the cluster of micro-or nanoparticles, including nanoplates, tripods, and tetrapods. The wurtzite crystalline structure of the ZnO discs was verified by the hexagonal drum-like structure shown in the inset of Fig. 4.2 (a). Notably, the hexagonal ZnO structure reveals the wurtzite crystalline property of ZnO-White

The ZnO-Pharma (Fig. 4.2 (b)) is rich in rod-like structures with width ranging from 30–120 nm. Moreover, the nanorods have rounded or tapered ends. ZnO-Pharma tends to have minimal particle size than ZnO-White caused by the smaller size of rod-like structures compared with that of plate-like structures. As a result, ZnO-Pharma particles also have higher S/V ratio than ZnO-White, which accounts for the differences in optoelectronic and biological properties.

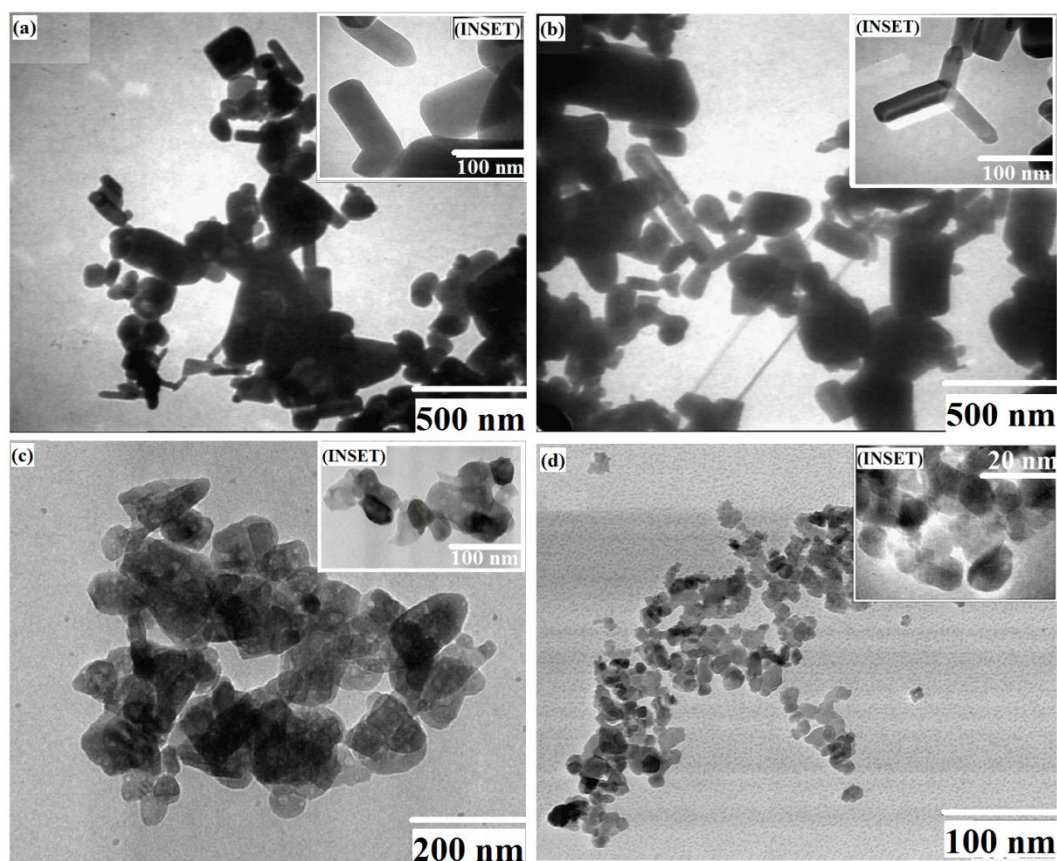


Figure 4.2. TEM micrographs of (a) White ZnO (W4), (b) Pharma ZnO (P8), (c) 40 nm ZnO, and (d) 20 nm ZnO and (INSET) a higher magnification of each ZnO type.

Fig. 4.2 (c) is a TEM micrograph of the ZnO nanopowder used to make the ZnO discs. The 40nm ZnO are present as granules with spindle-like shapes, and the average particle size was approximately 40 nm, which are polycrystalline in nature and uniform in shape.

Fig. 4.2 (d) is a TEM micrograph of the 20 nm ZnO nanopowder, which consisted of agglomerates of pebble-like ZnO nanoparticles with a diameter of approximately 20 nm.

Fig. 4.2 (c) and (d) (inset) show the pebble-like morphology of the ZnO nanoparticles with a highly porous appearance.

4.3.2 Scanning electron microscopy (SEM)

Fig. 4.3 shows the SEM micrographs of W4-Disc, P8-Disc, 40nm-Disc and 20nm-Disc, which were sintered at 1200 °C and then annealed at 700 °C in the oxygen and nitrogen ambients. In different types of ZnO discs at various annealing ambient, SEM images present that the morphology of the samples surface was basically dependent on the annealing temperature and the grains grew larger, more structured and resembled polygons (hexagon) compared to the as-sintered discs, and the pores became smaller as shown in Fig. 4.3. High temperatures are known to provide a large driving force for the internal atomic diffusion responsible for grain growth and pore elimination, and assist in developing a well-oriented crystal lattice.

Fig. 4.3, shows that W4-Disc, P8-Disc, 40nm-Disc and 20nm-Disc samples at different annealing conditions have a strong structure without pores. However, the average grain size of the discs annealed in nitrogen increased marginally compared with that in ambient oxygen, with the exception of the P8-Disc, in which the average grain size decreased in ambient nitrogen. Annealing in ambient O₂ induced a rather dense morphology, whereas annealing in ambient N₂ resulted in a partially porous morphology. On the one hand, the increase in the grain sizes in W4-Disc, 40nm-Disc and 20nm-Disc could be attributed to the generation of oxygen vacancies in the nitrogen ambient (as vacancy concentration exponentially grows with raising temperature) that may impact the grain growth kinetics via changing the diffusion flux of oxygen vacancy types. On the other hand, the decrease in grain size in the P8-Disc could be due to the destruction of disc surface caused by the contamination of hydrogen atoms that react with oxygen species on the surface; thus, weakening crystallinity as explained by the following XRD analysis.

The 20nm-Disc exhibit the largest particle size compared with the W4-Disc, P8-Disc and 40nm-Disc samples (Table 4.1). This phenomenon maybe attributed to the high S/V ratio in the nanoparticles. Two major factors dominating the characteristics of nanomaterials

are their size and surface features [270, 271]. These mentioned factors are correlated attributed to the S/V ratio raises as the size is reduced (Fig. 4.3).

The size of the nanoparticles is clearly significant in the determination of fundamental properties as discussed in the later sections of this thesis. In sintering, a large number of atoms will be exposed to high temperature, absorb more oxygen during the annealing process and then grow bigger.

Notably, tiny white spots in the 20nm-Disc (approximately 80–100 nm) were clearly present during oxygen annealing, which were not observed in the W4-Disc, P8-Disc and 40nm-Disc. Larger white spots might be agglomerates of these nanoparticles. Presumably, the sintered ZnO provided the excess free zinc that was oxidized into ZnO during the oxygen-rich annealing treatment. This phenomenon is not reported elsewhere to the best of our knowledge.

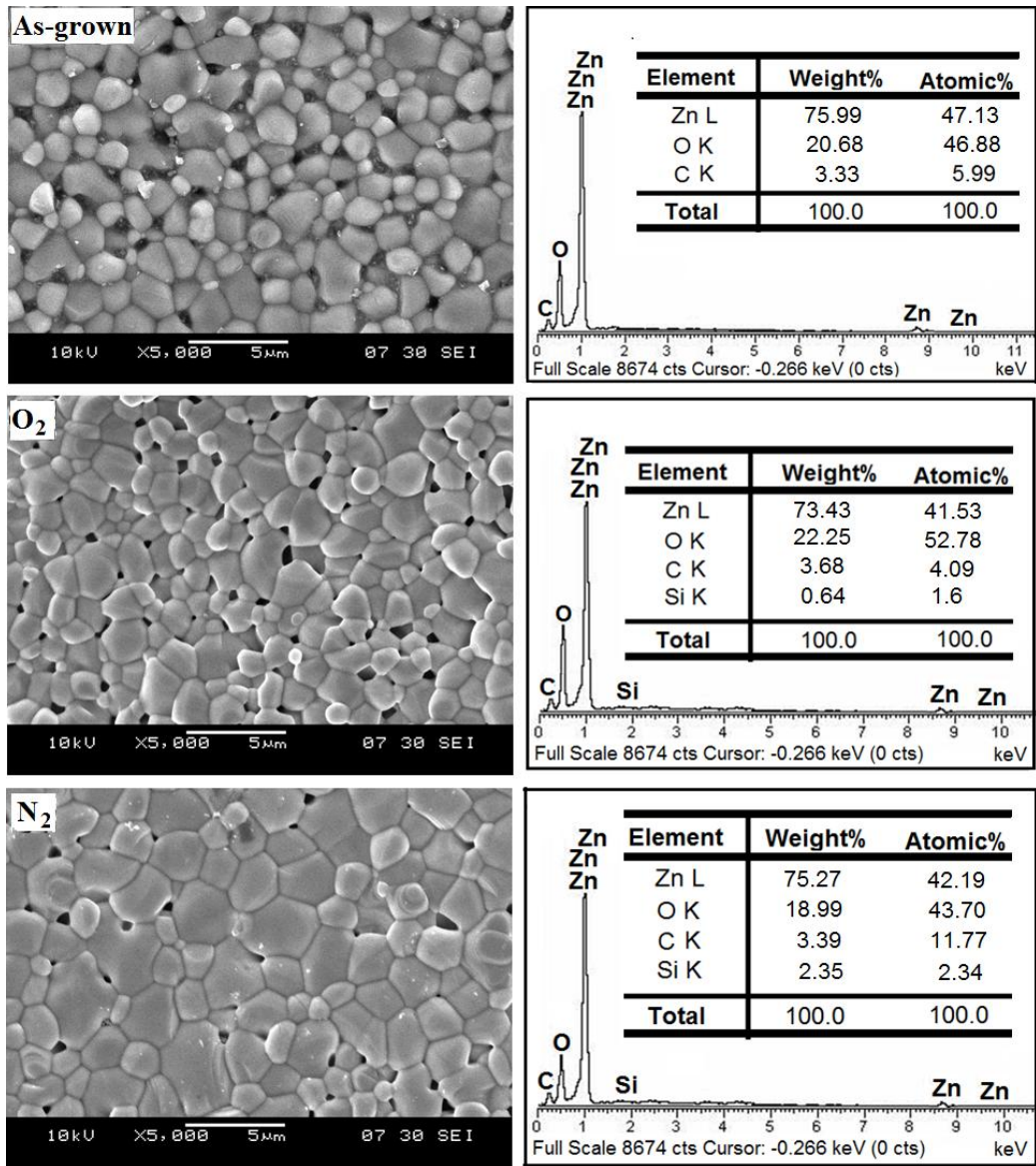
A layer-by-layer growth of several grains in the 20nm-Disc was also observed (Inset of Fig. 4.3 (d)). This secondary layer-growth occurred during the oxygen-rich annealing. Figure 4.3 (d) shows SEM micrographs of the polycrystalline layers with thickness of 80–120 nm. These multilayer growths were localized in several grains only; thus, a high concentration of free zinc allowed the secondary layer-growth.

Notably, significant grain growth has occurred in the 20nm-Disc in addition to a secondary growth involving ZnO nanoparticles and multilayer grains. This interesting phenomenon may be attributed to the strong surface reaction during annealing as a result of the significant surface area of the 20 nm nanoparticles used to make the ZnO discs.

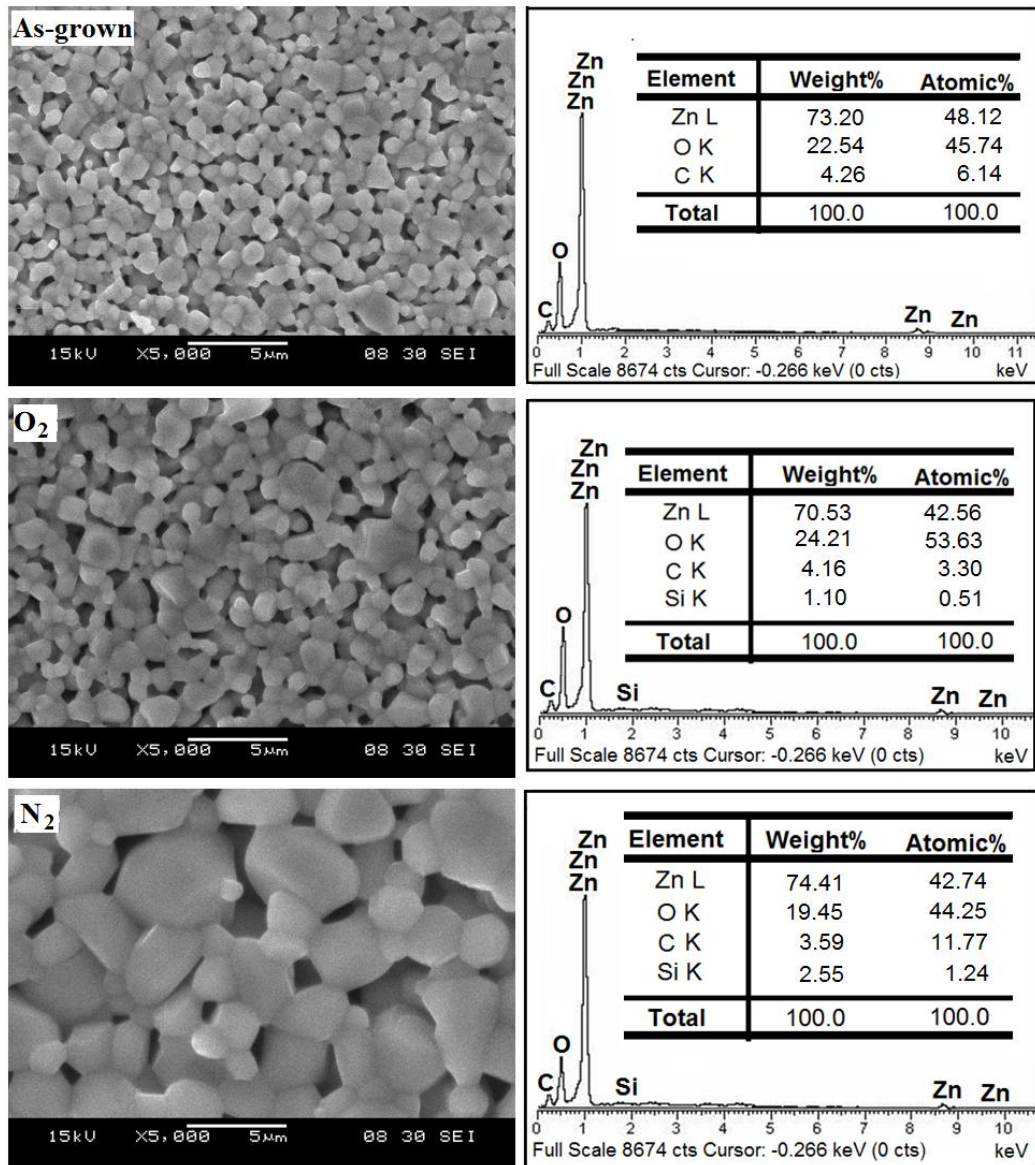
The thermal annealing process resulted in compression of the ZnO grains toward the center of the W4-Disc, P8-Disc, 40nm-Disc and 20nm-Disc, which resulted in the growth in grain size. Annealing increased oxygen concentration in the disc and caused a distortion. This result indicates the presence of tensile stress within the ZnO discs, as discussed in the following XRD analysis.

The EDX data (Fig. 4.3) show that the oxygen content in all disc samples increased with annealing in oxygen because of the increase in the oxygen diffusion energy. The high oxygen content in the annealed sample may be attributed to the interaction of ZnO with atmospheric oxygen during the annealing process under ambient conditions. The EDX results also reveal the presence of trace amounts of other elements (impurities) in the ZnO discs, which were introduced during the preparation and annealing processes.

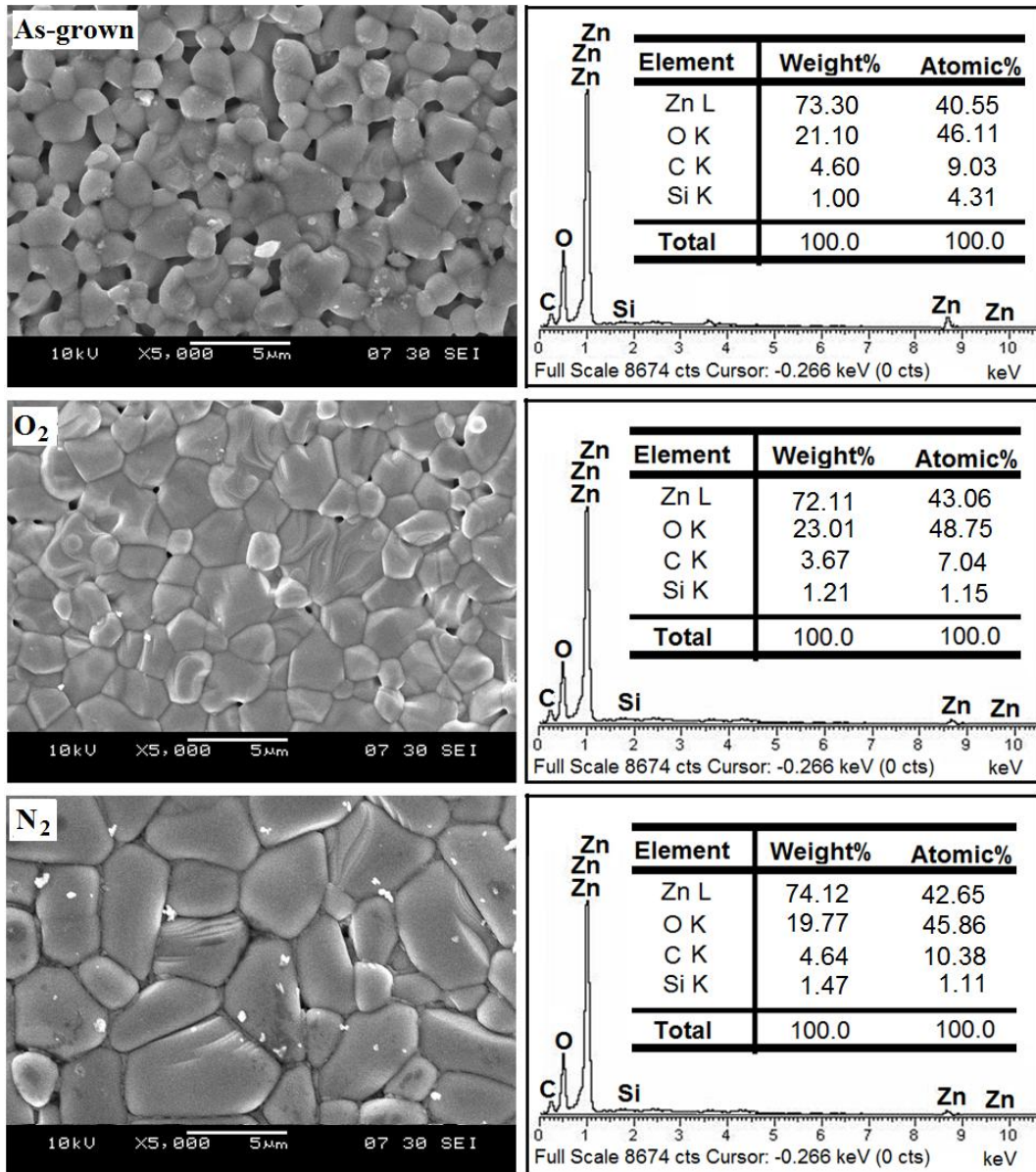
Note that the method used to measure average grain size can be seen in APPENDIX A.



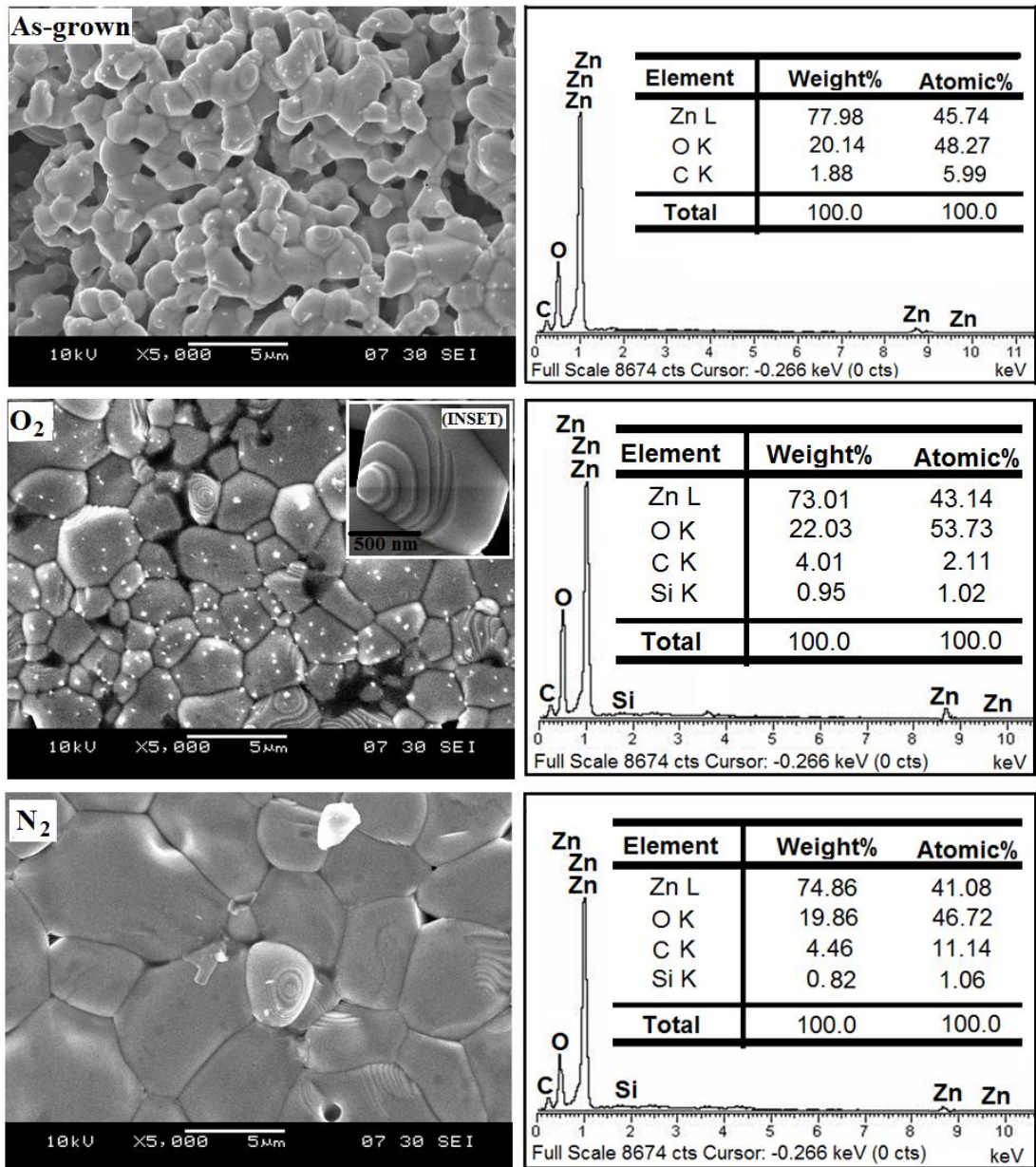
(a)



(b)



(c)



(d)

Figure 4.3. Typical SEM-EDX images of (a) W4-Disc, (b) P8-Disc, (c) 40nm-Disc, and (d) 20nm-Disc annealed at different ambients.

Table 4.1 summarizes the SEM results for ZnO discs fabricated with different particle sizes at different annealing conditions. Variation in the grain size is then plotted as a function of the different particle sizes (Fig. 4.4).

Table 4.1. Summary for SEM images of ZnO discs with different annealing atmospheres.

Sample	Annealing ambient	Grain size (μm)
W4-Disc	As-grown	1.113
	O ₂	1.701
	N ₂	2.830
P8-Disc	As-grown	0.911
	O ₂	1.523
	N ₂	3.302
40nm-Disc	As-grown	1.441
	O ₂	2.610
	N ₂	3.921
20nm-Disc	As-grown	1.544
	O ₂	3.423
	N ₂	5.204

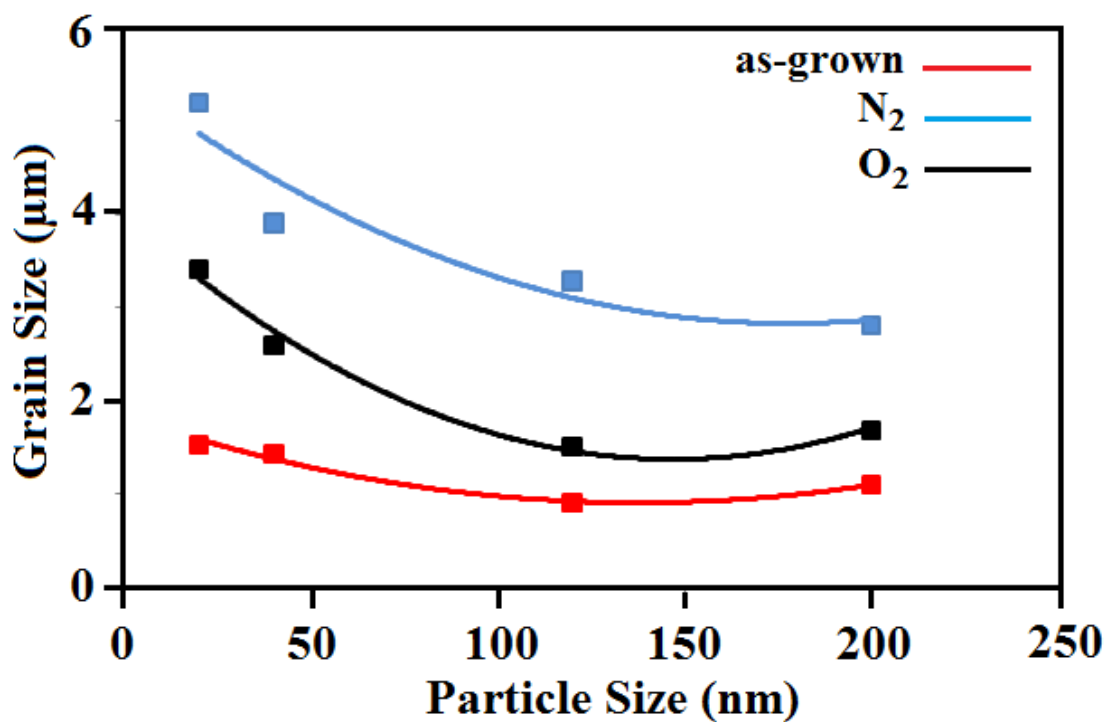


Figure 4.4. Plot of grain size of as-grown and annealed ZnO samples as a function of different particle sizes.

4.3.3 X-ray diffraction (XRD)

The XRD pattern of the W4-Disc, P8-Disc, 40nm-Disc and 20nm-Disc are presented in Fig. 4.5. A number of strong Bragg reflections at (101), (100), (002), and (110) was observed, which confirmed the polycrystalline nature of the discs. Spurious diffractions caused by crystallographic impurities were not found [272]. The common crystal habit of ZnO is hexagonal because of the crystal symmetry and related face velocities. In addition, the ZnO nanoparticle is in a thermodynamically stable crystallographic phase. The intensity of the peaks referred to the high degree of crystallinity of the ZnO nanoparticles. However, the width of the peaks in the 40nm-Disc and 20nm-Discs has increased, compared with the W4-Disc and P8-Discs, because of the quantum size effect.

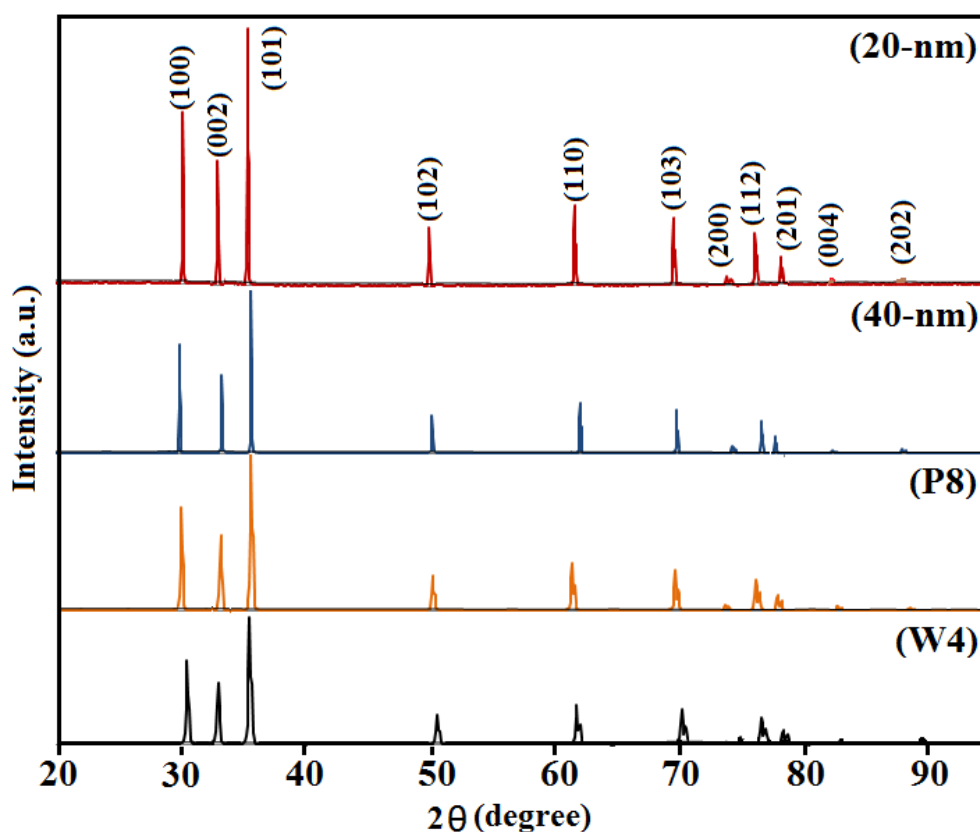


Figure 4.5. XRD pattern of as-grown ZnO discs fabricated from ZnO micro and nanoparticle powders.

The shape and broadening (breadth) of XRD peaks reveal microstructural information including the size distribution, average size and shape of crystallites (i.e. nanocrystalline and crystalline nanoparticles materials), twinning/lattice faulting, and density and spatial arrangement of dislocations. These microstructural information are usually combined together and can be grouped into size-broadening or strain- /distortion-broadening contributions. XRD peaks are designed to reflect microstructural information.

When the particle size is smaller than 100 nm, the broadening of the XRD peaks are measurable. The relation applied for the calculation of crystallite size is the Scherrer formula [69]:

$$D = \frac{K\lambda}{\beta \cos \theta_B} \quad (4.1)$$

whereby:

D is the volume-weighted apparent crystallite size.

β is the integral breadth of the line profile (XRD peak) caused by small crystallite size.

K is the factor of particle shape, which based on the particles shape and its value is about 0.94 for spherical particles.

λ is the CuK $_{\beta}$ radiations (1.54 Å).

and θ_B is the Bragg angle achieved from 2θ value compatible to the same plane.

However, besides the generic instrumental broadening, another substantial cause for broad peaks of XRD is strain broadening (distortion broadening caused by dislocations, twins, and stacking faults). This broadening is due to the microstrain $\varepsilon = \Delta d/d$ (where d is the interplanar distance between hkl planes) in the discs. Table 4.2 shows a summary of the XRD phases. Notably, the diffraction angle of the as-grown 40nm-Dics and 20nm-Disc increased by larger values compared with the W4-Disc and P8-Disc, which was due to an extremely high concentration of structural defects in the nanoparticles powder raw material, especially in the 20nm-Disc. In addition, the XRD pattern (101) peak demonstrates a peak

shift towards a higher diffraction angle for discs annealed in nitrogen and oxygen compared with that of the as-grown discs. Chemisorption process of nitrogen or oxygen on the surface after thermal annealing, which lead to the distortion of crystallites, may account for this phenomenon.

Several researches indicated that the residual stress in ZnO include an intrinsic stress component and a thermal stress component [273, 274]. In addition, intrinsic stress caused by deficiency of crystallites during growth was also present. The parameters of growth, such as pressure, gas mixture, power, and deposition temperature, may also have caused intrinsic stress. In a considerable number of studies [273, 274], the intrinsic stress of the as-grown ZnO was compressive. By contrast, extrinsic stress can be generated during pressing, sintering, and annealing. The thermal stress in the discs generates from the variation in the thermal expansion coefficient α as a result of the variations in the annealing conditions.

The effect of different annealing conditions on the W4-Disc, P8-Disc, 40nm-Disc and 20nm-Disc is shown in Fig. 4.6. The (101) peaks of the as-grown W4-Disc, P8-Disc, 40nm-Disc, and 20nm-Disc increased dramatically from $2\theta = 36.195^\circ$, 36.212° , 36.334° , and 36.375° to $2\theta = 36.197^\circ$, 36.271° , 36.345° , and 36.387° , respectively, after oxygen annealing. However, nitrogen annealing did not show any significant rise in the reflection peaks intensity, indicating the increase of tensile force and lattice constants for the ZnO disc annealed in ambient nitrogen. When N_2 gas was used for development of ZnO, the diffraction peak intensity of ZnO (101) is significantly reduced, and *FWHM* is relatively broad compared with the ZnO disc annealed in ambient oxygen. The broadening of the (101) peak for the samples annealed in ambient N_2 should be attributed to the defects related to the incorporation of N_2 in the discs, as observed by Li et al. [275].

The change in the (101) diffraction peak with different annealing atmospheres can be attributed to the stress in the ZnO disc or the N molecule on the O site ($(N_2) O$). Notably, the semiconductor band gap is influenced via the residual stress in the disc. A compressive stress lead to an increase in the band gap, while a tensile stress lead to a decrease in the band

gap. In the present work, the investigates of the PL spectra show that the band gap changes through the thermal treatment, indicating that the annealing process affected the stress in the ZnO disc. The change in the (101) peaks and *FWHM* are fundamentally induced by the N molecule on the O site because (N₂) O alters the lattice constants of the sample and decreases the quality of crystallization, leading to the increase in *FWHM* values. Therefore, ZnO ceramics annealed in N₂ atmosphere have a high concentration of defects, which results in a reduced quality of ZnO discs. However, the thermal energy of samples annealing in an O₂ atmosphere at a suitable temperature is sufficient to break the Zn–O bond; and acquiring oxygen and other atoms from the annealing ambient and consequently reducing defect density to improve crystallinity.

Generally, the difference of the intrinsic defects within ZnO disc V_{Zn} , V_O , O_{Zn} , and O_i with oxygen pressure (p_{O_2}) during annealing in ambient oxygen can be expressed as follows [91]:



where $[V_{Zn}]$ and $[V_O]$ are the concentrations of the non-ionized vacancies of zinc and oxygen, respectively. $[O_i]$, $[O_{Zn}]$, and $[Zn_i]$, are the concentrations of O_i , O_{Zn} , and Zn_i , respectively. Eqs. (4.2) and (4.4) reveal that concentrations of the V_O and Zn_i have to reduce with a rise in p_{O_2} , whereas Eqs. (4.3), (4.5), and (4.6) indicate that V_{Zn} , O_i , and O_{Zn} could be increased with an increment in p_{O_2} . Therefore, thermal treatment in ambient oxygen can increase V_{Zn} , O_i , and O_{Zn} and subsequently lead to generating oxygen-rich ZnO samples.

During the annealing process, most absorption and desorption of oxygen or nitrogen occurred at the surface of the discs. The small size of particle and huge S/V ratio of nanoparticles compared with the microparticles indicated that the considerable ratio of S/V gives these nanoparticles improved crystal qualities of ZnO nanoparticle-based discs and better crystallinity with more relaxation caused by annealing.

The XRD patterns in Fig. 4.6 show marked deviation of ZnO (101) diffraction peaks from the normal value with different annealing conditions. This phenomenon resulted in the high concentration of deep-level surface trap states inside the formed ZnO nanoparticle lattice, which determined most structural and optical property changes in the discs as discussed in the later sections.

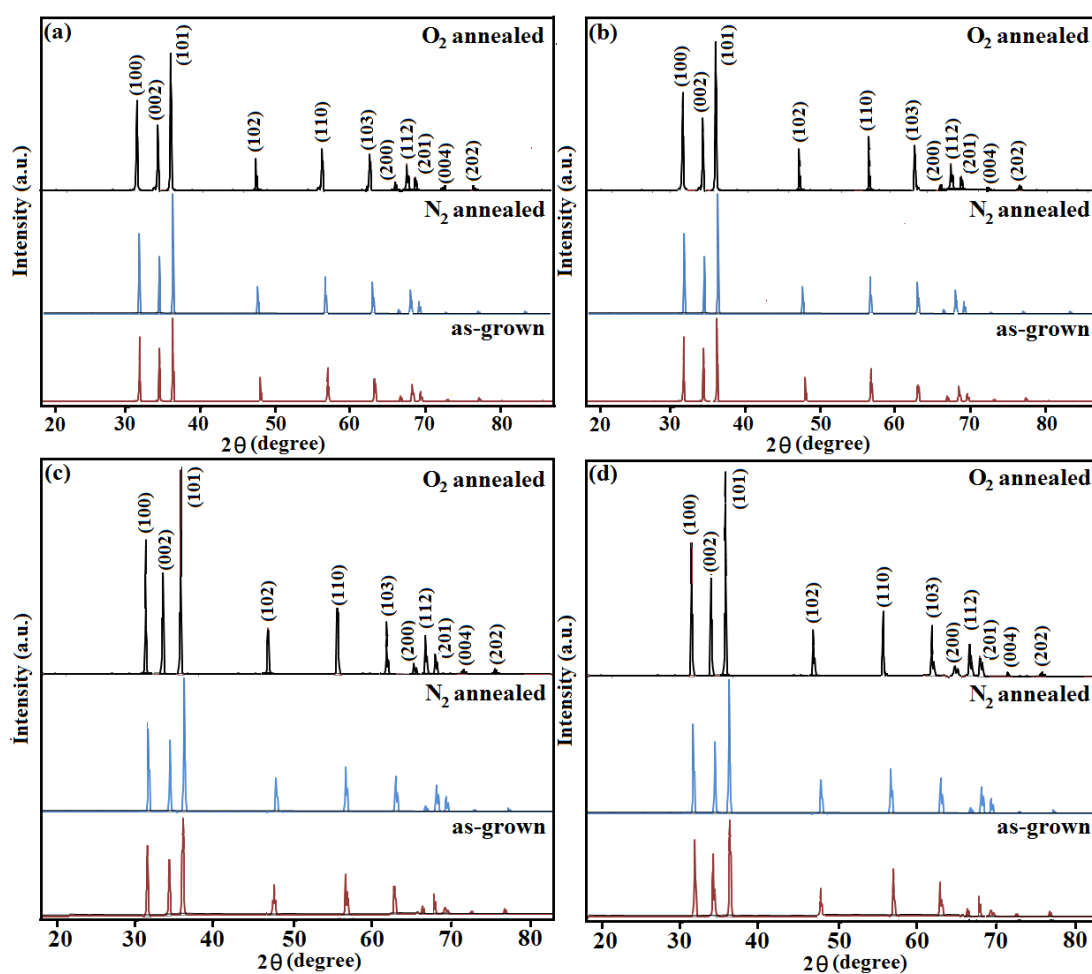


Figure 4.6. XRD pattern of ZnO discs fabricated from (a) White ZnO (W4), (b) Pharma ZnO (P8), (c) 40 nm ZnO, and (d) 20 nm ZnO at different annealing ambients.

XRD data show the significant shift of the diffraction peak (101) for the 40nm-Disc and 20nm-Discs from its as-grown value, which is related to the alter in the lattice constant of the ZnO nanoparticles. Figures 4.6 (c) and 4.6 (d) show the blue shift of the (101) diffraction peaks of 40nm-Disc and 20nm-Disc after annealing compared with as-grown ZnO. This blueshift evidenced the reduce in the lattice constant parallel to the *c*-axis of the ZnO nanoparticles. This phenomenon could be caused by the surface impact (the significant surface tension that produced from the small size of the nanoparticles can lead to lattice distortion and reduce the lattice constant) of ZnO nanoparticles. However, the small shift in the W4-Disc and P8-Disc can be observed in the (101) diffraction peaks (Figs. 4.6 (a) and 4.6 (b)).

Results show that the order of the relative intensities of the XRD peaks from the (101) plane is oxygen-annealed > nitrogen-annealed > as-grown. This order demonstrates that oxygen provides a superior annealing ambient than nitrogen for improving the crystallinity of all discs. Annealing in oxygen atmosphere enhances the reaction among oxygen and the Zn interstitials to generate crystalline ZnO. During the annealing in oxygen ambient, the oxidation rate is significantly faster because of greater dropping in the free-surface energy. Thus, the crystallinity of the oxygen-annealed ZnO nanoparticles is better than that of the nitrogen-annealed ZnO nanoparticles because annealing in ambient oxygen results in a decrease in oxygen vacancies that is the most general defect in ZnO according to literature.

The electronic structure of an oxygen vacancy within ZnO, which includes the four Zn dangling bonds and two electrons, is well known. These Zn dangling bonds collect into a fully symmetric a_1 state located in the band gap and three almost degenerate states in the conduction band. In the neutral charge state of the oxygen vacancy, the a_1 state is doubly occupied and the three states in the conduction band are empty. On the basis of the above mentioned, the V_0 within ZnO crystal can theoretically exist in three different charge states, namely, neutral, +1 and +2, in which the a_1 state is doubly occupied, singly occupied, and

empty, respectively. The a1 state occupation during the annealing process in ambient oxygen is related to the local lattice relaxation around the oxygen vacancy.

In annealing in ambient nitrogen, nitrogen can occupy an oxygen site (N_o) and produce a multicenter with bonds to the four nearest neighboring Zn atoms; thus, reducing the quality of the ZnO crystal.

Table 4.2 summarizes the XRD results. The lattice constant c was calculated for hexagonal system from the equaton 4.7 [69]:

$$\frac{1}{d^2} = \frac{3}{4} \left(\frac{h^2+hk+k^2}{a^2} \right) + \frac{l^2}{c^2} \quad (4.7)$$

where h , k , and l were evaluated by XRD analysis. The lattice spacing d was calculated based on Bragg's equation 4.8 [276]:

$$d = \frac{n\lambda}{2\sin\theta} \quad (4.8)$$

where λ ($=1.5405 \text{ \AA}$) is the X-ray wavelength, and θ is the diffraction angle.

From the peak positions of the ZnO (002) planes, the ZnO crystal parameters c were obtained, and a summary is presented in Table 4.2. These values were comparable with the c_0 of bulk ZnO at 5.206 \AA [10]. Subsequently, the stress σ in the ZnO disc was obtained by applying the strain model for hexagonal crystals, as shown in equation (4.9) [277, 278]:

$$\sigma = \left(\frac{2C_{13}^2 - C_{33}(C_{11} - C_{12})}{C_{13}} \right) \left(\frac{C_o - c}{C_o} \right) \quad (4.9)$$

where σ is the mean stress in the ZnO sample; $C_{11} = 209.7$ GPa, $C_{12} = 121.1$ GPa, $C_{13} = 105.1$ GPa, and $C_{33} = 210.9$ GPa are the elastic stiffness constants of bulk ZnO; c_0 is the lattice constant of strain-free bulk ZnO, and c the lattice constant of the ZnO disc. The estimated value of the bulk ZnO elastic stiffness constants is approximately -453.6 GPa. The calculated values of the stress σ in the W4-Disc, P8-Disc, 40nm-Disc and 20nm-Disc are listed in Table 4.2. The positive values of samples referred to a tensile stress generated by the stretching size of crystal, indicating that the lattice constant decreased compared with that of the stress-free sample. Whereas, the negative value and compressive stress indicated that the lattice constant was elongated compared with that of the stress-free sample [279].

Table 4.2 summarizes the XRD data and stress for W4-Disc, P8-Disc, 40nm-Disc and 20nm-Disc at different annealing conditions. Variation in the stress is then plotted as a function of the different particle sizes (Fig. 4.7). Calculations of stress can be seen in APPENDIX C.

Table 4.2. Summary for XRD phase analysis of ZnO discs fabricated from micro and nanoparticles size of ZnO powders at different annealing ambients.

Sample	Annealing ambient	2 θ (deg.)	a (Å)	c (Å)	Stress (σ) (G.Pa)
W4-Disc	As-grown	36.195	3.241	5.215	-0.784
	N ₂	36.199	3.238	5.201	0.436
	O ₂	36.197	3.236	5.204	0.174
P8-Disc	As-grown	36.212	3.238	5.213	-0.601
	N ₂	36.220	3.230	5.203	0.261
	O ₂	36.217	3.232	5.205	0.087
40nm-Disc	As-grown	36.334	3.220	5.210	-0.349
	N ₂	36.358	3.216	5.195	0.958
	O ₂	36.345	3.219	5.198	0.697
20nm-Disc	As-grown	36.375	3.211	5.209	-0.261
	N ₂	36.399	3.204	5.192	1.219
	O ₂	36.387	3.209	5.194	1.046

The stress values of as-grown and annealed samples are shown in Table 4.2. The stress values are negative for as-grown samples (compressive stress), which suggested that the lattice constant c is increased during the sintering process (compared with the stress-free powder), but the stress values become positive (tensile stress) with annealing.

The presence of residual stress in discs is fundamentally a result of lattice imperfections. The stress caused by this factor is called extrinsic stress. The stress caused by defect and impurities is called intrinsic stress. The stress and distortion of lattice parameters from single-crystal values inherently indicate the deficiencies existing in the crystal structure; thus, are serious criteria in the characterization of the structural defects of the obtained ZnO.

The residual stress greatly relaxes through annealing, and the tensile strain becomes more controlling than the compressive stress because of the reduction of the defects in the disc, and the oxygen will be out-diffused as a result of thermal expansion. The dominant tensile stress greatly influences the optical properties, and the optical band gap transfer to a minimal value (red shifts), as discussed in section 4.4.1.

Figure 4.10 shows the variation in the stress values with particle size. The observed shift from a compressive to a tensile stress may be caused by the grow in grain size. Hence, the difference in the stress with different annealing conditions are significantly correlated with the original particle size in the disc, which indicates that the high-oxygen annealing promoted the diffusion of oxygen in the discs and led to a decrease in the ZnO lattice constant; consequently increasing the tensile stress in the sample [280-282].

Previous studies [273, 274, 283, 284] have shown that an optimum thermal treatment improves the ZnO crystal quality and changes the Zn/O ratio, as well as the intrinsic defects of the sample. Meanwhile, a number of studies have focused on determining the effect of thermal or oxygen pressures on the stress and structure of ZnO [285, 286]. These two mentioned parameters are generally known to substantially affect the residual stresses in discs. However, annealing process significantly affects the ZnO structure because thermal

energy improves the crystallization of ZnO discs [287]. The stress increases through the growth process; hence, a perfect, stress-free crystallization of ZnO can be achieved through setting the annealing temperature and oxygen flow rates under optimal situations. In other word, the intrinsic growth stress in the ZnO disc can be dominated by adjusting the different atmospheres during the annealing process. The current study aims to demonstrate the conversion of stress from compressive to tensile during the annealing of ZnO discs by controlling the thermal annealing temperature at a fixed oxygen flow rate (2 L/m^2) and investigate the optimal conditions for manufacture of high-performance varistor devices.

For W4-Disc, P8-Disc, 40nm-Disc and 20nm-Disc, the variation of lattice parameters for the disc samples can be recognized by considering that the increase in the distance along (101) between closely packed atom layers in wurtzite-type structure (caused by the considerable concentration of dislocations) should be replaced by shortening inter-atomic distances between the layers perpendicular to it. In any case, the most deformed structure in ZnO disc is achieved from nanoparticles. The variations in stress values along and perpendicular to (101) caused by the preferential structure of packing defects in the hexagonal close-packed structure along the (101) direction.

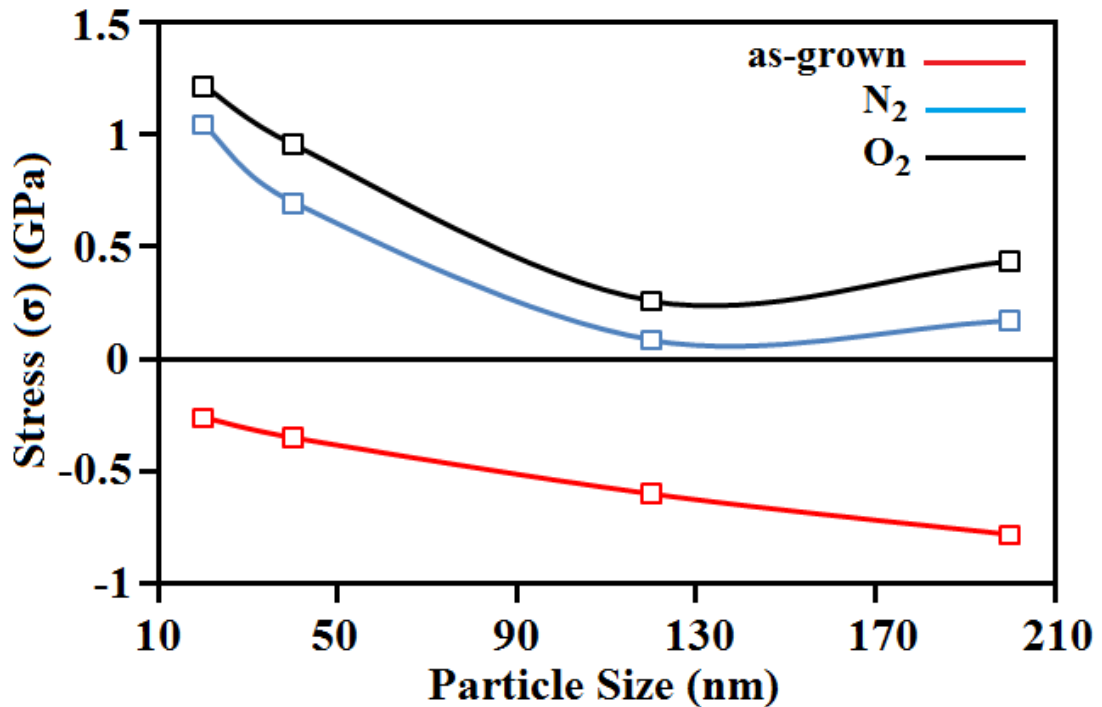


Figure 4.7. Variation of the stress with ZnO discs prepared from different particle sizes of ZnO powder at various annealing ambients.

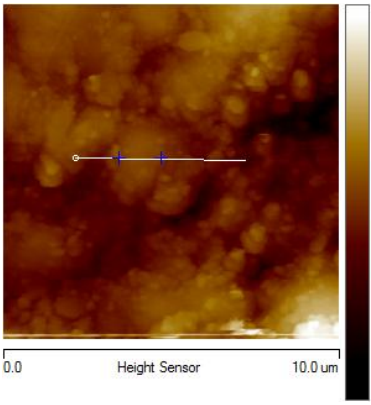
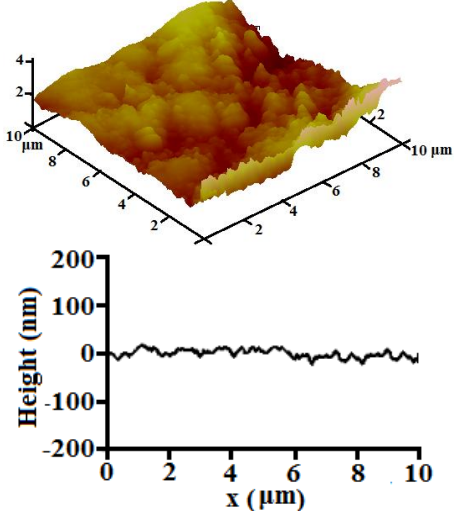
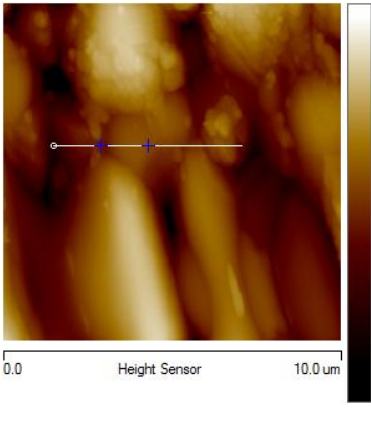
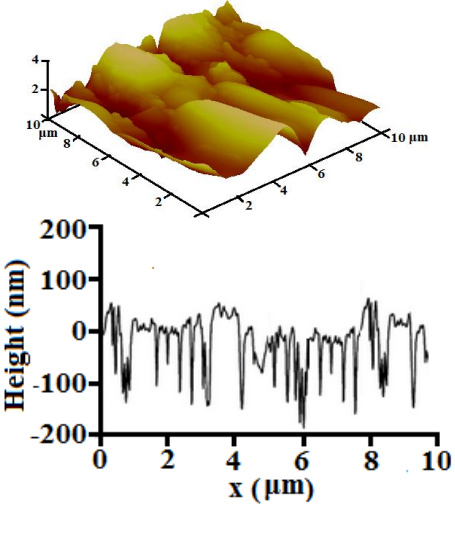
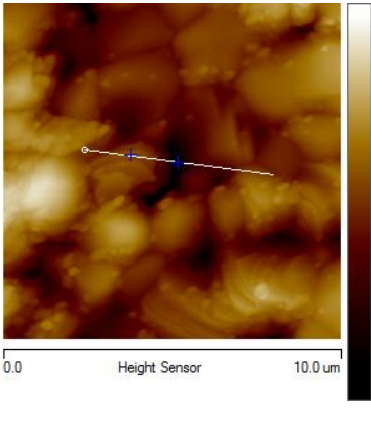
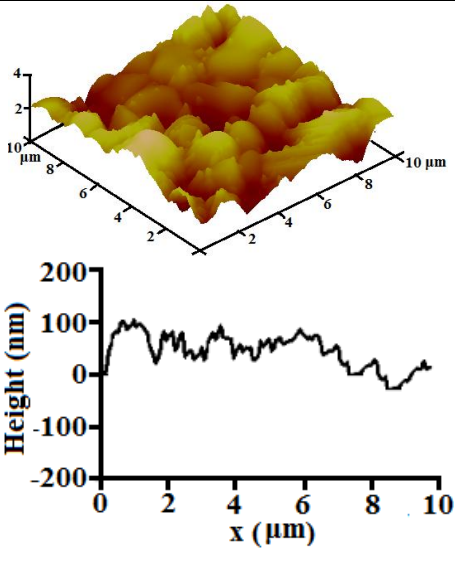
Note that the all XRD Reference pattern data obtained in Table 4.2 can be referred in Appendix B.

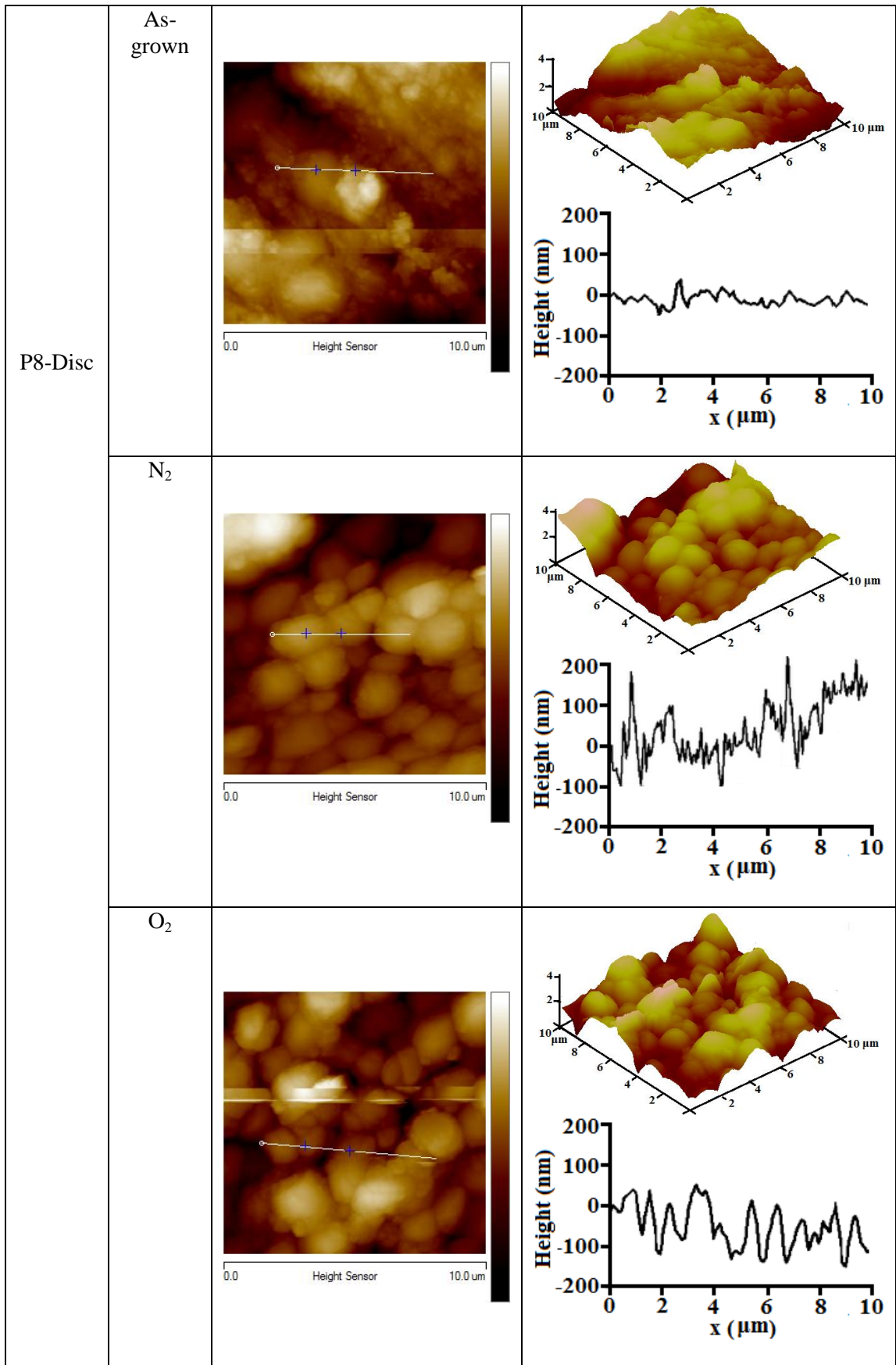
4.3.4 Atomic force microscopy (AFM)

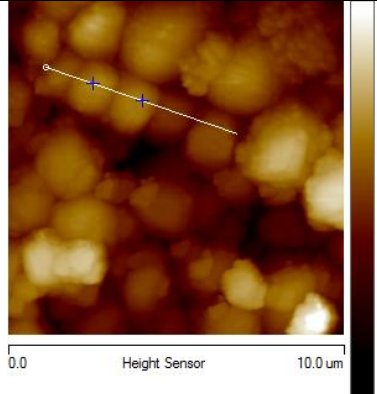
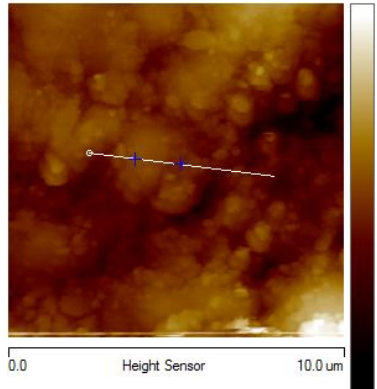
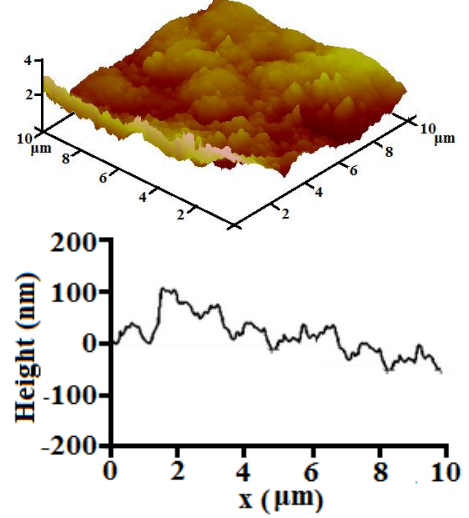
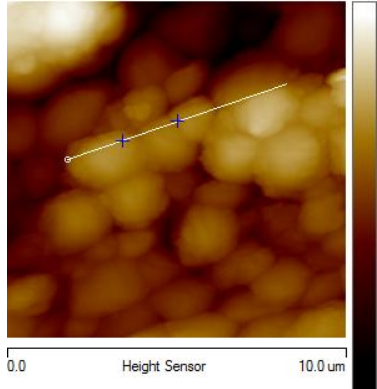
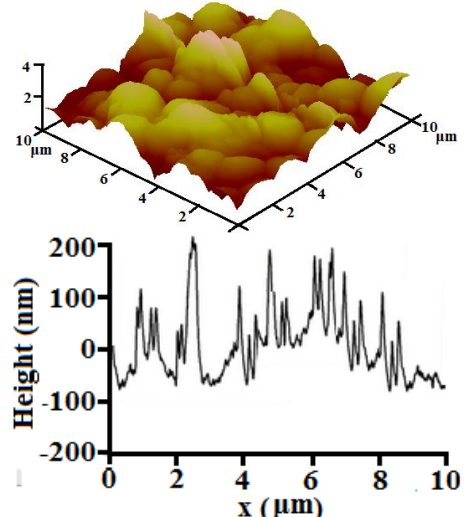
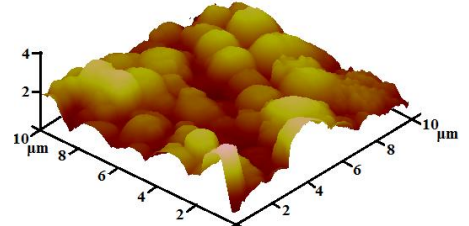
Figure 4.8 shows the AFM images of W4-Disc, P8-Disc, 40nm-Disc, and 20nm-Disc under different annealing conditions. All the samples have a continuous surface microstructure with no cracks and particulates. For the as-grown W4-Disc, P8-Disc, 40nm-Disc, and 20nm-Disc, robust sublimation and coalescence of ZnO grains took place. The morphology of discs surface before annealing is disordered. The grains are coalesced intimately, boundaries between the grains cannot be distanced clearly, and well-defined crystal facets cannot be determined. The average surface grain size and roughness increased when subjected to heat treatment. This growth was related to the tendency of the grains to grow by fusion with adjacent grains when adequate energy for surface rearrangement is get by the annealing process. Larger grains are associated with higher degree of surface

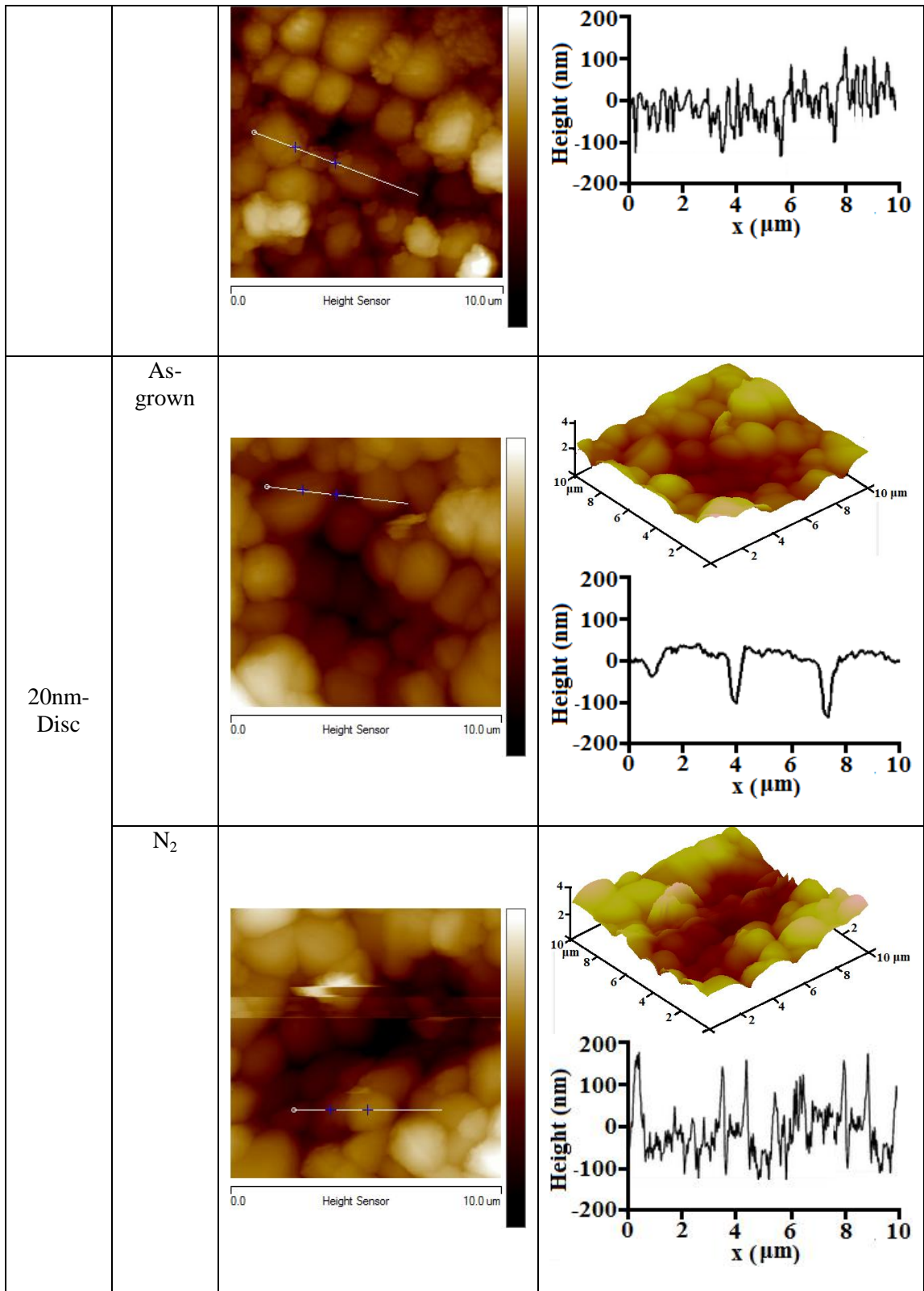
roughness. In this research, roughness of surface and the average surface grain size incremented with the different annealing ambients. However, the average grain size of the discs annealed in nitrogen ambient increased marginally as explained previously and consequently the average roughness of the sample also increased. Nitrogen may have reduced the surface of ZnO nanoparticles to Zn, followed by melting of Zn; thus, resulting in a rough morphology.

AFM images indicate that only the nitrogen-annealed discs presented a growth in grain size and a lowering in the boundary area (Larger grains for nitrogen-annealed discs are associated with higher degree of surface roughness, as mentioned in Table 4.3). The increase in ZnO grain size and average crystallite with nitrogen annealing can be attributed to the interface merging processes through the annealing process. The interface reactions can be related to the existing of interface defects at the ZnO grain or grain boundaries. In the grain or crystallite boundaries, defects of zinc or oxygen (dangling bonds) are abundant and were increased during annealing in nitrogen. These mentioned defects are suitable for the merging process, leading to larger ZnO grains or crystallites. Thermal annealing under different conditions only had a considerable impact on the surface roughness of the 40nm-Disc and 20nm-Disc (Fig. 4.8). The means of surface roughness are summarized in Table 4.3. After annealing, the grain size of the 20nm-Disc analyzed via SEM is greater than the W4-Disc, probably due to the very huge ratio of S/V in nanoparticles, which leads to more absorption during the annealing process and larger grain size. Nevertheless, the AFM analysis indicate that a superior annealing temperature at 700 °C forms atoms with more activation energy to grow larger size grains and higher degree of surface roughness, which is proportionate with the SEM results.

Sample	Annealing ambient	2-dimensional AFM topography	3-dimensional AFM topography
W4-Disc	As-grown		
	N ₂		
	O ₂		



			
40nm-Disc	As-grown		
	N ₂		
	O ₂		



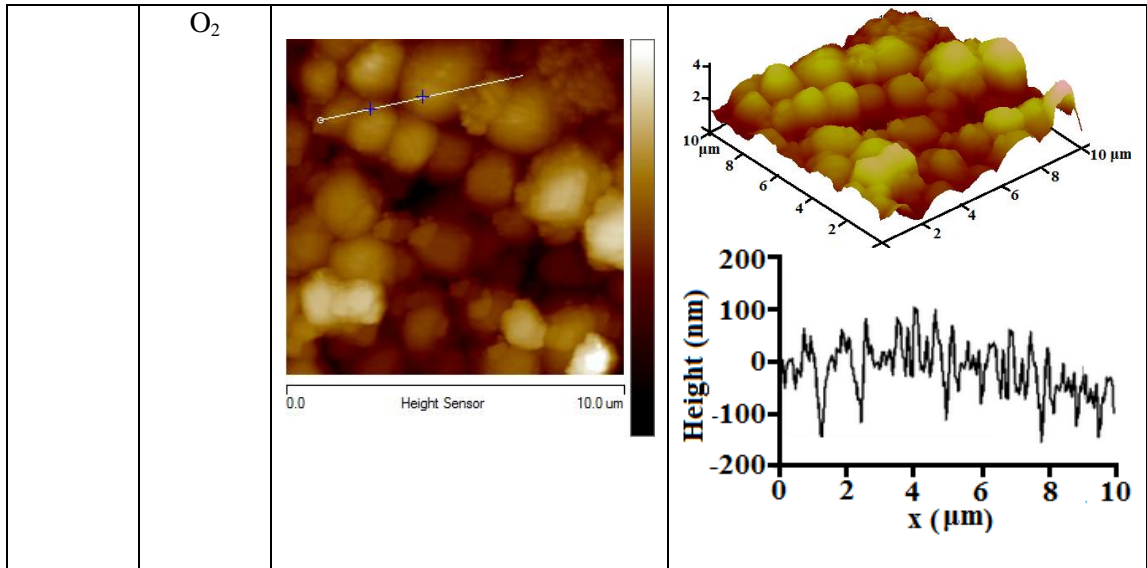


Figure 4.8. 2D and 3D AFM images, and cross section measurement along the line shown in panel of the discs prepared from different particle sizes of ZnO powder at different annealing ambients on a scan area of $5 \times 5 \mu\text{m}^2$.

Table 4.3 summarizes the surface roughness for W4-Disc, P8-Disc, 40nm-Disc and 20nm-Disc at different annealing conditions. Variation in the root mean square (RMS) surface roughness is then plotted as a function of the different particle sizes (Fig. 4.9).

Table 4.3. Surface roughness of the ZnO discs at different annealing ambients measured by AFM for scan areas of $5 \mu\text{m} \times 5 \mu\text{m}$.

Sample	Annealing ambient	Roughness (nm)
W4-Disc	As-grown	13.40
	N ₂	56.60
	O ₂	29.67
P8-Disc	As-grown	20.12
	N ₂	65.77
	O ₂	47.21
40nm-Disc	As-grown	88.42
	N ₂	137.2
	O ₂	95.74
20nm-Disc	As-grown	132.7
	N ₂	209.9
	O ₂	163.1

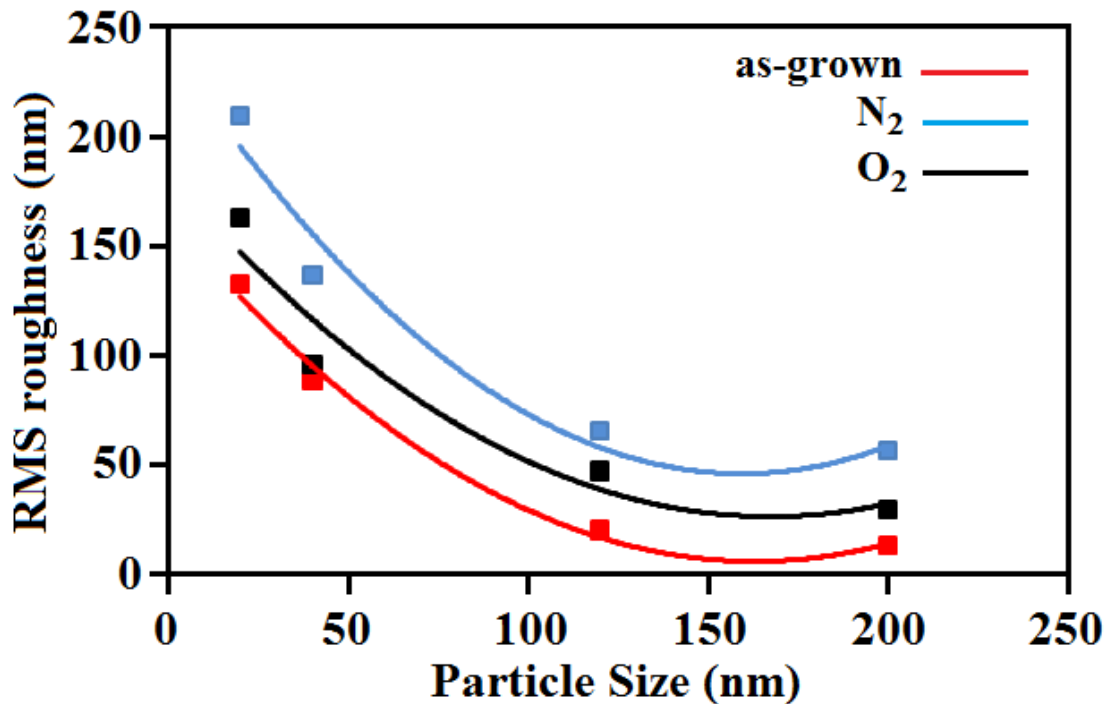


Figure 4.9. Plot of AFM roughness (RMS) of the ZnO samples as a function of different particle sizes.

Fig. 4.9 indicates the alteration of root mean square (RMS) roughness measured by AFM, by differing the particle size at different annealing ambients. The AFM data indicate that the 40nm-Disc and 20nm-Disc have higher values of RMS roughness compared with the W4-Disc and P8-Disc. This phenomena may be caused by the very large S/V ratio of ZnO nanoparticles, which is markedly affected by the thermal annealing process; suggesting that the roughness of sample surface depends on the annealing temperature.

The AFM images show that the surface of the 20nm-Disc annealed under different conditions is rougher than the W4 disc surface. Gu et al. reported that the atoms at the surface of nanoparticles have sufficient diffusion energy to occupy the right site within the lattice of ZnO crystal, and grains with the minimal surface energy will grow at elevated growth temperatures [216]. Since the (101) orientation surface energy is lowest within the

ZnO crystal [288], the orientation of growth enhances in one crystallographic direction at the low surface energy, leading to development of grain size. Then, the growth orientation develops into one crystallographic direction of the low surface energy, leading to the improvement of ZnO crystallinity. We conclude that the disc surface becomes rougher with increasing grain size due to the enlarged grains on the surface of the discs. The AFM analysis in agreement with the SEM images and the XRD data.

4.4 Optical properties of pure ZnO discs prepared from ZnO micro and nanoparticles size

4.4.1 Photoluminescence spectra

The luminescence of the nanoparticles (40nm-Disc and 20nm-Disc) is associated with the properties unique from those of microparticle crystalline materials (W4-Disc and P8-Disc) [289-291]. On the one hand, the nanoparticle size nears the exciton Bohr radius, each of the photoluminescence and band gap are influenced by the quantum confinement effect (QCE) [44, 292] that commonly provides stronger luminescence because of the enhancement of the oscillator strength (a dimensionless quantity that expresses the probability of absorption or emission of electromagnetic radiation in transitions between energy levels of an atom or molecule) [293]. On the other hand, the S/V ratio significantly affects the Hamiltonian of the system (used to describe a dynamic system (as the motion of a particle) in terms of components of momentum and coordinates of space and time and that is equal to the total energy of the system) when the particle size decreases to the nanometer scale. [294, 295]. Surface states and QCE contest together to affect the photoluminance spectra. Lately, the surface states produced from significant S/V ratios was confirmed to critically affect PL in nanoparticles; concurrent with the results in this work [98, 296]. We provided a group of ZnO particles with various diameters for the investigation of the dependence of PL properties on the nanoparticle size and for the statistical determination the roles of surface states in PL based on particle size.

Fig. 4.10 presents the PL spectra of the W4-Disc, P8-Disc, 40nm-Disc and 20nm-Disc. At the same excitation level, strong and fairly broad PL spectra ranging from the very short to long wavelengths were observed for all groups of ZnO discs.

The PL spectra of the samples under various annealing ambients were characterized by UV and broad visible peaks. The UV band is a result of the near-band-edge transition of ZnO and also the recombination of free excitons [110, 297]. The site of the band edge emission shifted toward the longer wavelength after annealing in oxygen and nitrogen conditions. Defects, surface states, and dangling bonds could have caused the redshift and the reduction of the UV emission [110, 298].

For the W4-Disc and P8-Disc, oxygen annealing led to a significant increase in the visible peak and a decrease in the UV luminescence. By contrast, nitrogen annealing led to a decrease in the visible peak and an increase in the UV luminescence rather than a decrease despite an increasing level of oxygen deficiency after nitrogen annealing. During oxygen annealing, excess zinc reacts with oxygen from the atmosphere and generates new ZnO that is different from the as-grown impacting the UV light emission.

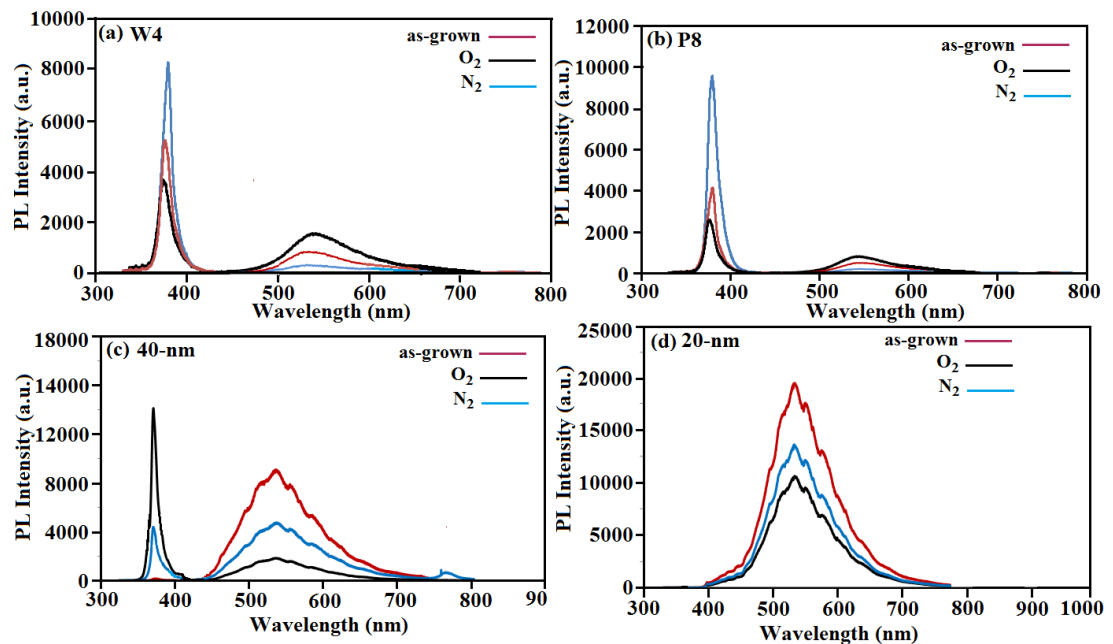


Figure 4.10. PL spectra of ZnO discs fabricated from (a) White ZnO (W4), (b) Pharma ZnO (P8), (c) 40 nm ZnO, and (d) 20 nm ZnO at different annealing ambients.

Presumably, the PL spectra can be primarily explained by the alteration of oxygen chemisorption levels at the surface after annealing under different conditions. Furthermore, oxygen chemisorption at the disc surface leads to an upward band bending by the electrons capture in regions close to the surface [110]. During excitation, the photo-generated holes and electrons close to sample surface are moved to opposite directions across the depletion region, therefore decreasing their recombination chances through excitonic processes.

The depth of the surface recombination layer was approximately 30 nm [212]. Any shift of the depletion layer will have a significant effect on the comprehensive luminescence properties because a great number of photo-generated electron-hole pairs drop within the surface depletion region. A number of researchers demonstrated that the 0.72 eV thermal activation energy necessary for the charge move over the surface potential barrier is the main limiting factor in the identification of the chemisorption rate. Furthermore, they have demonstrated that the rate of charge transfer linearly increments with growing oxygen pressure during the annealing process [270]. In this work, the annealing of W4-Disc and P8-Disc ambient oxygen significantly increased the amount of chemisorbed oxygen species, which caused the improved visibility of the emission (Figs. 4.10 (a) and 4.10 (b)). Annealing in ambient nitrogen partially extracted the pre-existing chemisorbed oxygen at the surface of the as-grown samples, which resulted in the enhanced UV emission. In addition to the dissociation of the photo-generated electron-hole pairs, the surface band bending further supported the ionization of V_o .

The effects of the surface band bending on the UV and green emissions for W4-Disc and P8-Disc are summarized in Fig. 4.11. During annealing in ambient oxygen, the extent of band bending increased, and the depletion region grew in size, resulting in the separation of more photo-generated electron-hole pairs. An increasing number of V_o were ionized into V_o^+ , which were localized within the depletion region. The free holes swept for the depletion region then recombined with the electrons occupying V_o^+ to generate the green emission. The UV emission was suppressed (Figs. 4.11 (a) and 4.11 (b)) and further penetrated the

interior of the ZnO sample. The reverse processes that occurred through the annealing in ambient nitrogen enhanced the UV emission, suppressed the green emission, and pushed it further out to the surface (Fig. 4.11 (c)).

The increase in the relative intensity of green emission after oxygen annealing of W4-Disc and P8-Disc can be confirmed by the greater extent of the oxygen chemisorption and the subsequent surface band bending. The surface band bending influences PL by two mechanisms, namely, the disintegration of the photogenerated electron-hole pairs and the generation of V_o^+ within the depletion region, both of which enhance the green emission. The effect of nitrogen annealing on oxygen chemisorption and surface band bending is opposite of the effect of oxygen annealing.

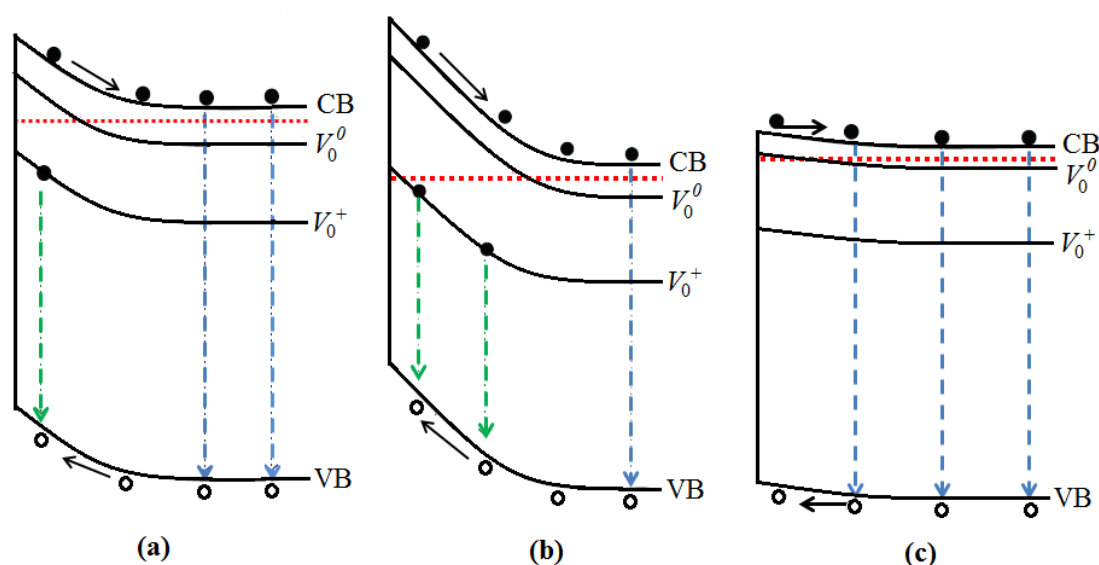


Figure 4.11. Schematics of the energy band diagram for (a) as-grown, (b) oxygen annealed, and (c) after nitrogen annealed W4-Disc and P8-Disc samples.

The significant ratio of S/V in nanoparticles indicates the greater bulk density of dangling bonds [299, 300]. The presence of dangling bonds in a material surface probably alters a more localized state by splitting the state out of the energy gap border [301, 302].

Thus, surface states could be responsible for the photoluminescence in 40nm-Disc and 20nm-Disc. The PL peaks for 40nm-Disc and 20nm-Disc show that (1) the peak site lies below the band gap of ZnO nanoparticles, which refers to the presence of primary states in the forbidden energy band gap, and these initial states within band gap possess their own ground or excited energy levels; and (2) the PL intensity decreased with the increase in grain size, which possible to be produced as follows:

$$n_s \propto S/V \propto 1/R \quad (4.10)$$

whereby:

n_s is the number of the surface atoms surface per unit volume.

R is the size of crystallite.

Whereas the PL intensity I_{PL} is proportional to the square of the transition rate W^2 as following:

$$I_{PL} \propto |W_{PL}|^2 \propto 1/R^2 \quad (4.11)$$

Thus, a surface-related mechanism can account for the reduction of the PL intensity with growing grain size as observed in the 20nm-Disc that exhibited the highest PL intensity among the W4-Disc, P8-Disc and 40nm-Disc (Fig. 4.10), in which this particular growth can be caused by the effects of the surface states. Moreover, the whole PL intensity rapidly decreases accompanied with the growth in particle size as evidenced with the total PL intensity of the 40nm-Disc and 20nm-Disc. The size-dependent decrease also emphasizes that the density of charge is specified by the number of atoms on the surface. For large particle size (W4-Disc and P8-Disc), the relative PL intensity decreased dramatically (Fig. 4.10), which detects that several surface states will precipitous frequently under small size of grain, in which the luminescence characteristics for nanoparticles are controlled by surface

recombination; else, the inhabitation of surface states would be decreased extremely which results in a corresponding radiative transition weakened quickly.

The PL band of the sample discs centered at the UV region is attributed to the band edge transition from conduction to valence band. During the rise or decrease of grain size, the intensity of PL also decreases or increases, which reveals that the crystallinity is a significant factor in NBE emission from samples.

In the visible region, different mechanisms were proposed for the visible luminescence. A statistically appropriate mechanism is more complicate to find partially because it is critical to the conditions of specimen preparation [131, 150]. To our understanding, visible emission is fundamentally a result of defects, which are attributed to deep level emissions such as Zn_i and V_o [149, 301]. In the present work, the PL spectra of the 20nm-Disc (Fig. 4.10 (d)) show broad emission in the blue–green–red regions with band peaks (519–533 nm), and the characteristic UV band-edge PL peak is absent. In general, the UV luminescence in ZnO nanoparticles vanish in two situations, namely, when the energy of excitation is extremely minimal than its energy of band gap and when the intensity of the visible luminescence peak is significantly higher because of the development defect density. In this work, the UV luminescence is not seen in Fig. 4.10 (d) because of the high intensity of the blue–green–red emission. Furthermore, this phenomenon indicates that in the 20nm-Disc sample, the exciton pair recombination takes place in non-radiative recombination centers, such as low-angle inter-grain boundaries, dislocations, and heterogeneously distributed impurity atoms within the lattice of ZnO nanoparticles [303, 304]. Therefore, the blue–green–red visible PL emission was related to the extremely elevated concentration of structural defects within the raw material (20nm ZnO powder). The structural defects were intrinsic (Zn_i and V_o), which acted as deep-level acceptors for electronic transitions with near-conduction band edge.

Fig. 4.10 (d) shows the green luminescence of the as-grown annealed ZnO discs based on the emission spectra. But, the optical recombination process varies in as-grown and

annealed samples. This difference exhibit that thermal treatment of ZnO nanoparticles affects different channels of radiative recombination. The optical characteristics of ZnO nanoparticles can be explained by radiative transitions happening through the band structure. The schematic of the band structure and optical transitions in unannealed and annealed ZnO nanoparticles are explained in Fig. 4.12. For wurtzite ZnO, the valence band (VB) characteristics is often O-2p, while the Zn 4s-O 2p σ^* interaction is initially responsible for the two minimal conduction bands (CB). The ZnO nanoparticle is often n-type in character; thus, generality of defects are V_O and Zn_i . The visible luminescence is fundamentally caused by defects that are related to deep level emissions such as V_O and Zn_i . The ZnO visible emission is foremost due to the transition from the deep donor level to the VB because of V_O and by the transition from the CB to the deep acceptor level because of state defects and impurities. The ZnO nanoparticles crystal structure consist of significant voids that can readily include interstitial atoms within the lattice that affect the appearance of visible luminescence within annealed ZnO nanoparticles.

In the ZnO lattice, Zn has tightly bound 3d electrons, and oxygen has tightly bound 2p electrons, which indicates efficient nuclear attraction [305]. The Zn 3d electrons were found to highly interact with the O 2p electron in ZnO nanoparticles. As the center energy of the green luminescence is comparable to the energy of ZnO bandgap (3.2 eV), the visible luminescence peak cannot be attributed to the direct recombination of a hole in the O 2p valence band and a conduction electron in the Zn 3d band. Subsequently, the green luminescence peak must be related to the local level within the band gap of ZnO. The green luminescence peak is a product of the radiative recombination of the photo-generated hole and an electron occupying the oxygen vacancy.

Surface states can also contribute to the green emission in 20nm-Disc. A significantly higher number of surface defects are present in the 20nm-Disc compared with the W4-Disc and P8-Discs, and the valence band hole can be trapped by the surface defects and subsequently tunnels back into the oxygen vacancies, together with one electron, to

create the V_0^{**} recombination center. The recombination of a shallowly trapped electron with a deeply trapped hole within a V_0^{**} center results in visible emission. The most probable clarification for the green emission includes redouble defects or/and defect compounds, and the essential portion of the visible luminescence are created from the nanoparticles surface centers. Xu et al. [106] investigated the levels of diverse defects involving the compounds defects $V_O: Zn_i$ and $V_{Zn}: Zn_i$. They observed no cases in the gap from $V_{Zn}: Zn_i$, while two levels above the valence band at 1.2 and 2.4 eV were noted for $V_O: Zn_i$; thus, this defect type explains a potential candidate for the 20nm-Disc green luminescence rather than for the W4-Disc.

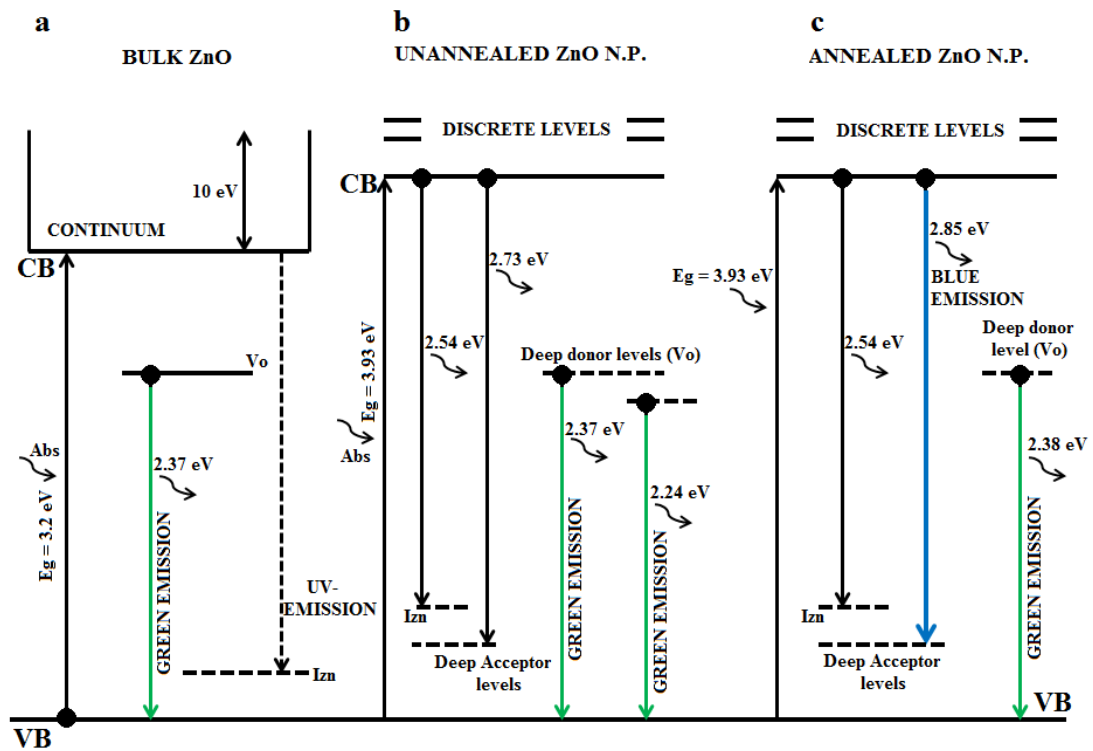


Figure 4.12. The UV and visible emissions occurring in the (a) bulk ZnO (b) unannealed and (c) annealed 20nm-Disc.

ZnO nanoparticle discs prepared by conventional ceramic method have Zn-rich, O-deficient state. Some investigators have reported that these defect sites are related with the

emissions from ZnO nanoparticles. Studenikin et al. [152] suggested that green luminescence results from oxygen-poor states within the ZnO lattice. On the contrary, Lin et al. [306] indicated that the green luminescence from ZnO nanoparticles agrees to a local level that consists of O_{Zn} rather than V_{Zn} , V_O , O_i , or Zn_i . Compared with the previously mentioned results, in this work, the results are consistent with those of Ref. 306. Therefore, the following argument can be assumed: the as-grown ZnO disc has an unstable state, including an O-deficient, Zn-rich (or V_O) state. The unstable state is then stabilized by annealing process.

(I) When annealed in N_2 ambient, the unstable phase is changed to the stoichiometric ZnO phase, and the excess Zn is reduced either by stable ZnO formation (at low temperature) or Zn evaporation (at high temperature). Therefore, decrease in the visible emission during N_2 annealing arises for the same reasons.

(II) When annealed in O_2 ambient, stable ZnO is generated by the combination of excess Zn with oxygen rather than by evaporation process. At the same time, the oxygen amount starts to increase in the disc, wherein the excess oxygen has a significant function in O_{Zn} formation, leading to green emission from the disc fabricated from ZnO nanoparticles.

PL spectra for the 40nm-Disc before and after oxygen and nitrogen annealing are shown in Fig. 4.10 (c). A strong improvement in the PL spectra was observed after the annealing treatment with oxygen and nitrogen gas. UV emissions with band peaks at 370–376 nm had lower intensity compared with the broad visible emission with band peaks at 527–532 nm. The broad visible emission may be due to the electronic transitions from the near-conduction bandedge to the deep-level acceptors and transitions from deep donor levels to the valence band [307]. The visible emission was produced from the recombination of shallowly trapped electrons with deeply trapped holes in the V_o^{++} centers [308]. Other work [309, 310] attributed the increase in green emission to Zn/O interstitial centers.

The PL peak positions for the 40nm-Disc and the FWHM values drastically changed with annealing compared with W4-Disc and P8-Disc. The FWHM of the visible peak

gradually decreased and blue shifted with thermal annealing compared with that of the UV peak. However, the intensity of the UV peak drastically increased after oxygen annealing, but decreased after nitrogen annealing and red shifted with the annealing process. The red shift in the UV peak was attributed to the quantum size impact within the ZnO nanoparticles, while the blue shift in the visible emission was caused by surface defects. For the intrinsic luminescence of the ZnO nanoparticles, the production of nanoparticles leads to a redshift in the photoluminescence peak because of the quantum size impact. The redshift in the UV emission peak with annealing process intimately follows the redshift in the band edge, indicating a certain relationship. The band gap of the as-grown 40nm-Disc was 3.32 eV, which decreased to 3.29 eV after oxygen annealing. This result probably attributed to the elimination of the defect levels from the disc and the controlling property of tensile strain. The annealing process removed the stacking errors, which led to the direction of the individual crystallites and appearance of defect-free grain boundaries. The XRD analysis finding indicated that the grain size of the 40nm-Disc and 20nm-Disc increased dramatically compared with the W4-Disc and P8-Disc after annealing in ambient oxygen, which possible to be related to a reduce in optical band gap. The red shift in the optical band gap can be associated with the XRD results. Grain growth occurred with annealing process, which led to reduction in strain energy caused by atom rearrangement, consequently relaxing the grain boundaries.

The grain size can also be related with the intrinsic stress that significantly alters the optical behaviors of the disc. Stresses are created because of vacancies and defects. The grain obviously grows and increases in size after annealing treatments, and the subsequent disc tensile stress reduces. This observation is attributed to the fact that the relaxed grain boundaries are eliminated, the atoms are rearranged, and the strain energy decreases as the grain grows, which improves the optical characteristics of discs. In W4-Disc and P8-Disc samples, firstly compressive stresses reduces with grain development after heat treatments. Given the decrease in compressive stress, the optical characteristics develop and the optical

band gap increases. However, the optical band gap decreases for the 40nm-Disc and 20nm-Disc. This observation may be caused by the independence conduct of the optical band gap from tensile or compressive stress up to a particular limit of thermal treatment. Therefore, grain size and tensile stress lead to a modify of high-energy band gap optical transitions to low energies. In this work, given the prevalent grain growth with reduced FWHM value and rising trend of tensile stress at oxygen annealing, a transfer of the optical band gap from high values to low values results.

Notably, the visible luminescence peak intensity of the annealed ZnO nanoparticle discs increased significantly with annealing process. Other work [311] has reported that this peak may be caused by the disorder and strain within the ZnO lattice produced by annealing. Strain of lattice can affects the band structure of nanoparticles and produce non-radiative recombination centers within the band gap [312]. During the annealing process, many impurities or contaminants were introduced into ZnO nanopowder and may have acted as non-radiative centers that caused the weak peak intensity. By contrast, the defects in the annealed ZnO nanoparticles, which were attributed to the increased oxygen concentration in the sample with annealing process, may have affected the emission peak intensity. Given that the UV peak intensity was weak in the annealed nanopowders, this phenomenon can be caused by the surface defects in the annealing samples. Many defects such as dislocations and vacancy-type defects formed in the samples during the annealing process. These defects were caused by the introduction of non-radiative recombination centers, which were likely responsible for the weakening of the photoluminescence emission.

The chemical component for the 40nm-Disc and 20nm-Disc is non-stoichiometric compared with the W4-Disc and P8-Disc, and usually consists of oxygen vacancies and excess Zn atoms, which increase with decreasing particles size. Therefore, several lattice and surface defects were included in the as-grown 40nm-Disc and 20nm-Disc samples. The optical characteristics of the samples improved after annealing treatment because of reduction in surface defects [313]. Annealed ZnO nanoparticles contain majority of the

defects associated with oxygen vacancies created by oxygen evaporation. Thus, the high deep-level emission (DLE) intensity for N₂-annealed 40nm sample may be attributed to the suppression of oxygen evaporation by the annealing process. On other contrary, oxygen diffuses to the lattice to fill the oxygen vacancies through oxygen thermal treatment in certain cases, which consequently quenches the deep-level emission because of effective decrease in oxygen vacancies [314].

Table 4.4 summarizes the PL and energy band gap for different discs fabricated from various ZnO particles sizes at different annealing conditions.

Table 4.4. PL and energy band gap of different discs prepared from different ZnO particles size at different annealing ambients.

Sample	Annealing ambient	Wavelength λ (nm)	Energy band gap and band peak energy (eV)
W4-Disc	As-grown	369.75	3.35
	N ₂	373.23	3.32
	O ₂	372.69	3.33
P8-Disc	As-grown	371.34	3.34
	N ₂	375.16	3.31
	O ₂	374.89	3.31
40nm-Disc	As-grown	373.75	3.32
	N ₂	375.45	3.30
	O ₂	376.98	3.29
20nm-Disc	As-grown	534.42	2.32
	N ₂	540.21	2.29
	O ₂	537.70	2.31

4.4.2 Raman spectroscopy

The wurtzite ZnO belong to the space group C_{6v}^4 with two formula units in the primitive cell. Every primitive cell of ZnO possess four atoms, each occupying C_{3v} sites, which leading to 12 phonon branches, 3 acoustic modes and 9 optical modes [315]. At the

Brillouine zone centres (Γ point); group theory suggests the subsequent lattice optical phonons:

$$\Gamma_{\text{opt}} = 1A_1 + 2B_1 + 1E_1 + 2E_2 \quad (4.12)$$

where E_1 and A_1 are polar modes and are both infrared and Raman active, whereas E_2 modes are non-polar and only Raman active. The E_2 modes possess two wave numbers, namely, E_2 (high) and E_2 (low) related with the motion of oxygen and Zn sub lattice, respectively [315]. Strong E_2 (high) mode is distinguishes of the wurtzite lattice and revealed to good crystallinity. The vibrations of A_1 and E_1 modes can polarize in unit cell, which forms a long range electrostatic field separates the polar modes into transverse optical (TO) and longitudinal optical (LO) component. The E_1 (LO) mode is related to the existence of Zn_i , V_o or their complexes. The B_1 modes are infrared and Raman inactive (silent modes).

Raman spectroscopy is a non-destructive method to describe the vibrational characteristics of ZnO crystals, discs, microparticles, and nanoparticles [316-322]. The confined optical phonons in the grains of ZnO nanoparticles resulting a significant change in its vibrational spectra compared with that of their bulk counterparts. Several peak broadenings and shifts in the Raman spectra may be observed for ZnO crystals with reduced dimensionality. The Raman spectra of ZnO nanoparticles consistently present broadening and shift from the bulk phonon frequencies. In previous works on ZnO nanoparticles, many researchers attributed these changes to the confinement effects [323, 324] whereas others claim that the shifts in Raman peaks are attributed to compressive stress, strain, or local heating, rather than to spatial confinement [325, 326]. Understanding the origin of the obtained shift is very interesting for explaining the Raman spectra and the characteristics of the W4-Disc, P8-Disc, 40nm-Disc and 20nm-Disc.

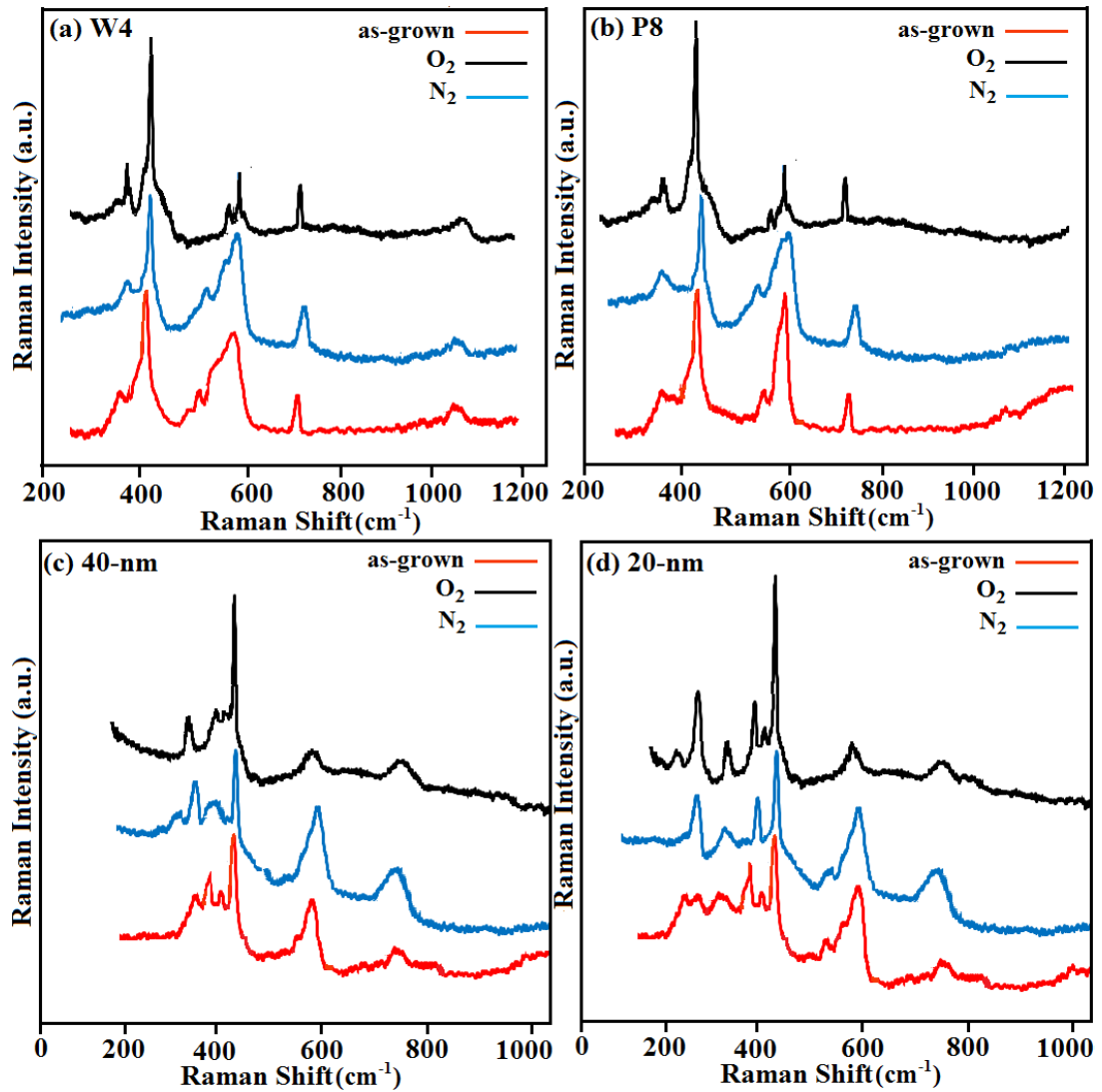


Figure 4.13. Raman spectra of ZnO discs fabricated from (a) White ZnO (W4), (b) Pharma ZnO (P8), (c) 40-nm ZnO, and (d) 20-nm ZnO at different annealing ambients.

The Raman spectra of the W4-Disc, P8-Disc, 40nm-Disc, and 20nm-Disc annealed in ambient N_2 and O_2 are demonstrated in Fig. 4.13 (a)–(d). A series of Raman modes was observed for the W4-Disc and annealed at various atmospheres: 378, 416, 446, 560, 584, and 1159 cm^{-1} . The spectrum of the P8-Disc was observed at 376, 415, 448, 563, and 582 cm^{-1} . The peaks at 446 and 448 cm^{-1} are due to the optical phonon E_2 (high) mode [327], whereas the peak at 1159 cm^{-1} for the W4-Disc is attributed to the E_3 mode of the ZnO single crystal. The peaks at 378 and 376 cm^{-1} correspond to the A_1 (TO) symmetry mode of ZnO and those

at 416 and 415 cm^{-1} to the E_1 (TO) Raman mode. The peaks at 584 and 582 cm^{-1} are attributed to the E_1 (LO) mode deduced from the creation of defects of V_o [322, 328, 329]. The peaks obviously correspond to the E_1 (LO) mode made high by annealing in N_2 ambient because of the oxygen defects, as shown in Fig. 4.13 (a) and (b). These peaks are hardly observed in the Raman mode of ZnO discs annealed in O_2 , referring to a prominent improvement of ZnO disc quality because of the chemisorption and supplement of oxygen. The peculiar peaks at 560 and 563 cm^{-1} , which correspond to A_1 (LO), can also be investigated. Fan et al. [330] suggest that the peak at 560 cm^{-1} is due to the Zn from the deficient Zn oxidation in their research. ZnO includes many voids within the crystal structure, and it can accommodate interstitial atoms readily because of its limited atomic diameter [331]. A Zn-rich disc is created readily by thermal treatment in N_2 ambient; thus, the Zn interstitial atom may have a significant role in the Raman mode at 560 cm^{-1} , which can be demonstrated by the alteration in peak intensity by treatment in various atmosphere, as shown in Fig. 4.13. The intensity of the peaks at 560 and 563 cm^{-1} was observed after annealing in N_2 atmosphere, forming adequate Zn_i atoms within the discs. But, the peaks were barely observed in discs annealed in O_2 ambient, indicating a significant decrease in the Zn interstitial atoms within the samples. The chemisorption of oxygen and recombination with Zn_i through thermal treatment in O_2 atmosphere reduce the concentration of Zn_i . During the thermal annealing process, the stress formed within the crystals clearly impacts the E_2 phonon frequency, and from which, the information on stress can be extracted [332]. The rise in the frequency of E_2 phonon is attributed to compressive stress, while the reduce in the E_2 phonon frequency is due to tensile stress. Thus, the elevated Raman scattering of the E_2 phonon is of significant benefit for researches on the residual stress in ZnO crystals.

All described phonon modes that have been determined in the Raman-scattering spectra of the W4-Disc and P8-Disc are shifted in the spectra obtained from the 40nm-Disc and 20nm-Disc compared with their positions in the spectra from bulk ZnO, as observed in Fig. 4.13 (c) and (d). The spectrum of the 20nm-Disc shows five prominent peaks at 208,

331, 376, 395, and 437 cm^{-1} in addition to broad and weak peaks at 542 and 653 cm^{-1} . The spectrum of the 40nm-Disc is analogous with that of the 20nm-Disc except that two modes attributed to the multiphonon process are absent. For differentiation, a compilation of the mentioned frequencies of the Raman active phonon modes in bulk ZnO is listed in Table 4.5 [333]. A comparison of the investigated optical phonon modes of ZnO nanoparticles with that of the bulk shows that the modes of the 20nm-Disc at 437 and 376 cm^{-1} and of the 40 nm disc at 439 and 377 cm^{-1} peak at the E_2 (high) and A_1 (TO) modes, respectively. The peaks of the 20nm-Disc at 416 cm^{-1} and of the 40nm-Disc at 418 cm^{-1} are due to the E_1 (TO) mode. The 208, 331, and 542 cm^{-1} peaks of the 20nm disc are assigned to the multiphonon process and are caused by the second-order Raman spectrum that formed from the zone boundary phonons, namely, 2TA (M), 2 E_2 (M), or [E_2 (high)+ E_2 (low)] and [E_2 (high)- E_2 (low)], respectively [334]. The peak at 395 cm^{-1} corresponds to the quasi A_1 (TO) mode of the 20nm-Disc [315].

The Raman spectra of the 40nm-Disc also show a series of both first- and second-order features. The second-order features at 332 and 546 cm^{-1} are identified to be in the 20nm-Disc 2 E_2 (M) and [E_2 (high)+ E_2 (low)] assigned to overtones or series of first-order modes. Acoustic overtones with A_1 symmetry are located at 653 and 645 cm^{-1} for the 20nm-Disc and 40nm-Disc, respectively [334]. The peak at 257 cm^{-1} is related to laser plasma lines. In this geometry, no LO phonon peak is seen caused by the incident light is perpendicular to the c axis of wurtzite ZnO. A_1 (LO) phonon can be present only when the c axis is parallel to the disc surface. When perpendicular to the disc surface, E_1 (LO) phonon is shown [315]. Furthermore, scattering geometry and various phonon modes can be indicated by Raman spectroscopy. For example, in the Z(XX)Z geometry where in the detected and scattered polarizations are parallel, both the E_2 and A_1 (LO) modes can be indicated, whilst in the Z(XY)Z geometry where in the detected and scattered polarizations are perpendicular, only the E_2 mode is obtained [268]. Although, each ZnO nanoparticle is c-axis oriented, all

nanoparticles are in random sites. The E_1 (LO) peak at 587 cm^{-1} assigned to oxygen deficiency demonstrates that the prepared ZnO nanoparticles have very high optical quality.

Based on Fig. 4.13, the E_2 (high) mode is red shifted by 7 cm^{-1} for the 20nm-Disc and 5 cm^{-1} for the 40nm-Disc. In addition, the A_1 (TO) mode is red shifted by 4 cm^{-1} for the 20nm-Disc and 3 cm^{-1} for the 40nm-Disc compared to the W4-Disc. Furthermore, the E_2 (high) mode is not just broadened, but it also demonstrates an asymmetric broadening at the low-frequency side; the A_1 (TO) mode also shows the same results. In general, the three potential mechanisms that may be responsible for the shifts in phonon peak in the symmetric Raman spectra are the following: (1) spatial imprisonment of optical phonons in the nanoparticle grain boundaries; (2) defects such as zinc excess, oxygen deficiency, surface impurities, and others were localized phonon; (3) laser-resulted heating in nanoparticles and tensile strain. Given the large S/V ratio of the nanoparticles, the ZnO discs fabricated by conventional ceramic methods normally possess further defects than identical bulk ZnO crystals. The spatial confinement was investigated by Richter et al. [335] who observed that the nanocrystalline Raman spectra are redshifted and broadened because of the relaxation of the q -vector selection rule within the confine-sized nanocrystals. Hence, the most significant mechanism is the spatial confinement in ZnO nanoparticles. The asymmetry of line shape, the broadening of the Raman spectra, and the strong red shifts of the A_1 (TO) and E_2 (high) modes toward the low-frequency portion may be due to optical phonon confinement [335].

The peak at 430 cm^{-1} forms from the E_2 mode of ZnO related to the wurtzite structure, and the 570 cm^{-1} peak is contributed by the E_1 (LO) mode of ZnO related to oxygen insufficiency [328, 336]. Fig. 4.13 (c) and (d) show that the peak at 437 cm^{-1} is the most dominant after annealing in O_2 atmosphere, whereas the peak intensities at 437 cm^{-1} are extremely weak after annealing in N_2 ambient. The peak at 587 cm^{-1} ascribed to oxygen deficiency was clearly observed at O_2 atmosphere annealing, which indicates that a significant number of oxygen vacancies are present within the ZnO discs. The 587 cm^{-1} Raman peak was related by several investigators to the LO phonon of E_1 or LO phonon of A_1

[325, 337-339]. Certain researchers assumed that this Raman peak is accompanied by Z_i , V_o , or their combination because of its massive dependence on the oxygen stoichiometry [328, 338, 339]. Chen et al. considered this peak as a defect-generated mode [340]. In the present study, a correlation was found between the UV intensity and the 589 cm^{-1} Raman peak intensity in ZnO discs under resonant excitation. As the UV luminescence attained the lowest intensity in N_2 ambient for 40nm-disc, the Raman peak reached the highest intensity. An identical phenomenon is also achieved in O_2 ambient; the Raman peak reached the lowest intensity when the UV emission reached the highest intensity. The total PL intensity is dominated by the series of radiative and non-radiative processes. The depression of non-radiative recombination centered in the ZnO disc could enhance the luminescence efficiency [341-344]. Thus, given that the improvement of the UV peak is associated with an intensity lowering of the Raman peak, the 587 cm^{-1} Raman peak is therefore strongly influenced by a non-radiative center in ZnO discs. Zhou et al. provided substantiation that the weak excitonic luminescence of ZnO quantum dots is significantly related with the existence of surface hydroxide [344]. Ko et al. assumed that threading dislocations act as non-radiative centers within ZnO corresponding to the correlation among the PL intensity and the line width of the X-ray rocking curve [341]. Koida et al. investigated the point defects impact on the non-radiative processes in epitaxial and bulk ZnO by applying steady-state and time-resolved PL spectroscopy and found that non-radiative recombination processes are not only dominated by single point defects but by many defect species formed by the existence of V_{Zn} , such as vacancy complexes [345]. The high intensity of the 587 cm^{-1} Raman peak suggests the significant concentration of the non-radiative center; the difference of the Raman peak intensity with the thermal treatment ambient could provide information about this non-radiative center. The Raman peaks are more intense in O_2 ambient than in N_2 ambient at all ZnO grain sizes. Consequently, the non-radiative center is unlikely to be the Zn_i and V_o , which are reduced with the rise in oxygen pressure.

Table 4.5 summarize the results for Raman active modes at different annealing atmospheres of the various ZnO discs fabricated from different size of ZnO powders in comparison with the theoretical results. All peaks values are in cm^{-1} .

Table 4.5. A comparison of the Raman active modes of the discs fabricated from various ZnO particles size with the theoretical results at the different annealing ambients.

Symmetry	bulk (cm^{-1})	W4-Disc			P8-Disc			40nm-Disc			20nm-Disc		
		As-grown	O ₂	N ₂	As-grown	O ₂	N ₂	As-grown	O ₂	N ₂	As-grown	O ₂	N ₂
2TA(M)	200	ND	ND	ND	ND	ND	ND	ND	ND	ND	208	213	209
2E ₂ (M)	330	ND	ND	ND	ND	ND	ND	332	328	340	331	339	335
A ₁ (TO)	380	378	382	385	376	373	374	377	357	360	376	379	383
E ₁ (TO)	407	416	414	418	415	413	415	418	416	400	416	410	ND
E ₂ (high)	444	446	447	449	448	443	450	439	435	443	437	430	441
E _{2H} +E _{2L}	540	ND	ND	ND	ND	ND	ND	546	543	ND	542	ND	542
A ₁ (LO)	574	560	579	564	563	558	570	ND	ND	ND	ND	ND	ND
E ₁ (LO)	583	584	586	588	582	580	585	589	580	591	587	582	588
Acoust overton e	640	ND	ND	ND	ND	ND	ND	645	643	648	653	639	641
2(LO)	1155	1159	1160	1159	ND	ND	ND	ND	ND	ND	ND	ND	ND

*ND: below the detection limit.

4.5 Electrical properties of pure ZnO discs prepared from ZnO micro and nanoparticles size

ZnO is a distinguished material for gas sensors. The unique interaction of ZnO with the atmosphere was investigated, for example, with oxygen and nitrogen. The chemisorption of atmosphere gases at the ZnO surface during the annealing process is appropriate to have a considerable effect on the ZnO surface conductivity. ZnO has acquired interest because of the feasibility to fabrication bulk crystals and nanoparticles. The surface features essentially influence the ZnO nanoparticles because of their huge S/V ratio. In spite of the significant attention on ZnO micro- and nanoparticles, a comprehensive research on the surface

characteristics, specially, their effect on the electrical properties of crystalline ZnO, has not been achieved yet.

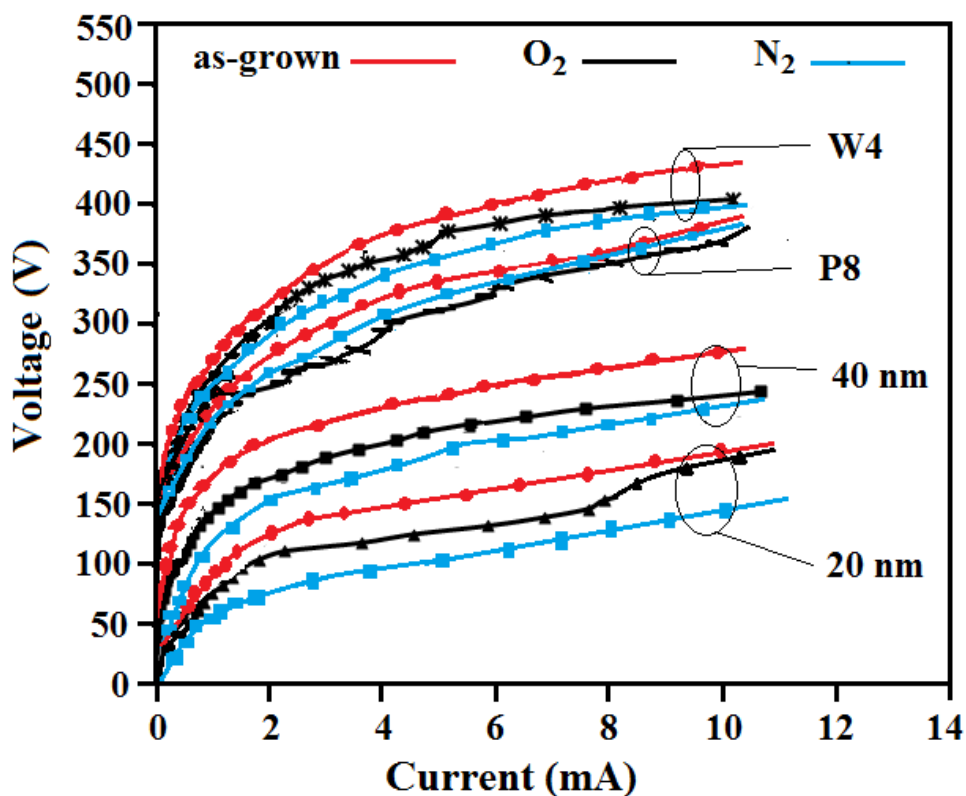


Figure 4.14. Current-voltage characteristics of ZnO discs fabricated from different size of ZnO powders at different annealing ambients.

Fig. 4.14 displays the I-V behaviours of as-grown and annealed W4-Disc, P8-Disc, 40nm-Disc and 20nm-Disc at different annealing ambients. Current was applied and the residual voltage was observed. The I-V curves in Fig. 4.14 resemble a diode response with a high-resistivity region (left of breakdown voltage) and a low-resistivity region (right of breakdown voltage). The low resistivity region is referred to as the nonlinear region, whereas the nonlinearity coefficient (α) can be determined as follows [346] and then plotted in Fig. 4.17:

$$\alpha = \frac{\log (I_1 / I_2)}{\log (V_1 / V_2)} \quad (4.13)$$

The electrical breakdown voltage in the W4-Disc, P8-Disc, 40nm-Disc and 20nm-Disc can be attributed to two different phenomena: **Zener breakdown** and **Avalanche breakdown**.

In Zener breakdown voltage, the electrical field across the P-N junction (thin junction) increases when the reverse bias voltage across the junction increases, thereby leading to a force of attraction on the negatively charged electrons at the P-N junction. This force imposes released electrons from its covalent bond and moves these electrons to the conduction band. With increasing electric field with applied voltage, more electrons are released from its covalent bonds, leading to the drift of electrons across the P-N junction and the occurrence of electron-hole pair recombination. Therefore, a net current rapidly increases with the increase in electric field and then the breakdown voltage occurs. Meanwhile, the Avalanche breakdown voltage happens in the P-N junction diode (thick junction) when a high reverse voltage is applied across the junction. With the increase in the applied reverse voltage, the electric field across the P-N junction also increases and therefore exerts a force on the electrons at the junction and releases them from covalent bonds. These electrons gain acceleration and start moving through the P-N junction at high velocity, leading to collision with neighboring atoms. These collisions occur repeatedly and generate more free electrons. These free electrons start drifting, and electron-hole recombination occurs across the P-N junction, thereby causing the net current to increase rapidly and consequently the breakdown voltage to occur.

Consequently, the reduction in the breakdown voltage in the 20nm-Disc compared with W4-Disc, P8-Disc and 40nm-Disc can be explained by the lowering in the P-N junctions among the ZnO grains, which resulted from the significant increase in the average grain size in the 20nm-Disc after sintering and annealing processes, as mentioned in SEM analysis, and reducing the amount of boundaries between the electrodes. Low P-N junctions produce low electron-hole pair recombination, thereby leading to a decrease in the breakdown voltage in the 20nm-Disc. However, in the W4-Disc and P8-Disc samples, the

number of grain boundaries among the grains and P-N junctions is high, leading to more electron-hole pair recombination and subsequently increasing the breakdown voltage in the W4-Disc and P8-Disc samples.

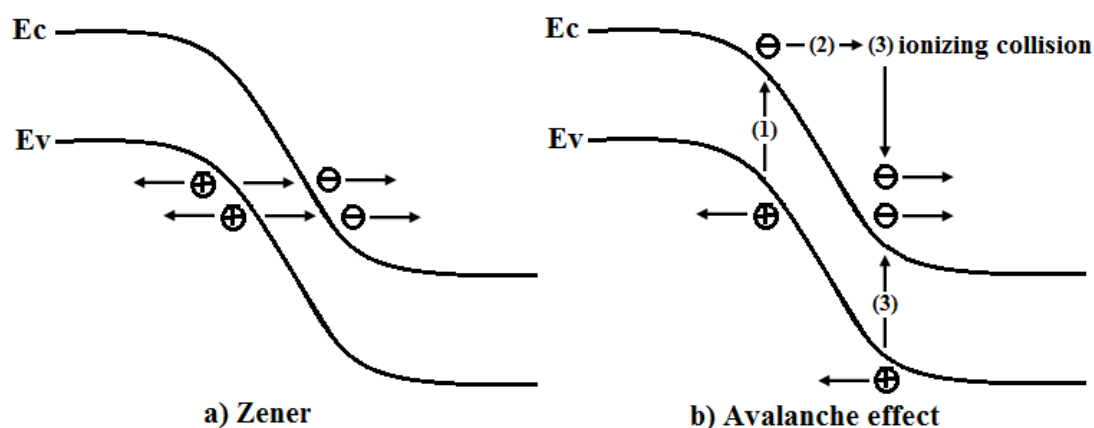


Figure 4.15. Mechanism of Zener and Avalanche breakdown voltage

The I-V non-linear behavior of the ZnO disc is a phenomenon of the boundaries among semiconducting grains. The ceramics' breakdown voltage is proportional to the number of grain boundaries per unit of thickness and subsequently to the inverse of the grain size. The ZnO disc breakdown voltage can be controlled by the thickness of the disc and the microstructure (i.e., ZnO grain size) of the disc body.

Another considerable change is that in the resistivity (ρ) at the high-resistivity region, whereby the ρ at the W4-Disc dropped significantly for the 20nm-Disc after the annealing process. The extreme gas absorption during the annealing treatment reduced the potential barrier of the P-N junctions, resulting in the significant drop in ρ .

Table 4.6 summarizes the electrical properties for ZnO samples at different annealing conditions. Variation in the breakdown voltage, nonlinear coefficient and

resistivity are then plotted as a function of the different particle sizes, as shown in Fig, 4.16, 4.17 and 4.18, respectively.

Table 4.6. Summarizes the electrical properties of ZnO discs fabricated from different particles sizes of ZnO powder at as-grown and different annealing ambients.

Sample	Annealing ambient	V_b (V)	I_b (mA)	α	ρ (k Ω .cm)
W4-Disc	As-grown	340	1.47	12.1	362.4
	O ₂	323	1.78	9.6	335.7
	N ₂	294	1.40	9.3	310.3
P8-Disc	As-grown	264	1.60	8.1	286.9
	O ₂	249	1.48	6.1	226.7
	N ₂	260	1.60	5.4	237.5
40nm-Disc	As-grown	183	0.40	3.9	220.8
	O ₂	150	0.48	2.4	179.3
	N ₂	138	0.60	2.1	145.2
20nm-Disc	As-grown	110	1.28	1.9	98.86
	O ₂	86	1.27	1.7	89.03
	N ₂	60	1.00	1.4	64.62

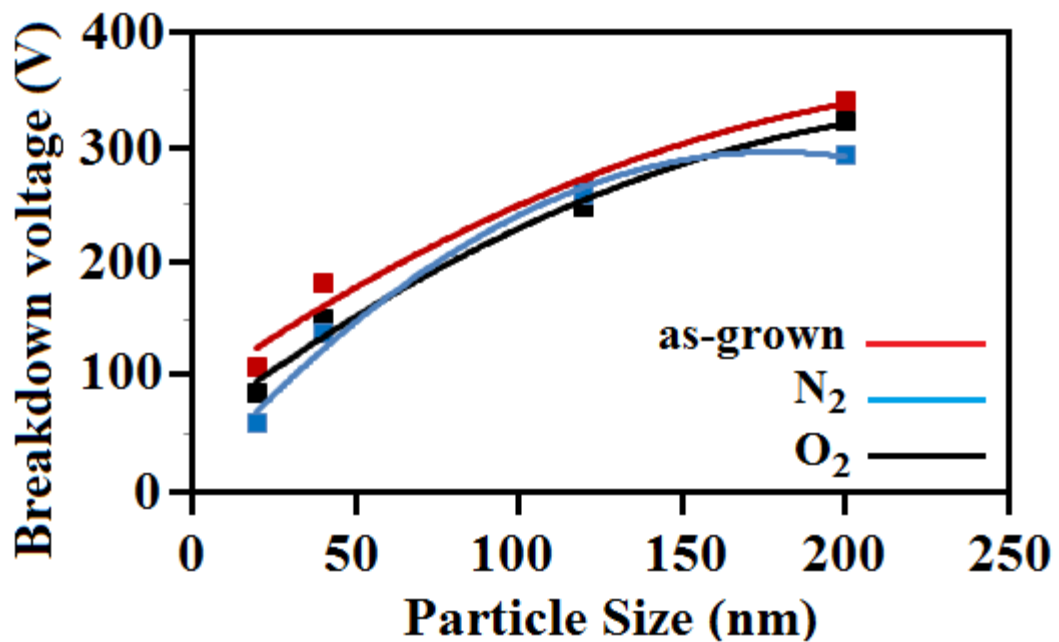


Figure 4.16. Plot of breakdown voltage of as-grown and annealed ZnO samples as a function of different particle sizes.

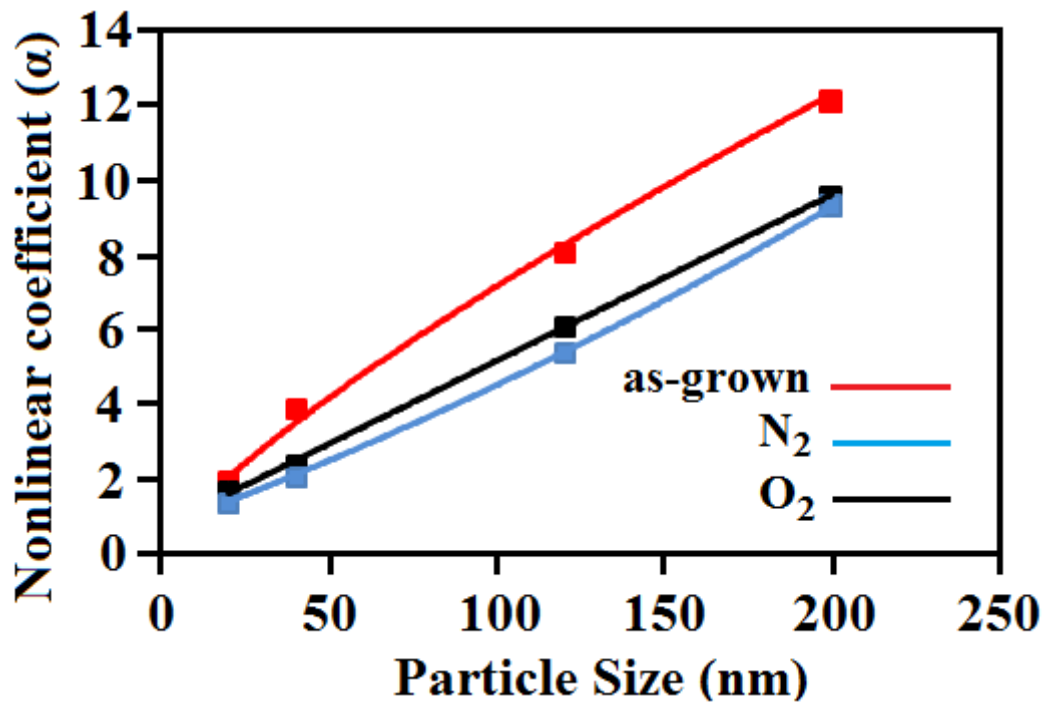


Figure 4.17. Plot of nonlinear coefficient α of as-grown and annealed ZnO samples as a function of different particle sizes.

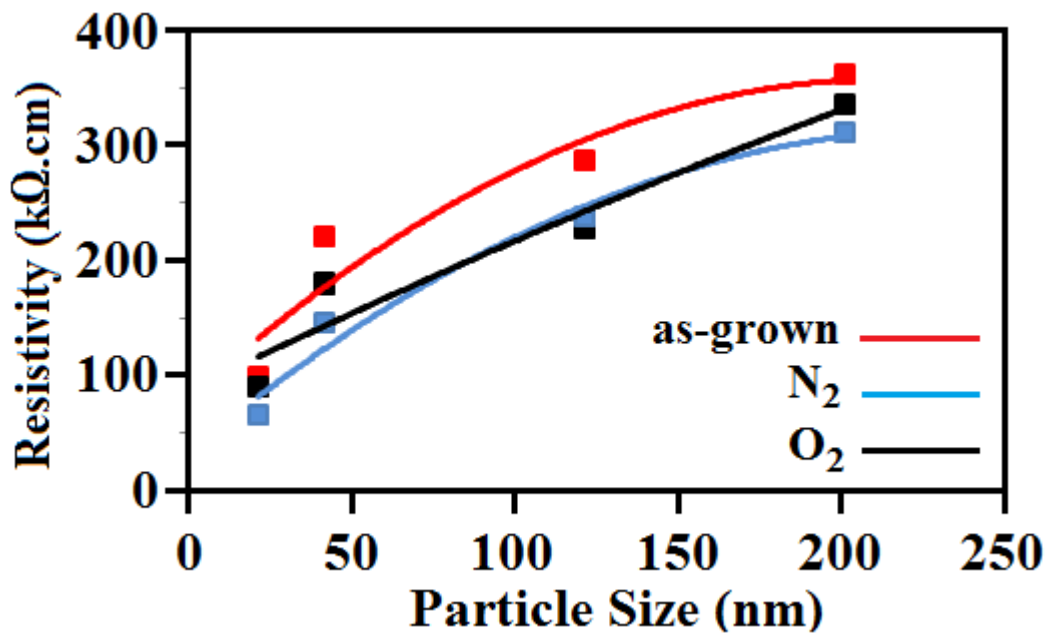


Figure 4.18. Plot of resistivity of as-grown and annealed ZnO samples as a function of different particle sizes.

The resistivity in the 40nm-Disc and 20nm-Disc are very low compared with that in the W4-Disc and P8-Disc. This phenomenon can be explained as follows: the surface to volume ratio in the 40nm-Disc and 20nm-Disc increases, the surface impacts become prominent, and the resistivity constantly decreases with the thermal annealing process, which conforms with the core-shell model (Fig. 4.19).

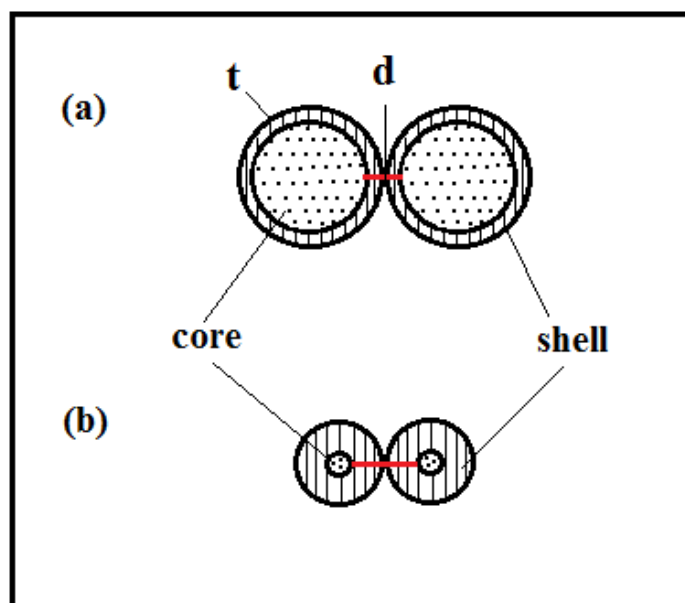


Figure 4.19. Core shell structure of nanoparticles grains for (a) as-grown and (b) annealed ZnO nanoparticles.

The effect of the decrease in resistivity can be interpreted by assuming that when the grain size is reduced to nanometers in the core-shell structure, the grain interior part (the core) would have the same characteristics as the bulk compound, whereas the outer layer of the grain (the shell width t) would consist most of the oxygen defects and deficiencies in the crystal structure. The shell thickness t of the grain increases with the decrease in grain size [347-349]. Substantially, with the reduction of grain size, the net interior core barrier thickness, that is, the sum shell thickness of two neighboring grains together with the inter granular distance d , increases. The schematic diagram in Fig. 4.19 explains that with the

decrease in grain size, core separation increases dramatically with the shell thickness. According to the core–shell model, nanoparticles have very large shell (surface region), in which defects are present, to the core (inner volume). Therefore, the annealing process has a significant effect on the 40nm-Disc and 20nm-Disc compared with the W4-Disc and P8-Disc, decreases the resistivity, and reduces the potential barrier between ZnO grains.

Various kinds of defects or vacancies on discs fabricated from nanoparticle powder (40nm-Disc and 20nm-Disc), which are diminished in W4-Disc and P8-Disc, are very electrically active. Given that the surface to volume ratio is very high and the charge carrier number is limited compared with the W4-Disc and P8-Disc samples, their electrical behaviors are critically dependent on the reaction and adsorption of gas molecules on surfaces during the annealing process. The breakdown voltage and resistivity are significantly affected by the surface molecular adsorption. The shift of electrical property is the shift of the charge transfer between the quasi-one-dimensional host and the chemisorbed species [350, 351]. With the surface adsorption of gas molecules at the vacancy sites, electrons are transferred from the nanoparticle surface to the adsorbed O₂, which leads to the surface depletion layer [352, 353]. Tuning the carrier number is possible by adjusting the amount of the gas molecular adsorption during thermal treatment. Thus, understanding the adsorption effect and gas molecules interaction on ZnO surfaces on the electrical properties is very important. In the present study, the changes in the electrical properties of the W4-Disc, P8-Disc, 40nm-Disc and 20nm-Disc samples after gas molecular adsorption during the annealing process were investigate.

The I–V characteristics of oxygen in the annealed 40nm-Disc and 20nm-Disc show a non-ohmic property that is very identical to that observed in the as-grown and nitrogen annealing. The nonlinearity in the W4-Disc and P8-Disc is a grain-boundary phenomenon, in which a barrier to majority carriers (electrons) dwells within the depletion region of close ZnO grains. During the oxygen thermal treatment, the incorporation of oxygen gas from the atmosphere might assist in saturating the defects at the grain boundary regions as well as in

reducing the oxygen vacancies concentration or associated defects in the ZnO crystallites, which could result in oxygen ion gradient that could generate the potential barrier among two close grains. Furthermore, as observed from the SEM analysis, thermal treatment also leads to the growth of the grains therefore decreasing the number of boundaries between them. The related influence of the dropping in oxygen vacancies and the grain development produces ZnO crystallites that are isolated from each other by an insulating grain boundary. This layer of insulating oxide sandwiched among two ZnO grains possible to be responsible for the electrical behaviors and nonlinear response in the I–V tests during the annealing process in oxygen ambient.

Based on the different electrical parameters provided in Table 4.6, the resistivity increases drastically after the annealing process in oxygen ambient for the 20nm-Disc, 40nm-Disc, P8-Disc, and W4-Disc, and the resistivity of the samples treated in O₂ is considerably larger than that of the samples treated in N₂. Furthermore, the resistivity for the 40nm-Disc and 20nm-Disc is smaller than that for the W4-Disc and P8-Disc at different annealing atmosphere. This result may be caused by the very large S/V ratio in nanoparticles, which makes it very prominent to the thermal treatment process. Therefore, the grain sizes of the 40nm-Disc and 20nm-Disc are larger than those of the W4-Disc and P8-Disc. Consequently, the grain boundary density in the discs and the carrier scattering at the grain boundaries decrease. Hence, the resistivity values of the discs decrease with growing grain size.

The thermal treatment has the impact of growing the size of grains and crystallinity of the W4-Disc and P8-Disc, which therefore leads to minimal grain boundary scattering. However, the treatment in oxygen atmosphere causes oxygen to prevalence inside the disc, thereby elimination the oxygen vacancies, chemisorbing to the grain boundary, and therefore diminution the carrier concentration. The severe rise in resistance after oxygen annealing may be attributed to the rapid fluxing of electrons from the crystal to the chemisorbed oxygen species, which results in the trapping of free carriers at the surface and the grain

boundaries and causes a rise in the barrier height. Sabioni et al. [354] suggested that the grain boundary might give a fast path for oxygen diffusion within sample. Under oxygen annealing, excessive oxygen could diffuse to the ZnO disc through the grain boundaries, and the oxygen in the boundaries could act as acceptor states that traps electrons and therefore reduces the carrier concentration [355].

Furthermore, annealing in oxygen atmosphere may form certain novel defects and impede grain incorporation, thereby enhancing the grain boundary scattering. Lin et al. found that surplus oxygen could introduce new defects relate to oxygen during the annealing process and deteriorate the quality of the ZnO disc [306].

The mechanism of the impact of oxygen environment on the electrical resistivity of the 40nm-Disc and 20nm-Disc samples can be explained as follows: in the case of nanoparticles, a significant number of junctions between the electrodes were connected in a network. Charge transport occurs through a ZnO grain boundary that presents a very high potential barrier for electrons to flow. The contact barrier with different heights and thicknesses determines the electron transport through the nanoparticles. The resistance of these discs is given by the following equation [356, 357]:

$$R = R_0 \exp \left[- \frac{e(V_0 - V_g)}{k_B T} \right] \quad (4.14)$$

whereby:

$\Delta V = (V_0 - V_g)$ is the change of the potential barrier in existence of any gas (V_g) from the contact potential in atmosphere (V_0).

R_0 is the resistance in atmosphere.

e is the electronic charge.

k_B is the Boltzmann's constant.

T is the absolute temperature.

ΔV can be modified by exposing various gases and becomes essential for nanoparticles with a significant surface to volume ratio. During the annealing in oxygen ambient, a depletion layer forms at the nanoparticle surface. The oxygen molecules adsorb and therefore induce band bending to the associated ZnO nanoparticles such that the contact potential barrier is modified based on the nature of the gas molecules. The modulation of the depletion width and the extent of band bending are high for nanoparticles with massive surface-to-volume ratios compared with the W4-Disc and P8-Disc samples, and surface depletion becomes a predominant factor in controlling the resistance of the 40nm-Disc and 20nm-Disc samples.

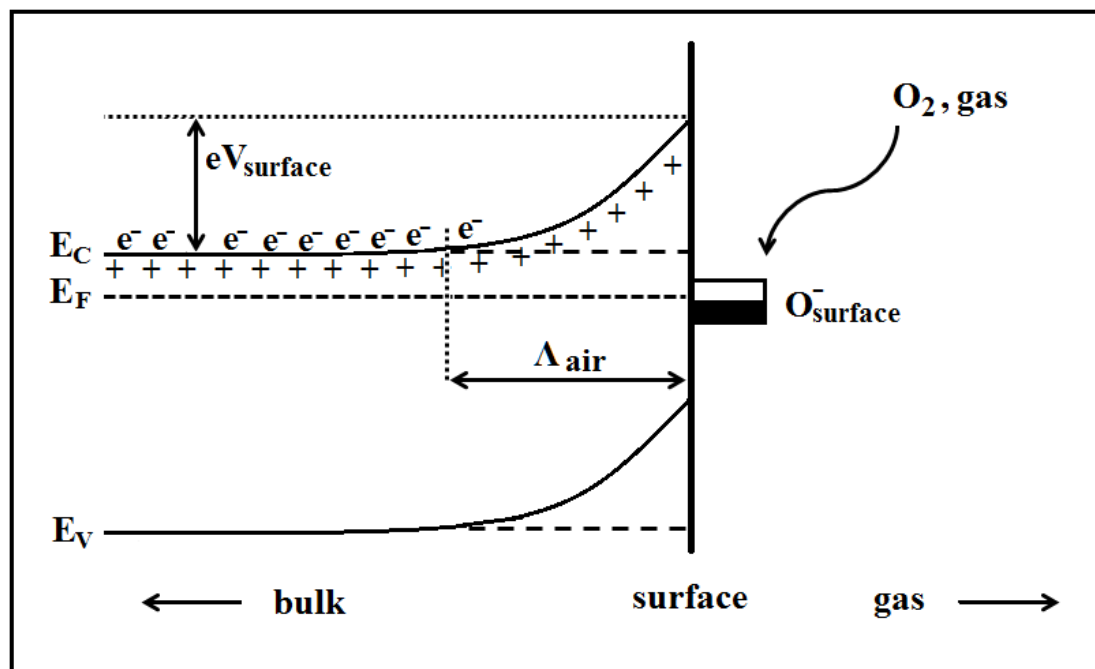


Figure 4.20. Schematic diagram of band bending after chemisorptions of oxygen during annealing process. E_F , E_C , and E_V indicate the energy of the Fermi level, conduction band and the valence band, respectively, while Δ_{air} indicates the thickness of the depletion layer, and eV_{surface} indicates the potential barrier. The conducting electrons are illustrated by e^- and + illustrated the donor sites. (taken from ref. [358]).

After the annealing process, oxygen is adsorbed on the surface of the 40nm-Disc and 20nm-Disc faster than on the W4-Disc and P8-Disc and the pores of the disc through sharing donor electrons from the ZnO nanoparticles. Negatively charged surface oxygen forms upward band bending and introduces a depletion layer. It decreases the conducting width across the disc electrode compared with the flat-band status and increases the potential barrier of the contacts among the nanoparticles, thereby leading to a drop in the conductivity. Fig. 4.20 describes the schematic diagram of band bending after the oxygen annealing process. When O_2 molecules are adsorbed on the disc surface, they would displace electrons from the conduction band E_C and then trap the electrons at the surface in ion form, which would result in band bending and an electron-depleted layer. The electron-depleted layer is also called the space-charge region, where the thickness is the length of the band bending layer. The reaction of these oxygen species with decreasing gases or the competitive adsorption and alteration of the adsorbed oxygen by other gas molecules can decrease and reverse the band bending, thereby leading to an increment conductivity, as in the case of annealing in nitrogen atmosphere. A band diagram of two nanoparticle grains after oxygen annealing, which hold O_2 molecules within the pore, is illustrated in Fig. 4.21.

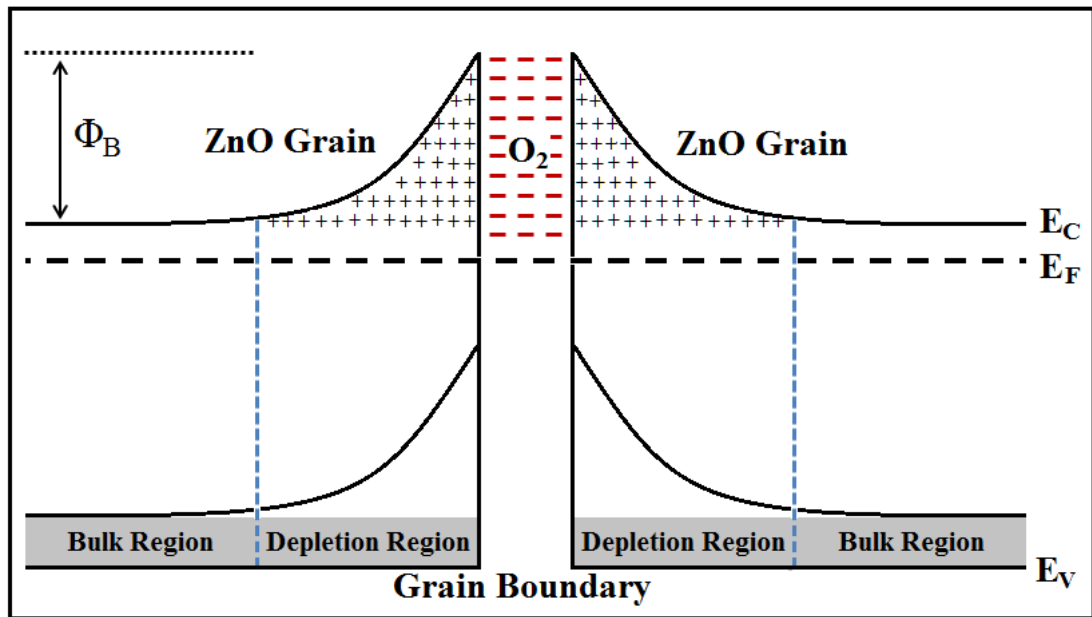


Figure 4.21. A model characterization the junction between two ZnO nanoparticles having adsorbed oxygen in the pores. Upward band bending due to oxygen promotes the contact potential between the nanoparticles.

In the case of annealing in nitrogen atmosphere, the resistance for the W4-Disc and P8-Disc show a slight decrease compared with the as-grown sample. A more rapid decrease in resistance is shown for the 40nm-Disc and 20nm-Disc under the nitrogen annealing process. The n-type conductivity in non-stoichiometric ZnO is attributed to V_o and Zn_i atoms [359]. Given that the ZnO electrical conductivity is directly associated with the number of electrons, the electrons generated by the ionization of the V_o and Zn_i atom affect the electrical conductivity of the ZnO crystals. The reduce in the resistivity of the discs during nitrogen treatment is influenced by both defects mentioned above but may be controlled by the V_o , which are created by oxygen extermination from the nanoparticle ZnO crystal lattice by the thermal treatment in a decreasing ambient (N_2 gas). Furthermore, when the annealing process is accomplished in a reducing oxygen ambient, the carrier concentration may improve by desorbing oxygen within the ZnO grain boundaries that act as traps for the carriers [163].

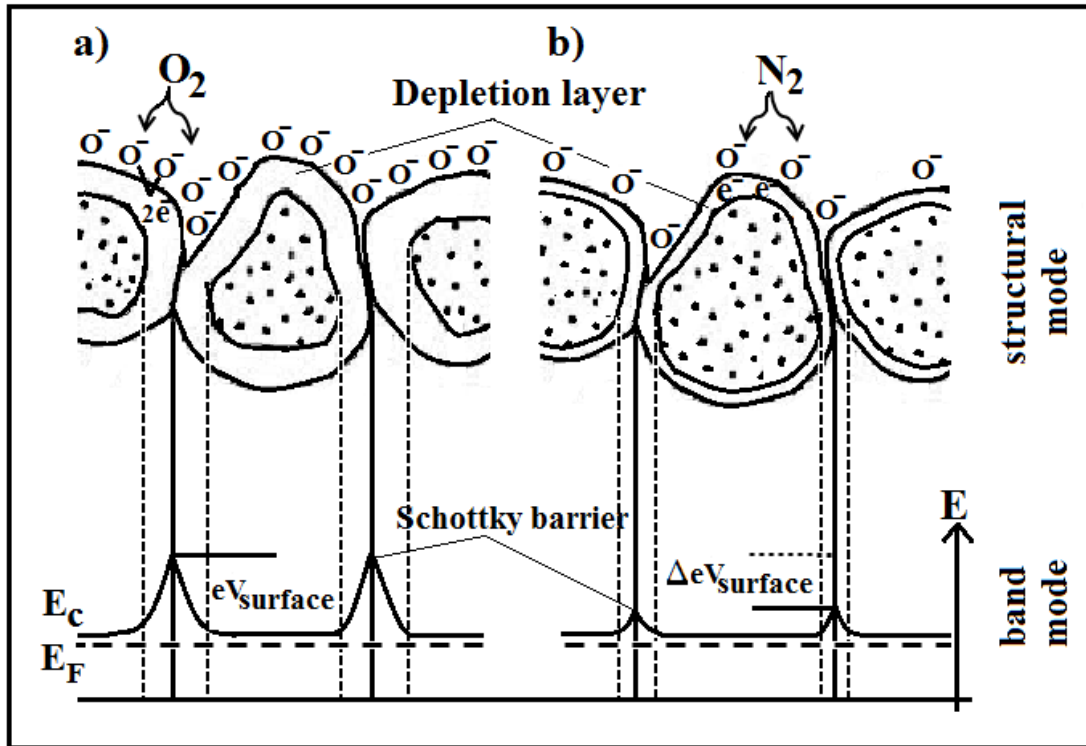
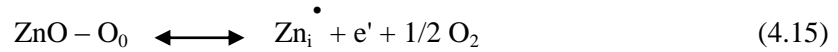


Figure 4.22. Structural and band modes showing the role of intergranular contact regions in determining the conductive mechanism during the annealing process. In (a) oxygen and (b) nitrogen atmospheres.

Therefore, the major factor that affects the resistivity is not the defect scattering that occurs within the ZnO grain but the boundary defect scattering. The decrease in resistivity after annealing in nitrogen ambient may be caused by the growth in the ZnO grain size, which decreases the interfaces among the nanocrystallites. All these observations agree with the SEM and AFM findings.

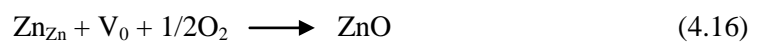
Many defects at grain boundary are exterminated, and the size of grain increases during the annealing process. Chopra et al. [360] and Studeniki et al. [152] reported that for the ZnO heat treatment in a reduction ambient such as nitrogen gas, an enormous decrease in resistance is achieved because of the rise in conductivity and oxygen defects, which act as electron donors. For W4-Disc, P8-Disc, 40nm-Disc and 20nm-Disc samples, a similar decrease in resistance is also obtained when the discs are thermal annealed under nitrogen ambient, resulting in desorption of oxygen and increase in V_o . On the contrary, the

deficiency of oxygen from the sample produces interstitial zinc atoms, as explained in the following reaction [361]:



The intrinsic donor possible to be increased by the nitrogen heat treatment, therefore rising conductivity. Nitrogen atoms would passivate the grain boundary surface through the thermal annealing in an N₂ ambient, and this nitrogen passivation would remove the depletion regions nearby the ZnO grain boundaries. The elimination of the depletion region, in turn, would increase the carrier concentration and diminish the resistivity. Besides the grain boundary passivation impact of nitrogen atoms, nitrogen impurity atoms also passivate Zn grain ions, leading to the rise in carrier concentration and therefore the reduce in resistivity because of the increase in the concentration of shallow donors that are localized at the semiconductor interface.

By contrast, oxygen annealing leads to the reduces in concentrations of the V_o and Zn_i in the W4-Disc, P8-Disc, 40nm-Disc and 20nm-Disc samples, thereby increasing the resistivity. This finding can be explained by the next Equations:



The decreases in V_o and Zn_i concentrations would lead to enhances in resistivity because they act as donors and produce impurity or ionized impurity scattering.

4.6 Summary

Therefore, based on the results, the discs fabricated from the 20 nm particle/grain size of ZnO powder exhibited good structural, optical, and electrical properties with low

breakdown voltage. The most important result for the 20nm ZnO is the widening of the energy band gap. This electronic structure change leads to major changes in the optical properties of the nanoparticle compared with its bulk counterpart. The 20nm ZnO has sufficient quality to open diverse areas and allow future experiments to functionalize and merge into devices. A critical application of the dependence of varistors made from ZnO on different properties, such as the size of nanoparticles, is that one type of semiconductor can be used to produce different kinds of varistor with different properties by simply changing the particle diameter. Another application that can be researched for these nanoparticles is their large surface-to-volume ratio, which has a significant effect on the varistor.

CHAPTER 5: RESULTS AND DISCUSSION 2

ZnO VARISTORS: COMPARISON OF THE STRUCTURAL, ELECTRICAL AND OPTICAL PROPERTIES OF VARISTORS MANUFACTURED FROM ZnO MICRO AND NANOPARTICLE POWDERS

5.1 Introduction

In the present work, W4-VDR, P8-VDR, 40nm-VDR and 20nm-VDR 20nmVDR were sintered at very high temperature for 3 h and then annealed in oxygen and nitrogen ambients. This process attempts to prevent the diffusion of any defects to the grain boundaries or the reaction of defects in the grain boundary with ambient oxygen during thermal treatments to obtain the impact of Bi and Mn on the different behaviors of the varistor. Bismuth oxide is experimentally known to be a key component in varistors, forming ceramics with a highly nonlinear current voltage response compared with pure W4-Disc, P8-Disc, 40nm-Disc and 20nm-Disc. The existence of a liquid Bi_2O_3 phase, as explained in the SEM images (Fig. 5.2), promotes densification and grain growth, and many studies have reported about the significant role of Bi_2O_3 in enhancing nonlinearity and low-field resistivity. However, very limited is known about the real influence of bismuth on the double Schottky barrier electronic structure in the varistor (see Fig. 5.1) that explains the electrical response of varistor ceramics. Furthermore, bismuth is known to aggregate to the grain boundaries among the ZnO grains, where it is assumed to contribute to the interface density of states, which forms the double Schottky barrier.

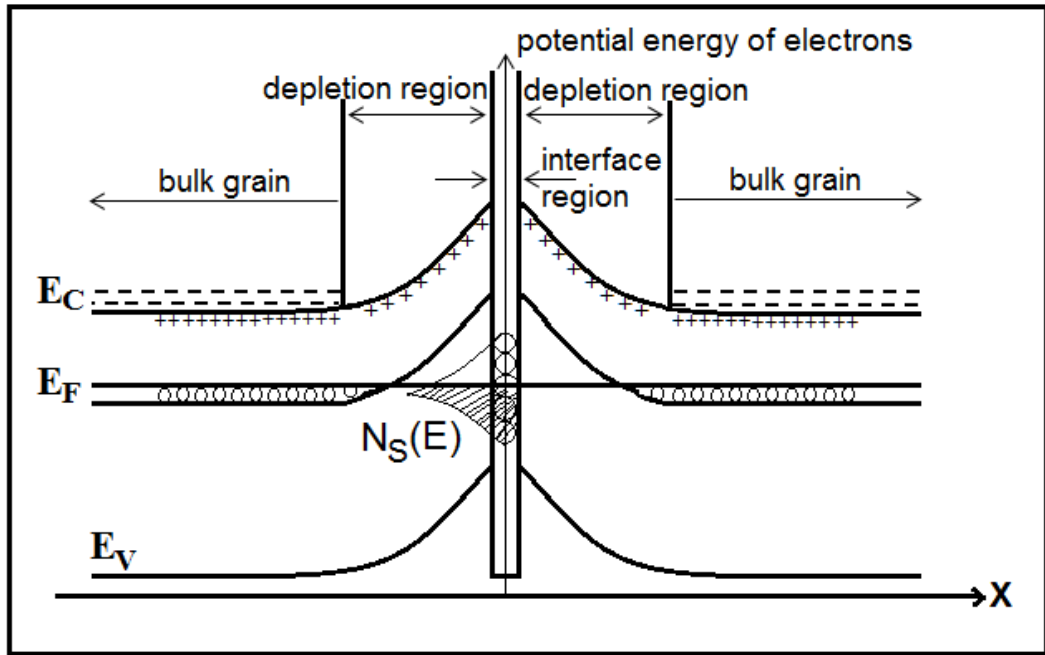


Figure 5.1. Energy band diagram of a double Schottky barrier in equilibrium. (taken from ref. [362]).

Furthermore, the other oxide additive Mn has been deduced as a deep donor in the ZnO varistor, and it considerably depresses the concentration of intrinsic donor and the interstitial zinc during the sintering process. Thus, Mn can make ZnO a more resistive material. Mn has no direct function on ZnO conductivity because it is a deep donor, but it dominates the carrier density by its interference on the intrinsic donor defect concentration. A similar result was drawn by Einzinger [363], who concluded that deep donors shift the intrinsic defect concentrations at the grain boundaries by reducing the donor concentration and increasing that of the acceptor, thereby leading to the built up of the electrical barriers in those regions. In this work, the varistors were prepared using micro- and nanoparticle ZnO with other oxide additives such as Bi_2O_3 and Mn_2O_3 , and then the different properties of these samples were studied under different annealing conditions to obtain a varistor device with good structural and electrical properties comparable with commercial devices.

5.2 Growth mechanism and structural properties of composite varistor under different particle sizes and annealing conditions

5.2.1 Scanning electron microscopy (SEM)

I. General microstructure

An overview of the general microstructure of the W4-VDR, P8-VDR, 40nm-VDR and 20nm-VDR at different annealing ambients is shown in Fig. 5.2. The prevailing constituent was relatively ZnO grains. Bi-rich phases were also found in many ZnO grain boundaries and within ZnO grain clusters.

Most of the aspects of the W4-VDR and P8-VDR are common with the 40nm-VDR and 20nm-VDR, which were exposed to liquid-phase sintering. ZnO–Bi₂O₃–Mn₂O₃ varistors are usually sintered at very high temperature (1200 °C), which is above the melting point for Bi₂O₃. Thus, the varistor is densified by liquid-phase sintering and the crystalline and amorphous phases that are formed through the cooling process of this liquid, which act as binder to cement the grains together.

II. ZnO grains

The exact element concentrations dissolved in ZnO grains have a significant interest for the varistors' electrical behaviors because these elements act as dopants and therefore substantially affect the ZnO grain conductivity.

Microanalyses by SEM/EDX (Fig. 5.2) indicated the presence of manganese in the solid solution within the ZnO grains. Other researchers have observed by optical spectroscopy, electron probe microanalysis [181] and chemical analysis [178] that identical small amounts of cobalt are dissolved within the grains of other associated varistor materials. Moreover, Inada et al. [178] also found that manganese is usually dissolved within the ZnO grain. Many different elements are also possibly dissolved in the ZnO grains, but the current analysis method cannot detect their low concentration levels.

III. Intergranular Bi-rich phases

As a consequence of the liquid phase that was created through the sintering process, a practically continuous intergranular Bi-rich material layer was found throughout the varistor microstructure, which was indicated to consist of different phases, such as amorphous and α - Bi_2O_3 phases. The morphology of the α - Bi_2O_3 phases indicates that these phases crystallized during cooling after the sintering process, which is further supported by the fact that intergranular crystalline phases are usually imbedded in an amorphous phase. One morphology of α - Bi_2O_3 shows small grains in impartially significant regions between ZnO grains. In many intergranular pockets, much smaller crystallites of α - Bi_2O_3 were also tightly packed. The boundaries among these small crystallites consisted of amorphous Bi-rich phase. Contrary to the present results, large amorphous phase pockets were observed by Clarke [194] in a comparable varistor material, and these pockets did not consist of any crystalline phases. The EDX analysis of the Bi-rich amorphous phase detected the presence of significant amounts of zinc. Thus, the substance studied by Clarke was possibly cooled from the highest sintering temperature at a rate that was fast enough to prevent crystallization.

III. Segregation of Bi to ZnO-ZnO grain boundaries

Similar with the investigations on W4-VDR, P8-VDR, 40nm-VDR and 20nm-VDR, the ZnO-ZnO grain boundaries had large amounts of bismuth aggregated to them. The fundamental divergence among the varistor sample obtained in this research and in other works, which employed similar conditions [182, 193-195], lies in the ZnO-ZnO grain boundary morphology. In the present work, most of the grain boundaries possessed thin second-phase films, whereas the boundaries observed in other works were at most free of intergranular films.

After analyzing the general microstructure of the W4-VDR, P8-VDR, 40nm-VDR and 20nm-VDR, the effects of different particle sizes and annealing ambient on the various properties of the varistor were then investigated. Fig. 5.2 shows the SEM micrographs of the W4-VDR, P8-VDR, 40nm-VDR and 20nm-VDR, which were sintered at 1200 °C for 1 h and then annealed at 700 °C in oxygen and nitrogen atmospheres. The results demonstrate that the surface morphology and grain growth in the W4-VDR, P8-VDR, 40nm-VDR and 20nm-VDR are dependent on the thermal treatment under different atmospheres. The size of ZnO grains is significantly higher when the varistor is treated in a nitrogen-rich ambient. Furthermore, they can be restored close to almost their original values when they are subjected to thermal treatment in an oxygen-rich ambient. More oxygen vacancies may have formed in strong reducing atmospheres (N₂ gas), and the growth process of the grains is controlled by the ZnO–ZnO grain boundary diffusion during the annealing process. As shown from the SEM analysis, the grain size of the 40nm-VDR and 20nm-VDR is greater compared with that of the W4-VDR and P8-VDR, which lead to the decrease in the grain boundaries and PN junctions among the grains and therefore affect the properties of the samples. Moreover, the grain size of the W4-VDR, P8-VDR, 40nm-VDR and 20nm-VDR increased significantly compared with the W4-Disc, P8-Disc, 40nm-Disc and 20nm-Disc. Low porosity and homogeneous structure are observed in all the samples, which indicate that the addition of bismuth in the varistor somehow supports the cationic inter-diffusion and the mass transport processes during the sintering process. The majority of bismuth-doped 40nm-VDR and 20nm-VDR are prepared by liquid-phase sintering. For this reason, the microstructural variations observed in the VDR could be associated with an ideal ceramic liquid-phase sintering process event. Given the ZnO–Bi₂O₃–Mn₂O₃ system eutectic point at 835 °C and the sample sintering process at 1200 °C, the microstructural changes, such as in grain size, are evidently caused by the formation process of the liquid phase.

In the case of Mn₂O₃ addition, several ions could be stabilized; through the sintering process, the next actions could occur:



Thereafter, the potential substitution equations are:



Mn^{+4} and Mn^{+3} exhibit smaller ionic radii than Zn^{+4} , but the Mn^{+2} radius is bigger. The SEM images show a development in the ZnO grain size with manganese addition, specifically in the 40nm-VDR and 20nm-VDR, which show a massive increase in grain size. However, the W4-VDR and P8-VDR display less growth with manganese addition, which indicates that manganese was stabilized as Mn^{+2} in the ZnO lattice. As can be observed from the previous equations, the addition of Mn_2O_3 , which stabilized as Mn^{+2} in the ZnO lattice, increased the V_O concentration, thereby enhancing the mass transport and favoring the densification of the 40 nm-VDR and 20 nm-VDR compared with the W4-VDR and P8-VDR. The addition of oxide dopants favors the production of V_O and allows the growth of ZnO grain through a solid-state diffusion mechanism. Manganese addition created a considerable grain growth. Gouvea et al. [364] did not observe formation of liquid phase by SEM. They believed that low solubility cannot significantly affect the intrinsic disorder of ZnO at elevated sintering temperature. Thus, they did not consider the improvement of volume diffusion to be caused by Mn dissolution. They determined that material transfer happens only at the surface of grains if the Mn surface concentration is minimal than a critical value ($5 \times 10^{-6} \text{ mol m}^{-2}$). If the surface Mn concentration is higher than the critical

concentration value, the aggregation layer thickness would be large to induce the prevalence in the volume located around the grains and not only on the surface. In the present work, a secondary phase located at the grain boundaries was indicated by SEM analyses, as shown in Fig. 5.2.

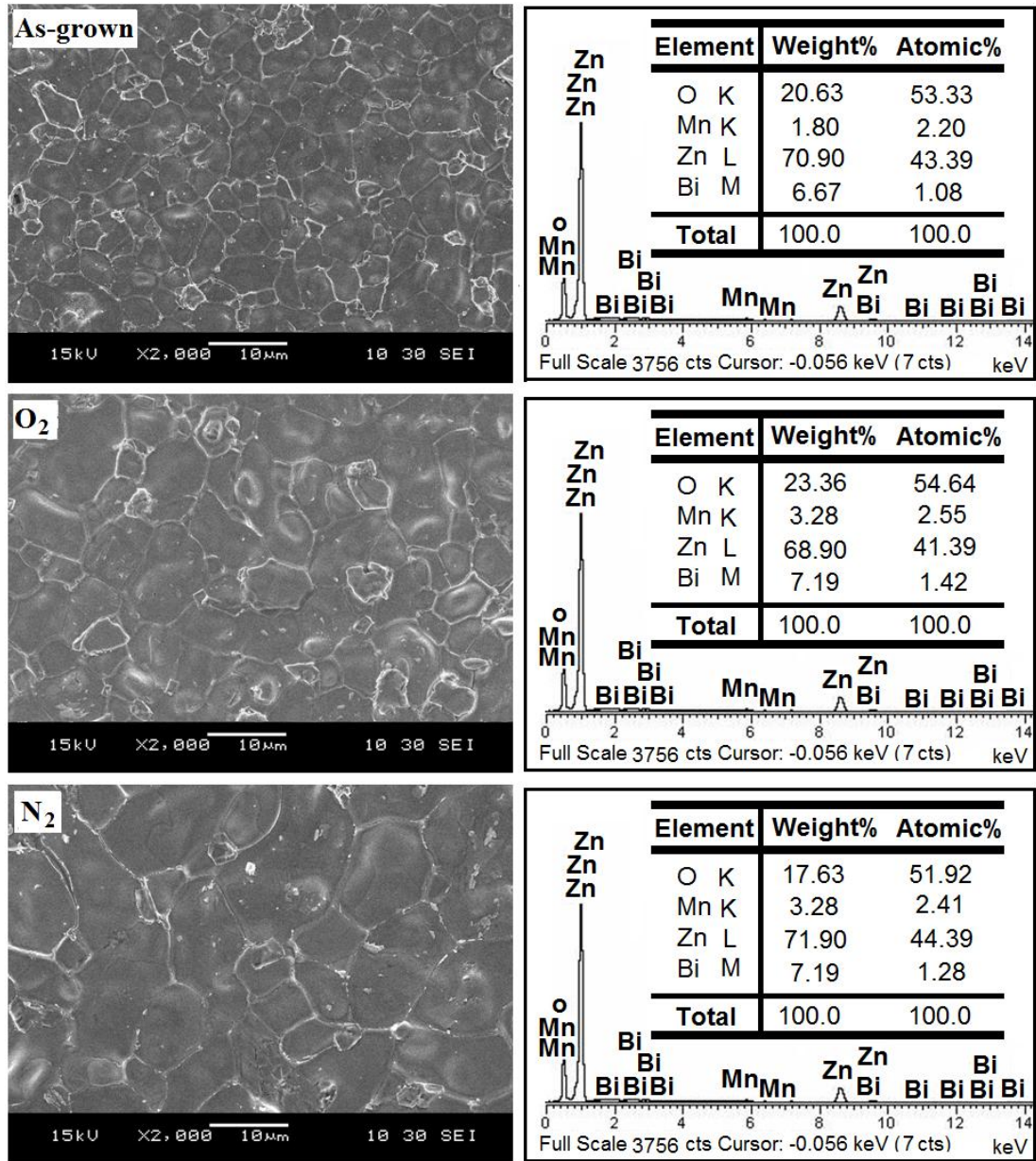
Significant evidence suggests that the similarities among the W4-VDR, P8-VDR, 40nm-VDR and 20nm-VDR are related with the oxygen amount within the ZnO–ZnO grain boundary and dopants in the form of metal oxide precipitate phases with a "nature of p-type semiconductor" (oxygen-rich phase and metal deficient) or that are perfect ionic conductors. The studies of Stucki and Greuter [365], for example, indicated that the oxygen and bismuth concentrations at the ZnO–ZnO grain boundaries are influenced variously by annealing in nitrogen and oxygen within varistors. Previously studies [366, 367] have also proposed that varistor properties are associated with the certain crystalline form that Bi_2O_3 takes on with oxygen at the ZnO grain boundary surface. The role of Bi as grain boundary activator" may, in the simplest form, be confined to providing surplus oxygen to the grain boundaries [368]. The Bi-rich phase is interconnected and continuous along the four- and three-grain junctions through the varistor microstructure. This topology is regarded by numerous to be critical for the oxygen transfer to the varistor during thermal treatment process. Certain investigators have also reported that non-ohmic characteristics can be improved by applying strongly oxygenated Bi_2O_3 as beginning material [369]. The present research on W4-VDR, P8-VDR, 40nm-VDR and 20nm-VDR indicated a similar conclusion.

For the W4-VDR and P8-VDR, transitional element addition, such as of Mn, is very significant to enhance varistor nonlinearity. The oxide formed by Mn is an acceptor, and their valence state may convert in the nearness of boundary among the grains, especially with local variations in the oxygen potential. Egashira et al. (1995) had another significant results that enhanced our findings [370]. Their research showed that porous varistors have nonlinear behavior at elevated heat treatment temperatures and that, similar to dense non-ohmic varistors, these properties are based on oxidizing gases. They deduce that the gas-

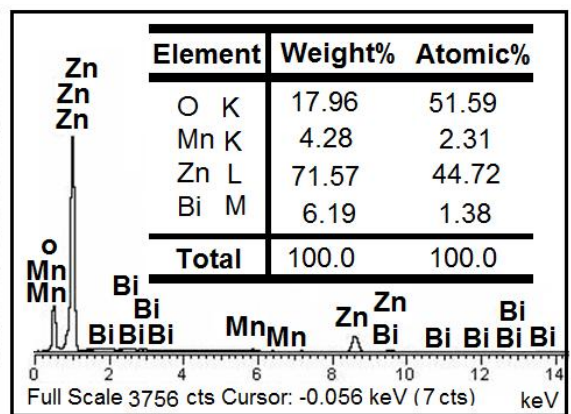
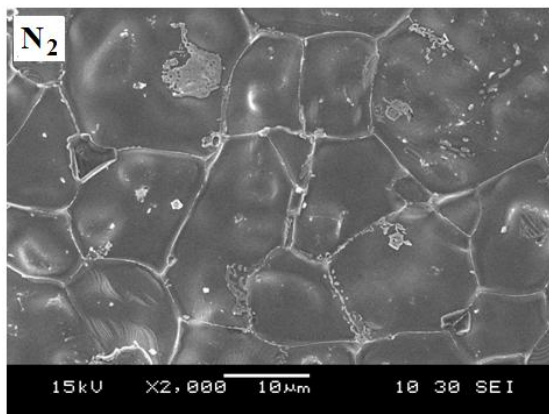
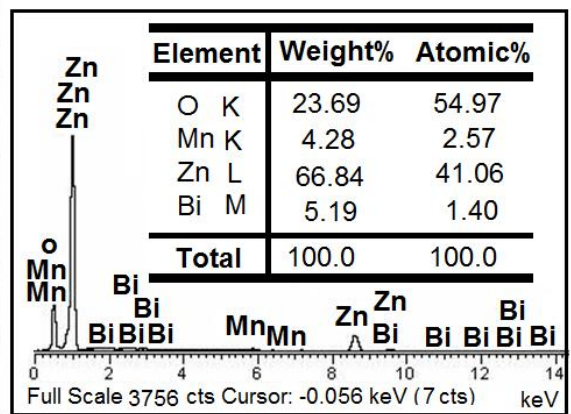
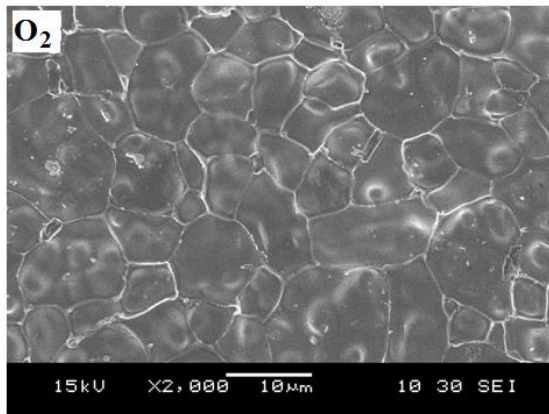
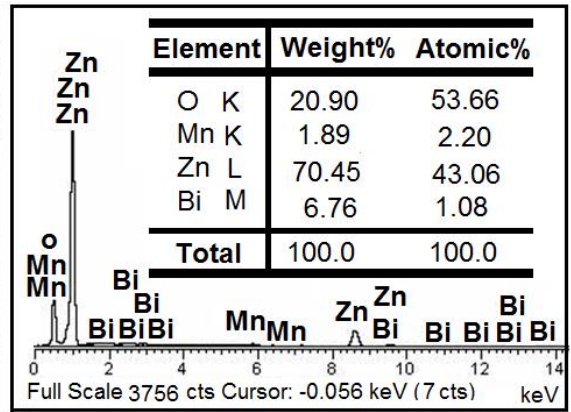
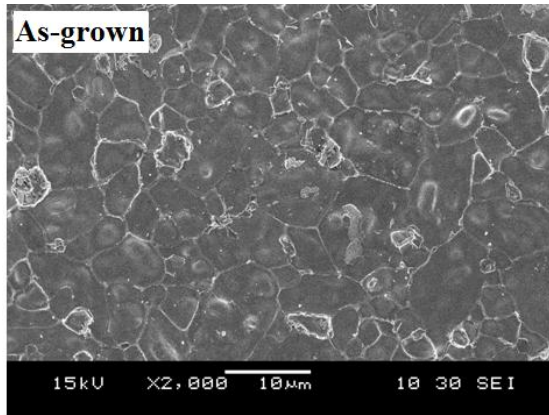
sensing mechanism of the W4-VDR and P8-VDR is triggered by negatively charged chemisorbed species, which propose the Schottky barrier rising at grain boundaries.

Explaining all these similar behaviors would be very difficult if no similitude exist in the forming of the potential barrier within polycrystalline ceramics that have much diverse microstructures and chemical compositions. Thus, these proofs and similarities suggest a phenomenological model for the barrier generation in varistors, which takes these similitude into account regardless of the composition. The model assumes that varistor samples with optimal electrical behaviors include an surplus of both acceptor metal atoms (such as Bi or Mn) and oxygen (precipitated on the surface of the grain boundary) in ZnO-based varistor. These metal oxide atoms are fundamentally transition metal oxides that usually have different oxidation states, which lead to the oxygen amount to rise at the grain boundary. Thus, the transition metal oxide that precipitates at the boundary becomes even much oxidized during treatment in an O₂-rich ambient (because of the ease of its valence state alterations), leading to the electron-trapping interfacial region to be rich in oxygen species. The boundary region among the grains has a "nature of p-type semiconductor" (because the phases precipitate at the boundary region), whereas the bulk has an "nature of n-type semiconductor" (ZnO-based varistor matrix). This composition allows the electrons to be centralize on the surfaces, presenting an increase in negative surfaces (negative interfacial states). To preserve local electrical neutrality, the charges are recompensed by bulk electron traps and ionized shallow donors. As a result, electron depletion layers are created and act as potential barriers. The potential barriers possess a Schottky-like nature, which is the identical nature frequently obtained in each varistor ceramics at high annealing temperatures [371], because of negative interfacial states. With this boundary formation, thermal treatment process under a decreasing ambient (N₂) removes surplus oxygen, thereby enabling the metal oxide atoms to remain and reducing the nonlinear behaviors of the varistor. Subsequently, the physical principle of the interfacial states is not essential because of the lattice mismatch

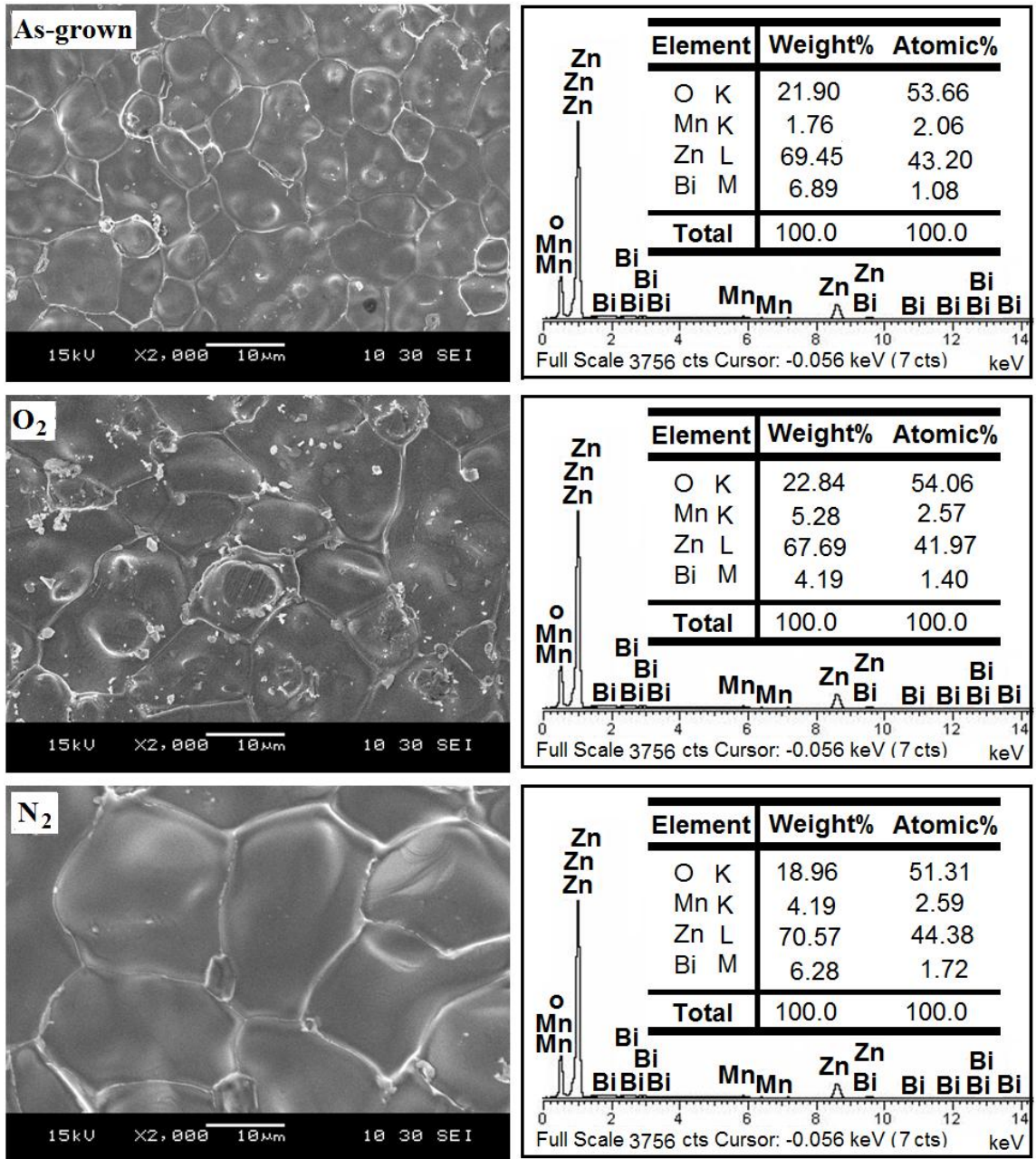
at the grain boundary; instead, it is extrinsic because the metal oxide atoms precipitated at the grain boundaries.



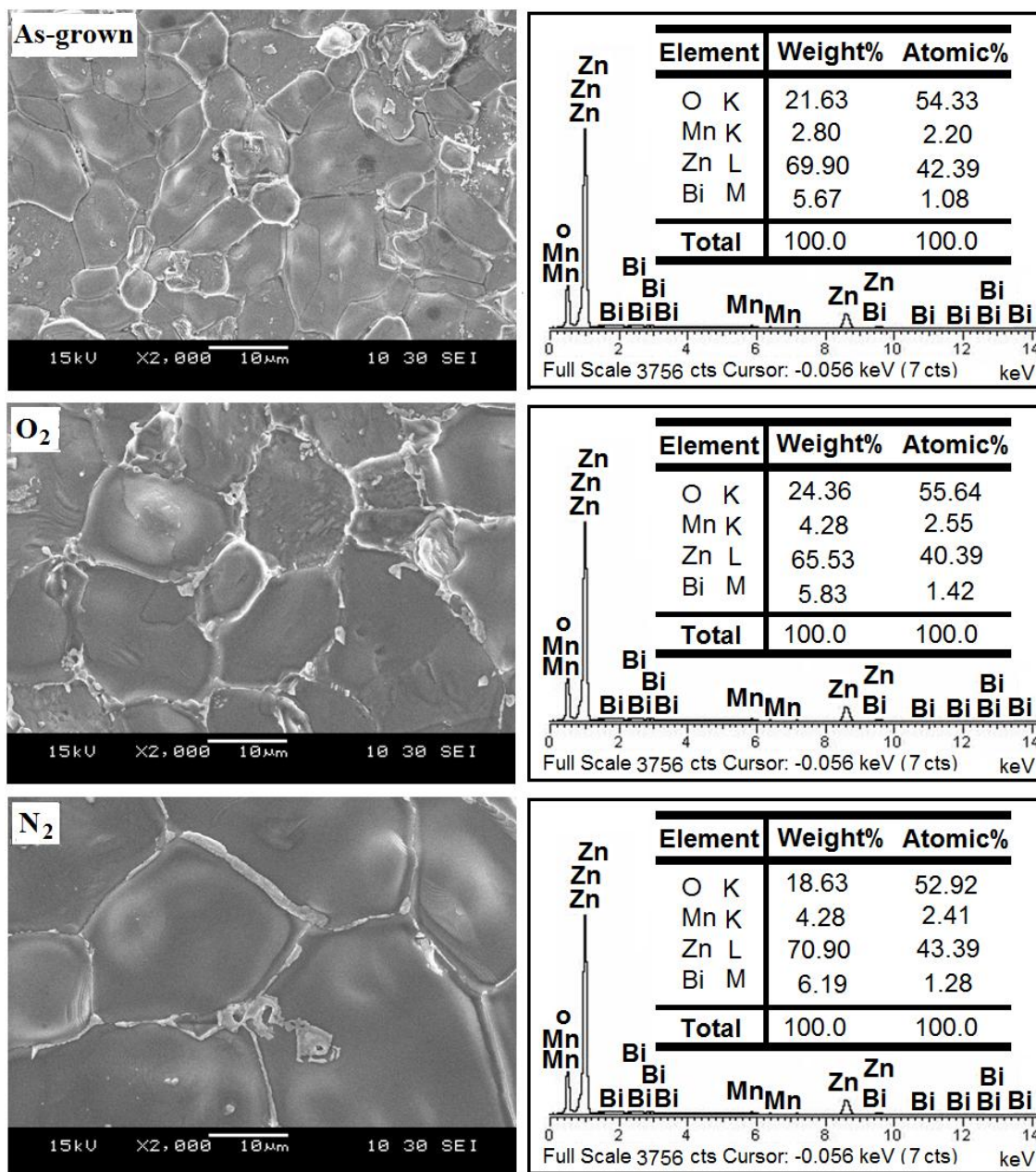
(a)



(b)



(c)



(d)

Figure 5.2. Typical SEM-EDX images of (a) W4-VDR, (b) P8-VDR, (c) 40nm-VDR, and (d) 20nm-VDR annealed at different ambients.

Table 5.1 summarizes the SEM results of ZnO varistors fabricated from different particle sizes of ZnO powders and annealed at different ambients. Variation of the grain size is then plotted as a function of the different particle sizes (Fig. 5.3).

Table 5.1. Summary for SEM images of ZnO varistors with different annealing atmospheres.

Sample	Annealing ambient	Grain size (μm)
W4-VDR	As-grown	2.114
	O ₂	2.651
	N ₂	4.724
P8-VDR	As-grown	2.440
	O ₂	4.322
	N ₂	8.240
40nm-VDR	As-grown	4.341
	O ₂	7.202
	N ₂	13.42
20nm-VDR	As-grown	5.533
	O ₂	9.610
	N ₂	17.73

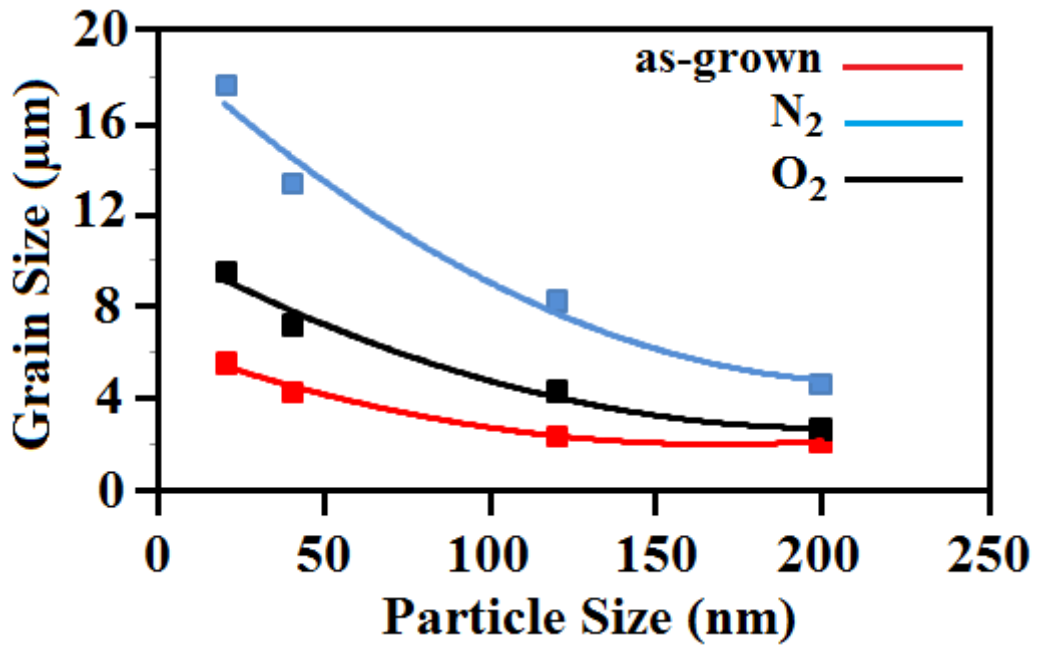


Figure 5.3. Plot of grain size of as-grown and annealed ZnO samples as a function of different particle sizes.

Based on the EDX data, different metallic oxides at different concentrations were detected in the W4-VDR, P8-VDR, 40nm-VDR and 20nm-VDR at various annealing conditions. At various ambients, Bi_2O_3 and Mn_2O_3 had average concentrations similar to the initial chemical nominal content.

The presence of bismuth is evident at the grain boundary between the grains in all samples, but no bismuth is detected in the ZnO grains. Large numbers of Bi ions with large ionic sizes may have aggregated to the grain boundary. These Bi ions could have encountered difficulties in occupying the interstitial sites inside the ZnO grains because of the occupation of the extra donor. Hence, they ended up at the grain boundary and formed Bi-rich grain boundary phases because they could not squeeze into the lattice atoms due to their large sizes. Bi-rich grain boundary phases have a crucial function in providing a conduction path for the transfer of oxygen into the sample through the heat treatment process [1, 12, 172, 372]. However, most of the ZnO–ZnO grain boundaries included a continuous intergranular Bi-rich material when significant amounts of Bi_2O_3 were detected in the discs after annealing may be because of the Bi_2O_3 liquid phase. The Bi_2O_3 liquid phase, which is caused by pyrochlore corruption at elevated annealing temperatures, wetted the grains and then froze them at room temperature. On the reverse, no segregated bismuth oxide intergranular phase was observed when the sample only had few Bi_2O_3 . ZnO–ZnO homojunctions were observed to have the most relative occurrence frequency [373].

5.2.2 X-ray diffraction (XRD)

Fig. 5.4 shows the XRD spectra of the W4-VDR, P8-VDR, 40nm-VDR and 20nm-VDR at different annealing ambients characterized by the strongest major peaks of (101), (100), (002), and (110), which arose from the ZnO layer and were emphasized through the polycrystalline nature of the varistors. Other peaks such as the ($\text{Bi}_{48}\text{ZnO}_{73}$) and (Mn_3O_4) phases seemed as secondary phases. Composite ZnO discs with other oxide additives are multiphase materials. ZnO varistor materials contain ZnO as a major phase. Spinal,

pyrochlore, and several other phases are present in the specimen. The presence of these phases depends on the nature and amount of the oxide additives in ZnO and on the processing parameters. The incorporation of these oxide additives forms atomic defects within the ZnO grain and grain boundary, with donor or donor-like defects controlling the depletion layer and acceptor and acceptor-like defects controlling the grain boundary states [374].

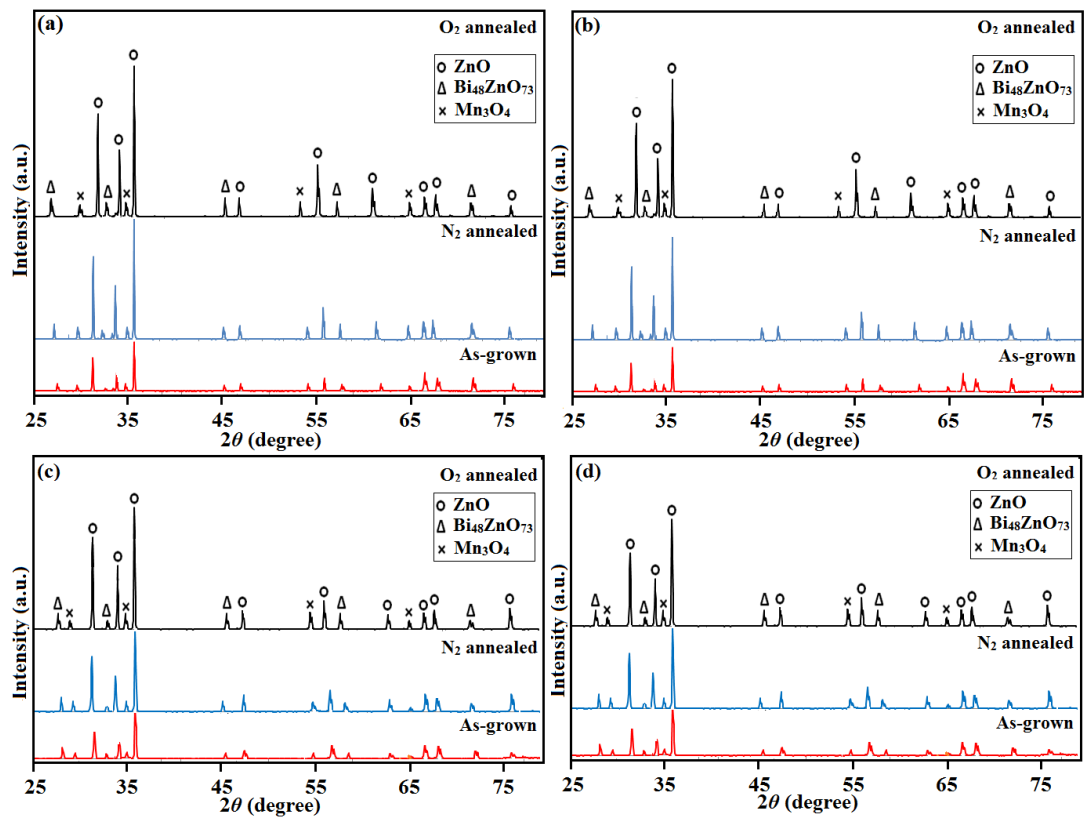


Figure 5.4. XRD pattern of ZnO-Bi₂O₃-Mn₂O₃ varistor system fabricated from (a) White ZnO (W4), (b) Pharma ZnO (P8), (c) 40 nm ZnO, and (d) 20 nm ZnO at different annealing ambients.

The data in Table 5.2 indicates that although several peaks of the sample annealed in an oxygen ambient are somewhat higher than those of the sample annealed in the other ambient, all samples exhibit higher and narrower diffraction peaks with smaller FWHM with

annealing process compared with the as-grown sample for the varistor, indicating better crystallinity and structure ordering of ZnO in the grain and grain boundaries. The 40nm-VDR and 20nm-VDR have thermodynamically stable crystallographic phase compared with the W4-VDR and P8-VDR, and the intensity of the peaks indicates the elevated degree of crystallinity. However, the width of the peaks in the W4-VDR and P8-VDR decreased dramatically, whereas it increased in the 40nm and 20nm-VDR because of the quantum size effect.

The shift in the position of the (101) peak of the W4-VDR, P8-VDR, 40nm-VDR, and 20nm-VDR, compared with the W4-Disc, P8-Disc, 40nm-Disc, and 20nm-Disc, indicates that adding Bi₂O₃ and Mn₂O₃ strengthens the tensile stress within the ZnO crystals. In theory, substituting Zn²⁺ by Bi³⁺ within the ZnO crystal is complicated because the radius of Bi³⁺ is larger than that of Zn²⁺. The findings of a previous study indicate that Bi₂O₃ aggregates fundamentally at the ZnO–ZnO grain boundaries as Bi-rich phases through the sintering process in the ZnO–Bi₂O₃–Mn₂O₃ system [375], as observed in the SEM analysis of the varistors β-Bi₂O₃. The liquid phase permeated into the boundaries among grains and improved the growth of grain and densification of the disc. This procedure would enhance the interfacial stress of the grains, which may be the major reason for the transfer of the (101) peak in the XRD spectra. Despite this, the effect of Bi³⁺ on the microstructure of the ZnO crystal could not be precluded because the Bi₂O₃ solid solubility within grain is lower than 0.06 mol% [376]. In addition to Bi₂O₃, the ion radii of Mn is comparable to that of Zn²⁺, and some of the Zn²⁺ ion within the ZnO lattice may possibly be replaced by Mn²⁺ or Mn⁴⁺ when the grains grow through the sintering process. The substitution would lead to the deformation of the ZnO lattice, which would lead to stress development. Thus, the deformation of ZnO surface lattice is attributed to the forming of secondary phases among the ZnO–ZnO grains, and the deformation of the lattice due to the substitution of dopant ions such as Mn²⁺ and Mn⁴⁺ for Zn²⁺ is assumed to be the major origin of the ZnO peak shift.

Table 5.2 summarizes the XRD phase analysis of W4-VDR, P8-VDR, 40nm-VDR and 20nm-VDR at different annealing ambients. Variation in the (101) peak intensity, diffraction angle and FWHM are then plotted as a function of the different particle sizes, as shown in Fig. 5.5, 5.6 and 5.7, respectively.

Table 5.2. Summary for XRD phase analysis of ZnO varistors at different annealing ambients.

Sample	Annealing ambient	XRD intensity (a.u.)	2θ (deg.)	FWHM (deg.)
W4-VDR	As-grown	1,447	36.175	0.1984
	O ₂	7,943	36.198	0.1958
	N ₂	3,488	36.251	0.1972
P8-VDR	As-grown	5,815	36.183	0.2021
	O ₂	12,471	36.220	0.1989
	N ₂	8,702	36.283	0.1992
40nm-VDR	As-grown	14,088	36.351	0.2952
	O ₂	45,718	36.264	0.1998
	N ₂	28,672	36.386	0.2573
20nm-VDR	As-grown	30,720	36.373	0.2980
	O ₂	74,241	36.392	0.2114
	N ₂	43,522	36.405	0.2773

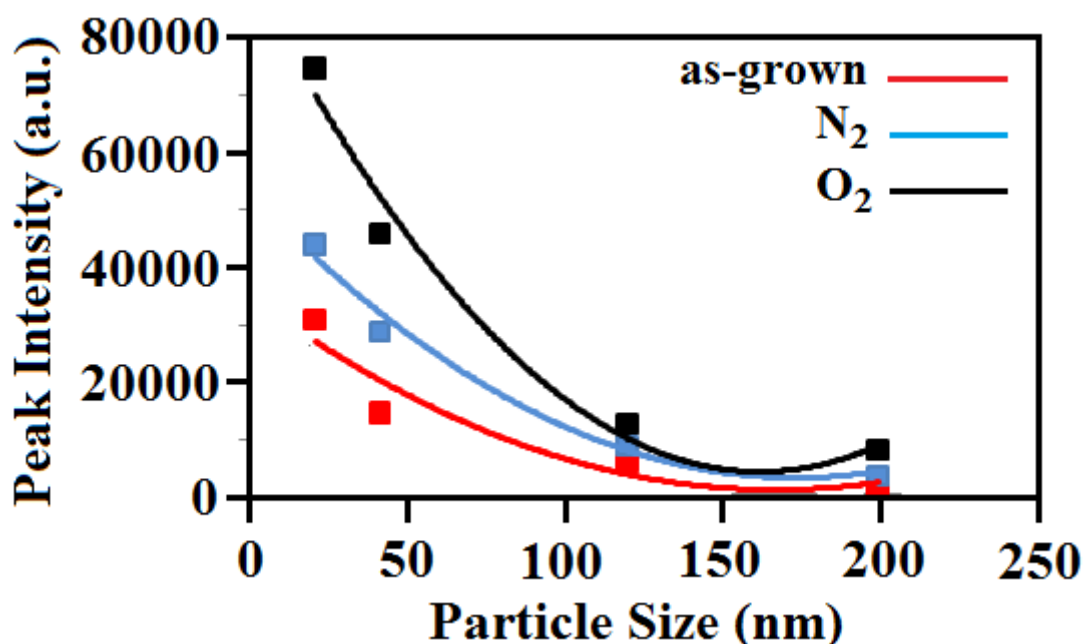


Figure 5.5. Plot of (101) peak intensity of as-grown and annealed composite ZnO varistors as a function of different particle sizes.

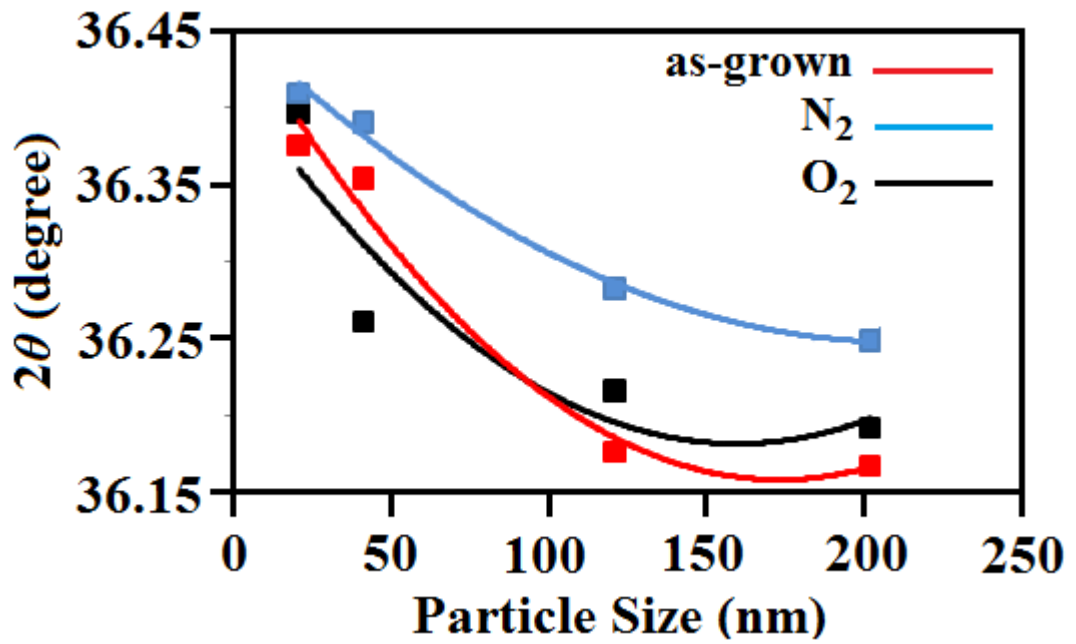


Figure 5.6. Plot of diffraction angle of as-grown and annealed composite ZnO varistors as a function of different particle sizes.

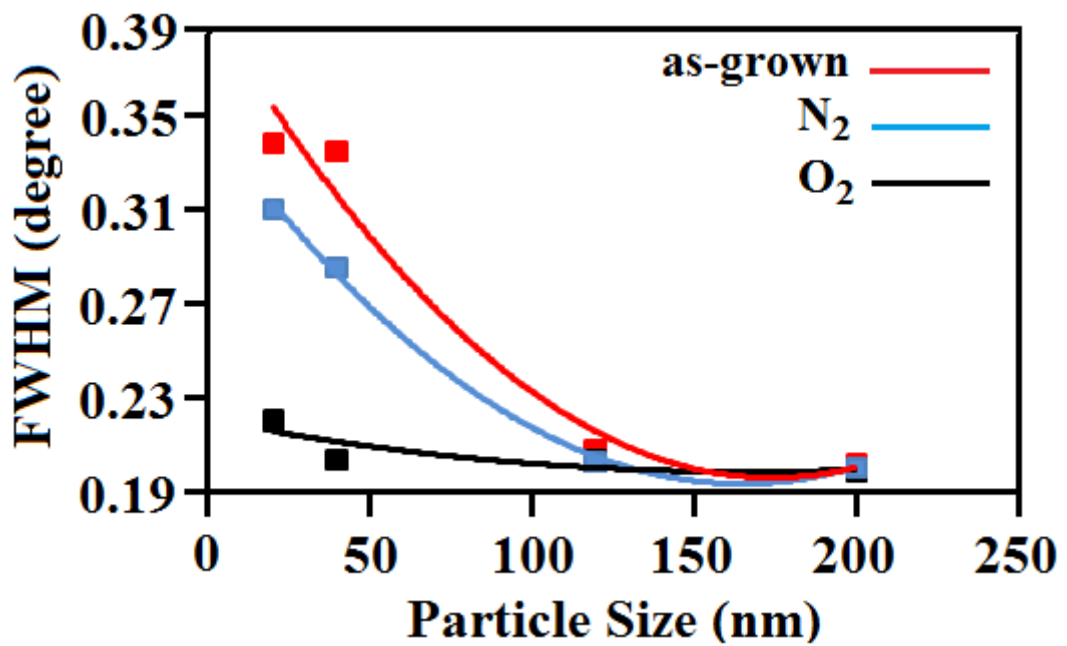


Figure 5.7. Plot of FWHM of as-grown and annealed composite ZnO varistors as a function of different particle sizes.

The intensity and diffraction angle of the (101) peak of the as-grown and annealed samples increased dramatically with decreasing particle size from the W4-VDR to 20nm-VDR (Fig. 5.5 and 5.6), indicating the occurrence of residual stress in the 20nm-VDR. The (101) peak became less asymmetric and gradually shifted to high 2θ values as the particle size decreased, which resulted in the decrease in the lattice constant. Moreover, the FWHM of the (101) diffraction peak increased with decreasing particle size from the W4-VDR to the 20nm-VDR, suggesting the exiting of the quantum size effect in the ZnO nanoparticles (Fig. 5.7).

The W4-VDR, P8-VDR, 40nm-VDR and 20nm-VDR annealed in oxygen and nitrogen atmospheres exhibit a powder pattern, as shown in Fig. 5.4. The 20nm-VDR annealed in N_2 atmosphere has a larger FWHM than the W4-VDR, P8-VDR, and 40nm-VDR and those treated in oxygen atmosphere. This result indicates that the crystalline of the ZnO varistors annealed in oxygen has high quality. Therefore, the 20nm-VDR annealed in N_2 ambient has a high defect concentration.

During heat treating in oxygen atmosphere, V_o are complemented predominantly through the chemisorption process, and this integrates with enough Zn atoms to produce new ZnO, leading to the increase in the XRD peaks. On the contrary, annealing in N_2 ambient can easily lead to the perversion from the stoichiometric state, producing significant oxygen insufficiency. The oxygen complemented by heat treated in the oxygen atmosphere predominantly reduces the oxygen defects. This finding is consistent with the observations on the W4-Disc, P8-Disc, 40nm-Disc, and 20nm-Disc in different annealing atmospheres and indicates that the structure and stoichiometry of the ZnO varistor heat treated in O_2 atmosphere is preferable than that annealed in N_2 ambient.

The XRD analysis studies of Clark [194], Olsson [183] and Kingery et al. [195] all indicated the development of a unceasing network of a Bi_2O_3 -rich phase at the boundaries among the grains in annealed ZnO varistor ceramics at oxygen atmosphere. The function that this grain boundary liquid layer phase supposes in the ZnO grain growth process during

liquid-phase annealing is thus of primary importance because most ZnO varistor formations are treated under these liquid-phase annealing conditions. The excess oxygen at the 20nm-VDR grain boundary interfaces compared with the W4-VDR, which is caused by the huge S/V ratio in nanoparticles, and the strong oxygen ion conduction of Bi₂O₃ at the ZnO grain boundaries perform a significant role for the varistor functionality.

5.3 Surface modification and ZnO size effects on optical properties of composite ZnO varistor

5.3.1 Photoluminescence spectra

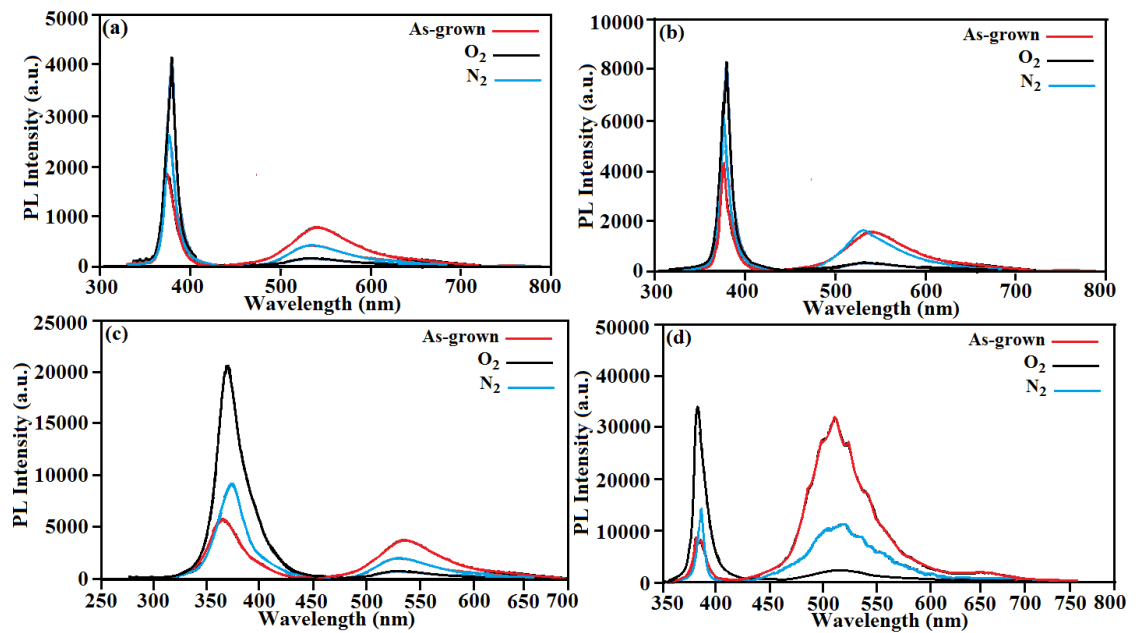


Figure 5.8. PL spectra of ZnO-Bi₂O₃-Mn₂O₃ varistor system fabricated from (a) White ZnO (W4), (b) Pharma ZnO (P8), (c) 40 nm ZnO, and (d) 20 nm ZnO at different annealing ambients.

Fig. 5.8 displays the PL of W4-VDR, P8-VDR, 20nm-VDR, and 40nm-VDR annealed in O₂ and in N₂ ambients. Under the identical excitation level, strong and rather broad PL spectra were noticed for whole varistor samples, covering wavelengths from very short (300 nm) to long (800 nm). With decreasing particle size from the W4-VDR to the

20nm-VDR, insignificant wavelength shifts are noticed for all the samples PL peaks, with peaks around 3.37, 3.38, 3.35, and 3.33 eV. The PL bands of the W4-VDR and P8-VDR centered at 3.37 and 3.38 eV are obviously associated with the transmission of band edge from the conduction band. The intensity of the bands of the W4-VDR and P8-VDR kept increasing, indicating that crystallinity is a main factor for the NBE emission of ZnO nanoparticles. The 40nm-VDR and 20nm-VDR peaks at 3.35 and 3.33 eV are completely proportionate with the transition related with the V_o within ZnO [91].

At visible region, even though several mechanisms were used for the visible emission of ZnO, a statistically appropriate mechanism is very complicated to be found partially because of its critical dependence on the varistor processing conditions [131]. According to our knowledge, visible emission is fundamentally caused by defects, which are associated with deep-level emissions, such as Zn_i and V_o [149].

For the 20nm-VDR and 40nm-VDR peaks at the lowest region, if the a semiconductor dimension is decreased to nanometer scale, then one of the main characteristic is the huge S/V ratio, which makes nanostructure samples very various from the W4-VDR and P8-VDR. The large S/V ratio in nanosized materials signifies large bulk density of dangling bands. The presence of dangling bands in a surface of crystal is probably to have a more localized change of state by splitting the state out of the energy gap border [299]. Thus, surface state can be responsible for the emission.

The peak position of the 20nm-VDR and 40nm-VDR, compared with the W4-VDR and P8-VDR, lies below the ZnO nanoparticles band gap (Table 5.3), which suggests the existence of such initial states in the forbidden energy band gap. These initial states within the band gap have their own ground or excited energy levels. Furthermore, the PL band intensity for the 20nm-VDR decreases with increasing grain size (W4-VDR), which can be produced as described below.

In general, the transition rate W_{PL} is proportional to the population of occupied surface states n_v . Furthermore, the photo carriers number n_{ex} in the surface states within a

crystallite is proportional to the number of atoms on the surface n_s [299]. As discussed in section 4.4.1.

Consequently, the surface-related mechanism can explicate the reduce of PL intensity in W4-VDR and P8-VDR with growing grain size, and this distinctive development can be due to the surface state impacts.

Moreover, based on the quantitative dependence of the total PL intensity on the grain size of the 20nm-VDR, as displayed in Fig. 5.8 (d), the total PL intensity decreased quickly in the W4-VDR. The size-dependence reduction also confirms that the charge density is obtained by the number of atoms on the surface. For the W4-VDR and P8-VDR, the PL band amplitude reduces substantially, which indicates that a number of surface states precipitate much under small grain size in the 40nm-VDR and 20nm-VDRs, in which the emission characteristics of the nanosized materials are controlled by surface recombination. On the other hand, the population of the surface states would be decreased significantly in the W4-VDR and P8-VDR, leading to the rapid weakening of the corresponding radiative transition.

A comparison of the PL spectra of the W4-VDR, P8-VDR, 40nm-VDR, and 20nm-VDR in Fig. 5.8 illustrates that, despite having similar behavior, they vary on the red shift of the UV peak with decreasing grain size from the W4-VDR to the 20nm-VDR. The shift is proposed to be due to band bending. During excitation, charge carriers are generated and divided in space via the built-in electric field. The electrons are confined at the surface of the W4-VDR grains, whereas the holes accumulate at the center of the W4-VDR grains, neutralizing the ionized acceptor states, as illustrated in Fig. 5.9 (a). The accumulation of the photo excited charge carriers continues until a dynamic equilibrium is obtained. An electron near the surface recombines with a hole in the center, giving transition energy of E_{low} , as shown in Fig. 5.9 (a). The separation in space results in a weak transition possibility because of the small wave functions overlap of electrons and holes. When the intensity of luminescence is improved, as shown in Fig. 5.9 (b), more charge carriers are produced,

decreasing the band bending within the 20nm-VDR grains. As a findings, the energy of emission rises to E_{high} and the transition possibility is strengthens as the segregation in space diminishes.

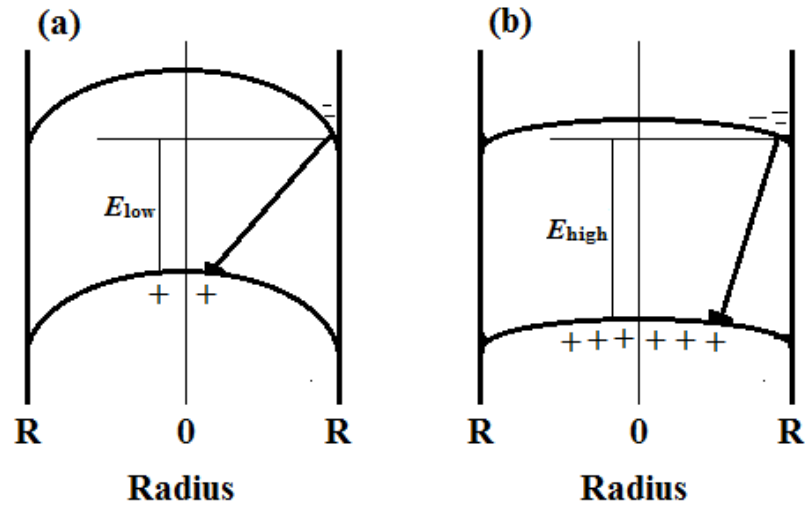


Figure 5.9. The impact of bandbending on the excitation. With weak luminescence intensity (a), the created charge carriers are divided in space, leading to low quantum efficiency. With higher luminescence intensity (b), the photoexcited charge carriers diminish the bandbending, leading to a higher PL energy as well as strengthens quantum efficiency.

The UV emission peaks are caused by the exciton luminescence from the conduction band to the valence band. As observed in Fig. 5.8, the UV luminescence for the varistors heat treated in O_2 atmosphere is the better. This result is proportionate with the observation in the XRD analysis. Heat treatment in O_2 atmosphere leads to the decrease in ZnO interstitials, which leads to the and reduce in nonradiative transition, thereby improving the quality of ZnO crystal [377]. The green emission peaks indicated at 2.34, 2.33, 2.32, and 2.30 eV for the W4-VDR, P8-VDR, 40nm-VDR, and 20nm-VDR, respectively, were caused by the defect level of O_{Zn} . The ZnO varistors fabricated at an elevated sintering temperature of 1200 °C have several intrinsic defects such as Zn vacancy (V_{Zn}), oxygen vacancy (V_O), interstitial zinc (Zn_i), antisite zinc (Zn_O), interstitial oxide (O_i), and antisite oxide (O_{Zn}).

Within the varistors thermal annealed at high temperature, the next reactions by oxygen evaporation may happen:



Consequently, the majority donors in the ZnO samples are the Zn_i and V_{O} . Hur et al. [378] reported that from the XPS spectra of ceramics heat treated in O_2 and N_2 atmospheres, the O/Zn ratio of the varistors annealed in N_2 atmosphere is higher than that of ZnO varistors annealed in O_2 atmosphere [379]. The concentration of oxygen associated with Zn–O bonding develops caused by the concentration of the O peak of the ZnO varistors annealed in N_2 ambient is in an O-rich condition. In this O-rich condition, the oxygen amount that diffuses into the varistor is significant, and the V_{O} concentration within the 40nm-VDR and 20nm-VDR decreases compared with the W4-VDR and P8-VDR. Moreover, O_{Zn} was easily produced from V_{Zn} and O_i because they have relatively low formation energy [380].



Subsequently, the concentration of O_{Zn} on the ZnO varistors annealed in N_2 atmosphere is higher than that on the ZnO varistors annealed in oxygen ambient. This phenomenon causes an rise in the PL spectra intensity for the W4-VDR, P8-VDR, 40nm-VDR, and 20nm-VDR by transformation from the conduction band to the O_{Zn} level. The W4-VDR annealed in N_2 ambient can produce nitrogen acceptor as low amount of nitrogen gas was injected in the bulk ZnO. When a pure N source is applied, N acceptors are significantly compensated by donor defects such as Zn_i , Zn_{O} , and V_{O} . The energy of formation for ZnO intrinsic defects on the O-rich condition was low on V_{Zn} , O_i , and O_{Zn} .

Thus, the O_{Zn} concentration increases when ZnO varistors have the N-compensation or O-rich condition.

The green emission of the 20nm-VDR annealed in N_2 ambient is high. The phonon included within the green band of the varistor is a longitudinal optical phonon with 0.072 eV energy, which matches the PL peaks energy separation on the significant energy side of the green band [381]. Fig. 5.10 (d) explains the typical process for the green luminescence peak in the PL spectra of the 20nm-VDR: the transition mechanism (1) from the near-conduction band edge to the deep acceptor level and (2) from the deep donor level to the valence band. The recombination of a shallowly trapped electron with a deeply trapped hole in a center leads to visible luminescence [382]. The difference in the highest green luminescence was investigated by preparing different ZnO varistors using a diversity of growth techniques. In certain cases, the existence of foreign elements have been suggested as the source of the green emission [383]. In addition, native defects have been proposed as potential sources. Investigators supposed that oxygen and Zn_i are the centers responsible for the green emission in ZnO [35, 381, 384, 385]. Earlier studies deduced that the green emission involves defect complexes and/or multiple defects, and the main part of the visible emission is created from localized defects at the surface of the nanoparticles [386]. In this work, the massive emission of green luminescence from the 20nm-VDR, compared with the 40nm-VDR, W4-VDR and P8-VDR, includes defect complexes and/or multiple defects, and the main part of the visible luminescence is produce from the defect centers at the ZnO nanoparticles surface. The transfer of the luminescence peaks with different treatment ambient is suggested to produce from the residual stress caused by lattice deformation. A reduction in the lattice constant c was noticed in the annealed samples, leading to a decrease in the band gap, as shown in Table 5.3.

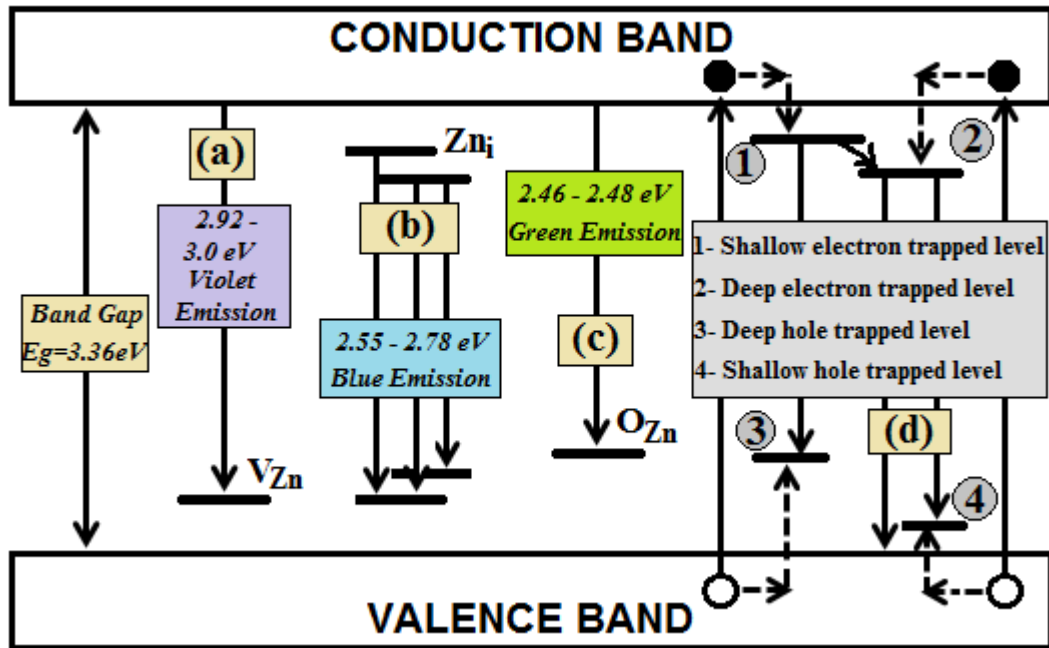


Figure 5.10. Schematic illustration of the energy band diagram proposed for ZnO nanoparticles.

The defect level transmission caused by O_{Zn} incremented, but the intensity of band edge emission was reduced when the ZnO varistors were annealed in N_2 ambient. This finding can be described by two mechanisms: first, the ZnO varistors annealed in oxygen atmosphere have an elevated donor concentration; second, the varistors annealed in N_2 ambient have a minimal donor concentration caused by donor defects were compensated with N-acceptors. Subsequently, the PL intensity of the W4-VDR, P8-VDR, 40nm-VDR and 20nm-VDR annealed in oxygen is high, which indicates that the quality of ZnO varistor crystal thermal treated in O_2 ambient is better compared with the other varistors annealed in different gases. Heat treatment in N_2 atmosphere is not the preferable procedure for the formation of a perfect structure. These results indicate that the structure of the varistor can be controlled to achieve the desired optical properties by varying the annealing conditions.

Table 5.3. Summarizes the PL and energy band gap of ZnO varistors at different annealing ambients.

Sample	Annealing ambient	Wavelength λ (nm)	Energy band-gap (eV)
W4-VDR	As-grown	368.38	3.37
	O ₂	372.65	3.33
	N ₂	370.44	3.35
P8-VDR	As-grown	367.10	3.38
	O ₂	371.38	3.34
	N ₂	369.32	3.36
40nm-VDR	As-grown	370.85	3.35
	O ₂	372.71	3.33
	N ₂	374.20	3.32
20nm-VDR	As-grown	372.64	3.33
	O ₂	373.97	3.32
	N ₂	375.22	3.30

A comparison of the PL spectra of the W4-VDR, P8-VDR, 40nm-VDR, and 20nm-VDR and W4-Disc, P8-Disc, 40nm-Disc, and 20nm-Disc shows that adding Bi₂O₃ and Mn₂O₃ to ZnO varistors leads to a remarkable rise in the visible luminescence intensity mostly in the 40nm-VDR, and 20nm-VDR samples. It also causes an obvious red shift of the asymmetric visible broadband. The UV emission peaks in the W4-VDR, P8-VDR, 40nm-VDR, and 20nm-VDR do not shift with Bi₂O₃ and Mn₂O₃, which suggests that the additives do not induce changes in energy gap. The asymmetric visible broadband indicates that two or more deep-level luminescence centers exist in the ZnO samples. The additives cause a migration of Bi₂O₃ and Mn₂O₃ atoms to the Zn vacancies. Therefore, the additives decrease the Zn vacancies such that the green band peak is suppressed in ZnO.

5.3.2 Raman spectroscopy

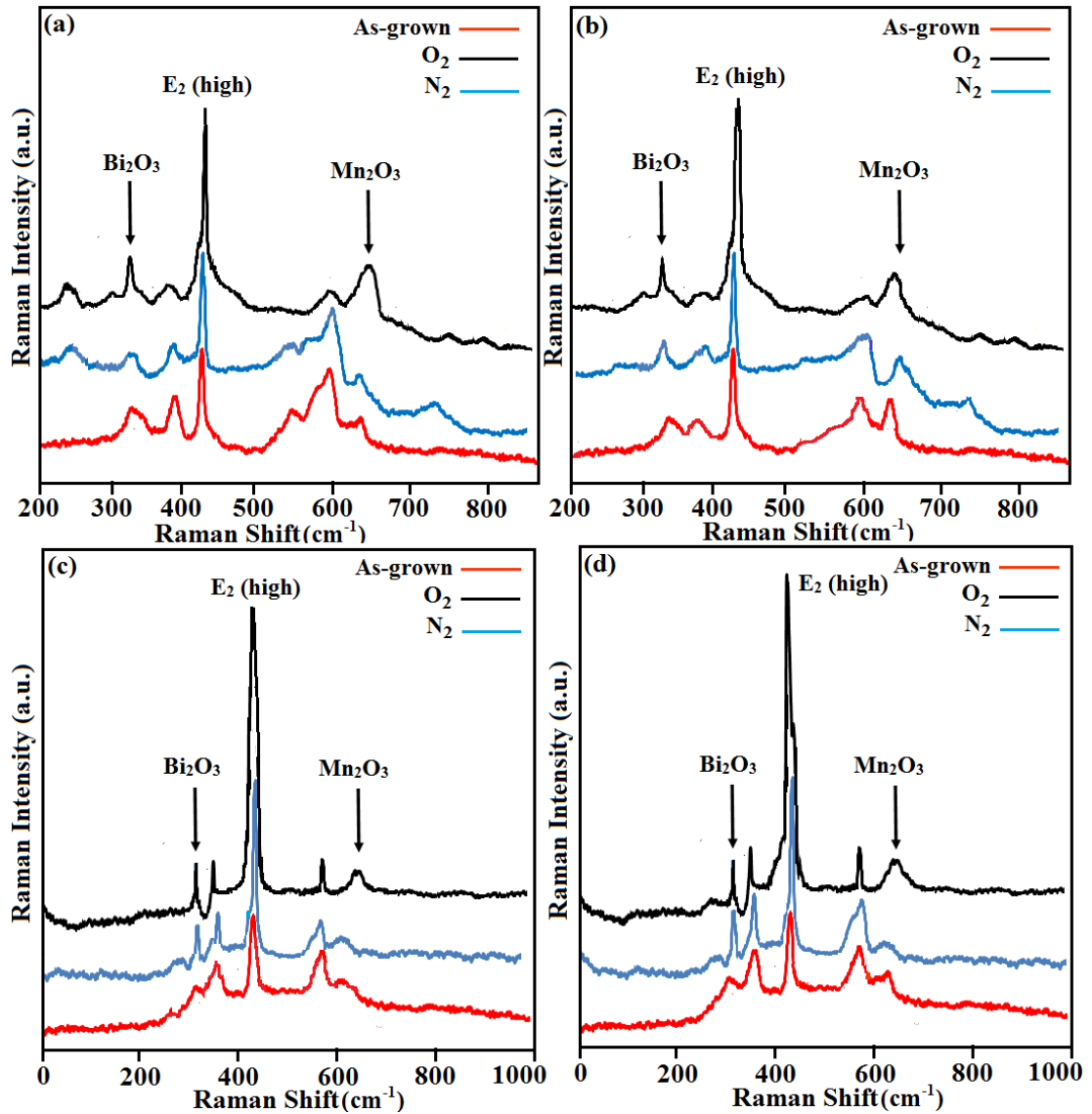


Figure 5.11. Raman spectra of ZnO-Bi₂O₃-Mn₂O₃ varistor system fabricated from from (a) White ZnO (W4), (b) Pharma ZnO (P8), (c) 40 nm ZnO, and (d) 20 nm ZnO at different annealing ambients.

The obtained Raman spectra of the W4-VDR, P8-VDR, 40nm-VDR, and 20nm-VDR systems at different annealing ambients are displayed in Fig. 5.11. A compilation of the presented frequencies of Raman active phonon modes in the W4-VDR, P8-VDR [387, 388] is reported in Table 5.4. In the spectrum of the W4-VDR (Fig. 5.11 (a)), the peak at 440 cm⁻¹ agrees with E₂ (high) phonon, the peak at 587 cm⁻¹ agrees with E₁(LO), and the peak at

385 cm^{-1} agrees with $A_1(\text{TO})$ phonons. In the spectrum of the 20nm-VDR, the LO phonon peak at 585 cm^{-1} has a frequency between those of $A_1(\text{LO})$ and $E_1(\text{LO})$ phonons, which is consistent with theoretical calculations. The broad peak at approximately 330 cm^{-1} observed in all spectra in Fig. 5.11 is caused by the second-order Raman processes.

The very large shift in the E_2 (high) mode position of the W4-VDR, P8-VDR, 40nm-VDR and 20nm-VDR compared with the W4-Disc, P8-Disc, 40nm-Disc and 20nm-Disc toward low wave numbers indicates that adding Bi_2O_3 and Mn_2O_3 strengthens the tensile stress within the samples, which is consistent with the XRD analysis. Furthermore, the aggregates of Bi_2O_3 at the ZnO–ZnO grain boundaries as Bi-rich phases through the sintering process in the ZnO– Bi_2O_3 – Mn_2O_3 system improved the grain growth and therefore strengthened the interfacial stress of the grains, which may be the major reason for the shift of the E_2 (high) mode in the Raman spectra, as mentioned previously. In addition, the substitution of Zn^{2+} within the lattice by Mn^{2+} or Mn^{4+} as the ZnO grains grow during the sintering process may lead to the distortion of the ZnO lattice, which therefore enhances the stress within the ZnO lattice. Thus, the distortion of the lattice due to the substitution of the dopant ions is supposed to be the main reason of the significant transfer of the E_2 (high) mode of the W4-VDR, P8-VDR, 40nm-VDR and 20nm-VDR.

The $A_1(\text{LO})$ Raman mode is critical to the variations in the free carrier concentration due to the polar semiconductor additive excitation of the free carrier react with the $A_1(\text{LO})$ longitudinal-optical phonons. In the GaN Raman research, the peak that corresponds to the A_1 (LO) mode shifts to high wave numbers, weakens, and broadens in intensity with rising carrier concentration [332]. Identical behaviors can be observed in the Raman spectra of the varistor for all types of ZnO powder. The addition of Bi_2O_3 and Mn_2O_3 to the ZnO discs increases the free carrier concentration within the varistor when the disc is doped with donors.

The bands of the secondary phases such as $\beta\text{-Bi}_2\text{O}_3$ and Mn_3O_4 were seen clearly in the Raman spectra. The situation of the $\beta\text{-Bi}_2\text{O}_3$ Raman peaks is at approximately 329 cm^{-1}

and that of Mn_3O_4 is at 566 cm^{-1} . Therefore, based on the Raman spectra, the E_2 phonon frequency and the $A_1(\text{LO})$ mode shift to low and high wave numbers, respectively, when the discs were doped with Bi_2O_3 and Mn_2O_3 , revealing that the tensile residual stress and the free carrier concentration were enhanced by doping.

The large stress induced the lattice deformation, which was attributed to the substitution of the doping ions such as Bi^{3+} and Mn^{2+} or Mn^{4+} for Zn^{2+} , and the interfacial phases and lattice mismatch among ZnO crystals.

As mentioned in the previous section, the peak at 430 cm^{-1} forms from the E_2 mode of ZnO related to the wurtzite structure, and the 570 cm^{-1} peak is a contribution of the $E_1(\text{LO})$ mode of ZnO related to oxygen insufficiency [328, 336]. Based on these facts, the impact of different treatment ambient on the Raman spectra of the ZnO varistor fabricated from various sizes of ZnO powder can be explained. Fig. 5.11 shows that the peak at 437 cm^{-1} was the most dominant during annealing in O_2 ambient, whereas the peak intensities at the E_2 (high) mode were extremely weak during annealing in N_2 ambient. The 587 cm^{-1} Raman peak, as mentioned above, was interpreted by certain investigators to be the LO phonon of E_1 or LO phonon of A_1 [325, 337-339]. Several researchers also assumed that this Raman peak is caused by Z_i , V_o , or their combination because of its robust dependence on the oxygen stoichiometry [328, 338, 339].

Table 5.4 summarize the results of Raman active modes at different annealing atmospheres of the W4-VDR, P8-VDR, 40nm-VDR and 20nm-VDR in comparison with the theoretical results. All peaks values are in cm^{-1} .

Table 5.4. A comparison of the Raman active modes of the ZnO-Bi₂O₃-Mn₂O₃ varistor fabricated from micro and nano ZnO powder with the theoretical results at the different annealing ambients.

Symmetry	Bulk	W4-VDR			P8-VDR			40nm-VDR			20nm-VDR		
		As-grown	O ₂	N ₂	As-grown	O ₂	N ₂	As-grown	O ₂	N ₂	As-grown	O ₂	N ₂
2TA(M)	200	ND	224	230	ND	ND	265	ND	ND	ND	ND	ND	ND
A ₁ (TO)	380	385	376	383	382	373	377	386	381	384	387	383	385
E ₂ (high)	444	440	443	439	442	445	444	435	438	436	434	430	436
E _{2H} +E _{2L}	540	547	ND	542	ND	ND	ND	ND	ND	ND	ND	ND	ND
E ₁ (LO)	583	587	585	583	586	588	589	583	585	580	585	587	580

*ND: below the detection limit.

5.4 Main annealing and ZnO size effects on the electrical properties of composite ZnO varistors and proposed mechanism of nonlinear behaviors

ZnO-Bi₂O₃-Mn₂O₃ varistors are semiconductor ceramics with superior nonlinear electrical behaviors that are produced from their grain boundaries and based on their microstructure properties. Theoretically, fine primary particles (20 and 40nm) with a narrow size distribution have good electrical characteristics. Therefore, these properties are correlated with the morphology and size of ZnO grains. In the present work, zinc oxide micro- and nanoparticles were used to make varistors, and the impact of the ZnO particle size on the electrical behaviors of ZnO-Bi₂O₃-Mn₂O₃ varistors was achieved. The findings displayed that when 40nm-ZnO and 20nm-ZnO were used instead of W4-ZnO and P8-ZnO for the fabrication of varistors, the electrical behaviors such as the nonlinear coefficient and breakdown voltage decrease dramatically. The varistors are induced from semiconducting ceramics such as ZnO and other metal oxides such as Bi₂O₃ and Mn₂O₃. The addition of various additives as well as the different annealing conditions in oxidizing and reducing ambients were established to affect the microstructure and electrical behaviors of varistors. The resistance and breakdown voltage of these varistors depend greatly on the microstructural conditions and thus, grain size and microstructural homogeneity are the most significant parameters in ZnO varistor production. One way to achieve these purposes is by applying homogeneous zinc oxide nanoparticles for varistor manufacturing. Homogeneous

ZnO powder is essential for making high-performance ZnO varistors because it increases the microstructure homogeneity that is necessary for the improvement of the electronic and electrical properties of these ceramics. Several researchers have studied the impacts of microstructure and processing on the electrical conduction in varistors [205, 389-391]. Therefore, exact control of the microstructure of varistor is required to achieve the values necessary for the nonlinearity and breakdown voltage. Nano-scale particles have various physical and chemical characteristics compared with the bulk materials. High homogeneity, good sinterability, and several uncommon behaviors may be anticipated due to their nano-sized crystallites, significant surface areas, and many surface characteristics. Subsequently, the varistors with ZnO nanoparticles should have drastically improved electrical properties, as shown in the present results.

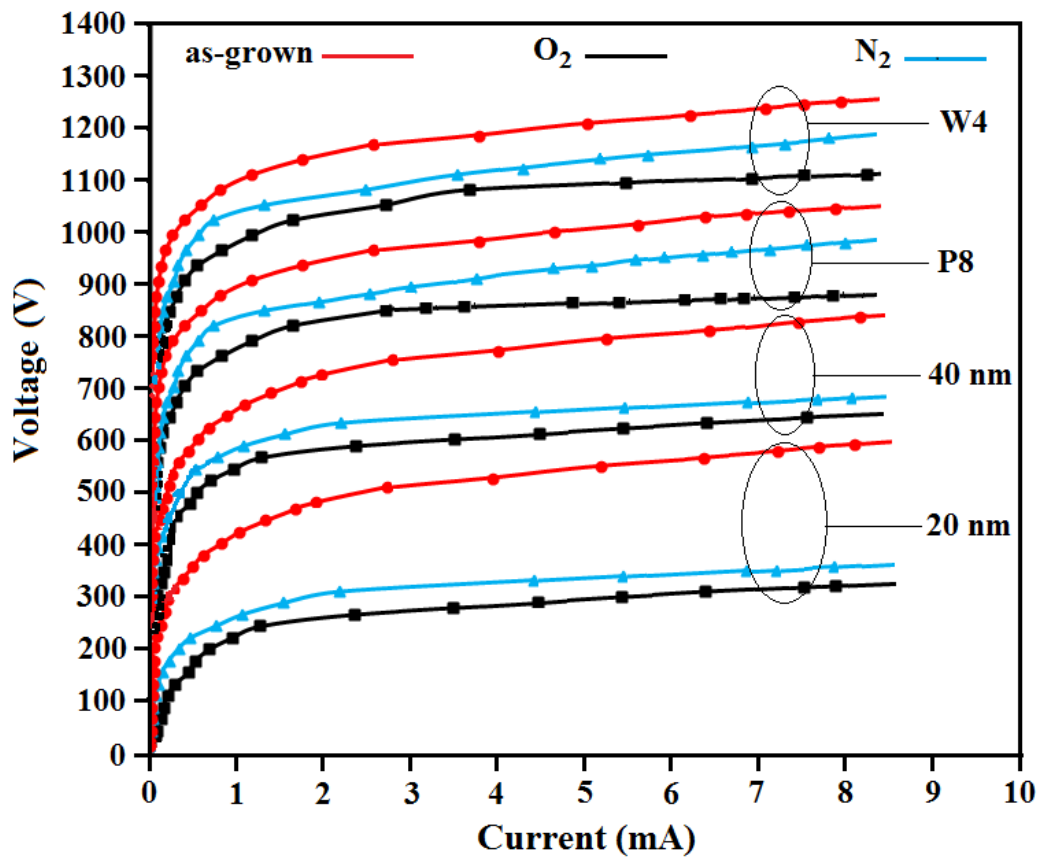


Figure 5.12. Current-Voltage characteristic of ZnO-Bi₂O₃-Mn₂O₃ varistor system fabricated from different size of ZnO powders at different annealing ambients.

The I–V curve of the as-grown W4-VDR, P8-VDR, 40nm-VDR and 20nm-VDR annealed at different ambients are plotted in Fig. 5.12. The breakdown voltage, resistivity, and nonlinear coefficient of the samples were calculated and are summarized in Table 5.5. The breakdown voltage for the 40nm-VDR and 20nm-VDR decreased dramatically compared with the W4-VDR and P8-VDR by decreasing the ZnO particle size from micro to nano size. The grain size within the 40nm-VDR and 20nm-VDR increased dramatically after the sintering process, which may be due to the significant ZnO nanoparticles surface area, which led to the reduction of the breakdown voltage.

By reducing the powder size from W4-ZnO to 20nm-ZnO, the sintering process would be completed fast and at a low temperature, and a large grain size with high density would be achieved. Moreover, the porosity of the 20nm-VDR decreased because of a complete sintering process and porosity isolation. Furthermore, the hardness of the 40nm-VDR and 20nm-VDR was improved more than that of the W4-VDR and P8-VDR. With the goal of manufacturing low-breakdown voltage (varistor voltage) varistors, the effect of adding Bi_2O_3 to the varistors on the size of grains was investigated. Studies have reported that adding Bi_2O_3 to ZnO enhances growth of grain and allows the grains to be large and therefore reduce the breakdown voltage in the varistor. The I–V nonlinear behavior of the ZnO disc is a phenomenon of the boundaries among semiconducting ZnO grains. The varistors' breakdown voltage is proportional to the quantities of boundaries between the grains per unit of thickness and therefore to the inverse of the grain size. The ZnO varistor fraction voltage can be controlled by the varistor thickness between two electrodes, whereas the fraction voltage increases with the thickness of the varistor.

Table 5.5. Summarizes the electrical properties of W4-VDR, P8-VDR, 40nm-VDR and 20nm-VDR at as-grown and different annealing ambients.

Sample	Annealing ambient	V_b (V)	I_b (mA)	α	ρ (k Ω .cm)
W4-VDR	As-grown	1100	0.47	17.2	3348.8
	O ₂	990	0.56	16.3	6426.3
	N ₂	1026	0.60	14.2	5520.1
P8-VDR	As-grown	908	0.46	13.1	3112.4
	O ₂	795	0.66	13.5	5216.3
	N ₂	820	0.50	11.8	5021.5
40nm-VDR	As-grown	697	0.72	11.1	2997.6
	O ₂	561	0.51	10.3	4285.5
	N ₂	603	0.64	9.6	3375.2
20nm-VDR	As-grown	426	0.52	9.1	1724.1
	O ₂	218	0.57	8.8	3887.4
	N ₂	264	0.36	8.5	2904.8

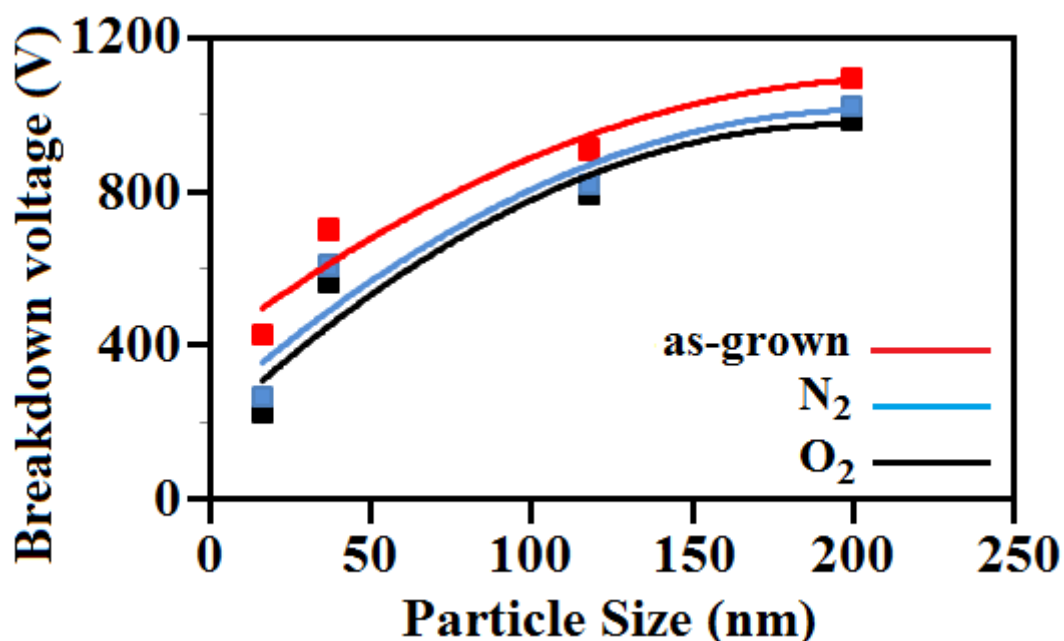


Figure 5.13. Plot of breakdown voltage of as-grown and annealed ZnO samples as a function of different particle sizes.

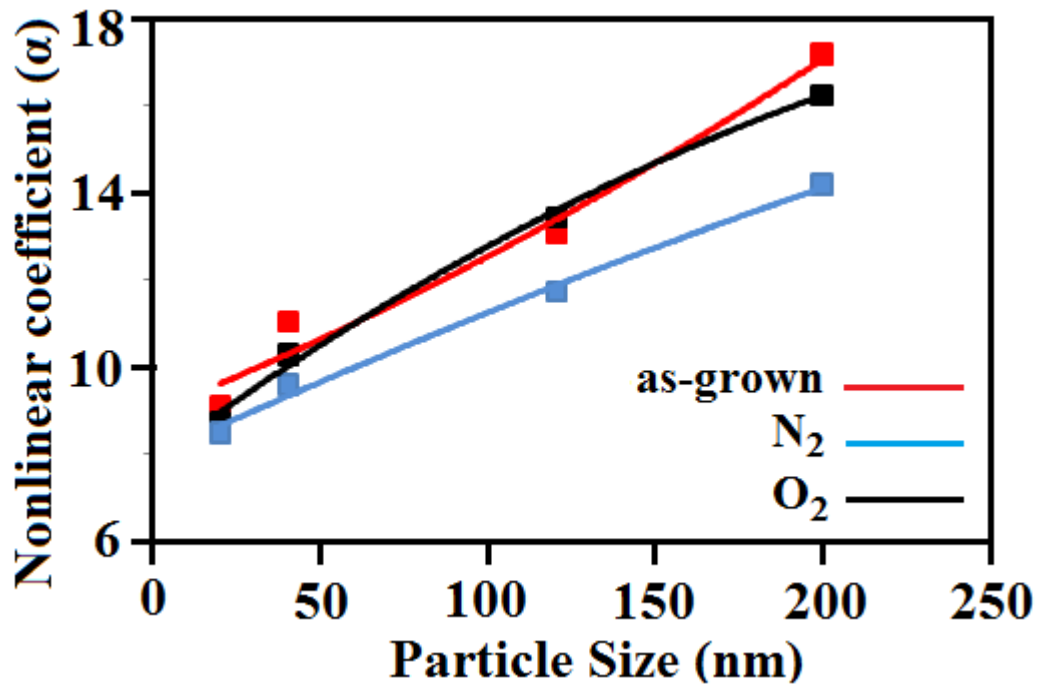


Figure 5.14. Plot of nonlinear coefficient α of as-grown and annealed ZnO samples as a function of different particle sizes.

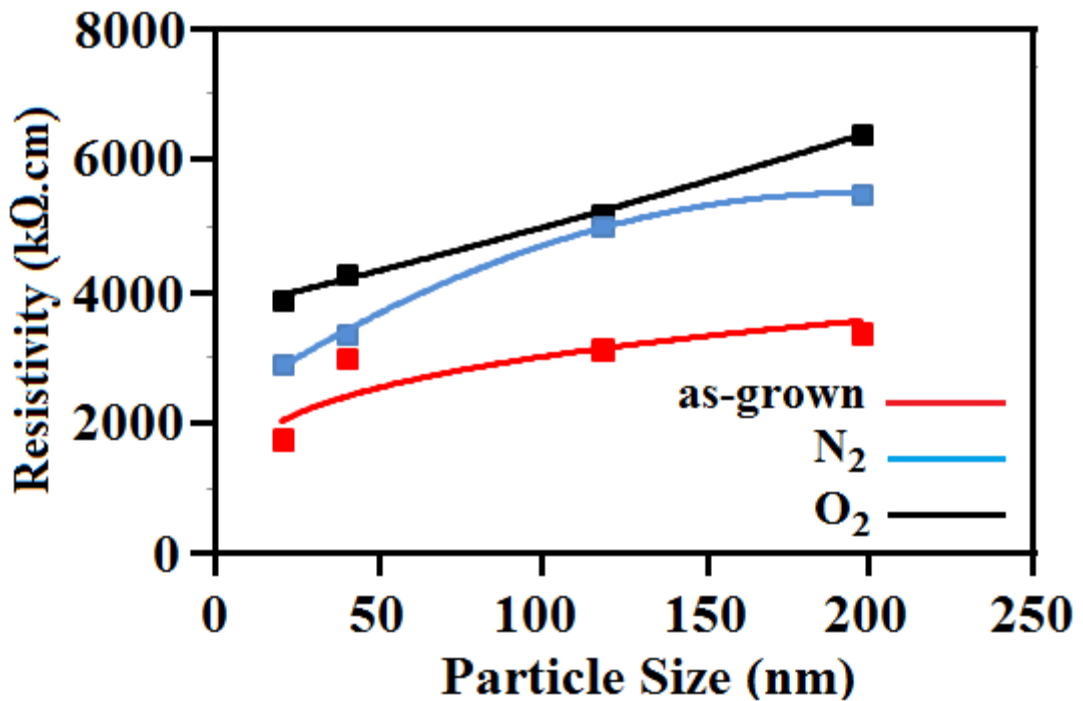


Figure 5.15. Plot of resistivity of as-grown and annealed ZnO samples as a function of different particle sizes.

On the contrary, the decrease in the nonlinear coefficient of the 40nm-VDR and 20nm-VDR compared with the W4-VDR and P8-VDR shown in Fig. 5.14 may be related to the reduction in the porosity in the varistors. Therefore, the maximum nonlinear coefficient (α) is obtained when the donor density at the boundary among the grains reaches the minimum and when the boundary potential barrier is the highest. The variation of α against ZnO particle size is depicted in Fig. 5.14, which shows that α is enhanced when the particle size increases from 20nm-ZnO to W4-ZnO. This result suggests that the quantities of boundaries is reduced because of the grain enlargement of the 20nm-ZnO after the sintering process. This enlargement is caused by the very large S/V ratio of nanoparticles, which eventually drops the highest potential barriers. A drop in the α value for the 20nm-VDR was observed compared with the 40nm-VDR, W4-VDR, and P8-VDR.

The symmetric nonlinear I–V response with different nonlinear coefficient values in the W4-VDR, P8-VDR, 40nm-VDR, and 20nm-VDR is caused by the electrical potential barriers created through the processing stages that involve thin insulating layers surround the consecutive grains [392]. These layers around the successive ZnO grains result in back-to-back electrical barriers that involve two close grains with one side as reverse bias (say right-side ZnO grain) and the another side as forward bias (say left-side ZnO grain). The existence of back-to-back electrical barriers is caused physically by the boundaries between grains. The depletion layer in the varistor expands to the grains across the ZnO grain boundaries. The mechanism responsible for the electrical barrier generation within the varistor can be explained as follows: at zero bias, the electrical barrier among the grains consistent with a finite depletion region contributed by the reverse ZnO grain and the forward ZnO grain. Given that the ZnO grain is an n-type semiconductor, considerable electron traps are created among the consecutive grains in the disordered grain boundary surfaces. The migration of electrons from the grains composes the negative grain boundary surface layers between two depletion regions. These empty electron traps generate the positive space charge regions (depletion regions), as shown in Fig. 5.16 (a) and (b). At zero bias, the right-side depletion

region width is assumed to be similar to the left-side depletion region width. During the applied bias (voltage), the forward part band bending diminishes the depletion region contribution, whereas the reverse part band bending promotes the depletion region contribution (Fig. 5.16 (c)). This drop in the forward-side depletion contribution changes with increment applied voltage till the ohmic bias range is obtained, in which the possibility drop in the forward side is equivalent to that in the reverse side. This condition keep the depletion region steady by enhancing the reverse depletion side and shrinking the forward depletion side evenly. As the voltage exceeds the ohmic range and enters the nonlinear range (breakdown region), the forward region pins and the reverse region continues to absorb the applied voltage and remains bending the band [92, 393]. This process increases the depletion region on the reverse side.

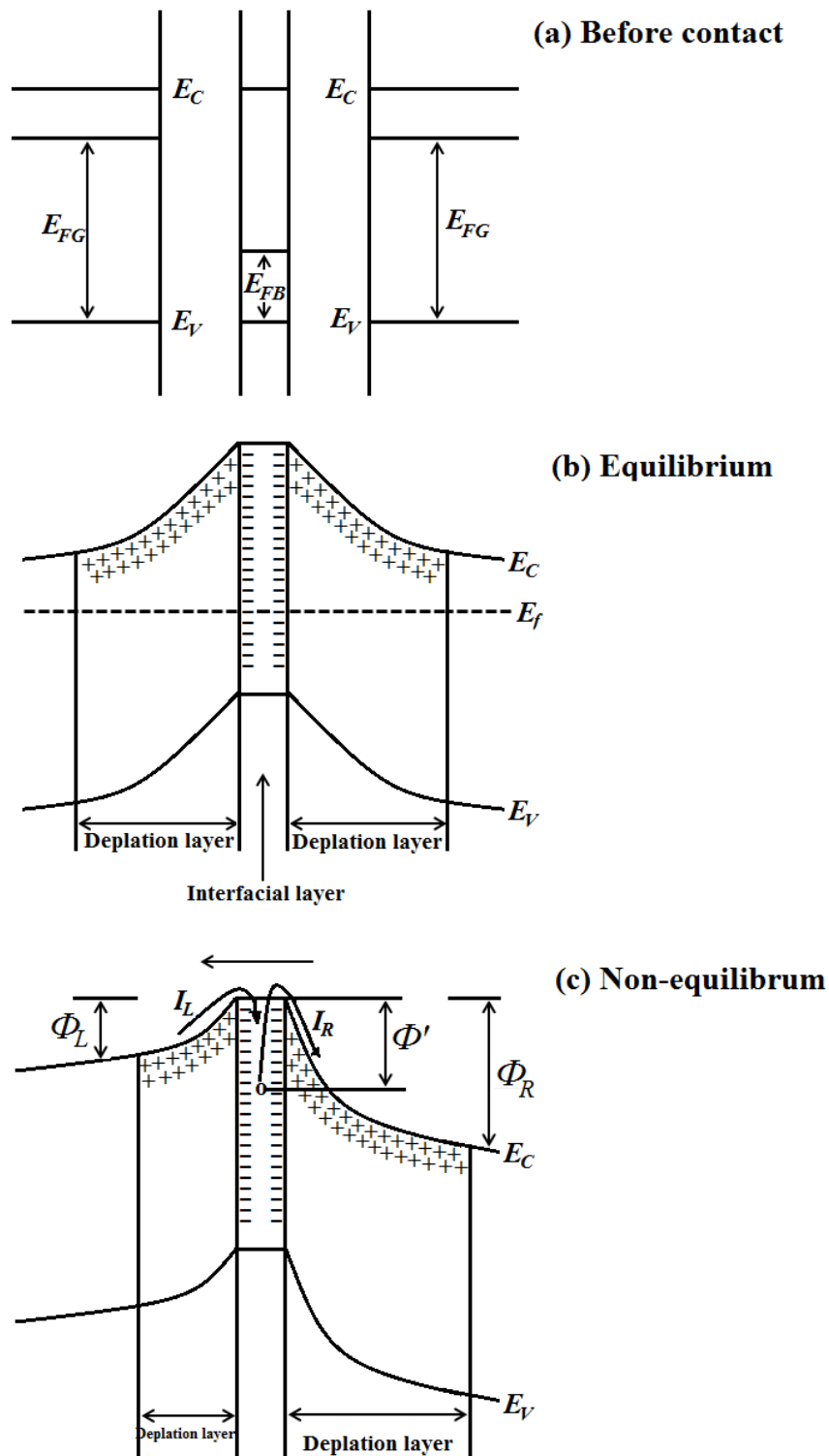


Figure 5.16. Band diagram of the double (back-to-back) Schottky barrier across ZnO grain boundaries (a) before contact, (b) at equilibrium state, and (c) at non-equilibrium conditions.

With regard to the oxide additives to the varistor such as Bi_2O_3 and Mn_2O_3 , the dominant defect states combined with the oxide dopants within the grains and grain boundaries form the depletion region in the close ZnO grains across the grain boundaries in the W4-VDR, P8-VDR, 40nm-VDR, and 20nm-VDR samples. These integrated depletion regions that consist of defect states at the boundary interfaces (surface of grains) eventually dictate the nonlinear coefficient (α), height of back-to-back barrier, capacitance, leakage resistance (ohmic range), and stability and/or degradation with the environment. Moreover, the height of back-to-back barrier is additionally based on the band bending amount within both sides of the connected ZnO grains caused by the concentration of defect within each ZnO grain.

A comparison of the α values of the W4-VDR, P8-VDR, 40nm-VDR, and 20nm-VDR and the W4-Disc, P8-Disc, 40nm-Disc, and 20nm-Disc shows that the value of α is increased when Bi_2O_3 and Mn_2O_3 are added to the disc. This result suggests that the aggregation of Bi in the grain boundary promoted the development of essential potential barrier at the interface [216]. Adversely, excessive Mn_2O_3 additive encouraged spinel formation (ZnMnO_3 and ZnMn_3O_7) that could lead to poor nonlinearity and high bulk resistance [394]. The reduction in the number of grain boundary per unit thickness caused by grain enlargement may have caused a drop in the α value, which is attributed to the reduction of essential potential barrier at the interface. Hence, the α value improves with increasing sintering temperature and time. During heating, the solubility of Mn ions was increased because of Mn^{2+} reduction to Mn^{3+} or Mn^{4+} with low ionic radii [395]. As a result, more Mn ions aggregated in the grain boundary and improved the nonlinearity characteristics.

Numerous studies on the effect of additives such as Bi_2O_3 and Co_3O_4 of ZnO varistors show that transition metal oxides can develop the non-ohmic behaviors of varistors via rise the surface state density through the generation of interstitial states and deep bulk traps. Many researchers have investigated ZnO ceramics doped with a reasonably large

amount of Mn_2O_3 , and most of the research have been consecrated to the nonlinear electrical behaviors that are correlated with the double Schottky barrier at the grain boundary [396].

The nonlinear electrical behavior of varistors is associated with the grain boundary phenomenon. Gupta and Carlson improved a grain boundary defect model for varistors. From a similarity to the model, the nonlinear property of Bi_2O_3 - and Mn_2O_3 -added ceramics can be explained. Fig. 5.17 displays the grain boundary defect model for the Bi_2O_3 - and Mn_2O_3 -added ceramics. Mn^{4+} has an ionic radius very adjacent to that of Zn^{4+} and a valence superior than Zn^{4+} ; hence, it readily solves into the ZnO lattice and forms the defects. The creation of electrons causes the Mn^{4+} to decrease the ZnO grains resistivity. At the same time, Bi^{3+} produces the defects and prefers to aggregate at the ZnO grain boundary. Therefore, both intrinsic ZnO defects (Zn_i^{2+} , $\text{V}_{\text{Zn}}^{2-}$, V_0^{2+}) and extrinsic defects (Mn_{Zn}^+ , $\text{Bi}_{\text{Zn}}^{2+}$) established at the ZnO grain boundaries. As shown in Fig. 5.17, the positive charges (Zn_i^{2+} , V_0^{2+} , Mn_{Zn}^+) are existing on both sides of the grain boundary, and the negative charges of a depletion layer is generated at the grain boundary. As a result, a voltage barrier to the transfer of the major charge carriers (electrons) is produced and caused the nonlinear electrical property of the W4-VDR, P8-VDR, 40nm-VDR, and 20nmVDR.

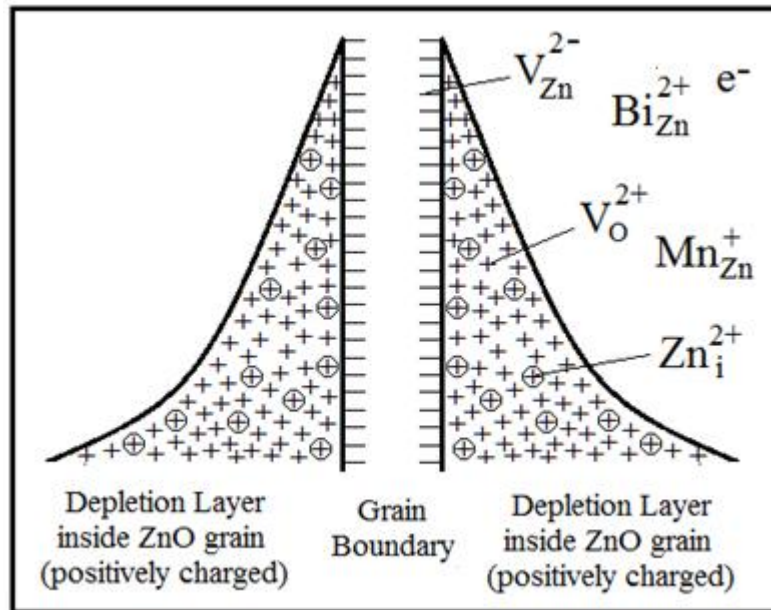


Figure 5.17. The grain boundary defect model for the (Bi₂O₃, Mn₂O₃)-composite ZnO varistors.

This study determined that the electrical behaviors of the 40nm-VDR and 20nm-VDR were superior to that of the W4-VDR and P8-VDR. The microstructure homogeneity performs a significant function in investigating the electrical characteristics of varistors, and the variations in the electrical behaviors of the different varistors (fabricated from micron and nano powders) are attributed to the difference in the defects and homogeneity in the microstructure. The microstructure homogeneity can influence the grain boundary characteristics, which dominate the electrical behaviors of the varistor samples.

Significant change in the resistivity (ρ) was also observed at the high-resistivity region, whereby the ρ for the W4-VDR dropped more than three times for the 20nm-VDR, as observed in Table 5.5. The significant drop in the resistivity can be caused by the reduction of the potential barrier between the ZnO grains that results from the very high grain growth in the ZnO nanoparticles after the sintering process, thereby leading to the decrease in the quantities of the grain boundaries and reducing the highest of the potential barrier.

Understanding the effect of atmosphere treatment on the electrical behaviors of the W4-VDR, P8-VDR, 40nm-VDR, and 20nm-VDR is also essential. The impact exerted by the ambient annealing at 700 °C on the breakdown voltage, resistivity, and nonlinearity values is considerable, as can be observed in Table 5.5. The table provides the various electrical parameter values for the W4-VDR, P8-VDR, 40nm-VDR, and 20nm-VDR sintered at 1200 °C and then annealed in an O₂-rich or N₂-rich ambient. The varistor behavior may be elucidated by the production of defects within the crystal lattice because they are responsible for the generation of the Schottky-type potential barrier at the boundary region. The dopant oxides form an electron-poor layer next to the boundary region, from which the potential barrier related to a double-charge density originates.

Annealing in the N₂-rich ambient reduces the nonlinear behaviors of this system. However, thermal annealing in the O₂-rich atmosphere significantly improved the non-ohmic value. The different behaviors of the varistors at various annealing atmospheres are attributed to the potential barrier generation and to the O₂ species at the ZnO grain boundary that form Schottky-like barrier and trapping states. This improvement in the nonlinear properties of the varistors is supposed to be related to the oxidation degree (during the varistor is annealed in an O₂ ambient) or lowering (During the varistor is annealed in an N₂ ambient) of the metal oxide additives precipitated at the boundary. Subsequently, the function of Bi₂O₃ is to produce the grain region with oxygen and improve the nonlinearity of the varistor, given that the barrier properties can be influenced by oxygen species at the boundary among the grains because of the chemical alteration within the ZnO grain boundary region. Similar results for varistors annealed in oxidizing and reducing ambients have previously been pointed out by Sonder et al. for the W4-VDR and P8-VDR. M. R Santos et al. [397] reported that the electrical behaviors of 40nm-VDR and 20nm-VDR are strongly affected by the atmosphere because of the oxidizing mechanism at the ZnO grain boundary. P. R. Bueno et al. [216] showed that heat annealing in an N₂-rich ambient leads to decreases fundamentally in the surface states (N_{IS}) of the double (back-to-back) Schottky

barrier and in the height of potential barrier values. However, heat annealing in an O₂-rich ambient leads to a considerable increment in the (N_d) and essentially in the (N_{IS}) states in the thin region of the boundary among the grains [398]. Many approaches suggest that thermal annealing fundamentally changes the electronic states of the boundary region. Thus, the interfacial states source is not a substantial impact due to the lattice mismatch at the grain boundary but an extrinsic one obtained from the metal atoms that precipitated at the ZnO grain boundaries [398, 399].

In parts of the suggested mechanism for the potential barrier generation, the transition metal such as Bi or Mn aggregated at the boundary becomes oxidized when annealed in an O₂ ambient, and the interfacial layer becomes rich in oxygen species that are the trapped electrons (enhancing the N_{IS}) [398]. The oxygen that induces the oxidation of the aggregates and keeps the electrostatic equilibrium of the interface results from the atmosphere and the bulk and raises the donor concentration N_d when it forms from the bulk. Thus, the density of trap state at the interface N_{IS} should rise when the grain boundary interface of the ZnO is oxidized, increasing the potential barrier values. On the contrary, thermal annealing in the N₂ atmosphere should exert the opposite effect. This act occurs to promote the suggested model for the potential barrier generation shown in Fig. 5.18. The potential barriers have a Schottky-like nature attributed to negative interfacial states, the same nature that often appears in most varistors at high temperatures [400]. With the grain boundary formation, thermal annealing under a reducing atmosphere (N₂) expels excess oxygen and keeps the metal atoms, thereby reducing the nonlinear electrical behaviors of the varistor.

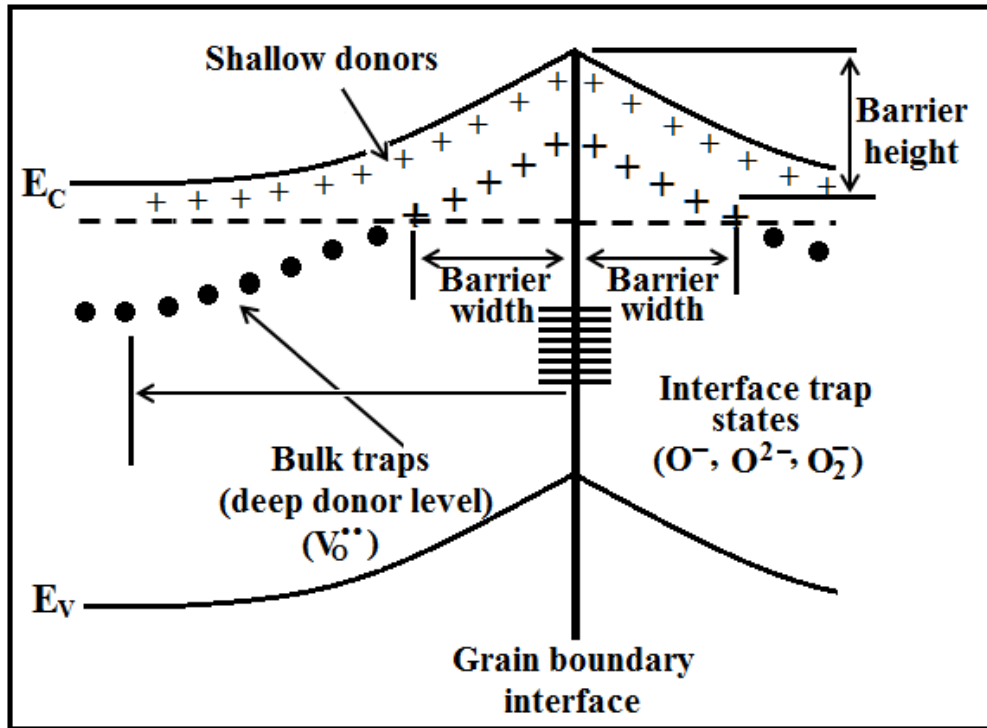


Figure 5.18. Electronic and atomic defect model suggested for the potential barrier formation in ZnO-Bi₂O₃-Mn₂O₃ varistors.

The barrier voltage and the nonlinear coefficient increase and breakdown voltage decreases when the varistors are annealed in oxygen atmosphere (Table 5.5). These results prove that the electrical behaviors of the varistors are sensitive to the oxygen species that exist on the boundary region. The thermal annealing in an oxygen ambient is beneficial in the manufacturing process to prolong the varistor life. In addition, the results re-establish the electrical behavior of deteriorated varistors attributed to the adsorption of oxygen species at the boundary regions after annealing in oxygen ambient.

The oxygen within the boundary region is necessary for the properties of various varistor ceramics such as ZnO, SnO₂, and SrTiO₃. However, when the diffusion rates of oxygen are completely different in these materials, the oxygen distribution and therefore the potential barrier distribution vary. In terms of the nonlinear coefficient of the W4-VDR, P8-VDR, 40nm-VDR, and 20nm-VDR, the addition of Bi₂O₃ promotes oxygen diffusion because it is a perfect grain boundary activator that is comparable with the W4-Disc, P8-

Disc, 40nm-Disc, and 20nm-Disc. Moreover, the Bi-rich phase is continuous and interconnected along the three-and four-ZnO grain functions throughout the microstructure of varistor. The interpretation and distribution status of Bi_2O_3 are critical for the oxygen transfer into the substance through the heat treatment process. Therefore, no surface effect was observed in the 40nm-VDR and 20nm-VDR.

The adsorbed molecules, especially oxygen, on the surface of oxide have been suggested to generate an electron-depleted space-charge layer in the inner surface region of the particles and on the surface of several anionic species, such as O^- , O^{2-} , or O_2^- . This type of charge polarization causes the potential barrier among adjacent grains (40nm-VDR and 20nm-VDR), whose width and height are functions of the nature and concentration of the anionic oxygen species, influence the nonlinear coefficient and breakdown voltage [359, 374, 380, 401]. Thus, investigations into the oxides' nonlinear behavior should consider the environmental impacts. The structural and electronic characteristics of varistor can be accurately dominated by methodically managing the factors that control the basic characteristics of the potential barriers among close grains within the varistor.

Carlson and Gupta [402], as well as Pike [165] and Leite [403], researched on the establish of this potential barrier in a try to expound the mechanisms responsible for the electrical behaviors in varistor. Pianaro et al. [404] suggested a model of the establish of the potential barrier within varistors. In most of the suggested models, an excessively defect-rich region distinguishes the potential barrier. The existence of these defects considerably alters the band gap energy, causing the grain boundary to possess a Fermi (potential) level dissimilar to the one presented by the ZnO grains; therefore, the electronic state density varies from that of the grains. The oxygen vacancies and electronic defects on the ZnO surface are correlated and have been exhaustively researched [405]. Oxygen has a significant role in the ZnO varistor grain boundaries, indicating that the grain boundary chemistry indicates the electrical nature of the varistor. A bismuth layer within the ZnO– Bi_2O_3 – Mn_2O_3 -varistors is required to produce potential barriers at the grain boundaries, and the height of

these potential barriers is strongly dependent on the surplus oxygen at the interface among the grains [365]. Identical findings have been achieved for different varistors, suggesting that the amount of oxygen at the interfaces of the grains determines the potential barrier formation.

5.5 Summary

In conclusion, the 40nm-VDR and 20nm-VDR annealed in oxygen atmosphere exhibited a very high performance and good quality with superior electrical behaviors compared with other varistors treated in other conditions. These 40nm-VDR and 20nm-VDR have higher surface-to-volume ratio in the grains than the W4-VDR and P8-VDR; thus, the grain boundary oxidation is conceivable when the varistors are slightly cooled down, and annealing at high-pressure oxygen ambient is not necessary. Furthermore, the dopants within the ZnO varistor structure can contribute to the ZnO grain boundary oxidation process as discussed by Einzinger [406]. In this case, Mn atoms tend to accumulate within the grain boundaries, leading to the migration of donors from the bulk to the grain boundaries to be annihilated during cooling.

The varistor behavior of the W4-VDR, P8-VDR, 40nm-VDR, and 20nm-VDR results from the diffusion of oxygen along the boundaries among grains. In this condition, the amount of intrinsic acceptors (zinc vacancies) could be higher than that of the intrinsic donors, and the electrical potential barrier is formed. Thus, the grain boundary oxidation guarantees the varistor behavior. Einzinger [363] confirmed that nonlinear I–V characteristics can be observed in the W4-Disc, P8-Disc, 40nm-Disc, and 20nm-Disc, indicating that the sintering procedure can be performed in a high-pressure oxygen ambient. This proposition agrees with the results obtained by Mantas et al. [407].

The level transition of defect caused by O_{Zn} incremented but the emission intensity of band edge was reduced when ZnO varistors were annealed in N_2 ambient. This finding can be described by two mechanisms: first, ZnO varistors annealed in oxygen atmosphere

have a high donor concentration; second, ZnO ceramics annealed in N₂ ambient have a low donor concentration due to the donor defects were compensated with N-acceptors. Subsequently, the intensity of PL of the ZnO varistors treated in oxygen is superior than that treated in nitrogen ambient, revealing that the quality of ZnO varistor crystal heat treated in O₂ ambient is the best compared with other differently annealed varistors. Thermal treatment in N₂ atmosphere is not the preferable procedure for the formation of a perfect structure. These results indicate that the structure of the varistor can be controlled to achieve the required optical characteristics by varying the heat treatment atmospheres.

CHAPTER 6: RESULTS AND DISCUSSION 3

POTENTIAL APPLICATIONS OF PURE AND COMPOSITE (VARISTOR) ZnO DISCS FABRICATED FROM ZnO MICRO- AND NANOPARTICLE POWDERS IN BIOMEDICAL FIELD

6.1 Introduction

Biomaterials refer to both naturalistic or man-made materials that are purposed to interface with biological systems or biomedical devices for evaluating, treating, augmenting, or replacing any tissue, organ, or the body function [408]. Biomaterial elements encompass medicine, biology, chemistry, tissue engineering, and material science. Biocompatibility and bioactivity are the essential properties that qualify any material as a biomaterial [409].

Biocompatibility is the material capability to accomplish with a suitable host response in a particular application, such as development of insights into how biomaterials interact with the human body and eventually how those interactions determine the clinical success of a medical device (such as pacemaker, hip replacement or stent). From the clinical perspective, these materials should not create toxic or injurious reactions and not cause immunological rejection. Bioactivity indicates to the a material ability to mineralize in a physiological environment. In orthopedic application, bioactivity refers to the ability of a material to induce the formation of an apatite layer [410].

Several classes of materials such as ceramics, metals, glass, and natural and synthetic polymeric materials have been investigated as biomaterials for medical use, especially in tissue engineering and orthopedic implementation [411]. However, several of these materials have obstacles and limitations. For example, metallic implants applied in bone repair can cause bone resorption and stress shielding due to its elasticity mismatch with the surrounding bone. Meantime, a varistor material is not favorable as a bone repair material because of its substandard resistance against fatigue insufficiency and weak fracture toughness. Even though the elasticity coefficient of minimal rigid titanium is five times

bigger than that of the human bone, it still has restrictions for comprehensive usage in bone reconstruction [412, 413].

In this chapter, cytotoxicity studies on the W4-Disc, P8-Disc, 40nm-Disc and on 20nm-Disc, and W4-VDR, P8-VDR, 40nm-VDR and 20nm-VDR as well as their effects on animal cells (L929) were successfully demonstrated, and these effects were associated with the particle size of the grains and the additives in the samples.

6.2 Key factors of toxicity effects

The 40nm-ZnO and 20nm-ZnO are highly cytotoxic at low concentrations and have very high abilities to adsorb oxygen compared with W4-ZnO and P8-ZnO [413], which may relate to their cytotoxicity. Brunner et al. [414] indicated that most cells of human or rodent die after subject to silica nanoparticles at concentrations more than 15 ppm. Sharma [223] found that the ZnO nanoparticle-produced cytotoxicity effects are dependent on time and concentration. Another destructions are produced by oxidative stress, which can be determined by improved level of hydroperoxide, exhausted level of glutathione, and decreased activity of catalase, all of these factors can lead to death of cell. Toxicity research in *Caenorhabditis elegans* indicated that ZnO nanoparticles have ability to prevent cell growth and generative ability. ZnO nanoparticles can produce cytotoxicity effects via enhancing the oxidative stress within the cell line L929 [236]; findings showed that 20nm-ZnO induced a dose- and time-dependent reduction of number of cells compared with W4-ZnO, P8-ZnO and 40nm-ZnO. ZnO nanoparticles increase the hydrogen peroxide levels (H_2O_2) and hydroxyl radicals ($\cdot OH$), reduced the molecular oxygen and glutathione levels, and decrease the release of interleukin-8 (IL-8). The main factors responsible for the toxicity after exposure to W4-VDR and P8-VDR are dose, exposure route, and chemical composition. However, for the 40nm-VDR and 20nm-VDR, extra factors involve nanosurface, nanostructures, nanosize, quantum impacts, dissolution, concentration, self-

assembly, and assemblage. The key factors that cause the nanoparticle toxicity are summarized in Fig. 6.1 [415].

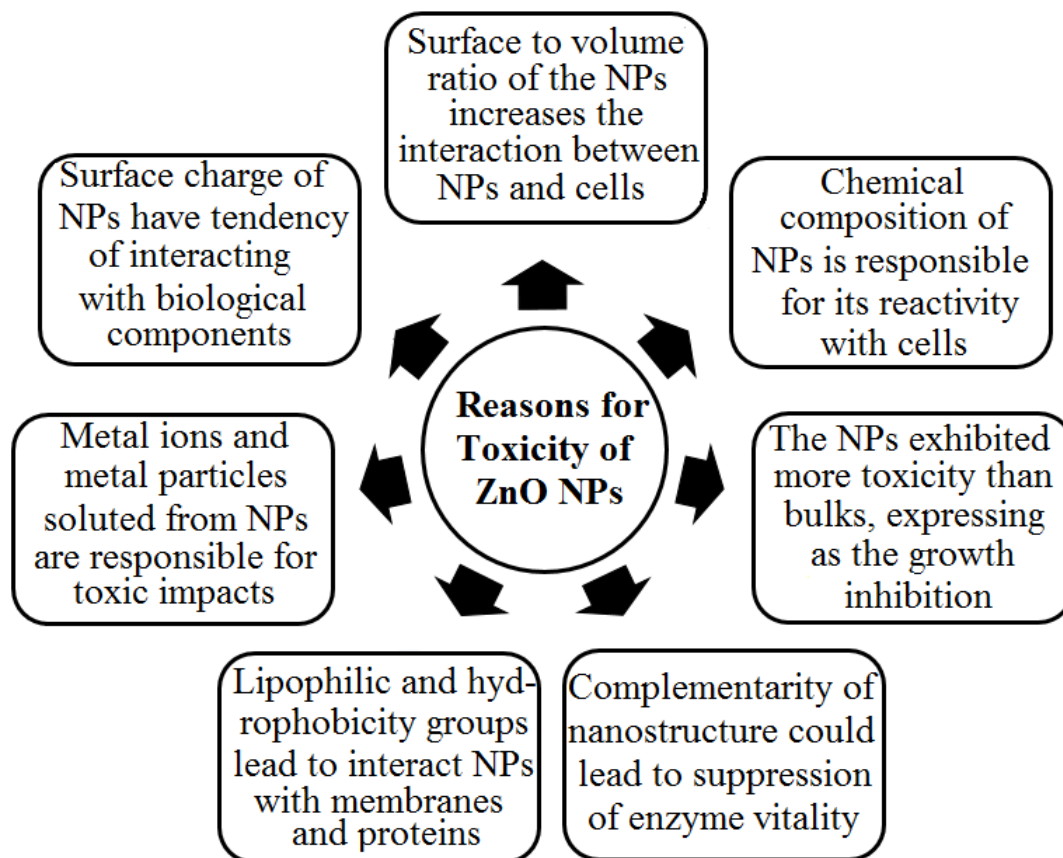


Figure 6.1. Schematic overview summarizing the factors responsible for toxic effect of ZnO NPs.

The toxicity of the 40nm-ZnO and 20nm-ZnO are attributed to their size. Many reports have indicated that nanoparticles sized constantly present more risky toxicity effects than W4-ZnO and P8-ZnO and proposed that particle size is one of the major factors that influence the toxicity of ZnO nanoparticles. Nanoparticles also cause granulocyte and thrombocyte activation and produce hemolysis and inflammation in human blood specimens [416].

The nanoparticle size is immediately related to several key characteristics, such as chemical reaction, solubility, and surface property, which affect the interactions between biomolecules and nanoparticles and therefore influence the nanotoxicological properties of ZnO nanoparticles *in vivo* [62]. For example, reducing the size of particle increases the particular surface area of particles, which enhances not only the aggregation of nanoparticle but also improves of reactivity and promotes the interactions between nanoparticles and biomolecules. Variations in the ZnO nanoparticles' radius size lead to several cell uptake rates, which impact toxicity. Particle toxicity is also correlated to dimension; particles with one-dimensional structures present high toxicity affects [417].

Besides particle size, surface characteristics such as the surface defect and surface charge of the nanoparticles are also main factors that determine the toxicity of ZnO nanoparticles. Hwang and colleagues [418] reported that the cytotoxicity of metal oxide nanoparticle was correlated to the surface charge, and the impact of toxic to bacterium decreased if the cation charge enhanced. Reports have demonstrated from the estimate of attractiveness of electrovalent that particles of zincative bacterium could be attracted by the metal oxide nanoparticle cation surface; particles with low charge are easy to attract. The same case applies when positively charged particles are adsorbed onto negatively charged proteins such as albumin. Even if particles have a negative charge, they can be absorbed onto albumin by mediating cations such as calcium (Ca^{2+}) [419]. Furthermore, Berardis et al. [236] compared the effects of cytotoxicity among same size of ZnO and TiO_2 nanoparticles and examined their differential impacts on marine algae, proposing that their chemical combinations also performed a significant function. The surface characteristics of nanoparticle can be adjusted by nanoparticle functionalization using functional molecules [420]. These functionalized nanoparticles have superior disparity in aqueous solution, which retains most of the size-dependent impacts. If the characteristics of surface cannot be demonstrated, nanoparticles might readily accumulate into significant particles and react with organs and biomolecules, probably leading to toxicity [421]. More research must be

done to develop the functionalization and nanoparticles synthesis for the preferred use of metal oxide nanoparticles while decreasing their toxic effects to human and environment.

The dissolution of nanoparticle metal ions is another major factor that causes toxicity. Solubility is a significant characteristic that responds to the impacts of toxic on several cells. Brunner et al. [414] observed that the soluble metal oxide nanoparticles showed higher toxic effect compared with the unsolvable ones at the identical concentration after six days. This phenomenon may be attributed to the larger surface areas of nanoparticles that interact with the solvent molecules compared with the bulk ones at the same weight. Nano sized particles exhibit fast dissolution. The solubility of the 40nm-ZnO and 20nm-ZnO in DMEM is higher than that of W4-ZnO and P8-ZnO. Hence, ZnO nanoparticle samples are more toxic, as shown in this work.

The emission of metal ions from the nanoparticles was low, and minimal Zn ions concentrations did not show any cytotoxic impacts. Many researchers have suggested that Zn^{2+} can be released from ZnO nanoparticles, and the quantity of soluble ions was diverse in different media. Cytotoxicity studies demonstrated that ZnO nanoparticles have toxic effects, and the Zn fraction released from the ZnO nanoparticles is considered for only a limited effect of this toxicity. Cell toxicity depends on the contact with the nanoparticles instead of exposure to solutions with soluble metal ions. However, researchers indicated that this toxicity may be dependent on the cell used types. When time of exposure was extended to 72 h, the Zn^{2+} released from the ZnO nanoparticles led to a considerable damage in DNA and believed for 31% of membrane damage [422]. Both the metal oxide nanoparticles and soluble ions may have a cytotoxicity effect. Consequently, the toxic impacts of ZnO nanoparticles are the combined influences of particles and dissolvable ions.

6.3 Biocompatibility of ZnO micro and nanoparticles-based discs

Before any material is used for medical application purposes, it must pass a series of tests for biocompatibility and toxicity to the tissue or cell. To reduce the extent of safety

studies in laboratory animals, utilizing cultured cells *in vitro* in controlled conditions is one of the most frequently used methods because *in vitro* studies give more advantages than *in vivo* during the screening and early evaluation of a biomaterial. One important parameter that affects the biocompatibility is the biomaterial–cell interaction characteristic [423-425].

The fibroblast cell line is one of the cell lines usually used for biocompatibility evaluation. L929 cells, which are originated from an immortalized mouse fibroblast cell line, are internationally well-known cells that are usually applied in *in vitro* cytotoxicity evaluations [426]. In this study, L929 cell line was used to investigate the *in vitro* cytotoxicity of different particle sizes of ZnO powder using trypan blue exclusion method, following the ISO-Standard 10993-5.

6.4 In vitro cytotoxicity trypan blue exclusion assay

In this study, the *in vitro* cytotoxicity evaluation was carried out using trypan blue exclusion assay method to obtain the viable cells number present in a cell suspension. The method is established from the principle that live cells have undamaged cell membranes that prohibit several dyes, such as trypan blue, propidium, or Eosin, whilst dead cells do not. A viable cell would have an obvious cytoplasm whilst a nonviable cell would have a blue cytoplasm [427].

Trypan blue, which is usually utilized to stain non-viable cells exclusively, provides the required elevated signal-to-noise ratio; but the disadvantages of trypan blue exclusion assay compared with other assay include the use of a traditional quantification technique, time-consuming cell counting method, sampling error, and bias-prone investigator [428]. In this study, trypan blue exclusion method was utilized to investigate the effect of introducing different particle sizes of ZnO powders into the cell culture.

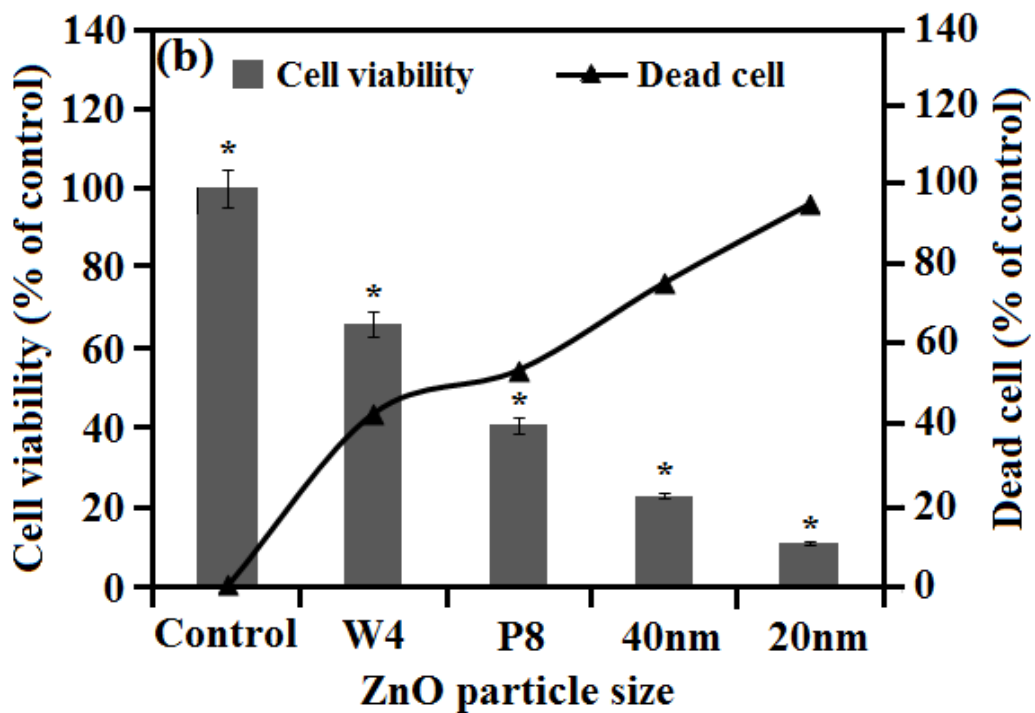
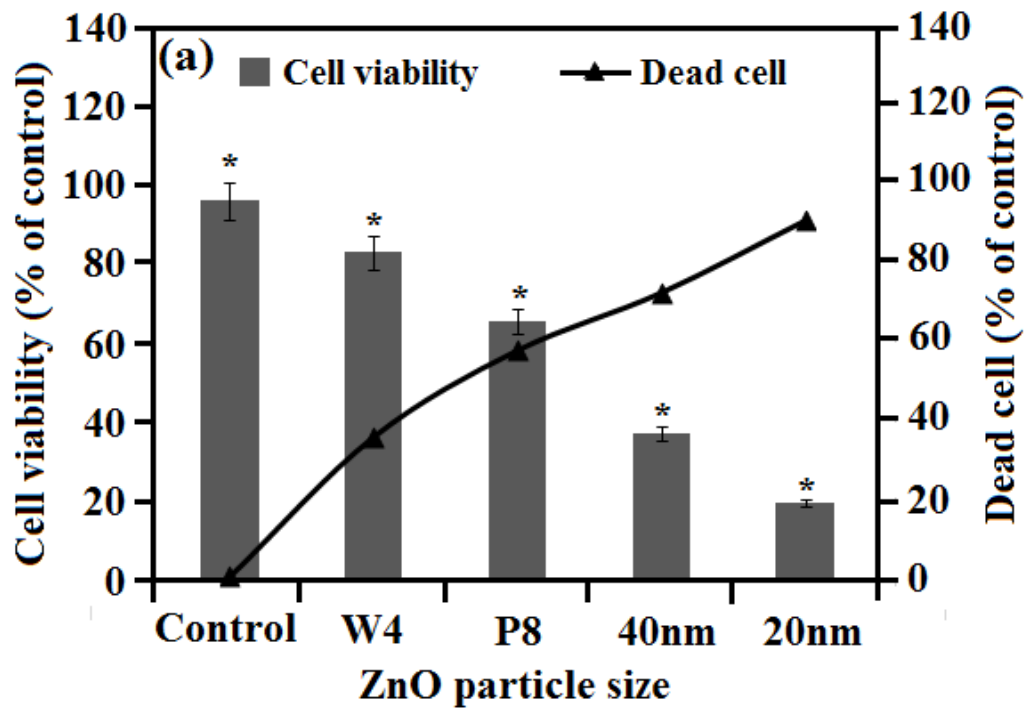


Figure 6.2. Percentage of cell viability and dead cell of L929 at (a) W4-Disc, P8-Disc, 40nm-Disc and 20nm-Disc, and (b) W4-VDR, P8-VDR, 40nm-VDR and 20nm-VDR after 72 hours in cultured with L929. Mean \pm SD (n = 3). (ANOVA) followed by Bonferroni correction suggested statistically obvious variation when compared with control (*P \leq 0.05).

Fig. 6.2 shows the percentage of cell viability and the percentage of dead cells of L929 at (a) W4-Disc, P8-Disc, 40nm-Disc, and 20nm-Disc and (b) W4-VDR, P8-VDR, 40nm-VDR, and 20nm-VDR. The figures show that the W4-Disc and W4-VDR had the highest percentages of cell viability of 83.5% and 64.9% L929 cell growth in the culture medium, respectively. Compared with the control, no significant differences can be seen. The results from this trypan blue exclusion method suggest that decreasing the ZnO particle size from W4-ZnO to 20nm-ZnO increases the toxicity to L929 cell line. The percentages of cell viability were 68.3%, 38.1%, and 19.8% for the P8-Disc, 40nm-Disc, and 20nm-Disc, respectively, and 41.5%, 22.2%, and 11.4% for the P8-VDR, 40nm-VDR, and 20nm-VDR, respectively.

On the contrary, the W4-VDR, P8-VDR, 40nm-VDR, and 20nm-VDR (Fig. 6.2 (b)) show higher percentages of dead cells compared with the W4-Disc, P8-Disc, 40nm-Disc and 20nm-Disc. This result may be attributed to the significant effect of Bi_2O_3 and Mn_2O_3 in the L929 cell growth, making the varistor more toxic than the pure disc.

Note that the counting of live and dead cells as we investigated by using trypan blue exclusion method can be seen in APPENDIX D.

6.5 Effect of different ZnO particle sizes and various concentrations on cell viability

The effects of various concentrations of W4-Disc, P8-Disc, 40nm-Disc, and 20nm-ZnO-Disc and varistors on the viability of L929 cells were evaluated by trypan blue exclusion assay (Fig. 6.3 (a and b)). The results show that exposure to different samples for 72 h leads to a dose-dependent increase in mitochondrial dysfunction. A statistically significant difference was observed among the different metal oxides. Compared with the untreated control in DMEM cultured medium, the 20nm-ZnO showed higher cytotoxicity at 25, 50, 75, and 100 $\mu\text{g}/\text{ml}$ concentrations. The trypan blue exclusion assay showed that the

20nm-ZnO was the most toxic to L929 cells, followed by the 40nm-ZnO, P8-ZnO, and W4-ZnO in descending order.

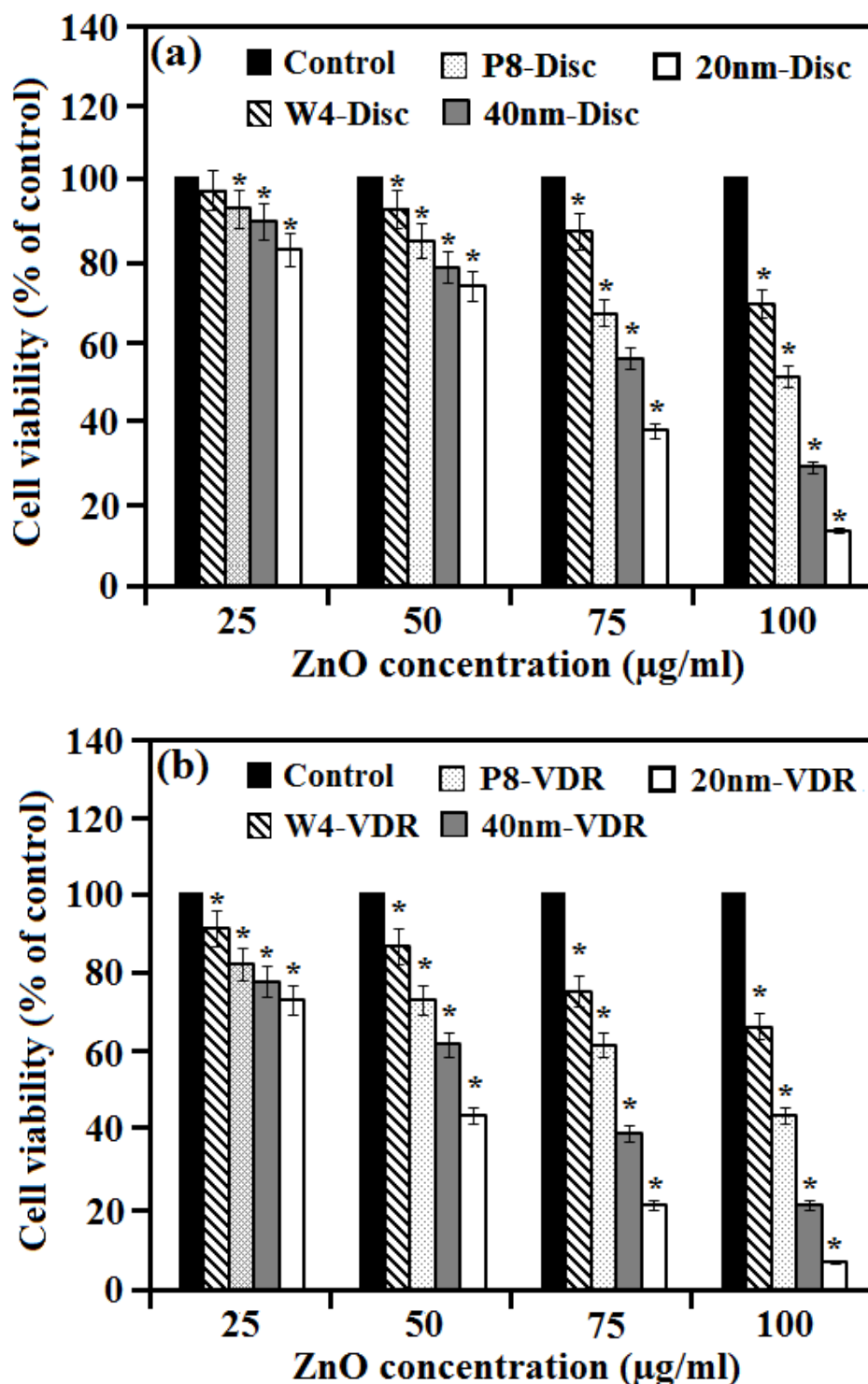


Figure 6.3. Percentage of cell viability of L929 at different concentration of (a) W4-Disc, P8-Disc, 40nm-Disc and 20nm-Disc, and (b) W4-VDR, P8-VDR, 40nm-VDR and 20nm-VDR. Mean \pm SD (n = 3). (ANOVA) followed by Bonferroni correction suggested statistically obvious variation when compared with control (*P \leq 0.05).

As the practical use of nanoparticles grows, considering their possible opposite impacts on the ambience and human health has become very important [421]. However, nanoparticle safety evaluation on the ambience and human health are not enough [429]. Several studies have discussed the toxicity of these nanoparticles and subsequently compared these toxic effects. The cellular effects of nanoparticles are significantly dependent on structural and chemical characteristics, solubility, shape, and surface/mass ratio. Furthermore, the actual particle sizes in suspension are different from the original primary size. The current research aimed to determine and compare the possible toxicity of four types of ZnO powders (W4, P8, 40nm, and 20nm) with different primary sizes that are significantly used in industrial manufacture.

In vitro, different particle sizes of ZnO powders were tested for their ability to induce toxicity in L929 cells. Various ZnO suspensions were prepared and subjected to the cells at concentrations of 25, 50, 75, and 100 µg/ml. After 72 h treatment of the W4-Disc, P8-Disc, 40nm-Disc, and 20nm-Disc and W4-VDR, P8-VDR, 40nm-VDR, and 20nm-VDR samples, the cell viability was calculated for each case. The results indicated that all types of ZnO samples induced reduction in cell viability compared with the cultured medium control. The viability of cells progressively reduced by increasing the concentrations of ZnO for both the disc and varistor samples. These four types of ZnO produced cytotoxicity in a dose-dependent manner over the 72 h treatment period. Microscopic observations were performed to determine the impacts of the different types of W4-ZnO, P8-ZnO, 40nm-ZnO, and 20nm-ZnO on cell morphology, and the results suggested that these particles could enter into the cells and produce morphologic alternation in a dose-dependent manner.

In agreement with the findings in this work, dose-dependent cytotoxicity in nanoparticles materials-exposed cells was also reported by several other research groups [430, 431]. The cell viability was obviously decreased by treatment with the media that contain various concentrations of ZnO samples. The metal oxide nanoparticles, such as 40nm-Disc and 20nm-Disc exhibited toxicity in mammalian cells, causing the generation of

reactive oxygen species (ROS), excitation of inflammation, oxidant injury, and cell death [237, 414, 432-434]. In addition, exposure to 20, 40, and 50 nm nanoparticles led to cytotoxicity in a dose-dependent manner at dosage levels between 10% and 100% in cultured L929 cells and human bronchoalveolar carcinoma-derived cells that were related to increased oxidative stress [435, 436]. Simon-Deckers et al. reported that metal oxide nanoparticles were able to rapidly enter into cells and be distributed inside the cytoplasm and intracellular vesicles [437]. Furthermore, Virgilio et al. reported that exposure to titanium oxide and aluminum oxide nanoparticles led to dose-related cytotoxic effects by alteration in the lysosomal and mitochondrial dehydrogenase activity in CHO-K1 cells [430]. These two nanoparticles were found to form vesicles within the cells.

Oxidative stress is the abnormal ROS level that causes oxidative damage in a cell, organ, or tissue in a steady-state level. These damages can affect a specific molecule and lead to toxic effects through the generation of peroxides and free radicals. Klaine et al. hold that the generation of intracellular oxidative stress is a major phenomenon in the mechanisms of toxicity of several nanoparticles [438]. Furthermore, many research groups confirmed that ZnO nanoparticles could produce intracellular oxidative stress and lead to adverse biological responses [237, 431, 436, 439-442].

6.6 Cell Morphology

The cell morphological changes of the control cells and the W4-ZnO, P8-ZnO, 40nm-ZnO and, 20nm-ZnO-exposed cells are illustrated in Fig. 6.5. The cell morphology observation was done using an integrated microscope (Integrated Microscope Zeiss-Axiovert 40-C). Fig. 6.5 shows the cell morphology of L929 after 72 h in culture medium at various concentrations. No morphological changes in control cells were induced. The control L929 cells were completely transparent, and the attached and well-confluent monolayer in the DMEM medium is shown in Fig. 6.4.

With the addition of different samples of ZnO-based discs, morphological changes were observed in the L929 cells, which are characterized by irregular shapes and cell shrinkage compared with the control cell. The alterations in morphology of cells can previously be revealed microscopically between 1 and 3 h after the exposure of the cell to particular ZnO. However, the changes in the cell became more prominent as the incubation period prolonged. Usually, after 1 day in culture medium, the L929 mouse fibroblast cells are large and spindle shaped, with adherent cells growing as a confluent monolayer [443].

After 72 h, at low ZnO concentration (25 µg/ml), the cell morphology appeared to be altered. With increasing doses of ZnO (50, 75, and 100 µg/ml), the morphology of L929 cells was destroyed, the cell became swollen, and the membrane integrity was lost, especially for the 40nm-ZnO and 20nm-ZnO; nanoparticle were probably accumulated inside the L929 cells. In addition, the transparency of the cell was lessened, and the amount of cell fragments increased after 72 h. Among the four types of ZnO powders, the morphology conversion was observed remarkably in the 20nm-ZnO-exposed cells, followed by the 40nm-ZnO, P8-ZnO, and W4-ZnO-exposed cells in descending order (Fig. 6.5).

Nanoparticle usage continues to grow rapidly and widely in areas such as pharmaceuticals, cosmetics, and many industrial applications. Carefully assessing the safety and toxicity of these nanoparticles to human health is of utmost importance. The toxicity results obtained in this work can probably be applied to assess human topical risk exposure to nanoparticles. This study found that the ZnO nanoparticles with high diameter exhibit toxicity *in vitro*; hence, further usage of ZnO nanoparticles in body fluid requires caution. Lin et al. [441] reported that 70 and 420 nm ZnO particles can remarkably reduce cell viability and lead to oxidative DNA destruction in A549 cells in a dose- and time-dependent method. Therefore, future works should focus on discussing the potential risk of nanoparticles to human health at the microscopic cellular level by implementing suitable microscopic techniques, such as TEM, to detect the general mechanisms of the toxicity process and to characterize exposure to nanoparticles.

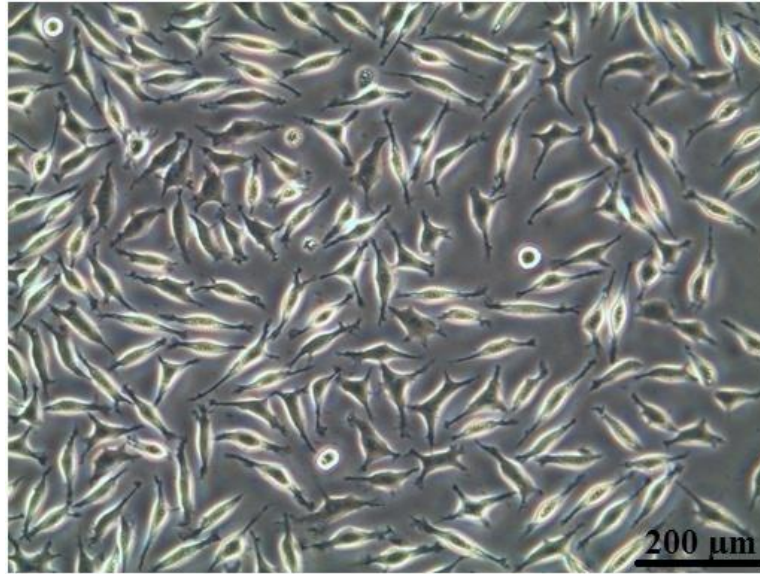
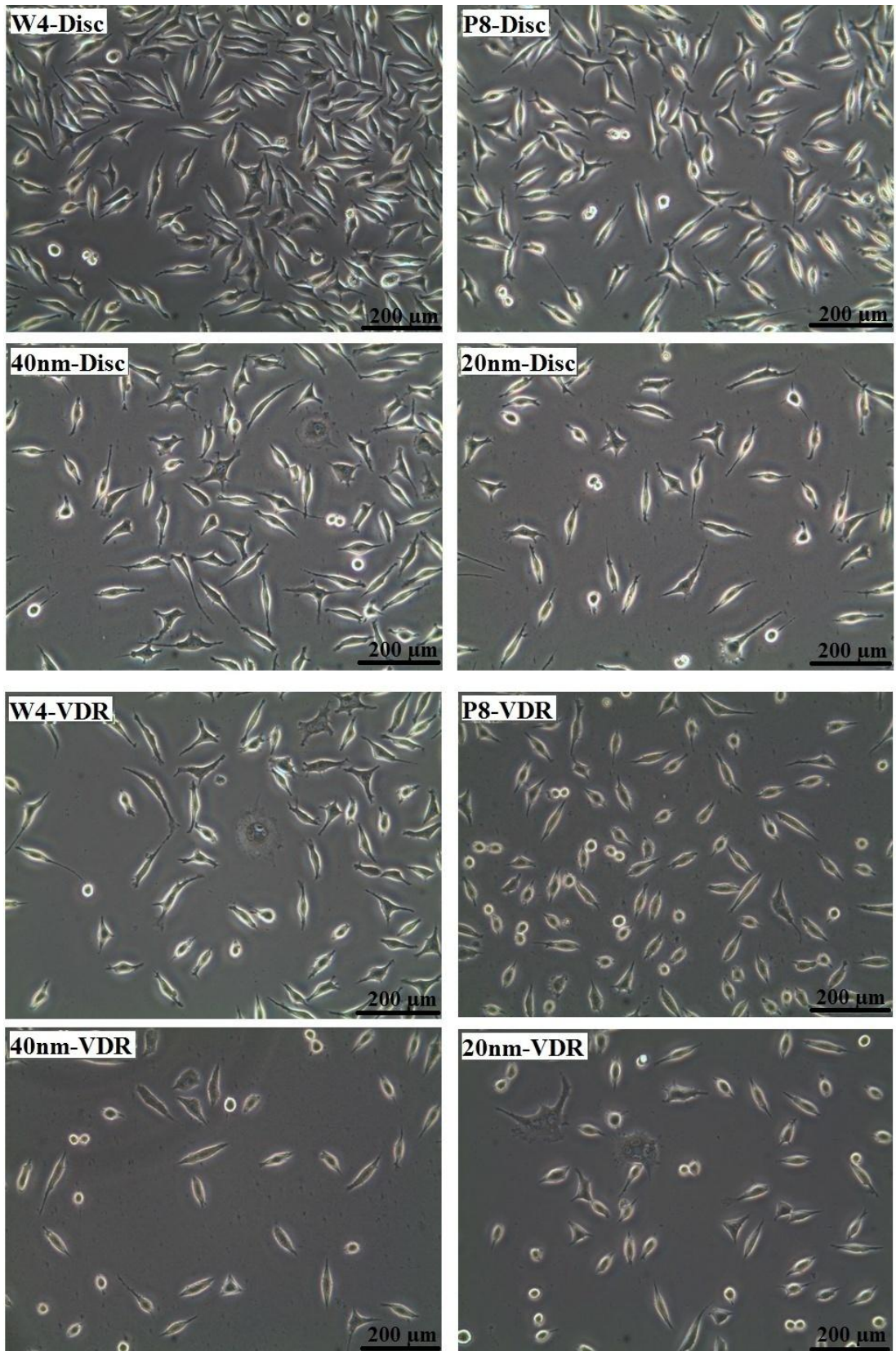
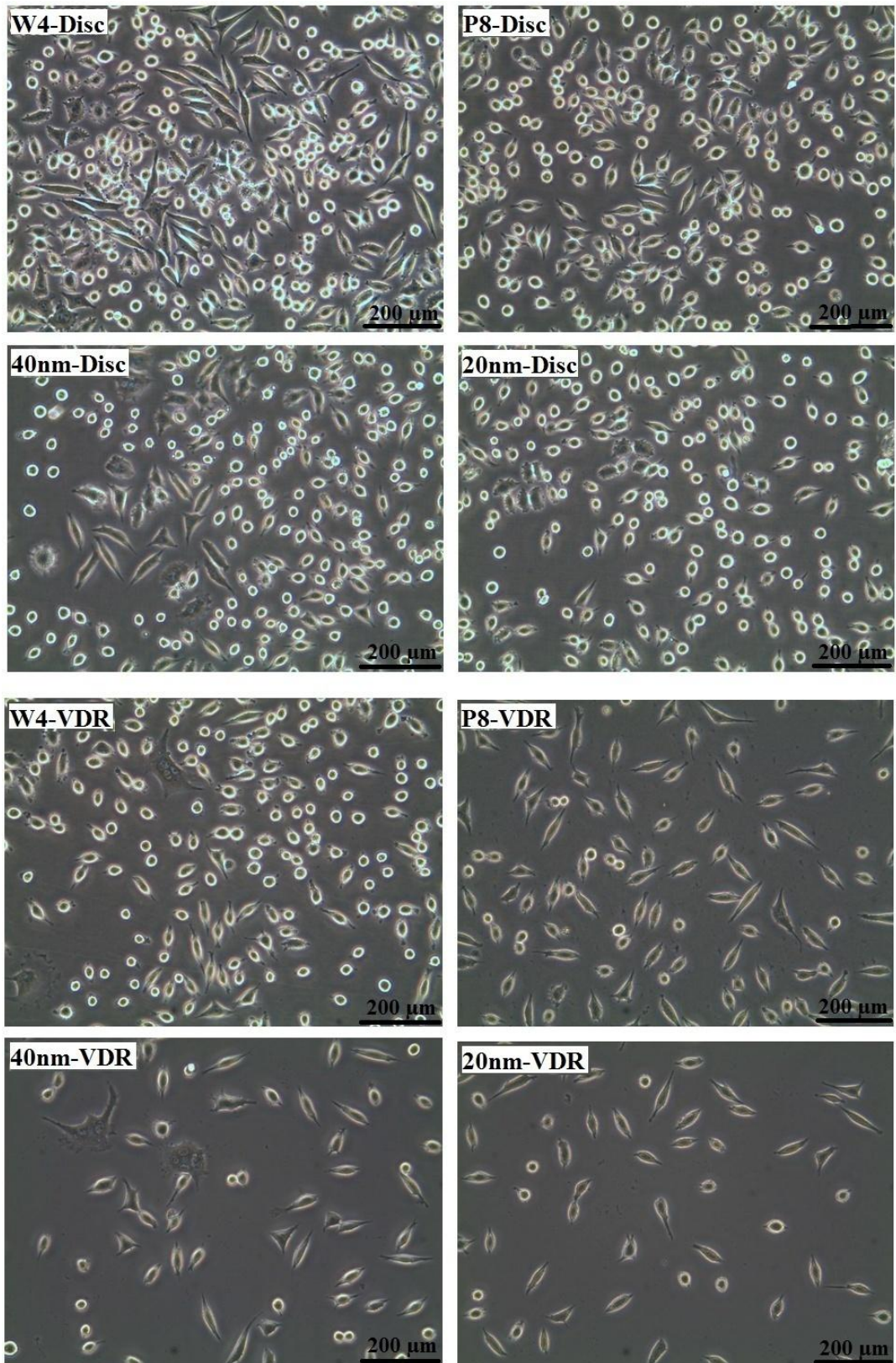


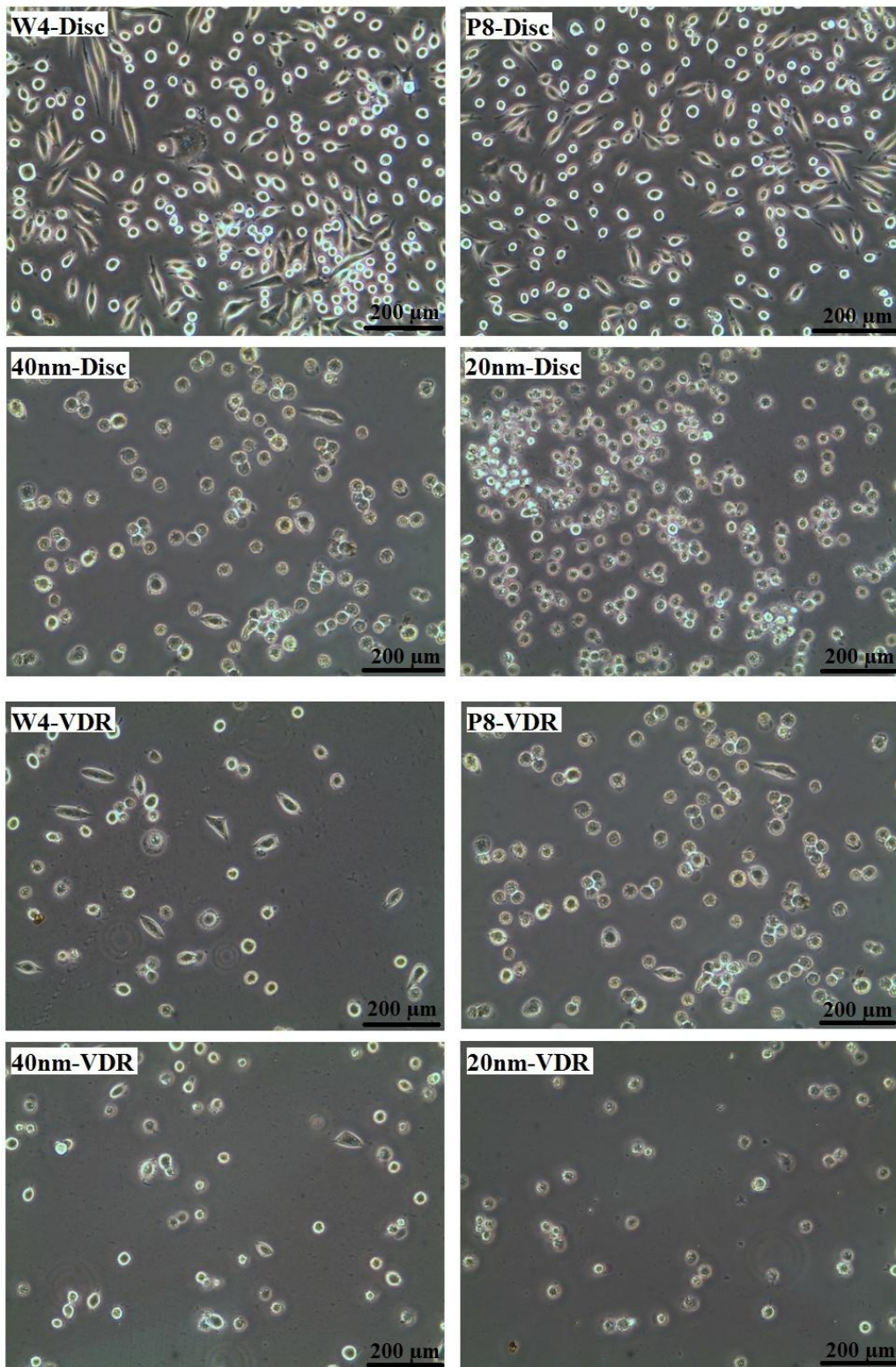
Figure 6.4. Cell morphology of L929 after 72 hours in culture medium, untreated with ZnO (Control).



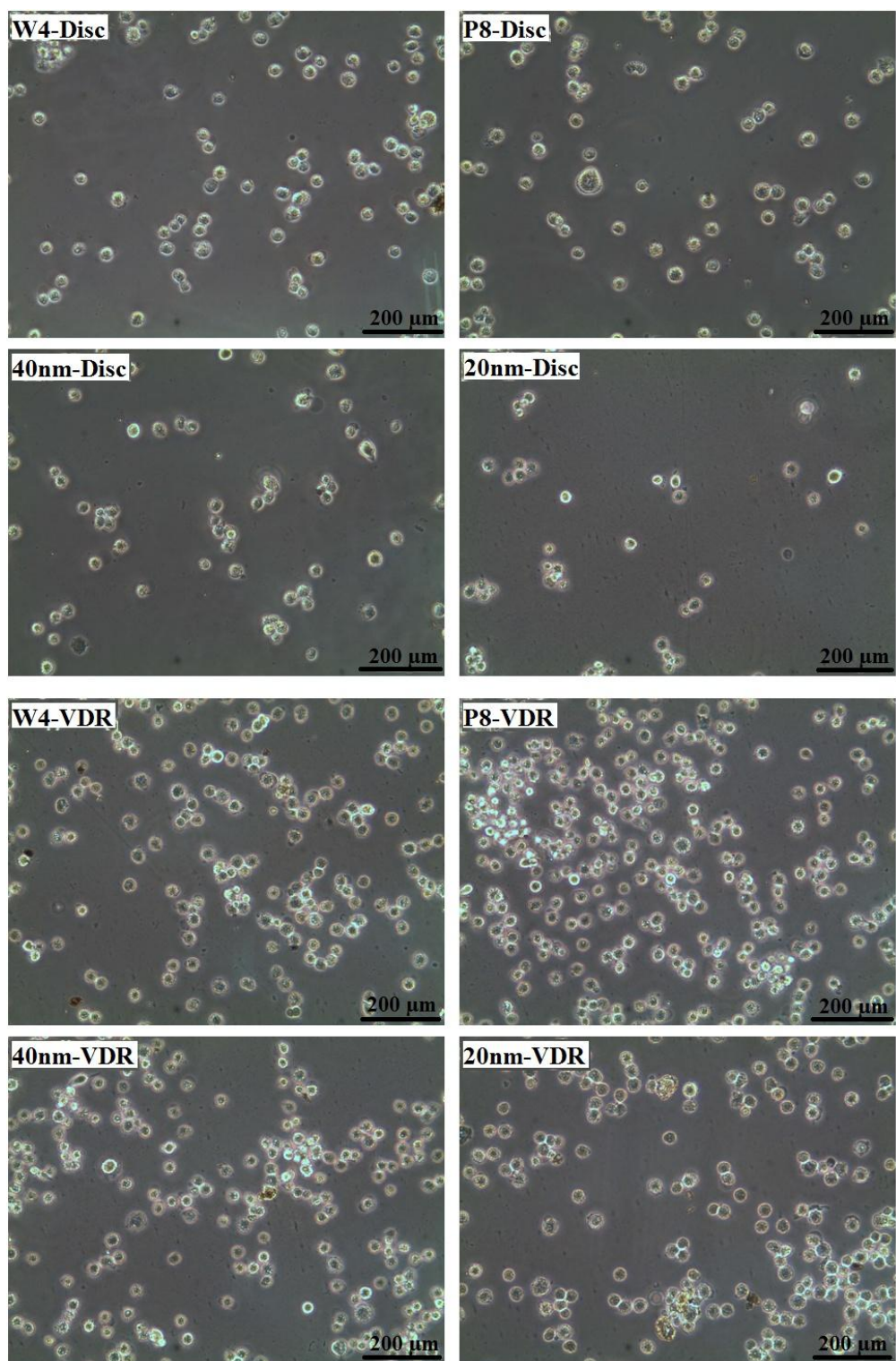
(a)



(b)



(c)



(d)

Figure 6.5. Cell morphology of L929 after 72 hours in culture medium at (a) 25; (b) 50; (c) 75; and (d) 100 concentrations ($\mu\text{g/ml}$) of pure and composite discs made from different particle sizes of ZnO powder.

6.7 Summary

ZnO–Bi₂O₃–Mn₂O₃ varistors fabricated from ZnO micro-and nanoparticle powders were prepared through a conventional ceramic processing method. SEM and XRD were utilized to characterize the morphologies and crystal structures of the varistors. The ZnO–Bi₂O₃–Mn₂O₃ varistors composed of ZnO nanoparticles exhibited higher performance, better quality, but greater toxicity than those composed of only ZnO microparticles with the same composition. Furthermore, the ZnO particles with different sizes induced DNA damage and different cytotoxicity levels.

The present work also demonstrates marked differences among the W4-ZnO, P8-ZnO, 40nm-ZnO, and 20nm-ZnO particles at the same concentration. Compared with low ZnO concentrations, high ZnO concentrations induced significantly higher percentages of cell viability reduction, cell apoptosis, and morphological alternation. Furthermore, the result of morphological observation suggests that the 20nm-ZnO showed the maximum cytotoxicity in L929 cells, and W4-ZnO was less cytotoxic than the other samples at the same concentration.

In summary, the present work found that the W4-ZnO, P8-ZnO, 40nm-ZnO, and 20nm-ZnO powders cause cellular mitochondrial dysfunction, apoptosis, and morphological modification at different concentrations (25, 50, 75, and 100 µg/ml), and the toxic effects are clearly shown in a dose-dependent manner. Based on the results, 20nm ZnO is the most toxic material. These findings highlight the different cytotoxicity related to the exposure to the different types of ZnO micro- and nanoparticle-based discs and propose an extreme attention to the safe use of these materials, especially ZnO nanoparticles, in biological fields.

This work points out several possible cytotoxicity mechanisms of 20nm-VDR compared with W4-VDR:

- Nanoparticles adhere to the cell surface, thereby changing the features of membrane. The small size and excessively huge surface area of the nanoparticles

enable them to produce intense contact with the surface of microorganism [444]. The cells attachment to such a surface relates with the nanoparticles surface zeta potential.

- ZnO nanoparticles penetrate inside the L929 cell, thereby leading to DNA destruction. In the study of Choi and Hu [445] the nitrifying organisms suppression was related with the fraction of ZnO nanoparticles less than 50 nm, which was more toxic than another ZnO form (W4 and P8). The author suggested that this finding may be caused by the simpler (active) transfer via the cell membrane of uncharged ZnO nanoparticles than of charged Zn ions.
- The degeneration of ZnO nanoparticles lead to release Zn^{2+} ions that can react with sulfur-containing proteins within the wall of L929 cell, thereby leading to compromised functionality. This phenomenon is predominantly considered as the essential mechanism of the cytotoxicity of ZnO nanoparticles [422], hence, the broad knowledge of the cytotoxic behaviors of Zn^{2+} ions can be used to ZnO nanoparticles. Simultaneously, the cellular resistance problem to Zn^{2+} ions stills significative for least particular functions of ZnO nanoparticles. The reaction of solved Zn^{2+} ions with the wall of cell and cytoplasmic proteins was also suggested by Choi et al. [446], who also highlighted that the interaction of Zn^{2+} ions with the thiol group of vital enzymes may lead to their impaired role or inhibition. The interchange of Zn^{2+} ions among inorganic sulfur compounds and thiols was likewise suggested by other researchers [447]. The disturbance of breathing and motive force of proton establishing caused by the reactions with the thiol groups of enzymes and another proteins were also reported by Sedlak et al. [448]. According to Samberg et al. [449], the cytotoxic activity of Zn^{2+} ions is attributed to the synergistic impact among the Zn^{2+} ions binding to the wall of cell, their

uptake and following aggregation within the cell, and their intervention with critical biomolecules within the cell. According to the researchers, the Zn^{2+} ions stable release from the dissolution of ZnO nanoparticles is a serious role of ZnO nanoparticles that must be believed previously to composition. According to Wong and Liu [450], Zn^{2+} ions have the ability to interact with phosphorus-consisting of compositions (e.g., DNA). The intervention with DNA duplication processes, which stops cellular reproduction and reduces the cells number over time, was also mentioned by several researchers as a result of subject to Zn^{2+} ions that dissolve from ZnO nanoparticles. The generation of free radicals and production of oxidative stress should also be considered subsequent the uptake of silver nanoparticles/ions, and these were reported by several researchers [444].

- Reactive oxygen species (ROS) can be created out the cell, in the medium, or within the cell likewise as a result of cell destruction/disturbance [450]. According to Choi and Hu [446], the growth of cell repression due to whole considered samples forms was related with intracellular ROS levels. Photocatalytic ROS fraction did not observe such a correlation. Given that the concentrations of ROS were various for every sample, the researchers concluded that different toxicity sources must also be taken in to account. Even though certain relationships exist between repression of cell growth and concentration of Zn^{2+} ion, ZnO nanoparticles were found to be more toxic than the similar Zn^{2+} ions concentration perhaps because of the enhanced localized the ions concentration that surround the nanoparticles and the differential localization caused by the active transport of ZnO nanoparticles into cells through receptor-mediated processes.

The following table explained the major variations among ionic, nanoparticle and bulk ZnO.

Table 6.1. Summary for main different between ionic, nanoparticle and bulk of ZnO.

Ionic	Nanoparticles	Bulk
No surface area	Large surface area-potential for rapid dissolution	Small surface area-slow dissolution
Highly reactive, precipitates	Highly reactive	-
-	Oxidative potential	Limited oxidative capacity
Easily gets inside cells (equilibrium partitioning)	Ability to uptake via active processes	No uptake by cells
Forms complexes with inorganic and organic	Binding of biomolecules	Limited binding of biomolecules

CHAPTER 7

CONCLUSIONS AND FUTURE WORK

7.1 Conclusions

W4-Disc, P8-Disc, 40nm-Disc and 20nm-Disc were successfully prepared by conventional ceramic processing, and then annealed at different conditions. SEM, XRD, and AFM were used to characterize the disc morphologies and crystal structures. The ZnO discs crystal quality significantly depended on the heat treatment ambient. The grains grew larger and more structured and resembled polygons (hexagon) compared with the as-sintered discs, and the pores became small. The thermal treatment in O₂ atmosphere enhanced the rather dense morphology of ZnO discs, whereas annealing in N₂ atmosphere led to a partially porous morphology.

The 20nm-Disc had the largest particle size compared with the W4-Disc, P8-Disc, and 40nm-Disc, which led to a big drop in breakdown voltage and improved the different electrical behaviors. This phenomenon may be caused by the huge S/V ratio in the 20nm-ZnO. The ceramics' breakdown voltage is immediately proportional to the quantities of boundaries among grains per unit of thickness and subsequently to the inverse of the size of ZnO grain. Another considerable change was that in the resistivity (ρ) at the high-resistivity region, whereby the ρ at the W4-Disc dropped significantly for the 20nm-Disc after annealing. The extreme gas absorption during the annealing treatment reduced the potential barrier of the "P-N junctions", there by resulting in the big drop in ρ . The annealing treatment in oxygen ambient also improved the crystallinity of grain, as explained by the relaxation of the compressive stress with heat treatment, which became tensile dependent on the XRD lattice constant and FWHM data. Furthermore, the intrinsic defects difference within disc such as zinc vacancy, oxygen vacancy, antisite oxygen, and interstitial oxygen with oxygen pressure (p_{O_2}) can be expressed during the oxygen annealing process.

Significant changes in the relative intensity of the ultraviolet and the green visible luminescence were observed with different particles size of ZnO powder and different annealing treatments. The chemisorption and desorption of oxygen during annealing and the subsequent surface band bending, instead of the oxygen vacancy concentration, were shown to be the mechanism that explains the observed changes in photoluminescence. The optical band gap decreased with improving grain size and rise tensile stress. The 20nm-Disc and 40nm-Disc were found to consist of an extremely high structural defects concentration, as denoted by the broad and dominant visible emission in photoluminescence spectra.

Therefore, based on the previous studies on the discs, the 20nm-Disc exhibited better structural, optical, and electrical properties with low breakdown voltage compared with the W4-Disc, P8-Disc, and 40nm-Disc. This electronic structure change led to major changes in the optical properties of the 40nm and 20nm discs compared with the W4-Disc and P8-Disc. The 20nm-ZnO possesses sufficient quality to open diverse areas and allow generation of experiments to functionalize and merge the material in to devices. A critical application of the dependence of the different properties of ZnO-based varistors on the nanoparticle size is that one type of semiconductor can be used to produce various kinds of varistor with different properties by simply changing the particle diameter. Another application being researched for these nanoparticles is their large surface-to-volume ratio, which has a significant effect on the varistor.

Meanwhile, 40nm-VDR and 20nm-VDR were fabricated by conventional ceramic processing method that involves ball milling, drying, pressing, and sintering. The different annealing ambient had comparable effects on the W4-VDR and P8-VDR. Thermal annealing treatments in oxygen and nitrogen atmospheres caused the grains to grow. Furthermore, the surface morphology of the ZnO microparticle- and nanoparticle-based varistors was found to be dependent on the annealing treatment under different atmospheres. The Bi-rich phase was interrelated and continuous over the four- and three-grain junctions throughout the microstructure of varistor. Annealing treatment also improved the crystallinity of grain, as

clarified through the XRD analysis. Several peaks of the varistor annealed in oxygen atmosphere were somewhat higher than those of the varistors annealed in the other atmosphere. However, the W4-VDR, P8-VDR, 40nm-VDR, and 20nm-VDR showed higher and narrower diffraction peaks with smaller FWHM with annealing process compared with the as-grown varistor sample, revealing better crystallinity and structure ordering of ZnO in the grain and grain boundaries. The 40nm-VDR and 20nm-VDR had thermodynamically stable crystallographic phase, and the peak intensity indicated the high degree of crystallinity. However, the peak width in the 40nm-VDR and 20nm-VDR increased compared with those in the W4-VDR and P8-VDR because of the quantum size effect in the nanoparticles. The UV luminescence for the varistor treated in O₂ atmosphere was the superior. This observation was agree with the XRD analysis results, which showed that thermal annealing in O₂ atmosphere decreased the ZnO interstitials, thereby increasing the radiation transition, decreasing the nonradiative transition, ultimately enhancing the ZnO crystal quality. The different behaviors of the varistors at various annealing atmosphere were attributed to the potential barrier generation and to the O₂ species at the boundary among grains that formed the Schottky-like barrier and trapping states. The excellent nonlinear I–V characteristic of the 20nm-VDR with low breakdown voltage and resistivity was caused by the significant surface area of the ZnO nanoparticles, which improved the homogeneity with low porosity and high sinterability. This study reflected that the electrical behaviors of the varistors manufactured from 20nm-ZnO were superior to those of the varistors made from W4-ZnO. The variance in the defects and homogeneity of the microstructure performs a significant function in distinguishing the electrical behaviors of ZnO varistors.

Bioactivity studies on the W4-Disc, P8-Disc, 40nm-Disc and, 20nm-Disc and W4-VDR, P8-VDR, 40nm-VDR and, 20nm-VDR were also carried out. For medical application purposes, samples must pass a series of tests for biocompatibility and toxicity to the tissue or cell. This study investigated the biocompatibility of different particle sizes of ZnO-based discs on connective mouse skin fibroblast (L929) by trypan blue exclusion assay. After 72 h,

the viability of L929 cell culture reduced with the rise in ZnO concentration ($\mu\text{g/ml}$). At concentrations between 50 $\mu\text{g/ml}$ and 100 $\mu\text{g/ml}$, the values indicated significant toxicity to the L929 cells and were various from the control at levels of $P < 0.05$. Low concentration (25 $\mu\text{g/ml}$) exhibited no considerable difference from the control.

No morphological changes were observed on the L929 cells when in contact with different particle sizes of ZnO at 25 $\mu\text{g/ml}$ concentration; the cells retained their original morphological characteristics. However, at concentrations greater than 25 $\mu\text{g/ml}$, the cells decreased in density, showed retraction and a round appearance that does not touch adjacent cells, became swollen, and lost integrity of membrane. The cells transparency was lessened, and the quantities cell fragments grow after 72 h.

The results indicated that all types of ZnO samples induced reduction in cell viability compared with the cultured medium control. The viability of cells gradually reduced by increasing the ZnO concentrations for both the disc and varistor samples. These four types of ZnO produced cytotoxicity in a dose-dependent manner over the 72 h treatment period. Furthermore, the result of morphological observation also suggested that the 20nm-ZnO caused maximal cytotoxicity in L929 cells, and W4-ZnO seemed to be less cytotoxic than the other samples at the same concentration.

In summary, our results show that the four types of ZnO lead to cellular mitochondrial dysfunction, apoptosis, and morphological modification at different concentrations (25, 50, 75, and 100 $\mu\text{g/ml}$), and the toxic effects are clearly shown in a dose-dependent manner. ZnO nanoparticle is a very toxic material. This finding highlights the differential cytotoxicity related to the exposure to the W4-Disc, P8-Disc, 40nm-Disc and, 20nm-Disc and W4-VDR, P8-VDR, 40nm-VDR and, 20nm-VDR and proposes an extreme attention on the safe use of these materials, especially ZnO nanoparticles, in biological field.

7.2 Future studies

The present research work leaves the following future prospects:

1. Investigate the lightening effect on the electrical properties of high-voltage ceramic varistors fabricated from micro- and nano-sized ZnO powder.
2. Given the many morphologies and kinds of ZnO nanoparticles, their transport characteristics in the varistor can be studied for the different structures and shapes as well as for the various diameters of nanoparticles or nanowires/rods.
3. Investigate the effects of various PVA percentages on the green strength of the varistor and particle size distribution of ZnO. PVA can be used as binder.
4. Study the effects of fritting certain varistor additives prior to mixing with the main varistor batch. Fritting can enhance wetting.
5. Study the bioactivity of ZnO varistor, including the toxicity, anti-bacterial, anti-fungal, or anti-cancer properties. Investigate in detail how these studies can affect the surface morphology and behaviors of varistor.
6. ZnO varistors manufactured from ZnO nanoparticles may be used on other industrial and medical applications, such as filing materials in bones.
7. The ZnO nanoparticles used to fabricate the varistor and discussed in this dissertation can be replaced by other metal oxide nanoparticles such as SnO₂ or TiO₂.

8. Study the effects of heat treatment annealing on the ZnO nanoparticle powder in oxygen-rich ambient and oxygen-deficient ambient before mixing with the additives. Oxygen is significantly electronegative with respect to zinc, and it tends to produce ZnO once bonded.

9. The UV and green band in the ZnO nanoparticles are very sensitive to defects and dopants in the varistor, as observed in this work. Therefore, they can be tuned by the type of dopants used during varistor preparation. The amorphous layer around the nanoparticles might possess useful properties and can possibly be doped and considered to understand the fundamental science and potential for useful applications.

REFERENCES

- [1] M. Elfving, R. Österlund, E. Olsson, Differences in wetting characteristics of Bi₂O₃ polymorphs in ZnO varistor materials, *Journal of The American Ceramic Society*, 83 (2000) 2311-2314.
- [2] D.R. Lide, *Handbook of chemistry and physics*, 78th ed., 1998.
- [3] F. Yuan, H. Ryu, Microstructure of varistors prepared with zinc oxide nanoparticles coated with Bi₂O₃, *Journal of the American Ceramic Society*, 87 (2004) 736-738.
- [4] S.S. Lee, R.M. White, Self-excited piezoelectric cantilever oscillators, *Sensors and Actuators A: Physical*, 52 (1996) 41-45.
- [5] P. Verghese, D. Clarke, Piezoelectric contributions to the electrical behavior of ZnO varistors, *Journal of Applied Physics*, 87 (2000) 4430-4438.
- [6] S.M. Chou, L.G. Teoh, W.H. Lai, Y.H. Su, M.H. Hon, ZnO: Al thin film gas sensor for detection of ethanol vapor, *Sensors*, 6 (2006) 1420-1427.
- [7] M. Wagh, G. Jain, D. Patil, S. Patil, L. Patil, Modified zinc oxide thick film resistors as NH₃ gas sensor, *Sensors and Actuators B: Chemical*, 115 (2006) 128-133.
- [8] T. Aeugle, H. Bialas, K. Heneka, W. Pleyer, Large area piezoelectric ZnO film transducers produced by rf diode sputtering, *Thin Solid Films*, 201 (1991) 293-304.
- [9] K.K. Zadeh, A. Trinchi, W. Wlodarski, A. Holland, A novel Love-mode device based on a ZnO/ST-cut quartz crystal structure for sensing applications, *Sensors and Actuators A: Physical*, 100 (2002) 135-143.
- [10] J. Yoo, J. Lee, S. Kim, K. Yoon, I.J. Park, S. Dhungel, B. Karunagaran, D. Mangalaraj, J. Yi, High transmittance and low resistive ZnO: Al films for thin film solar cells, *Thin Solid Films*, 480 (2005) 213-217.
- [11] S. Mahamuni, K. Borgohain, B. Bendre, V.J. Leppert, S.H. Risbud, Spectroscopic and structural characterization of electrochemically grown ZnO quantum dots, *Journal of Applied Physics*, 85 (1999) 2861-2865.
- [12] M. Matsuoka, Nonohmic properties of zinc oxide ceramics, *J. Appl. Phys.*, 10 (1971) 736-746.
- [13] T.K. Gupta, Application of zinc oxide varistors, *J. American Ceramic Society*, 73 (1990) 1817-1840.
- [14] S.C. Pillai, J.M. Kelly, D.E. McCormack, P. O'Brien, R. Ramesh, The effect of processing conditions on varistors prepared from nanocrystalline ZnO, *J. Mater. Chem.*, 13 (2003) 2586-2590.
- [15] T. Asokan, R. Freer, Characterization of spinel particles in zinc oxide varistors, *Journal of Materials Science*, 25 (1990) 2447-2453.
- [16] S.M. Haile, D.W. Johnson Jr, G.H. Wiseman, H.K. Bowen, Aqueous precipitation of

spherical zinc oxide powders for varistor applications, *Journal of The American Ceramic Society*, 72 (1989) 2004-2008.

- [17] S .Hingorani, V. Pillai, P. Kumar, M. Multani, D. Shah, Microemulsion mediated synthesis of zinc-oxide nanoparticles for varistor studies, *Materials Research Bulletin*, 28 (1993) 1303-1310.
- [18] S. Hishita, Y. Yao, S. Shirasaki, Zino oxide varistors made from powders prepared by amine processing, *Journal of The American Ceramic Society*, 72 (2005) 338-340.
- [19] G. Hohenberger, G. Tomandl, Sol-gel processing of varistor powders, *Journal of Materials Research*, 7 (1992) 546-548.
- [20] Y. Lin, Z. Zhang, Z. Tang ,F. Yuan, J. Li, Characterisation of ZnO-based varistors prepared from nanometre Precursor powders, *Advanced Materials for Optics and Electronics*, 9 (2000) 205-209.
- [21] S.C. Pillai, J.M. Kelly, D.E. McCormack, R. Ramesh, Self-assembled arrays of ZnO nanoparticles and their application as varistor materials, *Journal of Materials Chemistry*, 14 (2004) 1572-1578.
- [22] S.C. Pillai, J.M. Kelly, D.E. McCormack, R. Ramesh, High performance ZnO varistors prepared from nanocrystalline precursors for miniaturised electronic devices, *Journal of Materials Chemistry*, 18 (2008) 3926-3932.
- [23] V. Sousa, A. Segadaes, M. Morelli, R. Kiminami, Combustion synthesized ZnO powders for varistor ceramics, *International Journal of Inorganic Materials*, 1 (1999) 235-241.
- [24] R. Viswanath, S. Ramasamy, R. Ramamoorthy, P. Jayavel, T. Nagarajan, Preparation and characterization of nanocrystalline ZnO based materials for varistor applications, *Nanostructured Materials*, 6 (1995) 993-996.
- [25] G. Westin, Å. Ekstrand, M. Nygren, R. Österlund, P. Merkelbach, Preparation of ZnO-based varistors by the sol–gel technique, *Journal of Materials Chemistry*, 4 (1994) 615-621.
- [26] K. Xue Ya, H. Yin, T. Ming De, T. Ming Jing, Analysis of ZnO varistors prepared from nanosize ZnO precursors, *Materials Research Bulletin*, 33 (1998) 1703-1708.
- [27] P. Duran, F. Capel, J. Tartaj, C. Moure, A strategic two-stage low-temperature thermal processing leading to fully dense and fine-grained doped-ZnO varistors, *Advanced Materials*, 14 (2002) 137
- [28] S. Pillai, J. Kelly, D. McCormack, R. Ramesh, Effect of step sintering on breakdown voltage of varistors prepared from nanomaterials by sol gel route, *Advances in Applied Ceramics*, 105 (2006) 158-160.
- [29] K. Yang, R.T. Pinker, Y. Ma, T. Koike, M.M. Wonsick, S.J .Cox, Y. Zhang, P. Stackhouse, Evaluation of satellite estimates of downward shortwave radiation over the Tibetan Plateau, *Journal of Geophysical Research*, 113 (2008) D17204.

- [30] T. Butkhuzi, A. Bureyev, A. Georgobiani, N. Kekelidze, T. Khulordava, Optical and electrical properties of radical beam gettering epitaxy grown n-and p-type ZnO single crystals, *Journal of Crystal Growth*, 117 (1992) 366-369.
- [31] G. Xiong, J. Wilkinson, B. Mischuck, S. Tuzemen, K. Ucer, R. Williams, Control of p-and n-type conductivity in sputter deposition of undoped ZnO, *Applied Physics Letters*, 80 (2002) 1195-1197.
- [32] M. Alam, D. Cameron, Investigation of annealing effects on sol-gel deposited indium tin oxide thin films in different atmospheres, *Thin Solid Films*, 420 (2002) 82-76.
- [33] Y. Zeng, Z. Ye, W. Xu, J. Lu, H. He, L. Zhu, B. Zhao, Y. Che, S. Zhang, p -type behavior in nominally undoped ZnO thin films by oxygen plasma growth, *Applied physics letters*, 88 (2006) 262103-262103-262103.
- [34] T.M. Børseth, B. Svensson, A.Y. Kuznetsov, P. Klason, Q. Zhao, M. Willander, Identification of oxygen and zinc vacancy optical signals in ZnO, *Applied Physics Letters*, 89 (2006) 262112-262112-262113.
- [35] H.S. Kang, J.S. Kang, J.W. Kim, S.Y. Lee, Annealing effect on the property of ultraviolet and green emissions of ZnO thin films, *Journal of Applied Physics*, 95 (2004) 1246-1250.
- [36] K. Nam, H. Kim, H. Lee, D. Han, J. Lee, Electrical and optical properties of undoped p-type ZnO films, *Surface and Coatings Technology*, 202 (2008) 5463-5466.
- [37] M.S. Oh, S.H. Kim, T.Y. Seong, Growth of nominally undoped p -type ZnO on Si by pulsed-laser deposition, *Applied Physics Letters*, 87 (2005) 122103-122103-122103.
- [38] F. Shan, G. Liu, W. Lee, B. Shin, The role of oxygen vacancies in epitaxial-deposited ZnO thin films, *Journal of Applied Physics*, 101 (2007) 053106-053106-053108.
- [39] J. Huang, H. Lu, Z. Ye, L. Wang, B. Zhao, H. He, Microstructure and defect investigations of the as-grown and annealed ZnO/Si thin films, *Journal of Applied Physics*, 102 (2007) 053521-053521-053525.
- [40] A.L. Efros, A.L. Efros, Interband absorption of light in a semiconductor sphere, *Sov. Phys. Semicond.*, 16 (1982).
- [41] D. Brust, J. Phillips, F. Bassani, Critical points and ultraviolet reflectivity of semiconductors, *Physical Review Letters*, 9 (1962) 94-97.
- [42] T. Vossmeier, L. Katsikas, M. Giersig, I. Popovic, K. Diesner, A. Chemseddine, A. Eychmüller, H. Weller, CdS nanoclusters: synthesis, characterization, size dependent oscillator strength, temperature shift of the excitonic transition energy, and reversible absorbance shift, *The Journal of Physical Chemistry*, 98 (1994) 7665-7673.
- [43] A. Goldstein, C. Echer, A. Alivisatos, Melting in semiconductor nanocrystals, *Science (New York, NY)*, 256 (1992) 1425.

- [44] R. Rossetti, S. Nakahara, L. Brus, Quantum size effects in the redox potentials, resonance Raman spectra, and electronic spectra of CdS crystallites in aqueous solution, *The Journal of Chemical Physics*, 79 (1983) 1088-1086)
- [45] S. Wang, C. Shan, B. Yao, B. Li, J. Zhang, D. Zhao, D. Shen, X. Fan, Electrical and optical properties of ZnO films grown by molecular beam epitaxy, *Applied Surface Science*, 255 (2009) 4913-4915.
- [46] S.H. Tolbert, A. Alivisatos, High-pressure structural transformations in semiconductor nanocrystals, *Annual Review of Physical Chemistry*, 46 (1995) 595-626.
- [47] Y. Kayanuma, Wannier exciton in microcrystals, *Solid State Communications*, 59 (1986) 405-408.
- [48] Y. Kayanuma, Quantum-size effects of interacting electrons and holes in semiconductor microcrystals with spherical shape, *Physical Review B*, 38 (1988) 9797.
- [49] J.C. Slater, G. Koster, Simplified LCAO method for the periodic potential problem, *Physical Review*, 94 (1954) 1498.
- [50] R. Viswanatha, S. Sapra, B. Satpati, P. Satyam, B. Dev, D. Sarma, Understanding the quantum size effects in ZnO nanocrystals, *Journal of Materials Chemistry*, 14 (2004) 661-668.
- [51] D. Mittleman, R. Schoenlein, J. Shiang, V. Colvin, A. Alivisatos, C. Shank, Quantum size dependence of femtosecond electronic dephasing and vibrational dynamics in CdSe nanocrystals, *Physical Review B*, 49 (1994) 14435.
- [52] B. Dabbousi, J. Rodriguez-Viejo, F.V. Mikulec, J. Heine, H. Mattoussi, R. Ober, K. Jensen, M. Bawendi, (CdSe) ZnS core-shell quantum dots: synthesis and characterization of a size series of highly luminescent nanocrystallites, *The Journal of Physical Chemistry B*, 101 (1997) 9463-9475.
- [53] S. Sapra, J. Nanda, D. Sarma, F.A. El-Al, G. Hodes, Blue emission from cysteine ester passivated cadmium sulfide nanoclusters, *Chemical Communications*, (2001) 2188-2189.
- [54] R.D. Beck, P. St John, M.L. Homer, R.L. Whetten, Impact-induced cleaving and melting of alkali-halide nanocrystals, *Science*, 253 (1991) 879-883.
- [55] T. Castro, R. Reifengerger, E. Choi, R.P. Andres, Mechanochemical synthesis of intermetallic compounds, *Phys. Rev. B:Condens. Matter*, 42 (1990).
- [56] T. Martin, U. Näher, H. Schaber, U. Zimmermann, Evidence for a size-dependent melting of sodium clusters, *The Journal of Chemical Physics*, 100 (1994) 2322.
- [57] S. Tolbert, A. Alivisatos, Size dependence of a first order solid-solid phase transition: the wurtzite to rock salt transformation in CdSe nanocrystals, *Science-New York Then Washington-*, (1994) 373-373.

- [58] K. Donaldson, R. Aitken, L. Tran, V. Stone, R. Duffin, G. Forrest, A. Alexander, Carbon nanotubes: a review of their properties in relation to pulmonary toxicology and workplace safety, *Toxicological Sciences*, 92 (2006) 5-22.
- [59] N. Lewinski, V. Colvin, R. Drezek, Cytotoxicity of nanoparticles, *Small*, 4 (2008) 26-49.
- [60] C. Medina, M. Santos-Martinez, A. Radomski, O. Corrigan, M. Radomski, Nanoparticles: pharmacological and toxicological significance, *British Journal of Pharmacology*, 150 (2007) 558-552
- [61] S. Hussain, K. Hess, J. Gearhart, K. Geiss, J. Schlager, In vitro toxicity of nanoparticles in BRL 3A rat liver cells, *Toxicology in Vitro*, 19 (2005) 975-984.
- [62] G. Gattow and H. Schroder, Die Kristallstruktur der hochtemperaturmodifikation von Wismut(III)-oxid (δ -Bi₂O₃), *Z. Anorg. Allg. Chem. Band 318* (1962) 176.
- [63] B. Ekwall, Overview of the final meic results: II. The in vitro- in vivo evaluation, including the selection of a practical battery of cell tests for prediction of acute lethal blood concentrations in humans, *Toxicology in Vitro*, 13 (1999) 665-673.
- [64] R.B. Devlin, M.L. Frampton, A.J. Ghio, In vitro studies: What is their role in toxicology?, *Experimental and Toxicologic Pathology*, 57 (2005) 183-188.
- [65] Daly, W.J., *Experimental stress analysis in steel production*, Brusy Publishers: Orlando, FL, (1967).
- [66] B. Matuschka, Solidification and crystallization of steel ingots: The influence of the casting temperature and the undercooling capacity of the steel, *Iron and Steel Institute (London)*, 124 (1931) 361-376.
- [67] N. Lightfoot, The solidification of molten steel, *Proceedings of The London Mathematical Society*, 2 (1930) 97-116.
- [68] K. Brown, Metal oxide varistor degradation, *IAEI News March*, (2004).
- [69] D. Look, Recent advances in ZnO materials and devices, *Materials Science and Engineering: B*, 80 (2001) 383-387.
- [70] J.D. Norris, L.A. Efron, C.S. Erwin, Doped nanocrystals *Science* 319, (2008) 1776-1779.
- [71] E.M. Brown, ZnO-rediscovered in, *The New Jersey Zinc Company*, New York, 1957.
- [72] D. Reynolds, T. Collins, Excited Terminal States of a Bound Exciton-Donor Complex in ZnO, *Physical Review*, 185 (1969) 1099.
- [73] C. Bunn, The lattice-dimensions of zinc oxide, *Proceedings of The Physical Society*, 47 (2002) 835.
- [74] J. Bwrnasconi, S. Strässler, B. Knecht, H. Klein, A. Menth, Zinc oxide based varistors: a possible mechanism, *Solid State Communications*, 21 (1977) 867-870.

- [75] C. Bayram, F.H. Teherani, D. Rogers, M. Razeghi, A hybrid green light-emitting diode comprised of n-ZnO/(InGaN/GaN) multi-quantum-wells/p-GaN, *Applied Physics Letters*, 93 (2008) 081111.
- [76] Metal oxide varistors, in: *World Market Outlook: 2008-2013* ISBN # 1-893211-34-7, 2008.
- [77] S. Al-Hilli, M. Willander, Membrane potential measurements across a human fat cell using ZnO nanorods, *Nanotechnology*, 20 (2009) 175103.
- [78] J.J. Boland, Semiconductor physics: Transport news, *Nature*, 439 (2006) 671-673.
- [79] R. Dingle, Luminescent transitions associated with divalent copper impurities and the green emission from semiconducting zinc oxide, *Physical Review Letters*, 23 (1969) 579-581.
- [80] S.C. Erwin, L. Zu, M.I. Haftel, A.L. Efros, T.A. Kennedy, D.J. Norris, Doping semiconductor nanocrystals, *Nature*, 436 (2005) 91-94.
- [81] T. Heinzel, *Mesoscopic electronics in solid state nanostructures*, 2nd ed., Wiley-VCH, 2007.
- [82] C. Jagadish, S.J. Pearton, *Zinc oxide bulk, thin films and nanostructures: processing, properties, and applications*, Elsevier Science, 2006.
- [83] Z. Jing, J. Zhan, Fabrication and gas-sensing properties of porous ZnO nanoplates, *Advanced Materials*, 20 (2008) 4547-4551.
- [84] K. Johnston, M.O. Henry, D.M. Cabe, T. Agne, T. Wichert, Proceedings of the Second Workshop on "SOXESS european network on ZnO", in, Caernarfon, Wales, UK., 2004.
- [85] P.H. Kasai, Electron spin resonance studies of donors and acceptors in ZnO, *Physical Review*, 130 (1963) 989.
- [86] P. Klason, T. Moe Børseth, Q.X. Zhao, B.G. Svensson, A.Y. Kuznetsov, P.J. Bergman, M. Willander, Temperature dependence and decay times of zinc and oxygen vacancy related photoluminescence bands in zinc oxide, *Solid State Communications*, 145 (2008) 321-326.
- [87] L. Liao, H. Lu, J. Li, C. Liu, D. Fu, Y. Liu, The sensitivity of gas sensor based on single ZnO nanowire modulated by helium ion radiation, *Applied Physics Letters*, 91 (2007) 173110-173110-173113.
- [88] Z.M. Liao, K.J. Liu, J.M. Zhang, J. Xu, D.P. Yu, Effect of surface states on electron transport in individual ZnO nanowires, *Physics Letters A*, 367 (2007) 207-210.
- [89] Z.M. Liao, H.Z. Zhang, Y.B. Zhou, J. Xu, J.M. Zhang, D.P. Yu, Surface effects on photoluminescence of single ZnO nanowires, *Physics Letters A*, 372 (2008) 4505-4509.
- [90] S. Lima, F. Sigoli, M. Jafelicci Jr, M. Davolos, Luminescent properties and lattice defects correlation on zinc oxide, *International Journal of Inorganic Materials*, 3 (2001) 749-754.

- [91] B. Lin, Z. Fu, Y. Jia, Green luminescent center in undoped zinc oxide films deposited on silicon substrates, *Applied Physics Letters*, 79 (2001) 943-945.
- [92] Y.Y. Lin, Y.Y. Lee, L. Chang, J.J. Wu, C.W. Chen, The influence of interface modifier on the performance of nanostructured ZnO/polymer hybrid solar cells, *Applied Physics Letters*, 94 (2009) 063308-063308-063303.
- [93] M. Liu, A. Kitai, P. Mascher, Point defects and luminescence centres in zinc oxide and zinc oxide doped with manganese, *Journal of luminescence*, 54 (1992) 35-42.
- [94] H.P. Myers, *Introductory solid state physics*, in, Taylor and Francis Publisher. , Chalmers University of Technology, Sweden, 1997.
- [95] U. Ozgur, Y.I. Alivov, C. Liu, A. Teke, M. Reshchikov, S. Dogan, V. Avrutin, S.J. Cho, H. Morkoc, A comprehensive review of ZnO materials and devices, *Journal of Applied Physics*, 98 (2005) 041301-041301-041103.
- [96] E.F. Schubert, *Light-emitting diodes*, 2nd ed., Cambridge University Press, 2006.
- [97] Z. Seow, A. Wong, V. Thavasi, R. Jose, S. Ramakrishna, G. Ho, Controlled synthesis and application of ZnO nanoparticles, nanorods and nanospheres in dye-sensitized solar cells, *Nanotechnology*, 20 (2008) 04560.4
- [98] I. Shalish, H. Temkin, V. Narayanamurti, Size-dependent surface luminescence in ZnO nanowires, *Physical Review B*, 69 (2004) 245401_245401-245401_245404.
- [99] G.A. Somorjai, *The surface chemical bond*, *Angewandte Chemie International Edition in English*, 16 (1977) 92-99.
- [100] A. Umar, M. Rahman, S. Kim, Y. Hahn, ZnO nanonails: Synthesis and their application as glucose biosensor, *Journal of Nanoscience and Nanotechnology*, 8 (2008) 3216-3221.
- [101] K. Vanheusden, W. Warren, C. Seager, D. Tallant, J. Voigt, B. Gnade, Mechanisms behind green photoluminescence in ZnO phosphor powders, *Journal of Applied Physics*, 79 (1996) 7983-7990.
- [102] Q. Wan, T. Wang, J. Zhao, Enhanced photocatalytic activity of ZnO nanotetrapods, *Applied Physics Letters*, 87 (2005).083103-083105
- [103] A. Wei, X.W. Sun, J. Wang, Y. Lei, X. Cai, C.M. Li, Z.L. Dong, W. Huang, Enzymatic glucose biosensor based on ZnO nanorod array grown by hydrothermal decomposition, *Applied Physics Letters*, 89 (2006) 123902-123902-123903.
- [104] M. Willander, L. Yang, A. Wadeasa, S. Ali, M. Asif, Q. Zhao, O. Nur, Zinc oxide nanowires: controlled low temperature growth and some electrochemical and optical nano-devices, *Journal of Materials Chemistry*, 19 (2009) 1006-1018.
- [105] X. Wu, G. Siu, C. Fu, H. Ong, Photoluminescence and cathodoluminescence studies of stoichiometric and oxygen-deficient ZnO films, *Applied Physics Letters*, 78 (2001) 2285-2287.

- [106] P. Xu, Y. Sun, C. Shi, F. Xu, H. Pan, The electronic structure and spectral properties of ZnO and its defects, *Nuclear Instruments and Methods in Physics Research Section B: Beam Interactions with Materials and Atoms*, 199 (2003) 286-290.
- [107] S. Yamauchi, Y. Goto, T. Hariu, Photoluminescence studies of undoped and nitrogen-doped ZnO layers grown by plasma-assisted epitaxy, *Journal of Crystal Growth*, 260 (2004) 1-6.
- [108] J. Yang, L. Yang, Y. Zhang, D. Wang, J. Lang, Q. Zhao, Investigation on the origin of green light emission in ZnO bulk materials, *International Journal of Materials and Product Technology*, 34 (2009) 360-368.
- [109] K. Yang, G.W. She, H. Wang, X.M. Ou, X.H. Zhang, C.S. Lee, S.T. Lee, ZnO nanotube arrays as biosensors for glucose, *The Journal of Physical Chemistry C*, 113 (2009) 20169-20172.
- [110] L.L. Yang, Synthesis and characterization of ZnO nanostructures, in, Linköping, 2010.
- [111] X. Yang, G. Du, X. Wang, J. Wang, B. Liu, Y. Zhang, D. Liu, H.C. Ong, S. Yang, Effect of post-thermal annealing on properties of ZnO thin film grown on c-Al₂O₃ by metal-organic chemical vapor deposition, *J. Cryst. Growth* (2003) 275-278.
- [112] J. Ye, S. Gu, F. Qin, S. Zhu, S. Liu, X. Zhou, W. Liu, L. Hu, R. Zhang, Y. Shi, Correlation between green luminescence and morphology evolution of ZnO films, *Applied Physics A: Materials Science & Processing*.762-759 (2005) 81
- [113] H. Zhang, J. Wu, C. Zhai, N. Du, X. Ma, D. Yang, From ZnO nanorods to 3D hollow microhemispheres: solvothermal synthesis, photoluminescence and gas sensor properties, *Nanotechnology*, 18 (2007) 455604.
- [114] P. Zhang, E. Tevaarwerk ,B.N. Park, D.E. Savage, G.K. Celler, I. Knezevic, P.G. Evans, M.A. Eriksson, M.G. Lagally, Electronic transport in nanometre-scale silicon-on-insulator membranes, *Nature*, 439 (2006) 703-706.
- [115] Q. Zhao, P. Klason, M. Willander, H. Zhong, W. Lu, J. Yang, Deep-level emissions influenced by O and Zn implantations in ZnO, *Applied Physics Letters*, 87 (2005) 211912-211912-211913.
- [116] J. Zhong, A.H. Kitai, P. Mascher, W. Puff, The influence of processing conditions on point defects and luminescence centers in ZnO, *Journal of The Electrochemical Society*, 140 (1993) 3644-3649.
- [117] A. Wadeasa, Heterojunctions between zinc oxide nanostructures and organic semiconductor, in: Master, Linköping Studies in Science and Technology, 2011.
- [118] T. Olorunyolemi, A .Birnboim, Y. Carmel, O.C. Wilson Jr, I.K. Lloyd, S. Smith, R. Campbell, Thermal conductivity of zinc oxide: from green to sintered state, *Journal of the American Ceramic Society*, 85 (2002) 1249-1253.
- [119] D. Florescu, L. Mourokh, F.H. Pollak, D. Look ,G. Cantwell, X. Li, High spatial resolution thermal conductivity of bulk ZnO (0001), *Journal of Applied Physics*, 91 (2002) 890-892.

- [120] C. Klingshirn, ZnO: from basics towards applications, *Physica Status Solidi (b)*, 244 (2007) 3027-3073.
- [121] E.H. Kisi, M.M. Elcombe, u parameters for the wurtzite structure of ZnS and ZnO using powder neutron diffraction, *Acta Crystallographica Section C: Crystal Structure Communications*, 45 (1989) 1867-1870.
- [122] Z.L. Wang, Piezoelectric nanostructures: from growth phenomena to electric nanogenerators, *MRS Bulletin*, 32 (2007) 109-116.
- [123] M. Hassellöv, J.W. Readman, J.F. Ranville, K. Tiede, Nanoparticle analysis and characterization methodologies in environmental risk assessment of engineered nanoparticles, *Ecotoxicology*, 17 (2008) 344-361.
- [124] D. Thomas, The exciton spectrum of zinc oxide, *Journal of Physics and Chemistry of Solids*, 15 (1960) 86-96.
- [125] E. Bylander, Surface effects on the low-energy cathodoluminescence of zinc oxide, *Journal of Applied Physics*, 49 (1978) 1188-1195.
- [126] Y. Chen, J. Jiang, Z. He, Y. Su, D. Cai, L. Chen, Growth mechanism and characterization of ZnO microbelts and self-assembled microcombs, *Materials Letters*, 59 (2005) 3280-3283.
- [127] A.B. Djurišić, Y.H. Leung, Optical properties of ZnO nanostructures, *Small*, 2 (2006) 944-961.
- [128] M. Gomi, N. Oohira, K. Ozaki, M. Koyano, Photoluminescent and structural properties of precipitated ZnO fine particles, *Japanese Journal of Applied Physics*, 42 (2003) 481-485.
- [129] L.E. Greene, M. Law, J. Goldberger, F. Kim, J.C. Johnson, Y. Zhang, R.J. Saykally, P. Yang, Low-temperature wafer-scale production of ZnO nanowire arrays, *Angewandte Chemie International Edition*, 42 (2003) 3031-3034.
- [130] A. Janotti, C.G. Van de Walle, Absolute deformation potentials and band alignment of wurtzite ZnO, MgO, and CdO, *Physical Review B*, 75 (2007) 121201.
- [131] D. Li, Y. Leung, A. Djurišić, Z. Liu, M. Xie, S. Shi, S. Xu, W. Chan, Different origins of visible luminescence in ZnO nanostructures fabricated by the chemical and evaporation methods, *Applied Physics Letters*, 85 (2004) 1601.
- [132] X. Liu, X. Wu, H. Cao, R. Chang, Growth mechanism and properties of ZnO nanorods synthesized by plasma-enhanced chemical vapor deposition, *Journal of Applied Physics*, 95 (2004) 3141-3147.
- [133] X. Meng, D. Shen, J. Zhang, D. Zhao, Y. Lu, L. Dong, Z. Zhang, Y. Liu, X. Fan, The structural and optical properties of ZnO nanorod arrays, *Solid State Communications*, 135 (2005) 179-182.
- [134] F. Tuomisto, K. Saarinen, D. Look, G. Farlow, Introduction and recovery of point defects in electron-irradiated ZnO, *Physical Review B*, 72 (2005) 085206.

- [135] A. Ashrafi, C. Jagadish, Review of zincblende ZnO: Stability of metastable ZnO phases, *Journal of Applied Physics*, 102 (2007) 071101-071102.
- [136] A. Ashrafi, A. Ueta, A. Avramescu, H. Kumano, I. Suemune, Y.W. Ok, T.Y. Seong, Growth and characterization of hypothetical zinc-blende ZnO films on GaAs (001) substrates with ZnS buffer layers, *Applied Physics Letters*, 76 (2000) 550-552.
- [137] C.H. Bates, W.B. White, R. Roy, New high-pressure polymorph of zinc oxide, *Science*, 137 (1962) 993.
- [138] J.E. Jaffe, J.A. Snyder, Z. Lin, A.C. Hess, LDA and GGA calculations for high-pressure phase transitions in ZnO and MgO, *Physical Review B*, 62 (2000) 1660.
- [139] T. Kogure, S. Karasawa, T. Araki, K. Saito, M. Kinjo, A. Miyawaki, A fluorescent variant of a protein from the stony coral *Montipora* facilitates dual-color single-laser fluorescence cross-correlation spectroscopy, *Nature Biotechnology*, 24 (2006) 577-581.
- [140] A. Janotti, C.G. Van de Walle, Native point defects in ZnO, *Physical Review B*, 76 (2007) 165202.
- [141] Z. Fan, P. Chang, J.G. Lu, E.C. Walter, R.M. Penner, C. Lin, H.P. Lee, Photoluminescence and polarized photodetection of single ZnO nanowires, *Applied Physics Letters*, 85 (2004) 6128-6130.
- [142] C.H. Ahn, Y.Y. Kim, D.C. Kim, S.K. Mohanta, H.K. Cho, A comparative analysis of deep level emission in ZnO layers deposited by various methods, *Journal of Applied Physics*, 105 (2009) 013502-013505.
- [143] N. Alvi, S. Usman Ali, S. Hussain, O. Nur, M. Willander, Fabrication and comparative optical characterization of n-ZnO nanostructures (nanowalls, nanorods, nanoflowers and nanotubes)/p-GaN white-light-emitting diodes, *Scripta Materialia*, 64 (2011) 697-700.
- [144] N. Garces, L. Wang, L. Bai, N. Giles, L. Halliburton, G. Cantwell, Role of copper in the green luminescence from ZnO crystals, *Applied Physics Letters*, 81 (2002) 622-624.
- [145] Y. Heo, D. Norton, S. Pearton, Origin of green luminescence in ZnO thin film grown by molecular-beam epitaxy, *Journal of Applied Physics*, 98 (2005) 073502-073502-073506.
- [146] Y. Leung, K. Tam, A. Djurišić, M. Xie, W. Chan, D. Lu, W. Ge, ZnO nanoshells: synthesis, structure, and optical properties, *Journal of Crystal Growth*, 283 (2005) 134-140.
- [147] D. Reynolds, D. Look, B. Jogai, Fine structure on the green band in ZnO, *Journal of Applied Physics*, 89 (2001) 6189-6191.
- [148] A. Van Dijken, E. Meulenkaamp, D. Vanmaekelbergh, A. Meijerink, Identification of the transition responsible for the visible emission in ZnO using quantum size effects, *Journal of Luminescence*, 90 (2000) 123-128.

- [149] A. Van Dijken, E.A. Meulenkaamp, D. Vanmaekelbergh, A. Meijerink, The kinetics of the radiative and nonradiative processes in nanocrystalline ZnO particles upon photoexcitation, *The Journal of Physical Chemistry B*, 104 (2000) 1715-1723.
- [150] K. Vanheusden, C. Seager, W. Warren, D. Tallant, J. Voigt, Correlation between photoluminescence and oxygen vacancies in ZnO phosphors, *Applied Physics Letters*, 68 (1996) 403-405.
- [151] D.C. Reynolds, D.C. Look, B. Jogai, H. Morkoc, Similarities in the bandedge and deep-center photoluminescence mechanisms of ZnO and GaN, *Solid State Communications*, 101 (1997) 643.
- [152] S. Studenikin, N. Golego, M. Cocivera, Fabrication of green and orange photoluminescent, undoped ZnO films using spray pyrolysis, *Journal of Applied Physics*, 84 (1998) 2287-2294.
- [153] R. Knox, *Theory of Excitons*, Suppl. 5 of solid state physics, New York 1963.
- [154] M. Willander, O. Nur, Q. Zhao, L. Yang, M. Lorenz, B. Cao, J.Z. Pérez, C. Czekalla, G. Zimmermann, M. Grundmann, Zinc oxide nanorod based photonic devices: recent progress in growth, light emitting diodes and lasers, *Nanotechnology*, 20 (2009) 332001.
- [155] R. Cross, M. De Souza, E.M.S. Narayanan, A low temperature combination method for the production of ZnO nanowires, *Nanotechnology*, 16 (2005) 2188.
- [156] J.L. Freeouf, Far-ultraviolet reflectance of II-VI compounds and correlation with the penn—phillips gap, *Physical Review B*, 7 (1973) 3810
- [157] F. Kröger, H. Vink, The origin of the fluorescence in self-activated ZnS, CdS, and ZnO, *The Journal of Chemical Physics*, 22 (1954) 250.
- [158] W. Kwok, A. Djurisc, Y. Leung, W. Chan, D. Phillips, Time-resolved photoluminescence study of the stimulated emission in ZnO nanoneedles, *Applied Physics Letters*, 87 (2005) 093108-093108-093103.
- [159] O. Schirmer, D. Zwingel, The yellow luminescence of zinc oxide, *Solid State Communications*, 8 (1970) 1559-15.63
- [160] D. Zwingel, Trapping and recombination processes in the thermoluminescence of Li-doped ZnO single crystals, *Journal of Luminescence*, 5 (1972) 385-405.
- [161] C.G. Van de Walle, Hydrogen as a cause of doping in zinc oxide, *Physical Review Letters*, 85 (2000) 1012-1015.
- [162] V. Mohanraj, Y. Chen, Nanoparticles-a review, *Tropical Journal of Pharmaceutical Research*, 5 (2007) 561-573.
- [163] F. Reuss, C. Kirchner, T. Gruber, R. Kling, S. Maschek, W. Limmer, A. Waag, P. Ziemann, Optical investigations on the annealing behavior of gallium-and nitrogen-implanted ZnO, *Journal of Applied Physics*, 95 (2004) 3385-3390.
- [164] D.C. Reynolds, T.C. Collins, *Excitons: their properties and uses*, (1981).

- [165] G.E. Pike, Semiconducting polycrystalline ceramics, *J. Material Science and Technology*, 11 (1994) 731-754.
- [166] S. Nozaki, S. Sato, H. Ono, H. Morisaki, Blue Light Emission from Silicon Ultrafine Particles, in: *MRS Proceedings*, Cambridge Univ Press, 1994.
- [167] R.C. Dugan, M.F.M. Granaghan, S. Santoso, H.B .Wayne, Electrical power systems quality, in, McGraw-Hill Publication, 2003.
- [168] M. Matsuoka, Discovery of znO varistors and their progress for the two decades, in, Matsushita Electronic Components Co., Ltd, 1006 Kadoma Osaka 571, Japan, 1982, pp. 3-21.
- [169] A. Lagrange, Present and future of zinc oxide varistors, in, Thomson Corporation Publications, France, 1992.
- [170] A. Wang, H. Feng, K. Gong, R. Zhan, J. Stine, On-chip ESD protection design for integrated circuits: an overview for IC designers, *Microelectronics Journal*, 32 (2001) 733-747.
- [171] J. Harden, et al., Littelfuse varistrors- basic properties, terminology and theory, Application Note. AN.9767.1, (1999).
- [172] D.R. Clarke, Varistor ceramics, *Journal of The American Ceramic Society*, 82 (1999) 485-502.
- [173] T.K. Gupta, Engineered materials handbook, in, ASM Publication, 1991, pp. 1150-1155.
- [174] Thomson-CSF, Zinc oxide varistors catalogue manual, in, Thomson-CSF Corporate Publications, 1992.
- [175] M. Elfwing, Nanoscale characterisation of barriers to electron conduction in ZnO varistor materials, in, Uppsala University, 2002.
- [176] R.C. Dugan, S. Santoso, M.F. McGranaghan, H. Wayne Beaty, Electrical power systems quality, McGraw-Hill New York, 2003.
- [177] D. Fernandez-Hevia, J. De Frutos ,A. Caballero, J. Fernández, Bulk-grain resistivity and positive temperature coefficient of ZnO-based varistors, *Applied Physics Letters*, 82 (2003) 212-214.
- [178] M. Inada, Microstructure of nonohmic zinc oxide ceramics, *Jpn. J. Appl. Phys*, 17 (1978) 673-677.
- [179] M. Inada, Crystal phases of non-ohmic zinc oxide ceramics, *Jpn. J. Appl. Phys*, 17 (1978) 1-10.
- [180] M. Inada, Formation mechanism of nonohmic zinc oxide ceramics, *Jpn. J. Appl. Phys*, 19 (1980) 409-419.
- [181] J. Wong, Microstructure and phase transformation in a highly non-ohmic metal oxide varistor ceramic, *Journal of Applied Physics*, 46 (1975) 1653-1659.

- [182] A. Santhanam, T. Gupta, W. Carlson, Microstructural evaluation of multicomponent ZnO ceramics, *Journal of Applied Physics*, 50 (1979) 852-859.
- [183] E. Olsson, G. Dunlop, R. Österlund, Development of functional microstructure during sintering of a ZnO varistor material, *Journal of the American Ceramic Society*, 76 (1993) 65-71.
- [184] J. Wong, Sintering and varistor characteristics of ZnO-Bi₂O₃ ceramics, *Journal of Applied Physics*, 51 (1980) 4453-4459.
- [185] K. Eda, Zinc oxide varistors, *Electrical Insulation Magazine, IEEE*, 5 (1989) 28-30.
- [186] J.W. Medernach, R.L. Snyder, Powder diffraction patterns and structures of the bismuth oxides, *Journal of the American Ceramic Society*, 61 (2006) 494-497.
- [187] T. Takemura, M. Kobayashi, Y. Takada, K. SATO, Effects of bismuth sesquioxide on the characteristics of ZnO varistors, *Journal of the American Ceramic Society*, 69 (1986) 430-436.
- [188] E.M. Levin, R.S. Roth, Polymorphism of bismuth sesquioxide. II. effect of oxide additions on the polymorphism of Bi₂O₃, *Journal of Research of The National Bureau of Standards - A Physics and Chemistry*, 68 (1964) 197-206.
- [189] S.N. Bai, T.Y. Tseng, Influence of cooling rate on electrical-properties of zinc oxide-based varistors, *Jpn. J. Appl. Phys. Vol. 31* (1992).
- [190] M. Tsubaki, K. Koto, Superstructures and phase transitions of Bi₂O₃, *Materials Research Bulletin*, 19 (1984) 1613-1620.
- [191] Y. Chiang, H. Wang, J. Lee, HREM and STEM of intergranular films at zinc oxide varistor grain boundaries, *Journal of Microscopy*, 191 (1998) 275-285.
- [192] F. Greuter, G. Blatter, Electrical properties of grain boundaries in polycrystalline compound semiconductors, *Semiconductor Science and Technology*, 5 (1990) 110-137.
- [193] D. Clarke, Grain-boundary segregation in a commercial ZnO-based varistor, *Journal of Applied Physics*, 50 (1979) 6829-6832.
- [194] D.R. Clarke, The microstructural location of the intergranular metal-oxide phase in a zinc oxide varistor, *Journal of Applied Physics*, 49 (1978) 2407-2411.
- [195] W.D. Kingery, J.B. Sande, T. Mitamura, A scanning transmission electron microscopy investigation of grain-boundary segregation in a ZnO-Bi₂O₃ varistor, *Journal of The American Ceramic Society*, 62 (2006) 221-222.
- [196] E. Olsson, L. Falk, G. Dunlop, R. Österlund, The microstructure of a ZnO varistor material, *Journal of Materials Science*, 20 (1985) 4091-4098.
- [197] W.G. Morris, Physical properties of the electrical barriers in varistors, *Journal of Vacuum Science and Technology*, 13 (1976) 926-931.
- [198] F. Stucki, P. Brüesch, F. Greuter, Electron spectroscopic studies of electrically active grain boundaries in ZnO, *Surface Science*, 189 (1987) 294-299.

- [199] H. Wang, Y.M. Chiang, Thermodynamic stability of intergranular amorphous films in bismuth-doped zinc oxide, *Journal of the American Ceramic Society*, 81 (1998) 89-96.
- [200] E. Olsson, G.L. Dunlop, Characterization of individual interfacial barriers in a ZnO varistor material, *Journal of Applied Physics*, 66 (1989) 3666-3675.
- [201] K.K. Ng, Complete guide to semiconductor devices, in, McGraw Hill, New York, 1995, pp. 372-408.
- [202] Shahrom Mahmud, The effects of zinc oxide microstructure on the electrical characteristics of low-voltage ceramic varistors, in: School of physics, USM, Malaysia, 2004, pp. 296.
- [203] V. Associates, ZnO varistors –the evolution of a technology.
- [204] R.E. Stephens, I.H. Malitson, Index of refraction of magnesium oxide, *J. Res. Nat. Bur. Stand*, 49 (1952) 249-252.
- [205] S. Hingorani, D. Shah, M. Multani, Effect of process variables on the grain growth and microstructure of ZnO-Bi₂O₃ varistors and their nanosize ZnO precursors, *Journal of Materials Research*, 10 (1995) 461-467.
- [206] P. Bueno, M. de Cassia-Santos, E. Leite, E. Longo, J. Bisquert, G. Garcia-Belmonte, F. Fabregat-Santiago, Nature of the Schottky-type barrier of highly dense SnO systems displaying nonohmic behavior, *Journal of Applied Physics*, 88 (2000) 6545.
- [207] A.B. Alles, V.L. Burdick, The effect of liquid-phase sintering on the properties of Pr₆O₁₁-based ZnO varistors, *Journal of Applied Physics*, 70 (1991) 6883-6890.
- [208] C.S. Chen, C.T. Kuo, I.N. Lin, Improvement on the degradation of microwave sintered ZnO varistors by postannealing, *Journal of Materials Research*, 13 (1998) 1560-1567.
- [209] C.W. Nan, A. Tschope, S. Holten, H. Kliem, R. Birringer, Grain size-dependent electrical properties of nanocrystalline ZnO, *Journal of Applied Physics*, 85 (1999) 7735-7740.
- [210] S. Pianaro, P. Bueno, P. Olivi, E. Longo, J. Varela, Effect of Bi₂O₃ addition on the microstructure and electrical properties of the SnO₂. CoO. Nb₂O₅ varistor system, *Journal of Materials Science letters*, 16 (1997) 634-638.
- [211] A.L. Efros, A. Efros, Interband absorption of light in a semiconductor sphere, *Sov. Phys. Semicond.*, 16 (1982).
- [212] J.R. Lee, Y.M. Chiang, Bi segregation at ZnO grain boundaries in equilibrium with Bi₂O₃-ZnO liquid, *Solid State Ionics*, 75 (1995) 79-88.
- [213] J.R. Lee, Y.M. Chiang, G. Ceder, Pressure-thermodynamic study of grain boundaries: Bi segregation in ZnO, *Acta Materialia*, 45 (1997) 1247-1257.
- [214] Y.-M. Chiang, Mass and charge transport in ceramics, in, American Ceramic Soc.Inc, Nagoya., 1996, pp. 79-89.

- [215] K.-I. Kobayashi, O. Wada, M. Kobayashi, Y. Takada, Continuous existence of bismuth at grain boundaries of zinc oxide varistor without intergranular phase, *J. American Ceramic Society*, 81 (1998) 2071-2076.
- [216] P. Bueno, E. Leite, M. Oliveira, M. Orlandi, E. Longo, Role of oxygen at the grain boundary of metal oxide varistors: A potential barrier formation mechanism, *Applied Physics Letters*, 79 (2001) 48-50.
- [217] A. Peigney, A. Rousset, Phase transformations and melting effects during the sintering of bismuth-doped zinc oxide powders, *Journal of the American Ceramic Society*, 79 (2005) 2113-2126.
- [218] L. Beneš, V. Rambousek, M. PŘedota, J. Horak, Interaction of zinc oxide with bismuth oxide, *Journal of Materials Science*, 21 (1986) 3345-3347.
- [219] J.M. Carlsson, B. Hellsing, H.S. Domingos, P.D. Bristowe, Theoretical investigation of the pure and Zn-doped α and δ phases of Bi_2O_3 , *Physical Review B*, 65 (2002) 205122.
- [220] J. Han, P. Mantas, A. Senos, Effect of Al and Mn doping on the electrical conductivity of ZnO, *Journal of The European Ceramic Society*, 21 (2001) 1883-1886.
- [221] J. Han, P. Mantas, A. Senos, Defect chemistry and electrical characteristics of undoped and Mn-doped ZnO, *Journal of The European Ceramic Society*, 22 (2002) 49-59.
- [222] M. Srikanth, In vitro cytotoxicity tests of nanomaterials on 3T3 and 1929 cancerous cells, in, Wichita State University, 2012.
- [223] V. Sharma, R.K. Shukla, N. Saxena, D. Parmar, M. Das, A. Dhawan, DNA damaging potential of zinc oxide nanoparticles in human epidermal cells, *Toxicology Letters*, 185 (2009) 211-218.
- [224] C.M. Sayes, K.L. Reed, D.B. Warheit, Assessing toxicity of fine and nanoparticles: comparing in vitro measurements to in vivo pulmonary toxicity profiles, *Toxicological Sciences*, 97 (2007) 163-180.
- [225] C.-C. Huang, R.S. Aronstam, D.-R. Chen, Y.-W. Huang, Oxidative stress, calcium homeostasis, and altered gene expression in human lung epithelial cells exposed to ZnO nanoparticles, *Toxicology in Vitro*, 24 (2010) 45-55.
- [226] P.J. Moos, K. Chung, D. Woessner, M. Honegger, N.S. Cutler, J.M. Veranth, ZnO particulate matter requires cell contact for toxicity in human colon cancer cells, *Chemical Research in Toxicology*, 23 (2010) 733-739.
- [227] D. Warheit, C. Sayes, K. Reed, Nanoscale and fine zinc oxide particles: can in vitro assays accurately forecast lung hazards following inhalation exposures?, *Environmental Science & Technology*, 43 (2009) 7939-7945.
- [228] J. Zhao, L. Xu, T. Zhang, G. Ren, Z. Yang, Influences of nanoparticle zinc oxide on acutely isolated rat hippocampal CA3 pyramidal neurons, *Neurotoxicology*, 30 (2009) 220-230

- [229] R.W. Siegel, G.E. Fougere, Nanophase materials in, Kluwer Academic Publishers, Netherlands, 1994, pp. 233-261
- [230] T. Chatterjee, S. Chakraborti, P. Joshi, S.P. Singh, V .Gupta, P. Chakrabarti, The effect of zinc oxide nanoparticles on the structure of the periplasmic domain of the *Vibrio cholerae* ToxR protein, *FEBS Journal*, 277 (2010) 4184-4194.
- [231] A. Verma, O. Uzun, Y. Hu, Y. Hu, H.-S. Han, N. Watson, S. Chen, D.J. Irvine, F. Stellacci, Surface-structure-regulated cell-membrane penetration by monolayer-protected nanoparticles, *Nature Materials*, 7 (2008) 588-595.
- [232] R.A. Colvin, C.P. Fontaine, M. Laskowski, D. Thomas, Zn²⁺ transporters and Zn²⁺ homeostasis in neurons, *European Journal of Pharmacology*, 479 (2003) 171-185.
- [233] C.-L. Ho, S.-S. Teo, R.A. Rahim, S.-M. Phang, Transcripts of *Gracilaria changii* that improve copper tolerance of *Escherichia coli*, *Asia-Pacific Journal of Molecular Biology and Biotechnology* 18 (2010) 315-319.
- [234] Y. Toduka, T. Toyooka, Y. Ibuki, Flow cytometric evaluation of nanoparticles using side-scattered light and reactive oxygen species-mediated fluorescence–correlation with genotoxicity, *Environmental Science & Technology*, 46 (2012) 7629-7636.
- [235] D.X. Zhang, D.D. Gutterman, Mitochondrial reactive oxygen species-mediated signaling in endothelial cells, *American Journal of Physiology-Heart and Circulatory Physiology*, 292 (2007) H2023-H2031.
- [236] B. De Berardis, G. Civitelli, M. Condello, P. Lista, R. Pozzi, G. Arancia, S. Meschini, Exposure to ZnO nanoparticles induces oxidative stress and cytotoxicity in human colon carcinoma cells, *Toxicology and Applied Pharmacology*, 246 (2010) 116-127.
- [237] T. Xia, M. Kovoichich, M. Liong, L .Mädler, B. Gilbert, H. Shi, J.I. Yeh, J.I. Zink, A.E. Nel, Comparison of the mechanism of toxicity of zinc oxide and cerium oxide nanoparticles based on dissolution and oxidative stress properties, *ACS Nano*, 2 (2008) 2121-2134.
- [238] K. Pulskamp, S. Diabaté, H.F. Krug, Carbon nanotubes show no sign of acute toxicity but induce intracellular reactive oxygen species in dependence on contaminants, *Toxicology Letters*, 168 (2007) 58-74.
- [239] Y. Yamakoshi, N. Umezawa, A. Ryu, K. Arakane, N. Miyata, Y. Goda ,T. Masumizu, T. Nagano, Active oxygen species generated from photoexcited fullerene (C60) as potential medicines: O₂-versus 1O₂, *Journal of the American Chemical Society*, 125 (2003) 12803-12809.
- [240] T. Dudev, C. Lim, Metal binding affinity and selectivity in metalloproteins: insights from computational studies, *Annu. Rev. Biophys.*, 37 (2008) 97-116.
- [241] Y. Lu, S.M. Berry, T.D. Pfister, Engineering novel metalloproteins: design of metal-binding sites into native protein scaffolds, *Chemical Reviews*, 101 (2001) 3047-3080.
- [242] L. Rao, Q. Cui, X. Xu, Electronic properties and desolvation penalties of metal ions plus protein electrostatics dictate the metal binding affinity and selectivity in the

- copper efflux regulator, *Journal of the American Chemical Society*, 132 (2010) 18092-18102.
- [243] N. Singh, B. Manshian, G.J. Jenkins, S.M. Griffiths, P.M. Williams, T.G. Maffei, C.J. Wright, S.H. Doak, *NanoGenotoxicology: the DNA damaging potential of engineered nanomaterials*, *Biomaterials*, 30 (2009) 3891-3914.
- [244] S.J. Soenen, U. Himmelreich, N. Nuytten, T.R. Pisanic, A. Ferrari, M. De Cuyper, Intracellular nanoparticle coating stability determines nanoparticle diagnostics efficacy and cell functionality, *Small*, 6 (2010) 2136-2145.
- [245] D.M. Brown, K. Donaldson, P.J. Borm, R. Schins, M. Dehnhardt, P. Gilmour, L. Jimenez, V. Stone, Calcium and ROS-mediated activation of transcription factors and TNF- α cytokine gene expression in macrophages exposed to ultrafine particles, *American Journal of Physiology-Lung Cellular and Molecular Physiology*, 286 (2004) L344-L353.
- [246] F. Rapp, J. Melnick, Applications of tissue culture methods in the virus laboratory, *Progress in medical virology. Fortschritte der medizinischen virusforschung. Progress en virologie medicale*, 6 (1964) 268.
- [247] G. Bonelli, M.C. Sacchi, G. Barbiero, F. Duranti, G. Goglio, L.V. di Cantogno, J.S. Amenta, M. Piacentini, C. Tacchetti, F.M. Baccino, Apoptosis of L929 cells by etoposide: a quantitative and kinetic approach, *Experimental Cell Research*, 228 (1996) 292-305.
- [248] G. Mahan, L.M. Levinson, H.R. Philipp, Theory of conduction in ZnO varistors, *Journal of Applied Physics*, 50 (1979) 2799-2812.
- [249] C. Seager, G. Pike, Anomalous low-frequency grain-boundary capacitance in silicon, *Applied Physics Letters*, 37 (1980) 747-749.
- [250] C. Seager, G. Pike, Electron tunneling through GaAs grain boundaries, *Applied Physics Letters*, 40 (1982) 471-474.
- [251] A.G. Guy, *Essentials of material science*, in, McGraw-Hill Inc., 1976.
- [252] M.N. Rahaman, *Ceramic processing and sintering*, in, Marcel Dekker Inc. , New your, 1995.
- [253] D.W. Richerson, *Modern ceramic engineering*, in, Marcel Dekker Inc., 1992.
- [254] S. Saito, *Fine ceramics*, in, Tokyo Institute of Technology, Elsevier Applied Science Publisher Ltd, England, 1988.
- [255] Y. Harada, In commemoration of *Journal of Electron Microscopy's* 60th anniversary, *Journal of Electron Microscopy*, 60 (2011) S279-S282.
- [256] V. BCcomponents, *Varistor*, in, 2009.
- [257] J. Goldstein, D.E. Newbury, D.C. Joy, C.E. Lyman, P. Echlin, E. Lifshin, L. Sawyer, J.R. Michael, *Scanning electron microscopy and X-ray microanalysis*, Springer, 2003.

- [258] T.B. Johansson, R. Akselsson, X-ray analysis: Elemental trace analysis at the 10⁻¹² g level, *Nuclear Instruments and Methods*, 84 (1970) 141-143.
- [259] J.F. Shackelford, Introduction to materials science for engineers, in, Prentice Hall International, Inc, 1996.
- [260] V.F.C. Veley, J.S. Parkinson, Christiansens's Electronics Problem-Solving Companion, in, McGraw-Hill, Inc., 2001.
- [261] Scintag, Basics of X-ray diffraction, in, Scintag Inc, 1999
- [262] T.t.a. physics, Discussion – optional: Deriving Bragg's law, in: E.-B. reflection (Ed.) Word, IOP Institute of Physics, 2003.
- [263] W.L. Hughes, Z.L. Wang, Nanobelts as nanocantilevers, *Applied Physics Letters*, 82 (2003) 2886-2888.
- [264] C.C.A.-S. License, Atomic force microscopy, in: A.c.A. setup (Ed.) PNG, Wikimedia Foundation, Inc., 2012.
- [265] H. Hess, E. Betzig, T. Harris, L. Pfeiffer, K. West, Near-field spectroscopy of the quantum constituents of, *Science*, 264 (1994) 17.
- [266] C.C.A.-S. License, Typical experimental set-up for PL measurements, in: P.a.t.-r. spectroscopy (Ed.) PDF, Wikimedia Foundation, Inc.
- [267] E. Smith, G. Dent, J. Wiley, Modern raman spectroscopy: a practical approach, J. Wiley Hoboken, NJ, 2005.
- [268] D.A. Long, D. Long, Raman spectroscopy, McGraw-Hill New York, 1977.
- [269] T.K. Gupta, W.G. Carlson, A grain-boundary defect model for instability/stability of a ZnO varistor, *Journal of Materials Science*, 20 (1985) 3487-3500.
- [270] T.S. Ahmadi, M.A. El-Sayed, Effect of lattice energy mismatch on the relative mass peak intensities of mixed alkali halide nanocrystals, *The Journal of Physical Chemistry A*, 101 (1997) 690-693.
- [271] C.B. Murray, D. Norris, M.G. Bawendi, Synthesis and characterization of nearly monodisperse CdE (E= sulfur, selenium, tellurium) semiconductor nanocrystallites, *Journal of the American Chemical Society*, 115 (1993) 8706-8715.
- [272] D.L. Bish, R. Reynolds, Sample preparation for X-ray diffraction, *Reviews in Mineralogy*, 73 (1989) 20.
- [273] R. Hong, J. Huang, H. He, Z. Fan, J. Shao, Influence of different post-treatments on the structure and optical properties of zinc oxide thin films, *Applied Surface Science*, 242 (2005) 346-352.
- [274] M. Wang, J. Wang, W. Chen, Y. Cui, L. Wang, Effect of preheating and annealing temperatures on quality characteristics of ZnO thin film prepared by sol-gel method, *Materials Chemistry and Physics*, 97 (2006) 219-225.

- [275] X. Li, Y. Yan, T. Gessert, C. DeHart, C. Perkins, D. Young, T. Coutts, p-Type ZnO thin films formed by CVD reaction of Diethylzinc and NO gas, *Electrochemical and Solid-State Letters*, 6 (2003) C56-C58.
- [276] G. Jia, H. Wang, L. Yan, X. Wang, R. Pei, T. Yan, Y. Zhao, X. Guo, Cytotoxicity of carbon nanomaterials: single-wall nanotube, multi-wall nanotube, and fullerene, *Environmental Science & Technology*, 39 (2005) 1378-1383.
- [277] N.A. Hill, U. Waghmare, First-principles study of strain-electronic interplay in ZnO: Stress and temperature dependence of the piezoelectric constants, *Physical Review B*, 62 (2000) 8802.
- [278] Y. Zhang, K. Yu, D. Jiang, Z. Zhu, H. Geng, L. Luo, Zinc oxide nanorod and nanowire for humidity sensor, *Applied Surface Science*, 242 (2005) 212-217.
- [279] Y. Li, B. Yao, Y. Lu, Y. Gai, C. Cong, Z. Zhang, D. Zhao, J. Zhang, B. Li, D. Shen, Biaxial stress-dependent optical band gap, crystalline, and electronic structure in wurtzite ZnO: Experimental and ab initio study, *Journal of Applied Physics*, 104 (2008) 083510-083516.
- [280] C. Jin, A. Tiwari, R.J. Narayan, Ultraviolet-illumination-enhanced photoluminescence effect in zinc oxide thin films, *Journal of Applied Physics*, 98 (2005) 083707.
- [281] W.Y. Su, J.S. Huang, C.F. Lin, Improving the property of ZnO nanorods using hydrogen peroxide solution, *Journal of Crystal Growth*, 310 (2008) 2806-2809.
- [282] Q. Zhao, X. Xu, X. Song, X. Zhang, D. Yu, C. Li, L. Guo, Enhanced field emission from ZnO nanorods via thermal annealing in oxygen, *Applied Physics Letters*, 88 (2006) 033102-033103.
- [283] M. Cui, X. Wu, L. Zhuge, Y. Meng, Effects of annealing temperature on the structure and photoluminescence properties of ZnO films, *Vacuum*, 81 (2007) 899-903.
- [284] S. Maniv, W. Westwood, E. Colombini, Pressure and angle of incidence effects in reactive planar magnetron sputtered ZnO layers, *Journal of Vacuum Science and Technology*, 20 (1982) 162-170.
- [285] Y.C. Lee, S.Y. Hu, W. Wate, Y.S. Huang, M.D. Yang, J.L. Shen, K.K. Tiong, C.C. Huang, Influence of annealing on optical properties and surface structure of ZnO thin films, *Solid State Commun.*, 143 (2007).
- [286] C. Wang, D. Xu, X. Xiao, Y. Zhang, D. Zhang, Effects of oxygen pressure on the structure and photoluminescence of ZnO thin films, *Journal of Materials Science*, 42 (2007) 9795-9800.
- [287] A. Mahmood, N. Ahmed, Q. Raza, T.M. Khan, M. Mehmood, M.M. Hassan, N. Mahmood, , Effect of thermal annealing on the structural and optical properties of ZnO thin films deposited by the reactive e-beam evaporation technique ,*Phys. Scr.*, 82 (2010).

- [288] T. Minami, H. Sato, H. Nanto, S. Takata, Group III impurity doped zinc oxide thin films prepared by RF magnetron sputtering, *Jpn. J. Appl. Phys.*, 24 (1985) L781-L784.
- [289] L. Bergman, X.B. Chen, J.L. Morrison, J. Huso, A.P. Purdy, Photoluminescence dynamics in ensembles of wide-band-gap nanocrystallites and powders, *Journal of Applied Physics*, 96 (2004) 675-682.
- [290] H. Morkoc, S. Strite, G. Gao, M. Lin, B. Sverdlov, M. Burns, Large-band-gap SiC, III-V nitride, and II-VI ZnSe-based semiconductor device technologies, *Journal of Applied Physics*, 76 (1994) 1363-1398.
- [291] S. Nakamura, M. Senoh, S. Nagahama, N. Iwasa, T. Yamada, T. Matsushita, Y. Sugimoto, H. Kiyoku, Room-temperature continuous-wave operation of InGaN multi-quantum-well structure laser diodes, *Applied Physics Letters*, 69 (1996) 4056-4058.
- [292] L. Canham, Silicon quantum wire array fabrication by electrochemical and chemical dissolution of wafers, *Applied Physics Letters*, 57 (1990) 1046-1048.
- [293] M. Mason, G. Credo, K. Weston, S. Buratto, Luminescence of individual porous Si chromophores, *Physical Review Letters*, 80 (1998) 5405-5408.
- [294] F. Koch, V. Petrova-Koch, T. Muschik, The luminescence of porous Si: the case for the surface state mechanism, *Journal of Luminescence*, 57 (1993) 271-281.
- [295] J.B. Xia, K. Chang, S.S. Li, Electronic structure and optical property of semiconductor nanocrystallites, *Computational Materials Science*, 30 (2004) 274-277.
- [296] J. Tsang, M. Tischler, R. Collins, Raman scattering from H or O terminated porous Si, *Applied Physics Letters*, 60 (1992) 2279-2281.
- [297] R. Singh, F. Singh, V. Kumar, R. Mehra, Growth kinetics of ZnO nanocrystallites: Structural, optical and photoluminescence properties tuned by thermal annealing, *Current Applied Physics*, 11 (2010) 624-630.
- [298] M.G. Bawendi, P. Carroll, W.L. Wilson, L. Brus, Luminescence properties of CdSe quantum crystallites: Resonance between interior and surface localized states, *The Journal of Chemical Physics*, 96 (1992) 946.
- [299] M.M. Woolfson, J.M. Ziman, *Introduction to the theory of solid surface*, Cambridge University Press, (1979).
- [300] F. Zhao, Z. Gong, S. Liang, N. Xu, S. Deng, J. Chen, H. Wang, Ultrafast optical emission of nanodiamond induced by laser excitation, *Applied Physics Letters*, 85 (2004) 914-916.
- [301] T. Matsumoto, H. Kato, K. Miyamoto, M. Sano, E.A. Zhukov, T. Yao, Correlation between grain size and optical properties in zinc oxide thin films, *Applied Physics Letters*, 81 (2002) 1231-1233.

- [302] A. Puzder, A. Williamson, F. Reboledo, G. Galli, Structural stability and optical properties of nanomaterials with reconstructed surfaces, *Physical Review Letters*, 91 (2003) 157405.
- [303] O. Lupan, G. Chai, L. Chow, G. Emelchenko, H. Heinrich, V. Ursaki, A. Gruzintsev, I. Tiginyanu, A. Redkin, Ultraviolet photoconductive sensor based on single ZnO nanowire, *Physica Status Solidi (a)*, 207 (2010) 1735-1740.
- [304] M. Zainizan Sahdan, M. Hafiz Mamat, M. Salina, Z. Khusaimi, U.M. Noor, M. Rusop, Heat treatment effects on the surface morphology and optical properties of ZnO nanostructures, *Physica Status Solidi (c)*, 7 (2010) 2286-2289.
- [305] S. Monticone, R. Tufeu, A. Kanaev, Complex nature of the UV and visible fluorescence of colloidal ZnO nanoparticles, *The Journal of Physical Chemistry B*, 102 (1998) 2854-2862.
- [306] B. Lin, Z. Fu, Y. Jia, G. Liao, Defect photoluminescence of undoping ZnO films and its dependence on annealing conditions, *Journal of The Electrochemical Society*, 148 (2001) G110-G113.
- [307] W. Kwok, A.B. Djurisc, Y.H. Leung, D. Li, K. Tam, D. Phillips, W. Chan, Influence of annealing on stimulated emission in ZnO nanorods, *Applied Physics Letters*, 89 (2006) 183112-183113.
- [308] A. Djurišić, Y. Leung, K. Tam, Y. Hsu, L. Ding, W. Ge, Y. Zhong, K. Wong, W. Chan, H. Tam, Defect emissions in ZnO nanostructures, *Nanotechnology*, 18 (2007) 095702.
- [309] V. Roy, A. Djurisc, W. Chan, J. Gao, H. Lui, C. Surya, Luminescent and structural properties of ZnO nanorods prepared under different conditions, *Applied Physics Letters*, 83 (2003) 141-143.
- [310] H.K. Yadav, K. Sreenivas, V. Gupta, S. Singh, R. Katiyar, Effect of surface defects on the visible emission from ZnO nanoparticles, *Journal of Materials Research*, 22 (2007) 2404-2409.
- [311] Y. Tong, Y. Liu, C. Shao, R. Mu, Structural and optical properties of ZnO nanotower bundles, *Applied Physics Letters*, 88 (2006) 123111-123113.
- [312] T. Sekiguchi, K. Haga, K. Inaba, ZnO films grown under the oxygen-rich condition, *Journal of Crystal Growth*, 214 (2000) 68-71.
- [313] L.H. Quang, S.J. Chua, K. Ping Loh, E. Fitzgerald, The effect of post-annealing treatment on photoluminescence of ZnO nanorods prepared by hydrothermal synthesis, *Journal of Crystal Growth*, 287 (2006) 157-161.
- [314] O. Lupan, T. Pauporté, L. Chow, B. Viana, F. Pellé, L.K. Ono, B. Roldan Cuenya, H. Heinrich, Effects of annealing on properties of ZnO thin films prepared by electrochemical deposition in chloride medium, *Applied Surface Science*, 256 (2010) 1895-1907.
- [315] C. Arguello, D. Rousseau, S. Porto, First-order raman effect in wurtzite-type crystals, *Physical Review*, 181 (1969) 1351.

- [316] G. Buinitskaya, L. Kulyuk, V. Mirovitskii, E. Rusu, E. Mishina, N. Sherstyuk, ZnO single crystal and epitaxial thin film studied by second harmonic generation and photoluminescence, *Superlattices and Microstructures*, 39 (2006) 83-90.
- [317] J. Guo, A quantum-mechanical treatment of phonon scattering in carbon nanotube transistors, *Journal of Applied Physics*, 98 (2005) 063519-063519-063516.
- [318] H.C. Hsu, H.M. Cheng, C.Y. Wu, H.S. Huang, Y.C. Lee, W.F. Hsieh, Luminescence of selective area growth of epitaxial ZnO nanowires and random-growth-oriented nanobelts, *Nanotechnology*, 17 (2006) 1404.
- [319] M.H. Huang, S. Mao, H. Feick, H. Yan, Y. Wu, H. Kind, E. Weber, R. Russo, P. Yang, Room-temperature ultraviolet nanowire nanolasers, *science*, 292 (2001) 1897-1899.
- [320] A. Umar, B. Karunagaran, E. Suh, Y. Hahn, Structural and optical properties of single-crystalline ZnO nanorods grown on silicon by thermal evaporation, *Nanotechnology*, 17 (2006) 4072.
- [321] Z. Wang, H. Zhang, L. Zhang, J. Yuan, S. Yan, C. Wang, Low-temperature synthesis of ZnO nanoparticles by solid-state pyrolytic reaction, *Nanotechnology*, 14 (2002) 11.
- [322] Y. Xing, Z. Xi, Z. Xue, X. Zhang, J. Song, R. Wang, J. Xu, Y. Song, S. Zhang, D. Yu, Optical properties of the ZnO nanotubes synthesized via vapor phase growth, *Applied Physics Letters*, 83 (2003) 1689-1691.
- [323] W.K. Campbell, C. Sedikides, Self-threat magnifies the self-serving bias: A meta-analytic integration, *Review of General Psychology*, 3 (1999) 23.
- [324] J. Zi, H. Buscher, C. Falter, W. Ludwig, K. Zhang, X. Xie, Raman shifts in Si nanocrystals, *Applied Physics Letters*, 69 (1996) 200-202.
- [325] K.A. Alim, V.A. Fonoberov, M. Shamsa, A.A. Balandin, Micro-Raman investigation of optical phonons in ZnO nanocrystals, *Journal of Applied Physics*, 97 (2005) 124313-124313-124315.
- [326] F. Demangeot, V. Paillard, P. Chassaing, M. Kahn, A. Maisonnat, B. Chaudret, Experimental study of LO phonons and excitons in ZnO nanoparticles produced by room-temperature organometallic synthesis, *Applied Physics Letters*, 88 (2006) 071921-071921-071923.
- [327] T. Damen, S. Porto, B. Tell, Raman effect in zinc oxide, *Physical Review*, 142 (1966) 570.
- [328] G.J. Exarhos, S.K. Sharma, Influence of processing variables on the structure and properties of ZnO films, *Thin Solid Films*, 270 (1995) 27-32.
- [329] M. Rajalakshmi, A.K. Arora, B. Bendre, S. Mahamuni, Optical phonon confinement in zinc oxide nanoparticles, *Journal of Applied Physics*, 87 (2000) 2445-2448.
- [330] H.J. Fan, R. Scholz, F.M. Kolb, M. Zacharias, Two-dimensional dendritic ZnO nanowires from oxidation of Zn microcrystals, *Applied Physics Letters*, 85 (2004) 4142.

- [331] L.V. Azaroff, Introduction to solids ,Tata McGraw-Hill Education, 1984.
- [332] M. Kuball, Raman spectroscopy of GaN, AlGaN and AlN for process and growth monitoring/control, Surface and Interface Analysis, 31 (2001) 987-999.
- [333] A. Khan, W.M. Jadwisienczak, H.J. Lozykowski, M.E. Kordesch ,Catalyst-free synthesis and luminescence of aligned ZnO nanorods, Physica E: Low-Dimensional Systems and Nanostructures, 39 (2007) 258-261.
- [334] K. Samanta, P. Bhattacharya, R. Katiyar, W. Iwamoto, P. Pagliuso, C. Rettori, Raman scattering studies in dilute magnetic semiconductor $Zn_{1-x}Co_xO$, Physical Review B, 73 (2006) 245213.
- [335] H. Richter, Z. Wang, L. Ley, The one phonon raman spectrum in microcrystalline silicon, Solid State Communications, 39 (1981) 625-629.
- [336] X. Xu, S. Lau, J. Chen ,G. Chen, B. Tay, Polycrystalline ZnO thin films on Si (100) deposited by filtered cathodic vacuum arc, Journal of Crystal Growth, 223 (2001) 201-205.
- [337] R. Al Asmar, J. Atanas, M. Ajaka, Y. Zaatari, G. Ferblantier, J. Sauvajol, J. Jabbour, S. Juillaget, A. Foucaran, Characterization and Raman investigations on high-quality ZnO thin films fabricated by reactive electron beam evaporation technique, Journal of Crystal Growth, 279 (2005) 394-402.
- [338] C. Youn, T. Jeong, M. Han, J. Kim, Optical properties of Zn-terminated ZnO bulk, Journal of Crystal Growth, 261 (2004) 526-532.
- [339] J.N. Zeng, J.K. Low, Z.M. Ren, T. Liew, Y.F. Lu, Effect of deposition conditions on optical and electrical properties of ZnO films prepared by pulsed laser deposition, Applied Surface Science, 197 (2002) 362-367.
- [340] Z. Chen, A. Kawasuso, Y. Xu, H. Naramoto, X. Yuan, T. Sekiguchi, R. Suzuki, T. Ohdaira, Production and recovery of defects in phosphorus-implanted ZnO, Journal of Applied Physics, 97 (2005) 013528-013528-013526.
- [341] H.J. Ko, T. Yao, Y. Chen, S.K. Hong, Investigation of ZnO epilayers grown under various Zn/O ratios by plasma-assisted molecular-beam epitaxy, Journal of Applied Physics, 92 (2002) 4354-4360.
- [342] A. Tsukazaki, A. Ohtomo, S. Yoshida, M. Kawasaki ,C. Chia, T. Makino, Y. Segawa, T. Koida, S. Chichibu, H. Koinuma, Layer-by-layer growth of high-optical-quality ZnO film on atomically smooth and lattice relaxed ZnO buffer layer, Applied Physics Letters, 83 (2003) 2784-2786.
- [343] Y. Wang, S. Lau, X. Zhang, H. Hng, H. Lee, S. Yu, B. Tay, Enhancement of near-band-edge photoluminescence from ZnO films by face-to-face annealing, Journal of Crystal Growth, 259 (2003) 335-342.
- [344] H. Zhou, H. Alves, D.M. Hofmann, W. Kriegeis, B.K. Meyer, G. Kaczmarczyk, A. Hoffmann, Behind the weak excitonic emission of ZnO quantum dots: ZnO/Zn(OH)₂core-shell structure Appl. Phys. Lett. , 80 (2002) 210.

- [345] T. Koida, S. Chichibu, A. Uedono, T. Sota, A. Tsukazaki, M. Kawasaki, Radiative and nonradiative excitonic transitions in nonpolar (112⁻0) and polar (0001⁻) and (0001) ZnO epilayers, *Applied Physics Letters*, 84 (2004) 1079-1081.
- [346] M. Matsuoka, Discovery of ZnO varistors and their progress for the two decades., in, Matsushita Electronic Components Co, Ltd: 1006 Kadoma Osaka 571, Japan, 1982, pp. 3-21.
- [347] L. Balcells, J. Fontcuberta, B. Martinez, X. Obradors, High-field magnetoresistance at interfaces in manganese perovskites, *Physical Review B*, 58 (1998) 14697-14700.
- [348] N. Zhang, W. Ding, W. Zhong, D. Xing, Y. Du, Tunnel-type giant magnetoresistance in the granular perovskite La_{0.85}Sr_{0.15}MnO₃, *Physical Review B*, 56 (1997) 8138.
- [349] T. Zhu, B. Shen, J. Sun, H. Zhao, W. Zhan, Surface spin-glass behavior in LaSrMnO nanoparticles, *Applied Physics Letters*, 78 (2001) 3863.
- [350] S. Jejurikar, A. Banpurkar, A. Limaye, S. Patil, K. Adhi, P. Misra, L. Kukreja, R. Bathe, Structural, morphological, and electrical characterization of heteroepitaxial ZnO thin films deposited on Si (100) by pulsed laser deposition, *Journal of Applied Physics*, 99 (2006) 014907-014907-014907.
- [351] U. Schwing, B. Hoffmann, Model experiments describing the microcontact of ZnO varistors, *Journal of Applied Physics*, 57 (1985) 5372-5379.
- [352] D. Look, D. Reynolds, J. Sizelove, R. Jones, C. Litton, G. Cantwell, W. Harsch, Electrical properties of bulk ZnO, *Solid State Communications*, 105 (1998) 399-401.
- [353] P. Wagner, R. Helbig, Halleffekt und anisotropie der beweglichkeit der elektronen in ZnO, *Journal of Physics and Chemistry of Solids*, 35 (1974) 327-335.
- [354] A. Sabioni, A. Huntz, F. Millot, C. Monty, Self-diffusion in Cr₂O₃ III. Chromium and oxygen grain-boundary diffusion in polycrystals, *Philosophical Magazine A*, 66 (1992) 361-374.
- [355] A.C.S. Sabioni, M.J.F. Ramos, W.B. Ferraz, Oxygen diffusion in pure and doped ZnO, *Materials Research*, 6 (2003) 173-178.
- [356] J. Frenkel, On the electrical resistance of contacts between solid conductors, *Physical Review*, 36 (1930) 1604.
- [357] S.H. Kang, D.K. Hwang, S.J. Park, Low-resistance and highly transparent Ni/indium-tin oxide ohmic contacts to phosphorous-doped p-type ZnO, *Applied Physics Letters*, 86 (2005) 211902-211902-211903.
- [358] M. Batzill, U. Diebold, The surface and materials science of tin oxide, *Progress in Surface Science*, 79 (2005) 47-154.
- [359] G. Mahan, Intrinsic defects in ZnO varistors, *Journal of Applied Physics*, 54 (1983) 3825-3832.

- [360] S. Chopra, S. Sharma, T. Goel, R. Mendiratta, Effect of annealing temperature on microstructure of chemically deposited calcium modified lead titanate thin films, *Applied Surface Science*, 230 (2004) 207-214.
- [361] S. Pearton, D. Norton, K. Ip, Y. Heo, T. Steiner, Recent progress in processing and properties of ZnO, *Progress in Materials Science*, 50 (2005) 293-340.
- [362] P.R. Bueno, J.A. Varela, E. Longo, SnO₂, ZnO and related polycrystalline compound semiconductors: An overview and review on the voltage-dependent resistance (non-ohmic) feature, *Journal of The European Ceramic Society*, 28 (2008) 505-529.
- [363] N. Enzinger, H. Cerjak, Calculation of the influence of the weld pattern on the final residual stress state and deformation, in: *Materials Science Forum (Switzerland)*, Trans Tech Publ, 2002, pp. 147-152.
- [364] D. Gouvea, M. Kobori, J. Varela, Electrical properties of SnO₂ varistor, in: *Ceramics Today- Tomorrow's Ceramics. Proc. 7 th Int. Meeting on Modern Ceramics Technologies (7 th CIMTEC- World Ceramics Congress). Part C Montecatini Terme, 24-30 June 1990, 1990*, pp. 2091-2098.
- [365] F. Stucki, F. Greuter, Key role of oxygen at zinc oxide varistor grain boundaries, *Applied Physics Letters*, 57 (1990) 446-448.
- [366] S. Pianaro, P. Bueno, E. Longo, J. Varela, Microstructure and electric properties of a SnO₂ based varistor, *Ceramics International*, 25 (1999) 1-6.
- [367] F. Souza, J. Gomes, P. Bueno, M. Cassia-Santos, A. Araujo, E. Leite, E. Longo, J. Varela, Effect of the addition of ZnO seeds on the electrical properties of ZnO-based varistors, *Materials Chemistry and Physics*, 80 (2003) 512-516.
- [368] T. Toyoda, S. Shimamoto, Effects of Bi₂O₃ impurities in ceramic ZnO on photoacoustic spectra and current-voltage characteristics, *Japanese Journal of Applied Physics*, 37 (1998) 2827-2831.
- [369] M. Peiteado, M. De la Rubia, M. Velasco, F. Valle, A. Caballero, Bi₂O₃ vaporization from ZnO-based varistors, *Journal of the European Ceramic Society*, 25 (2005) 1675-1680.
- [370] M. Egashira, Y. Shimizu, Y. Takao, Y. Fukuyama, Hydrogen-sensitive breakdown voltage in the IV characteristics of tin dioxide-based semiconductors, in: *Solid-State Sensors and Actuators, 1995 and Eurosensors IX.. Transducers' 95. The 8th International Conference on, IEEE, 1995*, pp. 718-721.
- [371] J.P. Gambino, W.D. Kingery, G.E. Pike, L.M. Levinson, H.R. Philipp, Effect of heat treatments on the wetting behavior of bismuth-rich intergranular phases in ZnO: Bi: Co varistors, *Journal of The American Ceramic Society*, 72 (2005) 642-645.
- [372] K.I. Kobayashi, O. Wada, M. Kobayashi, Y. Takada, Continuous existence of bismuth at grain boundaries of zinc oxide varistor without intergranular phase, *Journal of The American Ceramic Society*, 81 (1998) 2071-2076.
- [373] R. Metz, H. Delalu, J. Vignalou, N. Achard, M. Elkhatib, Electrical properties of varistors in relation to their true bismuth composition after sintering, *Materials Chemistry and Physics*, 63 (2000) 157-162.

- [374] F. Selim, T. Gupta, P. Hower, W. Carlson, Low voltage ZnO varistor: Device process and defect model, *Journal of Applied Physics*, 51 (1980) 765-768.
- [375] K.H. Kim, J.L. Ong, O. Okuno, The effect of filler loading and morphology on the mechanical properties of contemporary composites, *The Journal of Prosthetic Dentistry*, 87 (2002) 642-649.
- [376] J. Luo, Y.M. Chiang, Equilibrium-thickness Amorphous Films on {1120} surfaces of Bi₂O₃-doped ZnO, *Journal of the European Ceramic Society*, 19 (1999) 697-701.
- [377] A.K. Zak, M.E. Abrishami, W. Majid, R. Yousefi, S. Hosseini, Effects of annealing temperature on some structural and optical properties of ZnO nanoparticles prepared by a modified sol-gel combustion method, *Ceramics International*, 37 (2011) 393-398.
- [378] T.B. Hur, G.S. Jeon, Y.H. Hwang, H.K. Kim, Photoluminescence of polycrystalline ZnO under different annealing conditions, *Journal of Applied Physics*, 94 (2003) 5787-5790.
- [379] R.G. Palgrave, P. Borisov, M.S. Dyer, S.R.C. McMitchell, G.R. Darling, J.B. Claridge, M. Batuk, H. Tan, H. Tian, J. Verbeeck, Artificial construction of the layered ruddlesden-popper manganite La₂Sr₂Mn₃O₁₀ by reflection high energy electron diffraction monitored pulsed laser deposition, *J. Am. Chem. Soc.*, 134 (2012) 7700-7714.
- [380] P. Mantas, J. Baptista, The barrier height formation in ZnO varistors, *Journal of the European Ceramic Society*, 15 (1995) 605-615.
- [381] J. Garcia, A. Remon, J. Piqueras, Influence of Bi and Mn on the green luminescence of ZnO ceramics, *Journal of Applied Physics*, 62 (1987) 3058.
- [382] H. Zeng, W. Cai, J. Hu, G. Duan, P. Liu, Y. Li, Violet photoluminescence from shell layer of Zn/ZnO core-shell nanoparticles induced by laser ablation, *Applied Physics Letters*, 88 (2006) 171910.
- [383] A. Bougrine, A. El Hichou, M. Addou, J. Ebothé, A. Kachouane, M. Troyon, Structural, optical and cathodoluminescence characteristics of undoped and tin-doped ZnO thin films prepared by spray pyrolysis, *Materials Chemistry and Physics*, 80 (2003) 438-445.
- [384] H.S. Kang, J.W. Kim, S.H. Lim, H.W. Chang, G.H. Kim, J.H. Kim, S.Y. Lee, Investigation on the variation of green, yellow, and orange emission properties of ZnO thin film, *Superlattices and Microstructures*, 39 (226) 193-201.
- [385] M. Ramanachalam, A. Rohatgi, W. Carter, J. Schaffer, T. Gupta, Photoluminescence study of ZnO varistor stability, *Journal of Electronic Materials*, 24 (1995) 413-419.
- [386] A. Gruzintsev, E. Yakimov, Annealing effect on the luminescent properties and native defects of ZnO, *Inorganic Materials*, 41 (2005) 725-729.
- [387] N. Ashkenov, B. Mbenkum, C. Bundesmann, V. Riede, M. Lorenz, D. Spemann, E. Kaidashev, A. Kasic, M. Schubert, M. Grundmann, Infrared dielectric functions and phonon modes of high-quality ZnO films, *Journal of Applied Physics*, 93 (2003) 126-133.

- [388] J. Scott, UV resonant raman scattering in ZnO, *Physical Review B*, 2 (1970) 1209-1211.
- [389] G. Agarwal, R.F. Speyer, Effect of rate controlled sintering on microstructure and electrical properties of ZnO doped with bismuth and antimony oxides, *Journal of Materials Research*, 12 (1997) 2447-2454.
- [390] T. Asokan, G. Iyengar, G. Nagabhushana, Influence of Process Variables on Microstructure and V-I Characteristics of Multicomponent ZnO-Based Nonlinear Resistors, *Journal of the American Ceramic Society*, 70 (1987) 643-650.
- [391] F.J. Toal, J.P. Dougherty, C.A. Randall, Processing and electrical characterization of a varistor-capacitor cofired multilayer device, *Journal of the American Ceramic Society*, 81 (1998) 2371-2380.
- [392] H. Liu, X. Ma, D. Jiang, W. Shi, Microstructure and electrical properties of Y₂O₃-doped ZnO-based varistor ceramics prepared by high-energy ball milling, *Journal of University of Science and Technology Beijing, Mineral, Metallurgy, Material*, 14 (2007) 266-270.
- [393] N. Ohashi, K. Kataoka, T. Ohgaki, T. Miyagi, H. Haneda, K. Morinaga, Synthesis of zinc oxide varistors with a breakdown voltage of three volts using an intergranular glass phase in the bismuth–boron–oxide system, *Applied Physics Letters*, 83 (2003) 4857-4859.
- [394] A. Sawalha, M. Abu-Abdeen, A. Sedky, Electrical conductivity study in pure and doped ZnO ceramic system, *Physica B: Condensed Matter*, 404 (2009) 1316-1320.
- [395] M.O. Orlandi, P.R. Bueno, E.R. Leite, E. Longo, Nonohmic behavior of SnO₂. MnO₂-based ceramics, *Materials Research*, 6 (2003) 279-283.
- [396] H. Jiaping, A.M.R. Senos, P.Q. Mantas, Varistor behaviour of Mn-doped ZnO ceramics, *Journal of the European Ceramic Society* 22 (2002) 1653-1660.
- [397] M.R.C. Santos, P.R. Bueno, E. Longo, J.A. Varela, Effect of oxidizing and reducing atmospheres on the electrical properties of dense SnO₂-based varistors, *Journal of the European Ceramic Society*, 21 (2001) 161-167.
- [398] E. Zielinski, R. Vinci, J. Bravman, Effects of barrier layer and annealing on abnormal grain growth in copper thin films, *Journal of Applied Physics*, 76 (1994) 4516-4523.
- [399] E.D. Kim, M.H. Oh, C.H. Kim, Effects of annealing on the grain boundary potential barrier of ZnO varistor, *Journal of Materials Science*, 21 (1986) 3491-3496.
- [400] A. Antunes, S. Antunes, S. Pianaro, E. Longo, E. Leite, J. Varela, Effect of La₂O₃ doping on the microstructure and electrical properties of a SnO₂-based varistor, *Journal of Materials Science: Materials in Electronics*, 12 (2001) 69-74.
- [401] M. Takada, S. Yoshikado, Effect of thermal annealing on electrical degradation characteristics of Sb–Bi–Mn–Co-added ZnO varistors, *Journal of the European Ceramic Society*, 30 (2010) 531-538.

- [402] W. Carlson, T. Gupta, Improved varistor nonlinearity via donor impurity doping, *Journal of Applied Physics*, 53 (1982) 5746-5753.
- [403] E. Leite, J. Varela, E. Longo, Barrier voltage deformation of ZnO varistors by current pulse, *Journal of Applied Physics*, 7.150-147 (1992) 2.
- [404] S. Pianaro, P. Bueno, E. Longo, J. Varela, A new SnO₂-based varistor system, *Journal of Materials Science Letters*, 14 (1995) 692-694.
- [405] E. Leite, A. Nascimento, P. Bueno, E. Longo, J. Varela, The influence of sintering process and atmosphere on the non-ohmic properties of SnO₂ based varistor, *Journal of Materials Science: Materials in Electronics*, 10 (1999) 321-327.
- [406] R. Einzinger, Metal oxide varistor action-a homojunction breakdown mechanism, *Applications of Surface Science*, 1 (1978) 329-340.
- [407] P. Mantas, A. Senos, J. Baptista, Varistor-capacitor characteristics of ZnO ceramics, *Journal of Materials Science*, 21 (1986) 679-686.
- [408] C.M. Agrawal, Reconstructing the human body using biomaterials, *JOM*, 50 (1998) 31-35.
- [409] E. Entcheva, H. Bien, L. Yin, C.-Y. Chung, M. Farrell, Y. Kostov, Functional cardiac cell constructs on cellulose-based scaffolding, *Biomaterials*, 25 (2004) 5753-5762.
- [410] P.L. Granja, B. De Jéso, R. Bareille, F. Rouais, C. Baquey, M.A. Barbosa, Mineralization of regenerated cellulose hydrogels induced by human bone marrow stromal cells, *Eur Cell Mater* 10 (2005) 31-39.
- [411] K.J. Burg, S. Porter, J.F. Kellam, Biomaterial developments for bone tissue engineering, *Biomaterials*, 21 (2000) 2347-2359.
- [412] S.H. Li, Q. Liu, J.R. Wijn, B.L. Zhou, K. Groot, In vitro calcium phosphate formation on a natural composite material, bamboo, *Biomaterials*, 18 (1997) 389-395.
- [413] M. Horie, K. Nishio, K. Fujita, S. Endoh, A. Miyauchi, Y. Saito, H. Iwahashi, K. Yamamoto, H. Murayama, H. Nakano, Protein adsorption of ultrafine metal oxide and its influence on cytotoxicity toward cultured cells, *Chemical Research in Toxicology*, 22 (2009) 543-553.
- [414] T.J. Brunner, P. Wick, P. Manser, P. Spohn, R.N. Grass, L.K. Limbach, A. Bruinink, W.J. Stark, In vitro cytotoxicity of oxide nanoparticles: comparison to asbestos, silica, and the effect of particle solubility, *Environmental Science & Technology*, 40 (2006) 4374-4381.
- [415] L. Yan, F. Zhao, S. Li, Z. Hu, Y. Zhao, Low-toxic and safe nanomaterials by surface-chemical design, carbon nanotubes, fullerenes, metallofullerenes, and graphenes, *Nanoscale*, 3 (2011) 362-382.
- [416] A. Mayer, M. Vadon, B. Rinner, A. Novak, R. Wintersteiger, E. Fröhlich, The role of nanoparticle size in hemocompatibility, *Toxicology*, 258 (2009) 139-147.

- [417] X. Peng, S. Palma, N.S. Fisher, S.S. Wong, Effect of morphology of ZnO nanostructures on their toxicity to marine algae, *Aquatic Toxicology*, 102 (2011) 186-196.
- [418] X. Hu, S. Cook, P. Wang, H.-m. Hwang, In vitro evaluation of cytotoxicity of engineered metal oxide nanoparticles, *Science of The Total Environment*, 407 (2009) 3070-3072.
- [419] P.P.S.L. C. W. Bunn, The lattice-dimensions of zinc oxide.
- [420] A.H. Lu, E.e.L. Salabas, F. Schüth, Magnetic nanoparticles: synthesis, protection, functionalization, and application, *Angewandte Chemie International Edition*, 46 (2007) 1222-1244.
- [421] P.J. Borm, D. Robbins, S. Haubold, T. Kuhlbusch, H. Fissan, K. Donaldson, R. Schins, V. Stone, W. Kreyling, J. Lademann, The potential risks of nanomaterials: a review carried out for ECETOC, *Particle and Fibre Toxicology*, 3 (2006) 11.
- [422] S.B. Levy, B. Marshall, Antibacterial resistance worldwide: causes, challenges and responses, *Nature medicine* 10 (2004) 122-129.
- [423] F. Cui, D. Li, A review of investigations on biocompatibility of diamond-like carbon and carbon nitride films, *Surface and Coatings Technology*, 131 (2000) 481-487.
- [424] J. Dong, Q. Sun, J.-Y. Wang, Basic study of corn protein, zein, as a biomaterial in tissue engineering, surface morphology and biocompatibility, *Biomaterials*, 25 (2004) 4691-4697.
- [425] A. Marques, R. Reis, J. Hunt, The biocompatibility of novel starch-based polymers and composites: in vitro studies, *Biomaterials*, 23 (2002) 1471-1478.
- [426] L. Liu, M. Ge, H. Liu, C. Guo, Y. Wang, Z. Zhou, Controlled synthesis of ZnO with adjustable morphologies from nanosheets to microspheres, *Colloids and Surfaces A: Physicochemical and Engineering Aspects*, 348 (2009) 124-129.
- [427] W. Strober, Trypan blue exclusion test of cell viability, *Current Protocols in Immunology*, (2001) A. 3B. 1-A. 3B. 2.
- [428] T.F. Uliasz, S.J. Hewett, A microtiter trypan blue absorbance assay for the quantitative determination of excitotoxic neuronal injury in cell culture, *Journal of Neuroscience Methods*, 100 (2000) 157-163.
- [429] S. H., T. T., I. Y., Simple and easy method to evaluate uptake potential of nanoparticles in mammalian cells using a flow cytometric light scatter analysis, *Environ Sci Technol*, 41 (2007) 3018-3024.
- [430] A. Di Virgilio, M. Reigosa, P. Arnal, M. Fernández Lorenzo de Mele, Comparative study of the cytotoxic and genotoxic effects of titanium oxide and aluminium oxide nanoparticles in Chinese hamster ovary (CHO-K1) cells, *Journal of Hazardous Materials*, 177 (2010) 711-718.
- [431] C.-Y. Jin, B.-S. Zhu, X.-F. Wang, Q.-H. Lu, Cytotoxicity of titanium dioxide nanoparticles in mouse fibroblast cells, *Chemical Research in Toxicology*, 21 (2008) 1871-1877.

- [432] H.A. Jeng, J. Swanson, Toxicity of metal oxide nanoparticles in mammalian cells, *Journal of Environmental Science and Health Part A*, 41 (2006) 2699-2711.
- [433] S. Park, Y.K. Lee, M. Jung, K.H. Kim, N. Chung, E.-K. Ahn, Y. Lim, K.-H. Lee, Cellular toxicity of various inhalable metal nanoparticles on human alveolar epithelial cells, *Inhalation Toxicology*, 19 (2007) 59-65.
- [434] K. Soto, K. Garza, L. Murr, Cytotoxic effects of aggregated nanomaterials, *Acta Biomaterialia*, 3 (2007) 351-358.
- [435] Lin W, Huang YW, Zhou XD, In vitro toxicity of silica nanoparticles in human lung cancer cells, *Toxicol Appl Pharmacol*, 217 (2006) 252-259.
- [436] F. Wang, F. Gao, M. Lan, H. Yuan, Y. Huang, J. Liu, Oxidative stress contributes to silica nanoparticle-induced cytotoxicity in human embryonic kidney cells, *Toxicology In Vitro*, 23 (2009) 808-815.
- [437] A. Simon-Deckers, B. Gouget, M. Mayne-L'Hermite, N. Herlin-Boime, C. Reynaud, M. Carriere, In vitro investigation of oxide nanoparticle and carbon nanotube toxicity and intracellular accumulation in A549 human pneumocytes, *Toxicology*, 253 (2008) 137-146.
- [438] S.J. Klaine, P.J. Alvarez, G.E. Batley, T.F. Fernandes, R.D. Handy, D.Y. Lyon, S. Mahendra, M.J. McLaughlin, J.R. Lead, Nanomaterials in the environment: behavior, fate, bioavailability, and effects, *Environmental Toxicology and Chemistry*, 27 (2008) 1825-1851.
- [439] J.-R. Gurr, A.S. Wang, C.-H. Chen, K.-Y. Jan, Ultrafine titanium dioxide particles in the absence of photoactivation can induce oxidative damage to human bronchial epithelial cells, *Toxicology*, 213 (2005) 66-73.
- [440] I.-S. Kim, M. Baek, S.-J. Choi, Comparative cytotoxicity of Al₂O₃, CeO₂, TiO₂ and ZnO nanoparticles to human lung cells, *Journal of Nanoscience and Nanotechnology*, 10 (2010) 3453-3458.
- [441] W. Lin, Y. Xu, C.-C. Huang, Y. Ma, K.B. Shannon, D.-R. Chen, Y.-W. Huang, Toxicity of nano- and micro-sized ZnO particles in human lung epithelial cells, *Journal of Nanoparticle Research*, 11 (2009) 25-39.
- [442] Y. Ye, J. Liu, J. Xu, L. Sun, M. Chen, M. Lan, Nano-SiO₂ induces apoptosis via activation of p53 and Bax mediated by oxidative stress in human hepatic cell line, *Toxicology in Vitro*, 24 (2010) 751-758.
- [443] D. Fischera, Y. Lib, B. Ahlemeyerc, J. Krieglsteinc, T. Kissela, In vitro cytotoxicity testing of polycations: influence of polymer structure on cell viability and hemolysis *Biomaterials*, 24 (2003) 1121-1131.
- [444] K.K. Wong, X. Liu, Silver nanoparticles—the real “silver bullet” in clinical medicine?, *MedChemComm*, 1 (2010) 125-131.
- [445] K. Choi, J. Kim, Y. Lee, H. Kim, ITO/Ag/ITO multilayer films for the application of a very low resistance transparent electrode, *Thin Solid Films*, 341 (1999) 152-155.

- [446] O. Choi, Z. Hu, Size dependent and reactive oxygen species related nanosilver toxicity to nitrifying bacteria, *Environmental science & technology*, 42 (2008) 4583-4588.
- [447] N.W. Adams, J.R. Kramer, Silver speciation in wastewater effluent, surface waters, and pore waters, *Environmental toxicology and chemistry*, 18 (1999) 2667-2673.
- [448] H. Sedlak, M. Hnilova, C. Grosh, H. Fong, F. Baneyx, D. Schwartz, M. Sarikaya, C. Tamerler, B. Traxler, Engineered *Escherichia coli* silver-binding periplasmic protein that promotes silver tolerance, *Applied and environmental microbiology*, 78 (2012) 2289-2296.
- [449] M.E. Samberg, P.E. Orndorff, N.A. Monteiro-Riviere, Antibacterial efficacy of silver nanoparticles of different sizes, surface conditions and synthesis methods, *Nanotoxicology*, 5 (2011) 244-253.
- [450] J. Liu, D.A. Sonshine, S. Shervani, R.H. Hurt, Controlled release of biologically active silver from nanosilver surfaces, *ACS nano*, 4 (2010) 6903-6913.

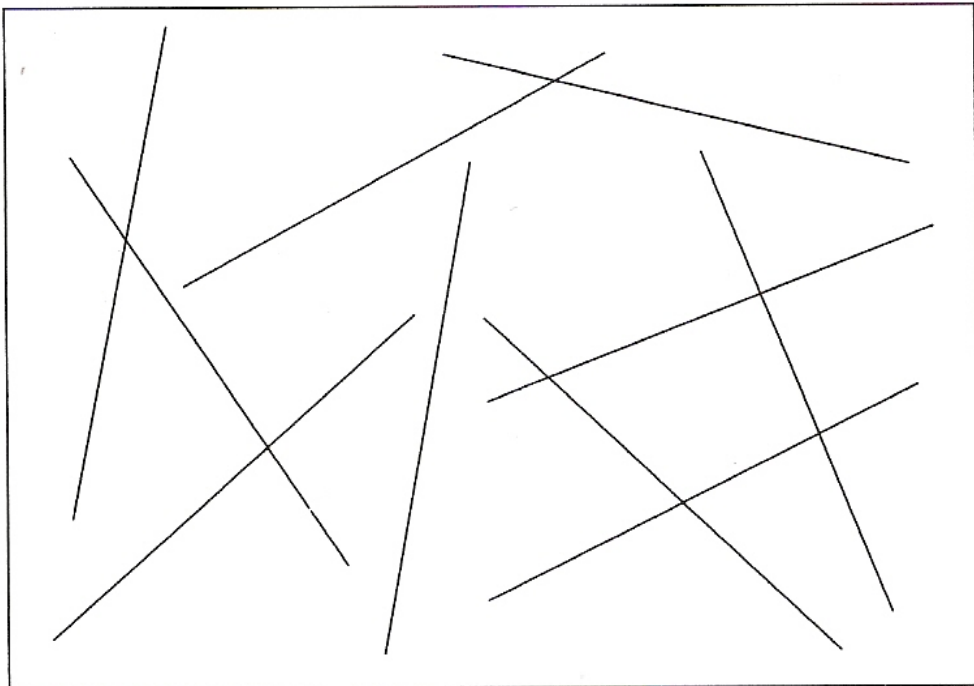
APPENDICES

APPENDIX A

AVERAGE GRAIN SIZE CALCULATION

The following describes the method used to measure average grain size.

1 – Ten lines of the same length are drawn onto a transparency, as shown in next Figure.



2 – The transparency is then placed on top of the micrograph photo containing the image of the grain distribution.

3 – Each line crosses several grain boundaries. The total crossing are then determined for each line.

4 – Data is tabulated; an example is shown below.

Line number	Total number of crossing
1	6
2	6
3	4
4	5
5	5
6	8
7	4
8	3
9	5
10	5
TOTAL	51

5 – Average grain size is calculated, as follows:

Length of line = 10 cm

Total lines = 10

Total length of line = 10 cm x 10 = 100 cm

Total number of crossings = 51

Therefore, one grain size is $100 \text{ cm} / 51 = 1.96 \text{ cm}$

6 – Referring to the micrograph photo in Figure 4.2, the average grain size can be determined by using the scale given as 1 mm : 5 micron or 1 cm : 50 micron.

$$50 \text{ micron} / 1 \text{ cm} \times 1.96 \text{ cm} = 98 \text{ micron.}$$

APPENDIX B

X-RAY DIFFRACTION REFERENCE DATA

```

REFERENCE PATTERN
Database: C:\APDW\USERDB
Card id.: 36-1451
Names: Zinc Oxide
      Zincite, syn
      zinc white

Formula: ZnO
Deleted: NO
Elements: O Zn
Groups:
Subfiles: Inorganic
          Minerals
          Alloys
          Common phases
          NBS patterns
          Forensics
          Educational patterns

F1=Next pattern F2=Previous pattern F8=Graphics F9=Print
    
```

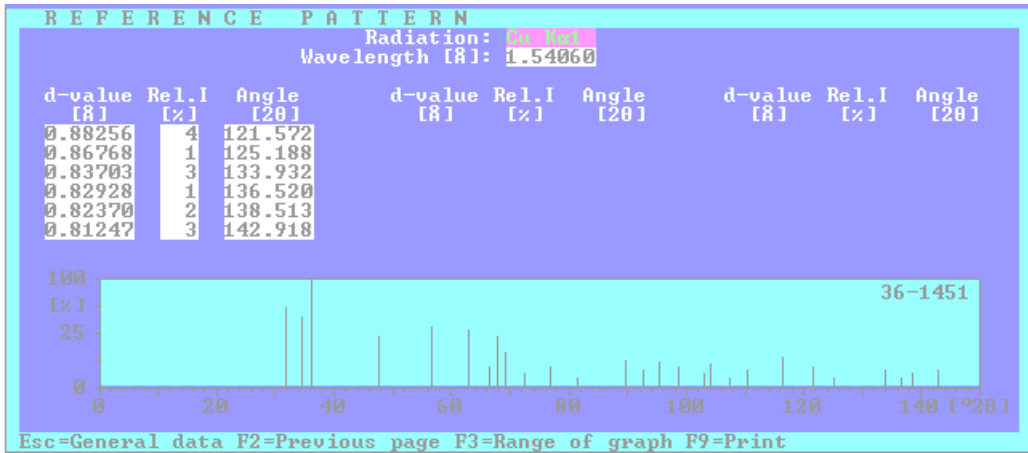
```

REFERENCE PATTERN
Radiation: Cu Kα1
Wavelength [Å]: 1.54060
    
```

d-value [Å]	Rel. I [%]	Angle [2θ]	d-value [Å]	Rel. I [%]	Angle [2θ]	d-value [Å]	Rel. I [%]	Angle [2θ]
2.81430	57	31.770	1.37818	23	67.963	1.04226	6	95.304
2.60332	44	34.422	1.35825	11	69.100	1.01595	4	98.613
2.47592	100	36.253	1.30174	2	72.562	0.98464	2	102.946
1.91114	23	47.539	1.23801	4	76.955	0.97663	5	104.134
1.62472	32	56.603	1.18162	1	81.370	0.95561	1	107.430
1.47712	29	62.864	1.09312	7	89.607	0.93812	3	110.392
1.40715	4	66.380	1.06384	3	92.784	0.90694	8	116.279

```

Esc=General data F1=Next page F3=Range of graph F9=Print
    
```

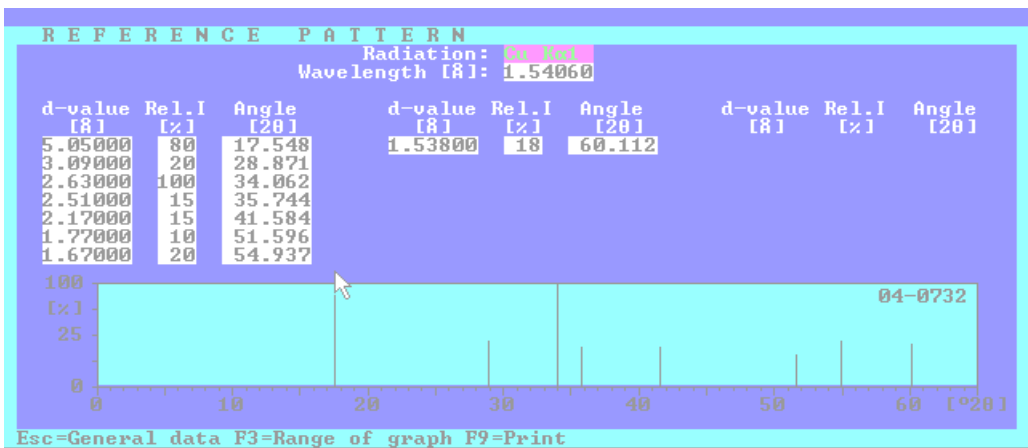


REFERENCE PATTERN

Database: C:\APDM\USERDB
Card id.: **04-0732**
Names: Manganese Oxide

Formula: Mn3O4
Deleted: NO
Elements: O Mn
Groups:
Subfiles: Inorganic
 Alloys
 Corrosion products

F1=Next pattern F2=Previous pattern F8=Graphics F9=Print



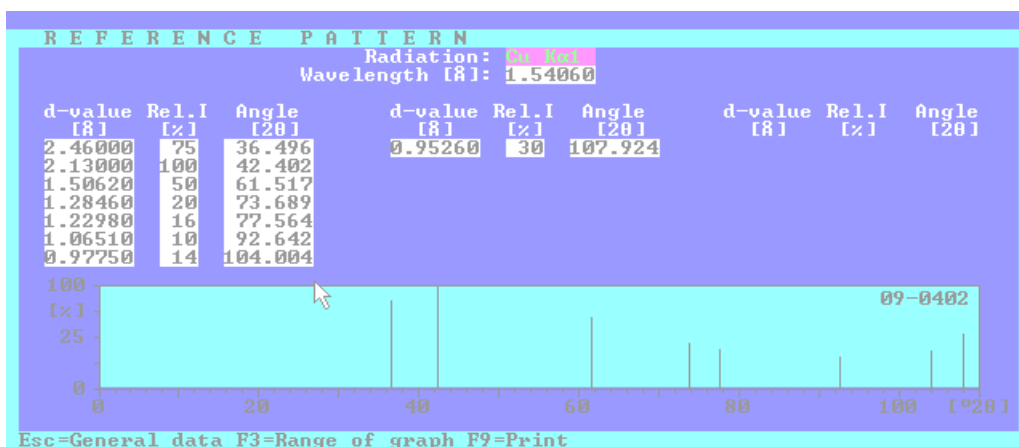
```

REFERENCE PATTERN
Database: C:\APDM\USERDB
Card id.: 09-0402
Names: Cobalt Oxide

Formula: CoO
Deleted: NO
Elements: O Co
Groups:
Subfiles: Inorganic
          Alloys
          Common phases
          NBS patterns
          Educational patterns
          Corrosion products

F1=Next pattern F2=Previous pattern F8=Graphics F9=Print

```



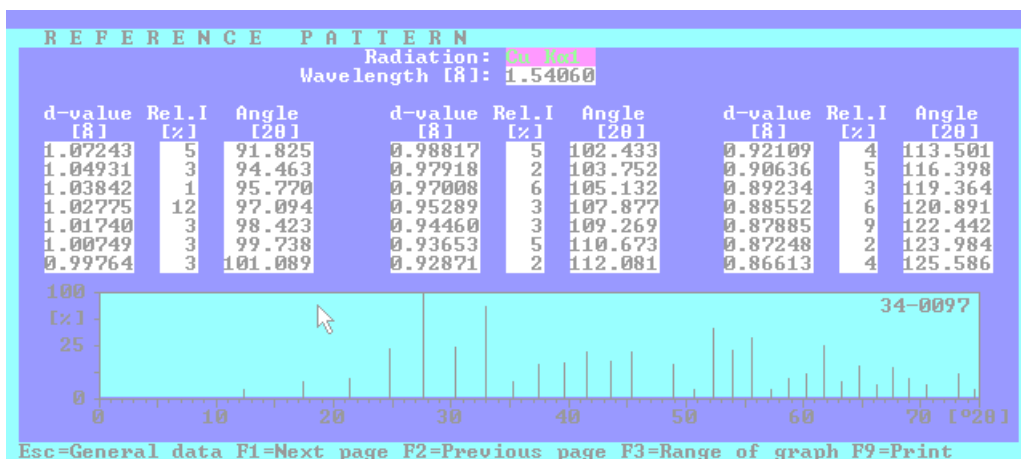
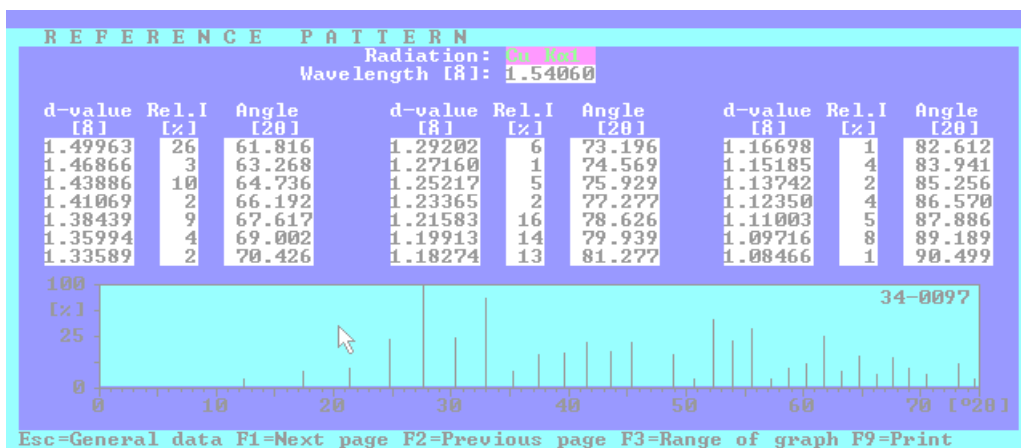
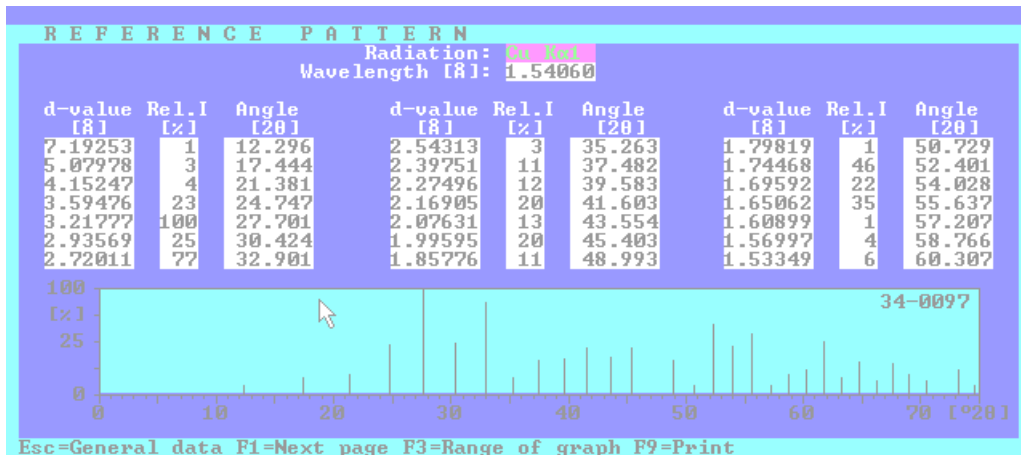
```

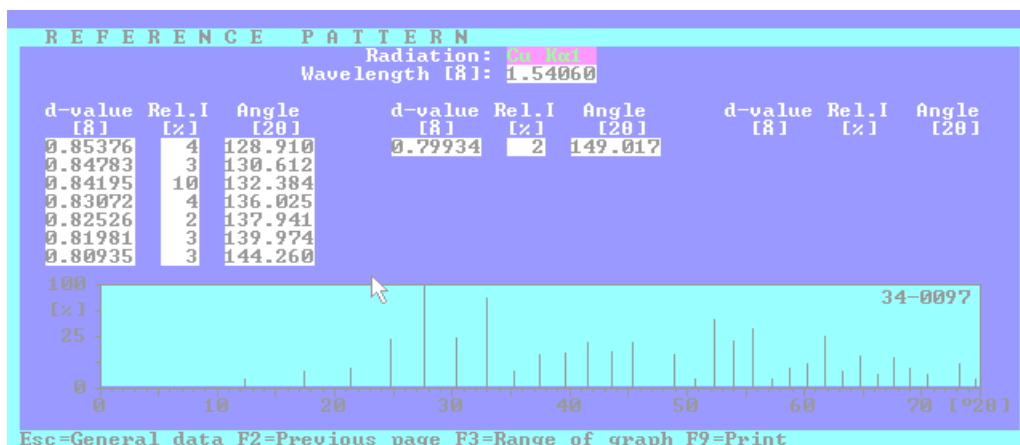
REFERENCE PATTERN
Database: C:\APDM\USERDB
Card id.: 34-0097
Names: Bismuth Titanium Oxide

Formula: Bi2TiO7
Deleted: NO
Elements: O Ti Bi
Groups:
Subfiles: Inorganic
          NBS patterns

F1=Next pattern F2=Previous pattern F8=Graphics F9=Print

```



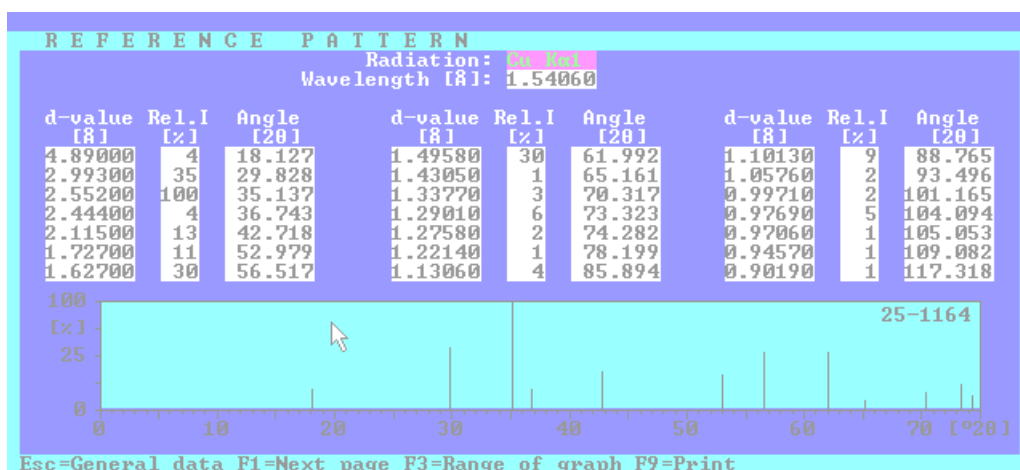


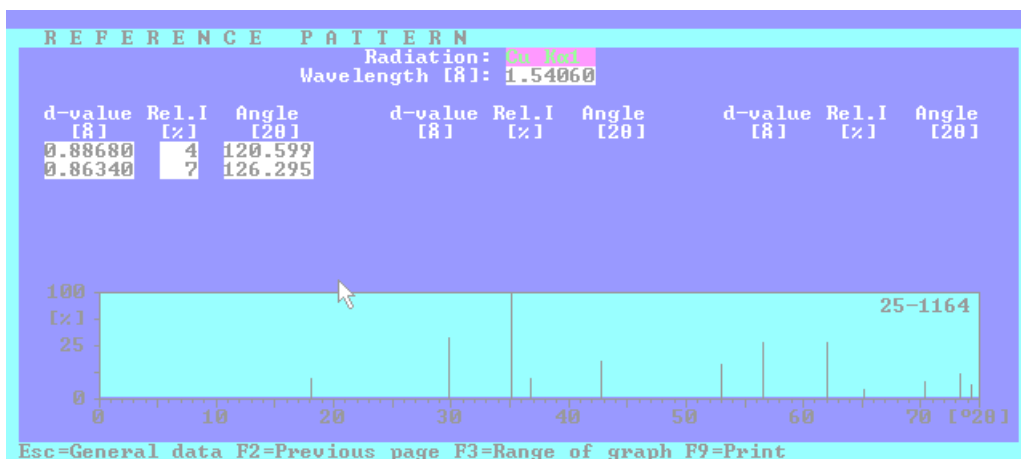
REFERENCE PATTERN

Database: C:\APDWIN\USERDB
Card id.: **25-1164**
Names: Zinc Titanium Oxide

Formula: Zn₂TiO₄
Deleted: NO
Elements: O Ti Zn
Groups:
Subfiles: Inorganic
NBS patterns

F1=Next pattern F2=Previous pattern F8=Graphics F9=Print



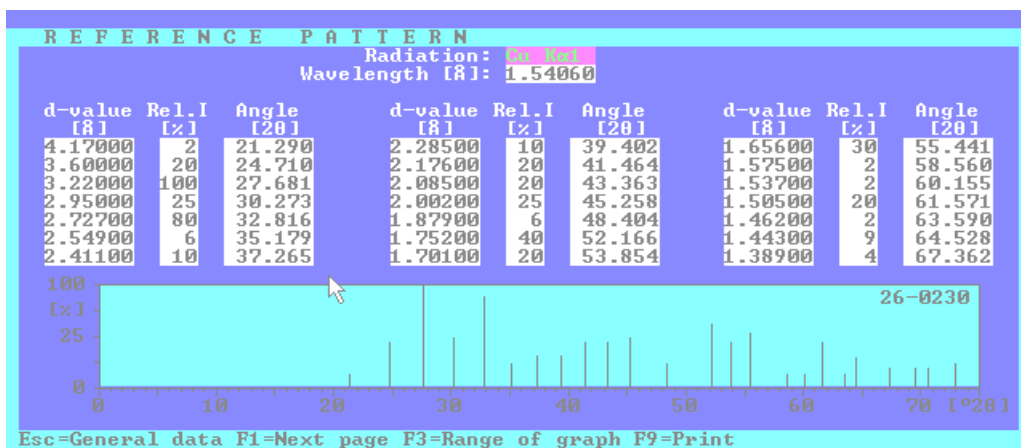


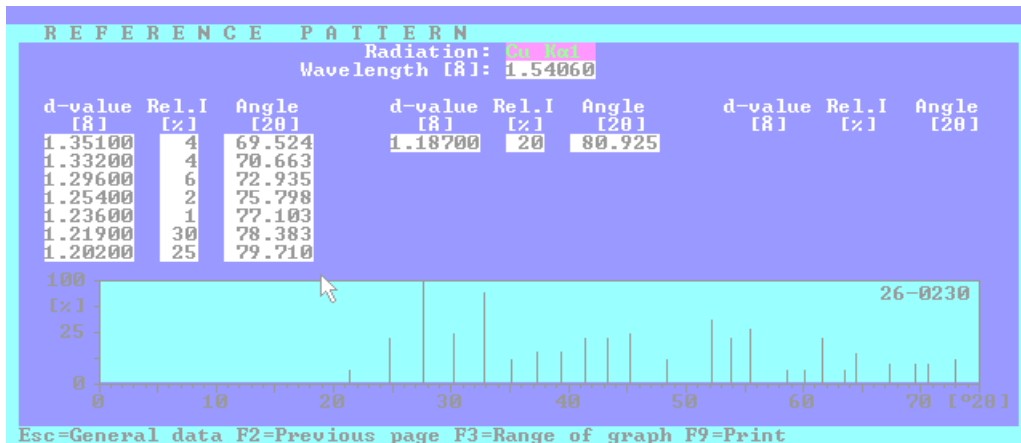
REFERENCE PATTERN

Database: C:\APDM\USERDB
Card id.: **26-0230**
Names: Zinc Bismuth Oxide

Formula: Bi₄₈ZnO₇₃
Deleted: NO
Elements: O Zn Bi
Groups:
Subfiles: Inorganic

F1=Next pattern F2=Previous pattern F8=Graphics F9=Print



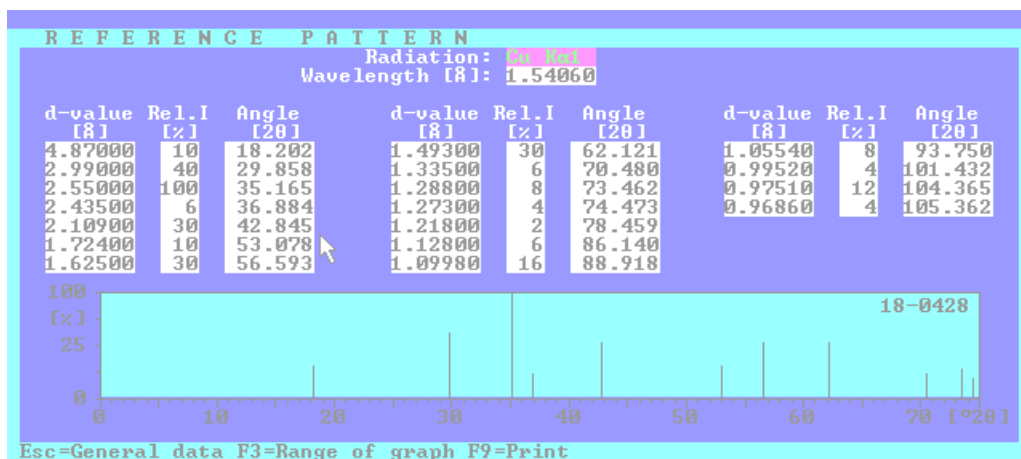


REFERENCE PATTERN

Database: C:\APDWIN\USERDB
Card id.: **18-0428**
Names: Cobalt Titanium Oxide

Formula: Co₂TiO₄
Deleted: YES
Elements: Ti Co
Groups:
Subfiles: Inorganic

F1=Next pattern F2=Previous pattern F8=Graphics F9=Print



APPENDIX C

CALCULATION THE STRESS IN TABLE 4.2 FOR X-RAY PHASE

ANALYSIS

By using the following equation: $\sigma = \left(\frac{2C_{13}^2 - C_{33}(C_{11} - C_{12})}{C_{13}} \right) \left(\frac{C_o - C}{C_o} \right)$

W4-Disc:

As-grown:

$$\sigma = (453.6) \left(\frac{5.206 - 5.215}{5.206} \right) = (453.6)(-0.00172877) = -0.784$$

N₂:

$$\sigma = (453.6) \left(\frac{5.206 - 5.201}{5.206} \right) = (453.6)(0.00096043) = 0.436$$

O₂:

$$\sigma = (453.6) \left(\frac{5.206 - 5.204}{5.206} \right) = (453.6)(0.00038417) = 0.174$$

P8-Disc:

As-grown:

$$\sigma = (453.6) \left(\frac{5.206 - 5.213}{5.206} \right) = (453.6)(-0.0013446) = -0.601$$

N₂:

$$\sigma = (453.6) \left(\frac{5.206 - 5.203}{5.206} \right) = (453.6)(0.00057626) = 0.261$$

O₂:

$$\sigma = (453.6) \left(\frac{5.206 - 5.205}{5.206} \right) = (453.6)(0.00019209) = 0.087$$

40nm-Disc:

As-grown:

$$\sigma = (453.6) \left(\frac{5.206 - 5.210}{5.206} \right) = (453.6)(-0.00076834) = -0.349$$

N₂:

$$\sigma = (453.6) \left(\frac{5.206 - 5.195}{5.206} \right) = (453.6)(0.00211295) = 0.958$$

O₂:

$$\sigma = (453.6) \left(\frac{5.206 - 5.198}{5.206} \right) = (453.6)(0.00153669) = 0.697$$

20nm-Disc:

As-grown:

$$\sigma = (453.6) \left(\frac{5.206 - 5.209}{5.206} \right) = (453.6)(-0.00057626) = -0.261$$

N₂:

$$\sigma = (453.6) \left(\frac{5.206 - 5.192}{5.206} \right) = (453.6)(0.0026892) = 1.219$$

O₂:

$$\sigma = (453.6) \left(\frac{5.206 - 5.194}{5.206} \right) = (453.6)(0.00230503) = 1.046$$

APPENDIX D

ISO 21348 information is provided courtesy of Space Environment Technologies
 spacenvironment@spacenvironment.net <http://SpaceWx.com>

ISO 21348 Definitions of Solar Irradiance Spectral Categories

Spectral category	Spectral sub-category	Wavelength range (nm)	Wavelength range (SI prefixes from Table 2)	Notes
Total Solar Irradiance				full-disk, 1 ua solar irradiance integrated across all wavelengths
Gamma-rays		$0.00001 \leq \lambda < 0.001$	$10 \text{ fm} \leq \lambda < 1 \text{ pm}$	
X-rays		$0.001 \leq \lambda < 0.1$	$1 \text{ pm} \leq \lambda < 0.10 \text{ nm}$	Hard X-rays
	XUV	$0.1 \leq \lambda < 10$	$0.10 \text{ nm} \leq \lambda < 10 \text{ nm}$	Soft X-rays
Ultraviolet		$100 \leq \lambda < 400$	$100 \text{ nm} \leq \lambda < 400 \text{ nm}$	Ultraviolet
	VUV	$10 \leq \lambda < 200$	$10 \text{ nm} \leq \lambda < 200 \text{ nm}$	Vacuum Ultraviolet
	EUV	$10 \leq \lambda < 121$	$10 \text{ nm} \leq \lambda < 121 \text{ nm}$	Extreme Ultraviolet
	H Lyman- α	$121 \leq \lambda < 122$	$121 \text{ nm} \leq \lambda < 122 \text{ nm}$	Hydrogen Lyman-alpha
	FUV	$122 \leq \lambda < 200$	$122 \text{ nm} \leq \lambda < 200 \text{ nm}$	Far Ultraviolet
	UVC	$100 \leq \lambda < 280$	$100 \text{ nm} \leq \lambda < 280 \text{ nm}$	Ultraviolet C
	MUV	$200 \leq \lambda < 300$	$200 \text{ nm} \leq \lambda < 300 \text{ nm}$	Middle Ultraviolet
	UVB	$280 \leq \lambda < 315$	$280 \text{ nm} \leq \lambda < 315 \text{ nm}$	Ultraviolet B
	NUV	$300 \leq \lambda < 400$	$300 \text{ nm} \leq \lambda < 400 \text{ nm}$	Near Ultraviolet
	UVA	$315 \leq \lambda < 400$	$315 \text{ nm} \leq \lambda < 400 \text{ nm}$	Ultraviolet A
Visible		$380 \leq \lambda < 760$	$380 \text{ nm} \leq \lambda < 760 \text{ nm}$	optical
	VIS	$360 \leq \lambda < 450$	$360 \text{ nm} \leq \lambda < 450 \text{ nm}$	purple
		$450 \leq \lambda < 500$	$450 \text{ nm} \leq \lambda < 500 \text{ nm}$	blue
		$500 \leq \lambda < 570$	$500 \text{ nm} \leq \lambda < 570 \text{ nm}$	green
		$570 \leq \lambda < 591$	$570 \text{ nm} \leq \lambda < 591 \text{ nm}$	yellow
		$591 \leq \lambda < 610$	$591 \text{ nm} \leq \lambda < 610 \text{ nm}$	orange
		$610 \leq \lambda < 760$	$610 \text{ nm} \leq \lambda < 760 \text{ nm}$	red
Infrared		$760 \leq \lambda < 1\,000\,000$	$760 \text{ nm} \leq \lambda < 1.00 \text{ mm}$	
	IR-A	$760 \leq \lambda < 1400$	$760 \text{ nm} \leq \lambda < 1.40 \text{ mm}$	Near Infrared
	IR-B	$1400 \leq \lambda < 3000$	$1.40 \text{ mm} \leq \lambda < 3.00 \text{ mm}$	Middle Infrared
	IR-C	$3000 \leq \lambda < 1\,000\,000$	$3.00 \text{ mm} \leq \lambda < 1.00 \text{ mm}$	Far Infrared
Microwave		$1\,000\,000 \leq \lambda < 15\,000\,000$	$1.00 \text{ mm} \leq \lambda < 15.00 \text{ mm}$	
	W	$3.00 \times 10^7 \leq \lambda < 5.35 \times 10^8$	$3.00 \text{ mm} \leq \lambda < 5.35 \text{ mm}$	$(100.0 \geq \nu > 56.0)$ GHz
	V	$5.35 \times 10^8 \leq \lambda < 6.52 \times 10^8$	$5.35 \text{ mm} \leq \lambda < 6.52 \text{ mm}$	$(56.0 \geq \nu > 46.0)$ GHz
	Q	$6.52 \times 10^8 \leq \lambda < 8.33 \times 10^8$	$6.52 \text{ mm} \leq \lambda < 8.33 \text{ mm}$	$(46.0 \geq \nu > 36.0)$ GHz
	K	$8.33 \times 10^8 \leq \lambda < 2.75 \times 10^7$	$8.33 \text{ mm} \leq \lambda < 27.5 \text{ mm}$	$(36.0 \geq \nu > 10.90)$ GHz
	X	$2.75 \times 10^7 \leq \lambda < 5.77 \times 10^7$	$27.50 \text{ mm} \leq \lambda < 57.70 \text{ mm}$	$(10.90 \geq \nu > 5.20)$ GHz
	C	$4.84 \times 10^7 \leq \lambda < 7.69 \times 10^7$	$48.40 \text{ mm} \leq \lambda < 76.90 \text{ mm}$	$(6.20 \geq \nu > 3.90)$ GHz
	S	$5.77 \times 10^7 \leq \lambda < 1.93 \times 10^8$	$57.70 \text{ mm} \leq \lambda < 193.00 \text{ mm}$	$(5.20 \geq \nu > 1.55)$ GHz
	L	$1.93 \times 10^8 \leq \lambda < 7.69 \times 10^8$	$193.00 \text{ mm} \leq \lambda < 769.00 \text{ mm}$	$(1.550 \geq \nu > 0.390)$ GHz
	P	$7.69 \times 10^8 \leq \lambda < 1.33 \times 10^9$	$769.00 \text{ mm} \leq \lambda < 1.33 \text{ m}$	$(0.390 \geq \nu > 0.225)$ GHz
Radio		$100\,000 \leq \lambda < 100\,000\,000\,000$	$0.10 \text{ mm} \leq \lambda < 100 \text{ m}$	measurements: $(1\,000\,000 \leq \lambda < 10\,000\,000\,000) \text{ nm}$
	EHF	$1.00 \times 10^8 \leq \lambda < 1.00 \times 10^7$	$1.00 \text{ mm} \leq \lambda < 10.00 \text{ mm}$	Extremely High Frequency ($300 \geq \nu > 30$) GHz
	SHF	$1.00 \times 10^7 \leq \lambda < 1.00 \times 10^6$	$10.00 \text{ mm} \leq \lambda < 100.00 \text{ mm}$	Super-High Frequency ($30 \geq \nu > 3$) GHz
	UHF	$1.00 \times 10^6 \leq \lambda < 1.00 \times 10^5$	$100.00 \text{ mm} \leq \lambda < 1.00 \text{ m}$	Ultra-High Frequency ($3000 \geq \nu > 300$) MHz
	VHF	$1.00 \times 10^5 \leq \lambda < 1.00 \times 10^4$	$1.00 \text{ m} \leq \lambda < 10.00 \text{ m}$	Very-High Frequency ($300 \geq \nu > 30$) MHz
	HF	$1.00 \times 10^4 \leq \lambda < 1.00 \times 10^3$	$10.00 \text{ m} \leq \lambda < 100.00 \text{ m}$	High Frequency ($30 \geq \nu > 3$) MHz

ISO 21348 Process for Determining Solar Irradiances Compliance Criteria

Rationale

The compliance criteria for this standard consist of activities that are common to solar irradiance product types (section 5) and solar irradiance spectral categories (section 6). These criteria specify a compliance process for the determination of solar irradiances that includes the reporting, documenting, publishing, and archiving of solar irradiance products.

APPENDIX E

CYTOTOXICITY RAW DATA

1- Live cells and dead cells for different samples of ZnO pure discs and doped discs (varistor) at 25 % ZnO concentration:

Sample	Live Cell	Dead Cell
Control (1)	417	6
	442	8
Control (2)	433	10
	449	6
W4-Disc (1)	311	22
	323	17
W4-Disc (2)	417	31
	403	13
P8-Disc (1)	345	20
	332	32
P8-Disc (2)	357	21
	417	34
40nm-Disc (1)	320	34
	313	27
40nm-Disc (2)	401	18
	327	29
20nm-Disc (1)	331	22
	338	30

20nm-Disc (2)	323	17
	315	39
W4-VDR (1)	361	12
	364	23
W4-VDR (2)	351	19
	371	20
P8-VDR (1)	382	22
	311	19
P8-VDR (2)	381	30
	380	31
40nm-VDR (1)	354	28
	360	22
40nm-VDR (2)	343	28
	381	31
20nm-VDR (1)	322	22
	370	30
20nm-VDR (2)	351	30
	362	29

2- Live cells and dead cells for different samples of ZnO pure discs and doped discs (varistor) at 50 % ZnO concentration:

Sample	Live Cell	Dead Cell
Control (1)	417	6
	442	8
Control (2)	433	10
	449	6
W4-Disc (1)	133	122
	223	117
W4-Disc (2)	315	131
	199	96
P8-Disc (1)	247	120
	135	78
P8-Disc (2)	98	221
	288	98
40nm-Disc (1)	192	134
	211	176
40nm-Disc (2)	199	180
	222	97
20nm-Disc (1)	177	122
	165	130
20nm-Disc (2)	274	107
	175	174
W4-VDR (1)	188	155
	197	123

W4-VDR (2)	295	189
	200	120
P8-VDR (1)	199	99
	132	119
P8-VDR (2)	95	180
	98	160
40nm-VDR (1)	86	176
	110	177
40nm-VDR (2)	79	165
	85	94
20nm-VDR (1)	76	118
	70	107
20nm-VDR (2)	151	178
	62	196

3- Live cells and dead cells for different samples of ZnO pure discs and doped discs (varistor) at 75 % ZnO concentration:

Sample	Live Cell	Dead Cell
Control (1)	417	6
	442	8
Control (2)	433	10
	449	6
W4-Disc (1)	101	122
	40	103
W4-Disc (2)	143	89
	141	154
P8-Disc (1)	110	190
	39	111
P8-Disc (2)	89	88
	121	138
40nm-Disc (1)	98	134
	77	166
40nm-Disc (2)	86	156
	121	208
20nm-Disc (1)	63	178
	103	222
20nm-Disc (2)	47	190
	43	210
W4-VDR (1)	83	218
	49	267

W4-VDR (2)	121	119
	43	220
P8-VDR (1)	111	135
	28	143
P8-VDR (2)	47	187
	11	131
40nm-VDR (1)	74	202
	34	151
40nm-VDR (2)	67	153
	88	104
20nm-VDR (1)	49	233
	53	130
20nm-VDR (2)	11	229
	27	245

4- Live cells and dead cells for different samples of ZnO pure discs and doped discs (varistor) at 100 % ZnO concentration:

Sample	Live Cell	Dead Cell
Control (1)	417	6
	442	8
Control (2)	433	10
	449	6
W4-Disc (1)	110	322
	131	317
W4-Disc (2)	93	231
	41	313
P8-Disc (1)	101	220
	71	232
P8-Disc (2)	35	321
	121	234
40nm-Disc (1)	57	134
	93	327
40nm-Disc (2)	67	218
	34	229
20nm-Disc (1)	43	322
	33	211
20nm-Disc (2)	22	307
	27	208
W4-VDR (1)	52	311
	61	290

W4-VDR (2)	33	319
	54	320
P8-VDR (1)	65	222
	55	319
P8-VDR (2)	34	230
	32	231
40nm-VDR (1)	20	328
	12	222
40nm-VDR (2)	14	228
	10	331
20nm-VDR (1)	9	322
	10	330
20nm-VDR (2)	7	330
	19	129

APPENDIX F

RESEARCH PAPER PUBLICATIONS AND CONFERENCES

(Total impact factor = 9.7)

1) Citation-Indexed journals

- 1) Rabab Sendi and Shahrom Mahmud; Particle size and Annealing Ambient Effect on Properties of ZnO-Bi₂O₃-Mn₂O₃ Varistor Derived from ZnO Micro-and Nanoparticle Powders; Superlattices and Microstructures; vol 69, pp. 212-225, 2014. IF= 1.564
- 2) Rabab Sendi and Shahrom Mahmud; Study on the Effects of High-Oxygen Thermal Annealing on the Structural, Electrical and Optical Properties of Undoped ZnO Discs Made from 40-nm ZnO Nanoparticles; Indian Journal of Physics, vol 87 (6), pp. 523-531, 2013. IF= 1.785
- 3) Rabab Sendi and Shahrom Mahmud; Impact of Sintering Temperature on the Structural, Electrical and Optical Properties of Doped ZnO Nanoparticle-Based Discs; Applied Surface Science, vol 261, pp. 128-136, 2012, Q1. IF= 2.112
- 4) Rabab Sendi and Shahrom Mahmud; Comparative Study on the Effects of Different Annealing Conditions on the Surface Morphology, Crystallinity, and Optical Properties of ZnO Micro/Nanoparticle-Based Discs; Applied Surface Science, vol 258 (24), pp. 9954-9960, 2012, Q1. IF= 2.112
- 5) Rabab Sendi and Shahrom Mahmud; Stress Control in ZnO Nanoparticle-Based Discs via High-Oxygen Thermal Annealing at Various Temperatures; Journal of Physical Science, vol 24 (1), pp. 1-15, 2013. IF= 0.03
- 6) Rabab Sendi and Shahrom Mahmud; Quantum Size Effect on ZnO Nanoparticle-Based Discs Synthesized by Mechanical Milling; Applied Surface Science, vol 258 (20), pp. 8026-8031, 2012, Q1. IF= 2.112
- 7) Rabab Sendi, Shahrom Mahmud and Azman Seeni; In Vitro Cytotoxicity Tests of ZnO-Bi₂O₃-Mn₂O₃-Based Varistor Fabricated From ZnO Micro and Nanoparticle Powders on L929 Mouse Cells; AIP Proceedings, vol 1621, pp. 663-669, 2014.
- 8) Rabab Sendi, Shahrom Mahmud, and Amna Sirelkhatim; Comparative Study Between the Effects of Oxidizing and Reducing Atmosphere on the Properties of

ZnO-Bi₂O₃-Mn₂O₃ Varistor Fabricated From Micro and Nanoparticles of ZnO; *Advanced Materials Research*, vol 925, pp. 428-432, 2014.

- 9) Rabab Sendi and Shahrom Mahmud; Analysis of Stress and Strain in ZnO Nanoparticle-Bi₂O₃-Mn₂O₃ Varistor Ceramics at Different Annealing Temperatures Fabricated From Micro and Nanoparticles of ZnO; *Advanced Materials Research*, vol 795, pp. 35-41, 2013.
- 10) Rabab Sendi and Shahrom Mahmud; Post-growth Annealing Effects on the Photoluminescence of ZnO Nanoparticles-Based Disc; *Advanced Materials Research*, vol 626, pp. 844-848, 2013.
- 11) Rabab Sendi and Shahrom Mahmud; Effect of Temperature Treatment on the Properties of ZnO Nanoparticle-Bi₂O₃-Mn₂O₃ Varistor Ceramics; 2012 10th IEEE International Conference on Semiconductor Electronics, ICSE 2012-Proceedings, art. No. 6417115, pp. 163-167, 2012.
- 12) Rabab Sendi and Shahrom Mahmud; Impact of High-Oxygen Thermal Annealing on the Structural, Optical and Electrical Properties of ZnO Discs Made from 20-nm ZnO Nanoparticles; *AIP Proceedings*, vol 1482, pp. 655-660, 2012.
- 13) Rabab Sendi and Shahrom Mahmud; Density Impact of Doped ZnO Discs on the Structural, Electrical and Optical Properties in the Ohmic Region; *AIP Proceedings*, vol 1482, pp. 706-711, 2012.
- 14) Rabab Sendi and Shahrom Mahmud; Comparative Study of the Cytotoxic Effects of ZnO-Bi₂O₃-Mn₂O₃-Based Varistor derived from ZnO Micro and Nanoparticle Powders on L929 Mouse Cells under Various Concentrations. (under review)
- 15) Rabab Sendi and Shahrom Mahmud; Borosilicate Frit addition Impact on the Structure, Electric and Dielectric Behaviors of ZnO nanoparticles-Based Varistors. (under review)

2) Conferences

- 1) Rabab Sendi, Shahrom Mahmud and Azman Seeni; In Vitro Cytotoxicity Tests of ZnO-Bi₂O₃-Mn₂O₃-Based Varistor Fabricated From ZnO Micro and Nanoparticle Powders on L929 Mouse Cells; *AIP Proceedings*, vol 1621, pp. 663-669, 2014.
- 2) Rabab Sendi, Shahrom Mahmud, and Amna Sirelkhatim; Comparative Study Between the Effects of Oxidizing and Reducing Atmosphere on the Properties of

ZnO-Bi₂O₃-Mn₂O₃ Varistor Fabricated From Micro and Nanoparticles of ZnO; *Advanced Materials Research*, vol 925, pp. 428-432, 2014.

- 3) Rabab Sendi and Shahrom Mahmud; Analysis of Stress and Strain in ZnO Nanoparticle-Bi₂O₃-Mn₂O₃ Varistor Ceramics at Different Annealing Temperatures Fabricated From Micro and Nanoparticles of ZnO; *Advanced Materials Research*, vol 795, pp. 35-41, 2013.
- 4) Rabab Sendi and Shahrom Mahmud; Post-growth Annealing Effects on the Photoluminescence of ZnO Nonoparticles-Based Disc; *Advanced Materials Research*, vol 626, pp. 844-848, 2013.
- 5) Rabab Sendi and Shahrom Mahmud; Effect of Temperature Treatment on the Properties of ZnO Nanoparticle-Bi₂O₃-Mn₂O₃ Varistor Ceramics; 2012 10th IEEE International Conference on Semiconductor Electronics, ICSE 2012-Proceedings, art. No. 6417115, pp. 163-167, 2012.
- 6) Rabab Sendi and Shahrom Mahmud; Impact of High-Oxygen Thermal Annealing on the Structural, Optical and Electrical Properties of ZnO Discs Made from 20-nm ZnO Nanoparticles; *AIP Proceedings*, vol 1482, pp. 655-660, 2012.
- 7) Rabab Sendi and Shahrom Mahmud; Density Impact of Doped ZnO Discs on the Structural, Electrical and Optical Properties in the Ohmic Region; *AIP Proceedings*, vol 1482, pp. 706-711, 2012.